



**HAL**  
open science

# Où et quand se produisent les grands séismes ? Comment les anticiper ?

Quentin Bletery

► **To cite this version:**

Quentin Bletery. Où et quand se produisent les grands séismes ? Comment les anticiper ?. Géophysique [physics.geo-ph]. Université Côte d'Azur; ED n°364 : Sciences fondamentales et appliquées, 2022. tel-03869413

**HAL Id: tel-03869413**

**<https://hal.science/tel-03869413v1>**

Submitted on 24 Nov 2022

**HAL** is a multi-disciplinary open access archive for the deposit and dissemination of scientific research documents, whether they are published or not. The documents may come from teaching and research institutions in France or abroad, or from public or private research centers.

L'archive ouverte pluridisciplinaire **HAL**, est destinée au dépôt et à la diffusion de documents scientifiques de niveau recherche, publiés ou non, émanant des établissements d'enseignement et de recherche français ou étrangers, des laboratoires publics ou privés.



Distributed under a Creative Commons Attribution 4.0 International License



---

# HABILITATION À DIRIGER DES RECHERCHES

DE L'UNIVERSITÉ CÔTE D'AZUR

ÉCOLE DOCTORALE SCIENCES FONDAMENTALES ET APPLIQUÉES

Présentée par

**Quentin Bletery**

---

---

**Où et quand se produisent les grands séismes ?  
Comment les anticiper ?**

---

Soutenue le 4 Novembre 2022  
Devant la Commission d'Examen composée de :

## JURY

Isabelle Manighetti	Physicienne à l'Observatoire de la Côte d'Azur	Présidente du Jury
Cécile Lasserre	Directrice de Recherche au CNRS	Rapportrice
Jean-Philippe Avouac	Professeur au California Institute of Technology	Rapporteur
Jean-Paul Montagner	Professeur à l'Institut de Physique du Globe de Paris	Rapporteur
Cécile Cornou	Directrice de Recherche à l'IRD	Examinatrice
Michel Campillo	Professeur à l'Université Grenoble Alpes	Examineur





---

# Remerciements

Je remercie les membres du Jury, Isabelle Manighetti, Cécile Lasserre, Cécile Cornou, Jean-Philippe Avouac, Jean-Paul Montagner et Michel Campillo d'avoir considéré mon travail avec intérêt et pris le temps de le juger.

Je remercie les personnes qui ont participé à la rédaction des publications qui composent, en partie ce manuscrit, Amanda M. Thomas, Alan W. Rempel, Leif Karlstrom, Anthony Sladen, Louis de Barros, Jeanne L. Hardebeck, Olivier Cavalié, Jean-Mathieu Nocquet, Théa Ragon, Jessica C. Hawthorne, Robert M. Skarbek, Randy D. Krogstad, Andrea Licciardi, Bertrand Rouet-Leduc, Jean-Paul Ampuero et Kévin Juhel.

Je remercie plus personnellement les chercheurs qui m'ont formé au métier de la recherche, Luis Rivera, Mark Simons, Anthony Sladen, Bertrand Delouis, Amanda M. Thomas et Alan W. Rempel ainsi que les doctorants et postdoctorants avec qui j'ai la chance de travailler, Gabriela Arias, Pablo Lara, Andrea Licciardi et Kévin Juhel.

Merci au Seismological Laboratory du California Institute of Technology, au département de Sciences de la Terre de l'Université d'Oregon et à Géoazur, ainsi qu'à tous les chercheurs qui y travaillent, de m'avoir accueilli aux différentes étapes de ma carrière.

Merci à ma famille, à mes amis, ma compagne, pour avoir traverser des moments difficiles avec moi, Aline, Anne-Laure, Nicolas, Joris, Niels, François-Xavier, Raphaël, Agnès, Jacques et bien sûr Laure. Merci infiniment.

*« Le Vrai est le Tout »*

Georg Wilhelm Friedrich Hegel

## Remerciements

---

*À mon père,*

## Table des matières

---

---

# Table des matières

<b>Introduction</b>	<b>1</b>
<b>I Anticiper les séismes, pourquoi est-ce si difficile ?</b>	<b>3</b>
1 Qu'est-ce qu'un séisme ? . . . . .	3
1.1 Observations en surface . . . . .	3
1.2 Mécanisme . . . . .	5
1.3 Que se passe-t'il en profondeur ? . . . . .	7
2 Que font les failles entre deux séismes ? . . . . .	9
2.1 Glissement post-sismique . . . . .	10
2.2 Glissement inter-sismique . . . . .	11
2.3 Glissement transitoire . . . . .	12
3 Est-il possible de prédire les séismes ? . . . . .	14
3.1 Approche physique . . . . .	14
3.2 Approche statistique . . . . .	16
3.3 Approche observationnelle . . . . .	18
4 Anticiper les séismes autrement : l'alerte précoce . . . . .	19
4.1 L'alerte sismique . . . . .	19
4.2 L'alerte tsunami . . . . .	21
4.3 La découverte prometteuse des PEGS . . . . .	22
5 Possibilités offertes par l'émergence de l'IA . . . . .	24
5.1 Principes simplifiés de l'IA à l'usage des non-spécialistes . . . . .	24
5.2 Accomplissements récents en sismologie . . . . .	26

<b>II</b>	<b>Où se produisent les grands séismes ?</b>	<b>27</b>
1	Liens entre failles et séismes . . . . .	27
2	Les grands séismes se produisent sur les grandes failles planes . . . . .	28
3	Imager le seuil de rupture le long des grandes failles . . . . .	35
4	Imager la distribution du couplage le long des grandes failles . . . . .	47
5	Perspectives . . . . .	59
<b>III</b>	<b>Quand se produisent les grands séismes ?</b>	<b>61</b>
1	Comment étudier la dynamique des grandes failles ? . . . . .	61
2	Les fronts secondaires de glissement associés aux séismes lents . . . . .	62
3	La coalescence de séismes lents comme possible mécanisme d’initiation des grands séismes . . . . .	72
4	Perspectives . . . . .	80
<b>IV</b>	<b>Comment anticiper les grands séismes ?</b>	<b>83</b>
1	L’alerte sismique/tsunami, une course contre le temps . . . . .	83
2	Estimation instantanée de la croissance des très grands séismes . . . . .	85
3	Perspectives . . . . .	106
3.1	Applications régionales . . . . .	106
3.2	Débruitage des PEGS par IA . . . . .	108
3.3	Vers un algorithme d’alerte global . . . . .	109
3.4	Un algorithme alternatif efficace dans les toutes premières secondes . . .	110
	<b>Conclusion</b>	<b>115</b>
	<b>Références bibliographiques</b>	<b>117</b>
	<b>Annexe</b>	<b>141</b>
1	Curriculum Vitae . . . . .	141
2	Liste des publications . . . . .	145

---

# Introduction

Pourquoi la Terre tremble ? Cette question, que se posent les hommes – probablement – depuis toujours, a trouvé, à la fin des années 1960, une réponse partielle avec la théorie de la tectonique des plaques : des plaques rigides, entraînées par un manteau asthénosphérique en mouvement, glissent les unes par rapport aux autres. Leur mouvement relatif est accommodé lors d'évènements rares mais violents : les séismes. Si ce cadre conceptuel simple a permis de comprendre l'origine des tremblements de terre, il ne permet pas de répondre aux deux questions fondamentales qui permettraient de limiter le coût humain de ces catastrophes : Où et Quand se produisent les grands séismes ? Ce mémoire synthétise mes travaux de recherche réalisés depuis la soutenance de mon doctorat qui, par divers angles, ont tenté de répondre à ces questions.

Le chapitre 1 présente un bref état de l'art autour des concepts de rupture sismique, cycle sismique, séismes lents, des observations qui les contraignent ainsi que des outils et méthodes utilisés pour étudier le comportement des failles. Je mettrai en relief les difficultés à anticiper les ruptures sismiques, un phénomène impossible à prédire à partir des observations et outils que l'on utilise à l'heure actuelle. Je présenterai brièvement les méthodes d'alerte sismique et tsunami, une alternative à la prédiction pour réduire le coût sociétal des tremblements de terre. Enfin, je présenterai un outil émergent ayant le potentiel pour révolutionner la recherche autour de l'alerte : l'Intelligence Artificielle (IA).

Le chapitre 2 s'intéresse à la question du « Où ? ». Où les grands séismes sont-ils le plus susceptible de se produire ? Je présenterai dans ce chapitre trois études tentant de répondre à cette question par trois angles différents. La première montre que les grandes ruptures sismiques se produisent sur des portions de failles particulièrement planes. La seconde décrit un cadre théorique permettant d'évaluer la distribution spatiale du seuil de rupture en contraintes le long



des failles. Appliquée au Japon cette approche révèle que les grands séismes se produisent sur des portions de faille présentant un seuil de rupture particulièrement homogène. La troisième approche est une inversion Bayésienne de la distribution spatiale du couplage inter-sismique le long des failles Nord- et Est- Anatolienne, en Turquie. Cette approche permet d'identifier où les contraintes s'accumulent le long de ces grandes failles, et donc où celles-ci sont susceptibles d'être relâchées au cours d'un événement sismique à venir.

Le chapitre 3 s'intéresse à la question du « Quand ? ». Répondre à cette question est un échec notoire de la sismologie contemporaine. Mais est-ce réellement impossible ? Serait-il possible de connaître la dynamique des failles au point de pouvoir « prédire » quand de grands événements pourraient se produire. Comment étudier cette dynamique ? L'identification d'événements de glissement transitoires – les séismes lents – ouvre une fenêtre pour *monitorer* les failles en ce sens. Je présenterai dans ce chapitre une étude sur la dynamique interne des séismes lents, laquelle a mis en évidence que ces derniers sont constitués de sous-épisodes de glissement. Puis je présenterai une étude dans laquelle nous montrons que la coalescence de séismes lents distincts génère un « emballement » du glissement, un mécanisme observable sur les failles naturelles qui pourrait être à l'origine de la nucléation de grands séismes.

Si le chapitre 3 suggère la possibilité de la prédiction des séismes, celle-ci reste pour l'heure très hypothétique. Le chapitre 4 vise à dépasser la question de la prédictibilité pratique ou théorique des séismes à travers une approche concrète pour anticiper les tremblements de terre et les tsunamis. Je présenterai PEGSnet, un algorithme d'IA que nous avons développé, qui utilise un signal, identifié récemment, d'amplitude très faible mais précédant les premières ondes sismiques. Ce signal d'origine gravitationnelle a la propriété de se propager à la vitesse de la lumière. Grâce à cette propriété, PEGSnet est capable d'évaluer quasi-instantanément l'évolution de la magnitude des grands séismes et ainsi apporter des informations cruciales dans la décision de lancer une alerte sismique/tsunami avant les premières secousses et les raz de marée. Le chapitre se poursuivra par quelques perspectives sur lesquelles nous travaillons actuellement avec les doctorants et postdoctorants que j'encadre. Je présenterai quelques uns des développements en cours autour de PEGSnet, l'un de nos grands objectifs étant de développer un algorithme d'alerte global capable de suivre l'évolution de la magnitude des grands séismes en tout point de la Terre à partir de sismomètres installés partout sur Terre. Je présenterai ensuite un second algorithme d'IA qui vise à combler le déficit de performance de PEGSnet pour les séismes de magnitude inférieure à 8.3. Cet algorithme n'utilise que 3 secondes d'enregistrement sur une unique station, procurant ainsi des informations pertinentes pour l'alerte en des temps records.

Enfin, ce mémoire s'achèvera par quelques réflexions sur les possibilités apportées par l'IA en sismologie : la prédiction est-elle réellement impossible ?

---

---

# Chapitre I

---

## Anticiper les séismes, pourquoi est-ce si difficile ?

### 1 Qu'est-ce qu'un séisme ?

Un séisme est un glissement rapide le long d'une faille, interface entre deux « blocs de Terre » en mouvement relatif l'un par rapport à l'autre. Il existe des séismes de toutes tailles. Les plus petits se produisent de manière quasi-continue sans qu'on les ressente. Les plus grands génèrent des secousses capables de détruire des villes. Certains peuvent générer des tsunamis qui font encore plus de dégâts. Le bilan humain de ces catastrophes naturelles s'élève à près d'un million de morts sur les trois dernières décennies. Ces phénomènes apparaissent comme des événements chaotiques que la Science moderne n'arrive pas à prédire. Nous disposons pourtant de nombreuses observations à partir desquelles nous essayons de comprendre ce qu'est un séisme, dans l'espoir, un jour, de savoir où et quand la Terre tremblera.

#### 1.1 Observations en surface

Les séismes se produisent sur des failles à plusieurs kilomètres de profondeur. Les observations de ces événements dont l'on dispose sont malheureusement toutes obtenues à partir de capteurs à la surface de la Terre. Nous ne disposons donc que d'observations indirectes pour étudier ces phénomènes. Les deux grands types d'observations que l'on utilise à cette fin sont les observations sismologiques et les observations géodésiques.

##### Observations sismologiques

Les ruptures sismiques génèrent un champ d'onde responsable des « tremblements » de la Terre ressentis aux alentours de la rupture. Ce champ d'onde est enregistré localement, et globalement sur la planète, par des appareils de mesure appelés sismomètres. Il existe deux grands types de sismomètres : les vélocimètres qui enregistrent la vitesse des mouvements du

sol et les accéléromètres qui enregistrent leur accélération.

Passer d'un sismogramme en vitesse à un sismogramme en accélération est très simple et ne nécessite que de dériver le signal. La réelle différence entre les deux types d'instruments est leur sensibilité à différentes fréquences. Les vélocimètres sont également appelés sismomètres large-bande car ils sont capables d'enregistrer des signaux sur une gamme de fréquences très large ( $\sim 0.01 - 20$  Hz). Ce sont les instruments les plus employés pour étudier les séismes. Ils contraignent par exemple les signatures basse fréquence des séismes qui permettent de déterminer leur magnitude [*Hanks and Kanamori, 1979*].

Les accéléromètres sont beaucoup plus bruités à basse fréquence ( $< 1$  Hz) mais sont utiles pour enregistrer les mouvements forts du sol. En effet, proches d'une forte source sismique ils saturent moins que les vélocimètres. Ils sont ainsi utiles pour caractériser rapidement la source sismique dans une optique d'alerte [*Wu and Kanamori, 2008*].

### Observations géodésiques

Les observations géodésiques sont des mesures de déplacement du sol au cours du temps. Elles sont très utiles pour contraindre la distribution spatiale des ruptures sismiques. Les deux techniques géodésiques les plus utilisées pour étudier la source sismique sont le *Global Navigation Satellite System* (GNSS) et l'interférométrie radar.

Le système GNSS est constitué d'une constellation de satellites permettant de localiser précisément des récepteurs à la surface de la Terre. Le déploiement d'un grand nombre de récepteurs – appelés stations GNSS (ou abusivement stations GPS) – permet de déterminer de manière précise l'orbite des satellites dans un référentiel terrestre régulièrement mis à jour, l'*International Terrestrial Reference Frame* (ITRF) [*Altamimi et al., 2002, 2007, 2011, 2016*]. Après un post-traitement élaboré [*King, 1995*], les mesures GNSS peuvent atteindre une précision millimétrique. Lors d'un séisme, le GNSS enregistre le déplacement du sol à l'emplacement des stations sur les trois composantes de l'espace. Ces déplacements peuvent être de plusieurs mètres pour de grands événements [e.g., *Ozawa et al., 2011*]. Historiquement utilisé pour des mesures journalières – servant en particulier à la caractérisation du champ de déplacement long-terme [e.g., *DeMets et al., 2000; Nocquet and Calais, 2004; Calais et al., 2006*] – le GNSS permet aujourd'hui des mesures haute fréquence (jusqu'à 10 Hz) [*Melgar et al., 2020*]. Toutefois, la précision dépend d'un « moyennage » des erreurs sur un grand nombre de mesures. Elle a donc tendance à décroître lorsque l'on échantillonne à plus haute fréquence.

L'autre grande technique de géodésie spatiale utilisée pour étudier les tremblements de Terre est l'interférométrie radar, ou InSAR pour *Interferometric Synthetic Aperture Radar*. Le

principe de cette méthode est d'utiliser les différences de phase entre deux images radar (SAR). Un interférogramme entre une image SAR acquise après un séisme et une image acquise avant donne le champ de déplacement généré par le séisme en surface dans la direction de visée du satellite. Là où le GNSS permet des mesures ponctuelles, l'InSAR permet des mesures sur de vastes étendues spatiales. Obtenir un interférogramme nécessite toutefois un certain nombre d'étapes de traitement, l'étape la plus cruciale étant la correction atmosphérique [Doin *et al.*, 2009; Jolivet *et al.*, 2011]. La résolution d'un interférogramme bien corrigé est de l'ordre du centimètre mais dépend de la fréquence du radar, qui varie d'un satellite à l'autre. La résolution temporelle est déterminée par la fréquence de passage des satellites. Historiquement de l'ordre du mois avec les satellites d'ancienne génération ERS-1, ERS-2, ALOS, ENVISAT, elle est depuis le lancement du programme SENTINEL de moins d'une semaine. Comme le GNSS, l'InSAR est utilisé pour mesurer la déformation lors d'un séisme [e.g., Massonnet *et al.*, 1993; Lasserre *et al.*, 2005], mais également la déformation long-terme [e.g., Cavalié *et al.*, 2008].

### Autres types d'observations

La manifestation en surface la plus impressionnante des séismes est certainement le tsunami qui suit les plus grands d'entre eux. Des bouées dites DART (pour Deep-ocean Assessment and Reporting of Tsunamis) ou encore des capteurs de pression sous-marin [Hino *et al.*, 2001; Maeda *et al.*, 2011] permettent de mesurer l'élévation du niveau de l'eau et donc le passage éventuel d'un tsunami avant qu'il ne frappe les côtes. Des mesures de la perturbation des signaux GNSS dans l'ionosphère permettent également une mesure indirecte du déplacement co-sismique [Calais and Minster, 1995] et possiblement du tsunami [Heki *et al.*, 2006; Rolland *et al.*, 2011; Bagiya *et al.*, 2020; Sunil *et al.*, 2021].

La technologie la plus prometteuse en développement est certainement celle du *Distributed Acoustic Sensing* (DAS) appliquée à des câbles de télécommunication en fibre optique. Cette technologie permet virtuellement d'avoir accès à des milliers de sismogrammes le long des câbles, une densité instrumentale sans précédent à faible coût, qui pourrait révolutionner l'observation sismique en particulier en mer [Sladen *et al.*, 2019].

## 1.2 Mécanisme

Expliquer les diverses manifestations de la source sismique observées à la surface de la Terre nécessite de résoudre différents problèmes physiques, selon les type de de données. Les équations décrivant la résolution de ces divers problèmes sont détaillées dans ma thèse [Bletery, 2015]. Je me contenterai ici d'exposer succinctement les moyens couramment employées pour modéliser

les ondes sismiques, le déplacement du sol et le tsunami.

### Les ondes sismiques

Les ondes sismiques enregistrées sur les sismomètres sont bien expliquées par le théorème de représentation, qui donne le champ d'onde généré par une dislocation cisailante ponctuelle dans un milieu isotrope, homogène, infini [Aki and Richards, 2002]. Certains termes peuvent être négligés en champs lointain (si les stations sont loin de la source), comme dans le code développé par Nabelek [1984] dans une Terre stratifiée (1D). Dans le cas de stations proches, tous les termes de radiations doivent être pris en compte, ce que permet la méthode des nombres d'onde discrets [e.g., Bouchon, 1981], également dans une Terre stratifiée. Des méthodes de résolution numérique en 3D existent, comme SPECFEM ou sa version simplifiée (plus rapide) AXISEM [Nissen-Meyer et al., 2014], mais sont limitées par leur coût en terme de temps de calcul ainsi que par notre connaissance limitée de la complexité 3D de la Terre, limitant l'intérêt d'une complexification numérique top poussée pour l'étude de la source.

### Le déplacement du sol

Le déplacement du sol enregistré par les données géodésiques est donné par une solution analytique pour une dislocation « rectangulaire » dans un milieu élastique homogène semi-infini. Cette solution analytique connue sous le nom de solution d'Okada a en fait été résolue par Mansinha and Smylie [1971] à partir d'une intégrale proposée par Steketee [1958]. Okada [1985] a, des années plus tard, implémenté cette solution analytique dans un script utilisé par toute la communauté depuis. Des codes intégrant des degrés de complexité supplémentaires ont depuis été développés, comme celui de Zhu and Rivera [2002] qui considère une Terre stratifiée par la technique des matrices propagatives de Thompson-Haskell ou celui de Pollitz [1996] qui permet de considérer une Terre sphérique stratifiée à partir de calculs de modes propres. Aujourd'hui, des codes comme PyLith permettent de prendre en compte la complexité 3D de la Terre [e.g., Romano et al., 2014], mais comme pour le champ d'onde sismique, notre connaissance limitée de cette complexité rend sa prise en compte presque superflue pour l'étude de la source.

### Le tsunami

Le mécanisme à l'origine des tsunamis est assez simple : un séisme entraîne une élévation du fond de l'océan qui peut, pour les plus grands événements, atteindre plusieurs mètres et s'étendre sur des centaines de kilomètres. La colonne d'eau située au dessus de la partie du fond de l'océan sur-élevée par le séisme est automatiquement translatée verticalement. Un immense volume

d'eau se retrouve alors au dessus du niveau de l'équipotentiel. Le ré-équilibrage du niveau de la mer se fait par propagation d'une onde de gravité : un tsunami. Des codes de simulation numérique comme COMCOT ou NEOWAVE [Yamazaki *et al.*, 2009, 2011] permettent calculer le tsunami partout sur Terre à partir des paramètres du séisme. Ces codes négligent toutefois la contribution du déplacement horizontal du fond de l'océan [Tanioka and Satake, 1996; Bletery *et al.*, 2015] ainsi que des phénomènes complexes de dispersion induits par la réponse élastique de la Terre et l'hétérogénéité de la densité des couches d'eau [Tsai *et al.*, 2013; Watada, 2013; Allgeyer and Cummins, 2014].

### 1.3 Que se passe-t'il en profondeur ?

Les observations sismologiques permettent depuis de nombreuses années de localiser la source des séismes en profondeur [e.g., Kennett and Engdahl, 1991]. On dispose ainsi de volumineux catalogues de sismicité nous renseignant sur où les séismes se produisent à travers le monde. Ces catalogues ont permis de modéliser la géométrie des grandes failles (Figure I.1) [Hayes *et al.*, 2012, 2018].

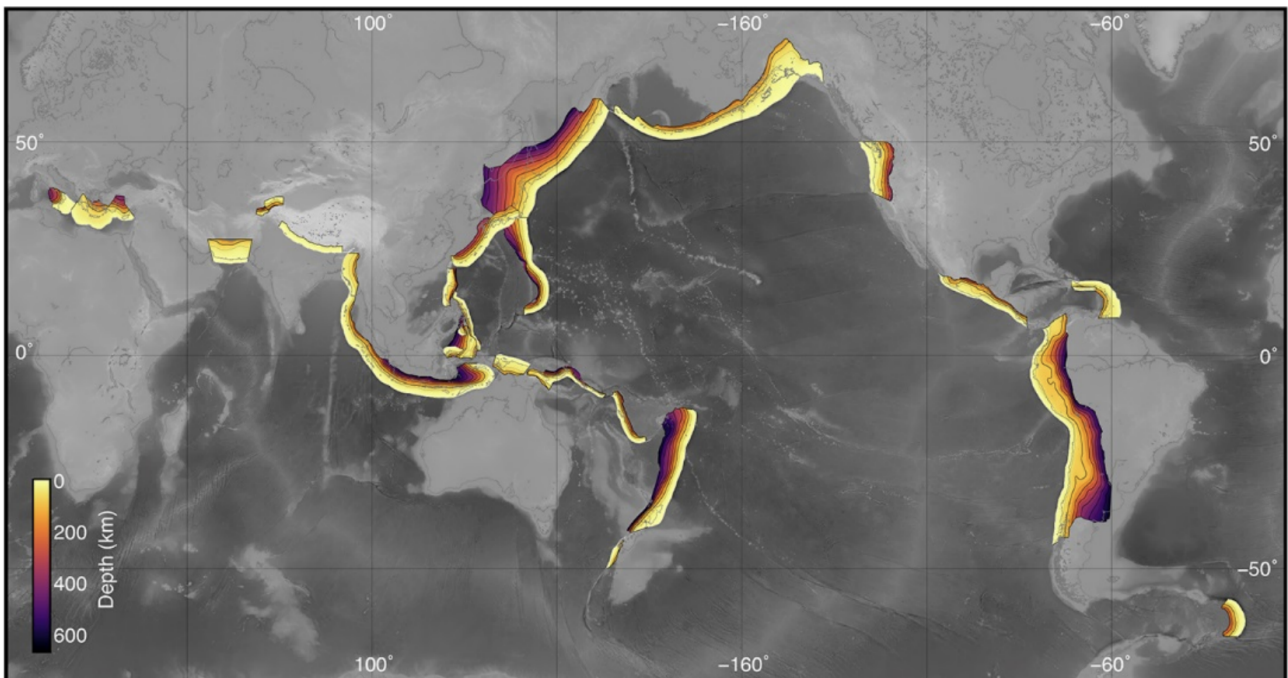


**Figure I.1** – Modèle slab2.0 décrivant la géométrie des failles de subduction [Hayes *et al.*, 2018].



## Chapitre I. Anticiper les séismes, pourquoi est-ce si difficile ?

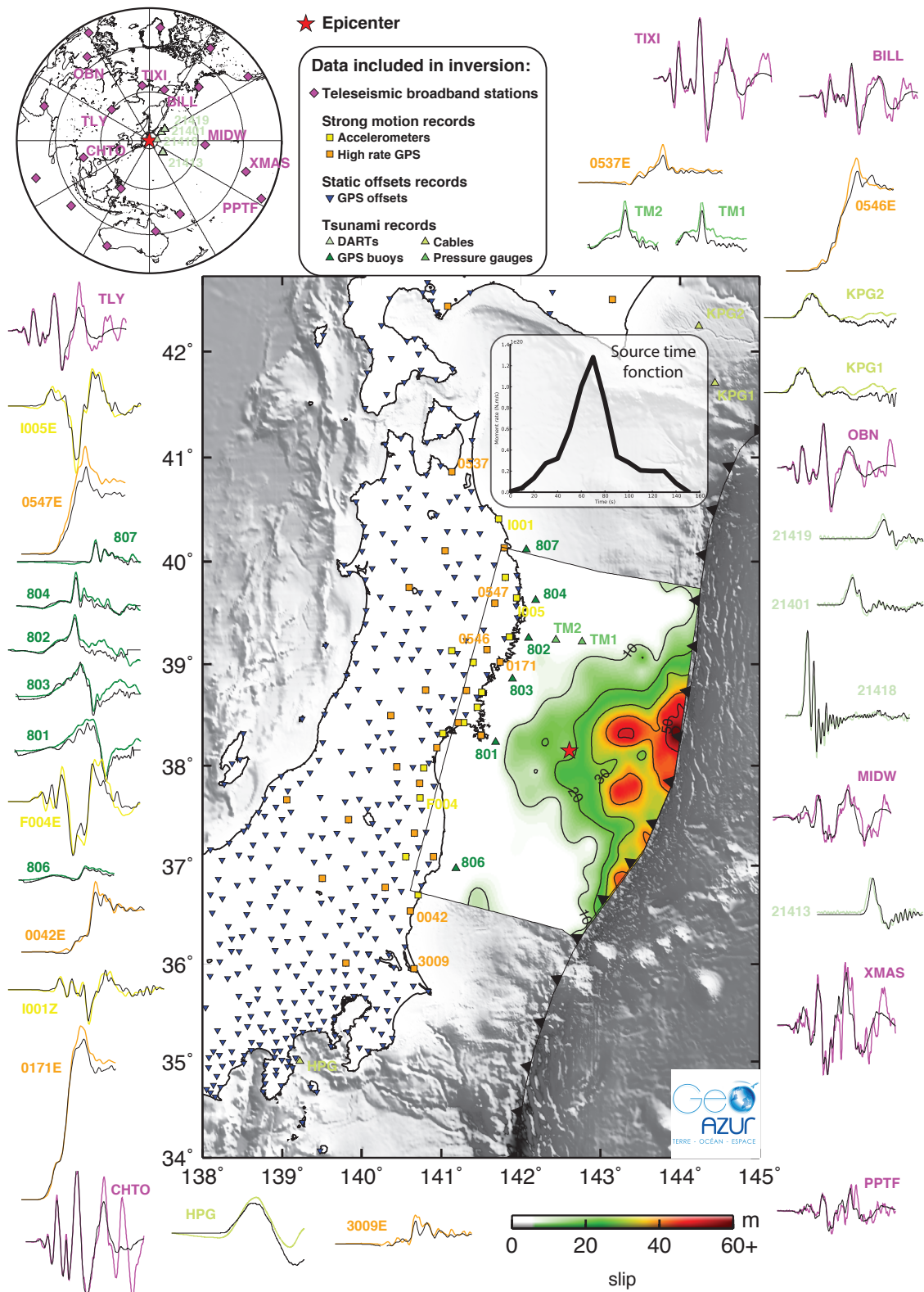


**Figure I.2** – Glissement sur la faille survenu lors du séisme de Tohoku-Oki ( $M_w$  9.0, 2011). Les formes d'ondes autour de la carte sont des exemples de données sismologiques, géodésiques et tsunami (couleur selon le type de données) expliquées par le modèle (courbes noires). La figure en insère donne le moment relâché en fonction du temps [Bletery et al., 2014].

Le long de ces grandes failles se produisent les plus grands séismes. Une approche populaire pour étudier la source sismique est d’imager le glissement le long des failles pendant les plus grands séismes. Cette approche consiste à chercher la distribution de glissement qui explique le mieux les différentes observations du séismes, i.e. les données sismologiques, géodésiques et éventuellement les mesures du tsunami. De nombreuses techniques, dites d’inversion, permettent ainsi d’obtenir un modèle de rupture en accord avec les données. Ces différentes techniques sont présentées en détails dans ma thèse [Bletery, 2015]. Leur principe de base est de discrétiser la faille rompue en sous-failles et chercher quelle amplitude de glissement sur chaque sous-faille à chaque instant explique le mieux les données. Cela permet d’obtenir une « image » de la rupture sur la faille (Figure I.2), et même un film [e.g., Bletery et al., 2014].

Les résultats donnés par les techniques d’inversion présentent toutefois une faiblesse fondamentale : la solution donnée par l’inversion n’est jamais unique. Cette faiblesse limite l’interprétation que l’on peut faire des modèles car différents groupes d’auteurs peuvent aboutir à des modèles très différents pour un même séisme [e.g., Lay, 2018]. Pour résoudre ce problème fondamental, des régularisations sont appliquées pour « guider » l’inversion vers la solution la plus lisse. Ce biais dans les modèles a été introduit car l’on pense qu’un modèle lisse (avec un glissement relativement homogène) est plus physique qu’un modèle rugueux (avec un glissement plus hétérogène), mais cet *a priori* n’est pas réellement fondé et les modèles les mieux contraints sont plutôt hétérogènes [e.g., Lay, 2018]. Une approche plus sophistiquée, permettant d’obtenir l’ensemble des solutions du problème et ainsi d’évaluer les incertitudes sur les modèles, a émergé récemment [Minson et al., 2013]. Le cadre théorique de cette approche permet même de prendre en compte les erreurs épistémologiques afin d’obtenir l’ensemble des solutions expliquant de manière satisfaisante les observations en fonction des incertitudes sur les données et sur les paramètres du modèle, comme les paramètres élastiques de la Terre ou la géométrie de la faille [Duputel et al., 2014; Bletery et al., 2016a; Ragon et al., 2018, 2019a, 2021].

## 2 Que font les failles entre deux séismes ?

Que se passe-t-il sur une faille lorsqu’il ne se passe rien ? Cette question est fondamentale pour comprendre ce que sont les séismes, comment, où et quand ils se produisent. La technique d’inversion décrite au paragraphe précédant peut être adaptée pour imager le glissement le long des failles entre 2 séismes. Celle-ci a permis de mettre en évidence différentes phases du cycle sismique : la phase post-sismique suivant les grands évènements, la phase inter-sismique et des épisodes de glissement transitoires.



## 2.1 Glissement post-sismique

Les inversions de données géodésiques enregistrées après les grands séismes ont révélé qu'après une grande rupture, le glissement sur la faille ne s'arrête pas soudainement, il décroît progressivement (suivant une décroissance logarithmique, Figure I.3). Les plus grandes amplitudes de glissement post-sismique semblent, par ailleurs, se concentrer en bordure des zones rompues co-sismiquement (Figure I.3).

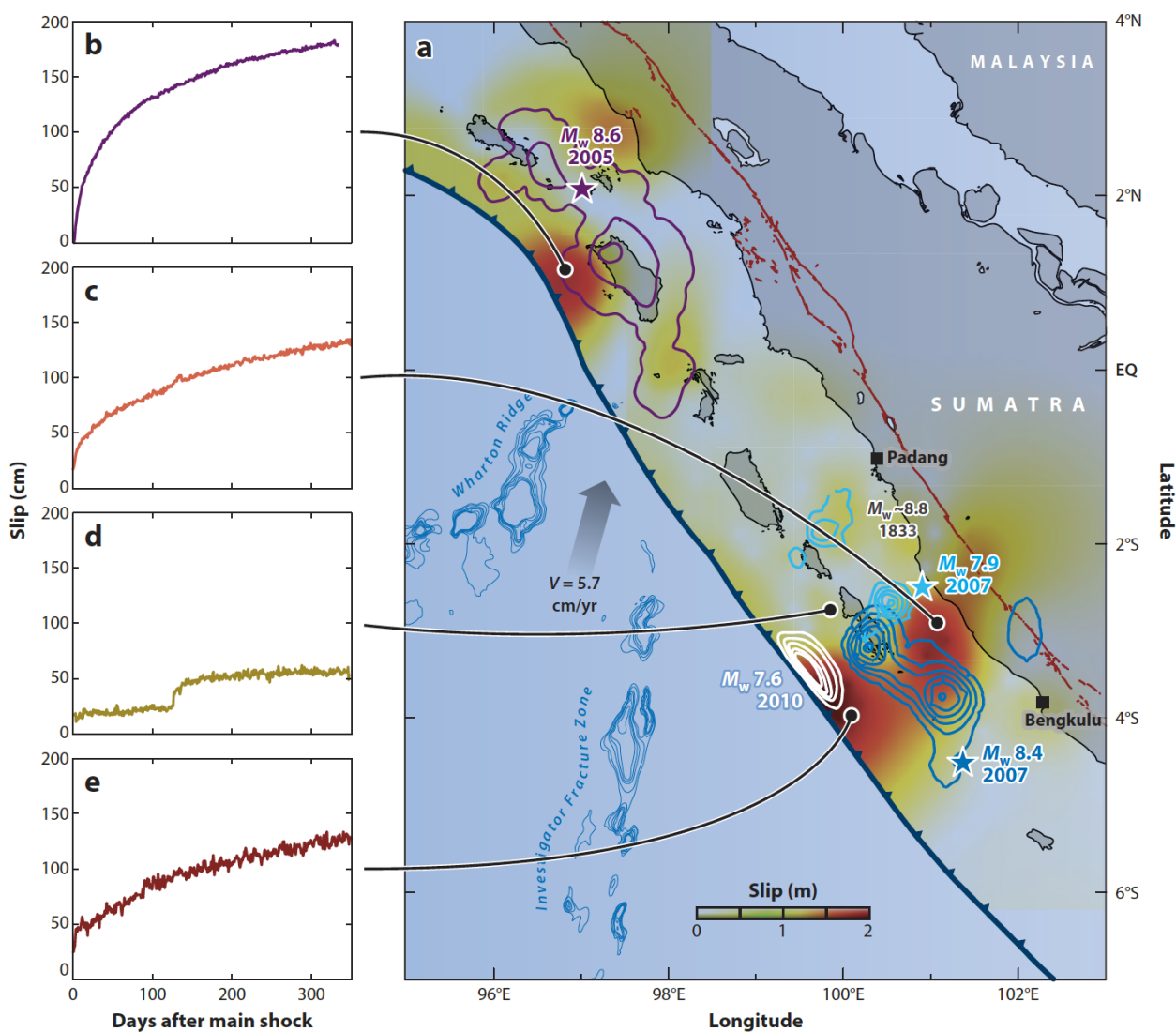


**Figure I.3** – Distribution spatiale (a) et temporelle (b - e) du glissement post-sismique suivant les séismes de Nias ( $M_w$  8.6, 2005) et Mentawai ( $M_w$  7.9, 2007) [Avouac, 2015].

La transition entre glissement co-sismique et post-sismique n'est pas évidente et une grande

partie du signal que l'on attribue généralement au glissement co-sismique pourrait bien être a-sismique [Twardzik *et al.*, 2019; Ragon *et al.*, 2019b]. Pour les très grands séismes, le glissement post-sismique peut durer des années. Au bout de quelques mois/années, le signal dans les données géodésiques devient toutefois dominé par la relaxation visco-élastique du milieu et non plus par le glissement sur la faille [e.g., Sun and Wang, 2015].

### 2.2 Glissement inter-sismique

Une fois la phase post-sismique terminée, le glissement sur les failles reprend progressivement son comportement long terme. Ce glissement inter-sismique n'est généralement pas homogène, certaines portions de failles « glissent » à la vitesse relative des plaques tectoniques, d'autres portions restent « bloquées », ou couplées.

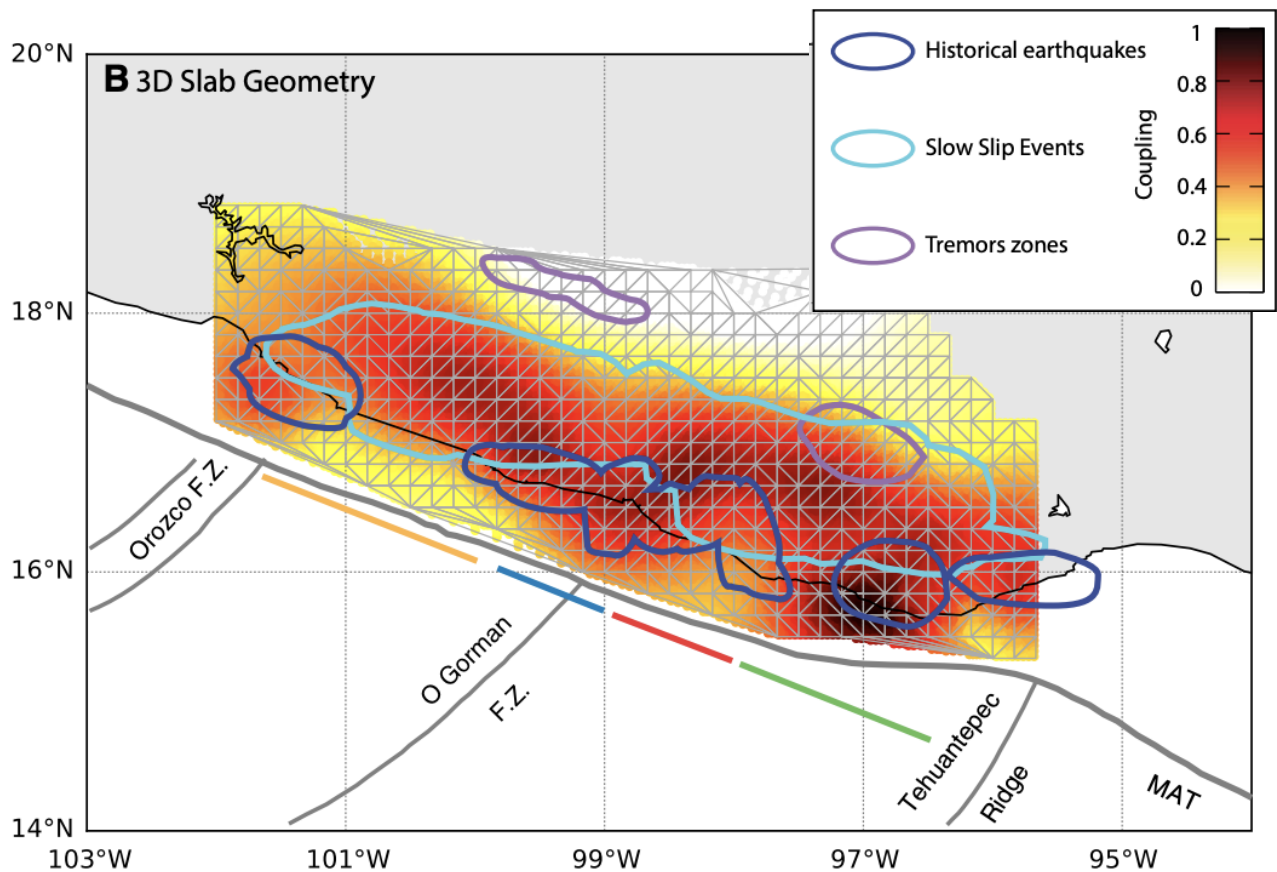


**Figure I.4** – Distribution du couplage intersismique le long de la faille de subduction du Mexique [Roussel *et al.*, 2016].

Le degré de couplage – variant entre 0, si la faille glisse à la vitesse des plaques, et 1 si

elle est complètement couplée – peut être imagé le long des grandes failles par inversion de données géodésiques long terme [e.g., [Loveless and Meade, 2011](#); [Stevens and Avouac, 2015](#); [Jolivet et al., 2015](#); [Metois et al., 2016](#); [Rousset et al., 2016](#); [Villegas-Lanza et al., 2016](#); [Jolivet et al., 2020](#)]. Imager la distribution du couplage le long des grandes failles permet d'identifier les zones où des déficits de glissement s'accumulent (Figure I.4). Les zones à fort couplage sont ainsi, dans le schéma conceptuel classique, considérées comme les zones les plus à risque de produire des grands séismes [e.g., [Avouac, 2015](#)].

### 2.3 Glissement transitoire

Le début des années 2000 a vu la découverte de signaux transitoires dans les données GNSS de la zone de subduction des Cascades [[Dragert et al., 2001](#); [Miller et al., 2002](#)]. Parallèlement, des signaux micro-sismiques, du nom de trémors, ont été reliés à l'activité tectonique au Japon [[Obara, 2002](#)]. [Rogers and Dragert \[2003\]](#) ont alors observé une forte corrélation temporelle entre ces deux types de signaux dans la zone des Cascades (Figure I.5).

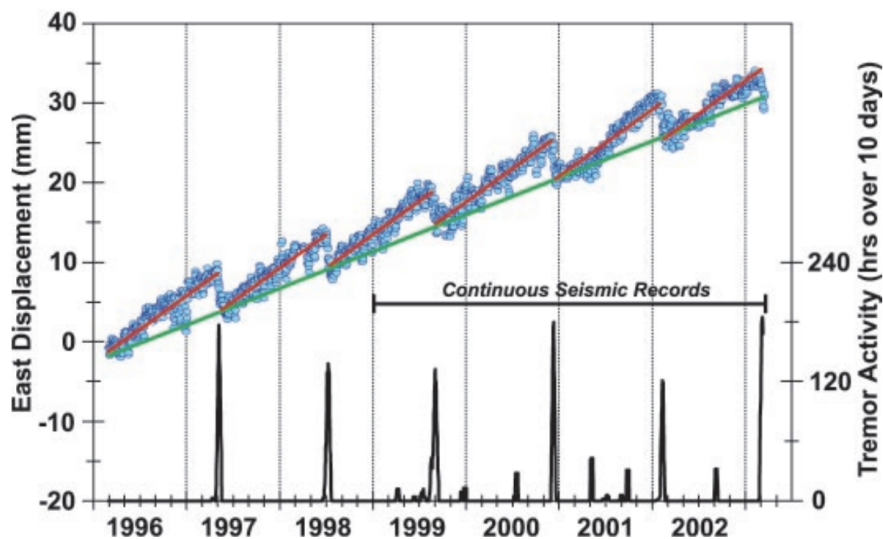


**Figure I.5** – Signal journalier enregistré sur une station GNSS aux Cascades (cercles bleus) et activité des trémors (courbe noire) [[Rogers and Dragert, 2003](#)].

Au delà de la corrélation temporelle frappante (Figure I.5), la périodicité du signal a énormément intéressé la communauté [[Schwartz and Rokosky, 2007](#)]. L'inversion des signaux GNSS a mis en évidence que ces phénomènes sont des épisodes de glissement transitoire sur la faille [e.g., [Bartlow et al., 2011](#)], accompagnés de millions de micro-séismes dont la superposition génère les trémors enregistrés par les sismomètres [[Shelly et al., 2007](#)]. Les épisodes de glissement

## I.2 Que font les failles entre deux séismes ?

transitoire ont été nommés *Slow Slip Events* (SSEs), ou séismes lents, les micro-séismes qui les accompagnent *Low-Frequency Earthquakes* (LFEs) car ces événements apparaissent comme dépourvus en hautes fréquences [Shelly et al., 2006]. Une propriété intéressante des LFEs est leur sensibilité à des perturbations de contraintes extrêmement faibles [Thomas et al., 2009]. Leur activité représente, par ailleurs, une fenêtre d'observation des conditions physiques en profondeur [Thomas et al., 2018]. D'autres événements, encore plus basses fréquences, nommés *Very-Low-Frequency Earthquakes* (VLFs) ont été identifiés [Ito et al., 2007]. Le cadre conceptuel classique est que les SSEs, des glissements lents a-sismiques, déstabilisent des micro-aspérités, générant ainsi des LFEs et des VLFs que l'on observe dans les données sismologiques sous forme de trémors. Toutefois la relation entre SSEs et LFEs n'est pas totalement établie, les LFEs n'étant pas toujours observés au centre des zones de glissement lent, mais souvent en bordure. La relation entre tous ces phénomènes, la distribution du couplage [Jolivet and Frank, 2020] et les grands séismes (Figure I.4) comporte peut-être la clé de la compréhension et de l'anticipation des séismes [Obara and Kato, 2016].

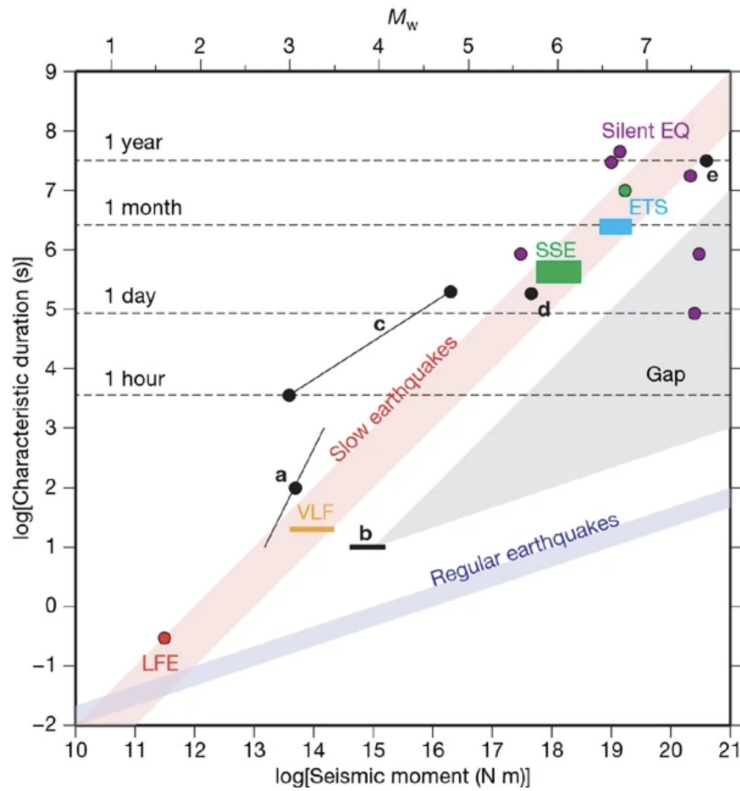


**Figure I.6** – Loi d'échelle proposée par Ide et al. [2007] liant SSEs, LFEs et VLFs, séparée de la loi d'échelle des séismes par un *gap* d'observations.

Des techniques de plus en plus fines ont permis de détecter des épisodes de glissement transitoire de plus en plus petits [Rousset *et al.*, 2017, 2019] et de partout sur la planète [Obara and Kato, 2016, et références citées]. S’est alors posée la question d’un continuum des phénomènes de glissement lent : existe-t-il des épisodes de glissement lent de toute magnitude, de toute durée [Frank *et al.*, 2018; Jolivet and Frank, 2020] ? Ce continuum inclut-il les évènements sismiques ou les glissements lents sont-ils un mode de glissement distinct des séismes ? Sur la base d’une loi d’échelle entre moment et durée (Figure I.6), Ide *et al.* [2007] ont proposé que SSEs, LFEs et VLFES sont différentes manifestations d’un même phénomène (à différentes échelles), distinct des séismes. Des études postérieures ont remis en question la pente (moment proportionnel à la durée) de la Figure I.6 pour les SSEs, la rapprochant plus ou moins de la pente observée pour les séismes (moment proportionnel au cube de la durée) [Gomberg *et al.*, 2016; Michel *et al.*, 2019]. Mais reste entière la question du *gap* d’observations entre « séismes lents » et « séismes rapides » (Figure I.6). Dans une gamme de magnitudes et de durées en théorie observables par l’instrumentation sismique et géodésique, pourquoi n’observe-t-on rien ?

### 3 Est-il possible de prédire les séismes ?

#### 3.1 Approche physique

Une approche naïve pour prédire les séismes serait de modéliser l’ensemble du cycle sismique (i.e. les phases post-sismique, inter-sismique, co-sismique ainsi que les épisodes transitoires) et de « calibrer » les différents paramètres physiques contrôlant le comportement des failles selon les observations enregistrées sur chaque faille. Une modélisation calibrée finement selon les propriétés d’une région donnée pourrait, en théorie, décrire le comportement passé et futur d’une faille. Si aucune prédiction n’a encore jamais pu être réalisée ainsi, des modèles de cycle sismique de ce type existent. Leur formalisme, dit *rate-and-state*, est basé sur des expériences réalisées en laboratoire [Marone, 1998]. Plusieurs lois ont été proposées [Dieterich, 1979; Ruina, 1983; Marone, 1998]. La plus populaire s’écrit

$$\mu = \mu_0 + a \ln \frac{V}{V_0} + b \ln \frac{\theta}{\theta_0}, \quad (\text{I-1})$$

où  $\mu$  est le coefficient de friction à l’équilibre (*steady-state*),  $V$  est la vitesse de glissement à l’équilibre,  $a$  et  $b$  sont des scalaires, l’indice 0 indique un état de référence et  $\theta$  est une variable d’état suivant la loi, dite de vieillissement (*aging law*) – une autre loi très utilisée est dite de

### I.3 Est-il possible de prédire les séismes ?

glissement (*slip law*) – suivante :

$$\frac{d\theta}{dt} = 1 - \frac{V\theta}{d_c}, \quad (\text{I-2})$$

$d_c$  étant une distance de glissement caractéristique.

À l'état d'équilibre, la loi ne dépend plus de la variable d'état, mais uniquement de la vitesse de glissement  $V$  :

$$\mu_{eq} = \mu_0 + (a - b) \ln \frac{V}{V_0}. \quad (\text{I-3})$$

Une analyse de stabilité de cette loi montre que le glissement ne peut être stable que si  $a - b > 0$  et qu'à l'inverse il ne peut être instable que si  $a - b < 0$  [Scholz, 2019]. Un glissement instable se produit si  $a - b$  est inférieur à une valeur critique négative, ce qui définit un domaine intermédiaire « conditionnellement stable ». Dans le cas d'un crack de taille  $L$  dans un milieu élastique avec un module de cisaillement  $G$ , cette condition d'instabilité s'écrit

$$b - a > \frac{\lambda G d_c}{L(\sigma_n - p)} \quad (\text{I-4})$$

où  $\lambda$  est de l'ordre de 1,  $\sigma_n$  est la contrainte normale et  $p$  la pression de pore [Avouac, 2015].

Ce formalisme dérivé d'expériences en laboratoire a permis le développement de modèles numériques du cycle sismique. Ces modèles reproduisent un certain nombre d'aspects caractérisants le comportement des failles [Tse and Rice, 1986; Dieterich, 1987, 1994], en particulier la décroissance logarithmique du glissement post-sismique avec le temps [Marone et al., 1991]. De manière intéressante, ils prédisent également que les séismes s'initient avec une phase de nucléation, puisque le crack doit attendre une taille critique avant que le glissement ne devienne instable [Dieterich, 1987; Rubin and Ampuero, 2005; Ampuero and Rubin, 2008].

En considérant des distributions de propriétés frictionnelles hétérogènes le long de la faille (i.e. des zones où  $a - b > 0$  et des zones où  $a - b < 0$ ) (Figure I.7), les modèles récents sont capable de reproduire des distributions de glissement très complexes [e.g., Kaneko et al., 2010; Barbot et al., 2012; Ader et al., 2014; Jiang and Lapusta, 2016] cohérents avec les modèles de glissement co-, post- et inter-sismique obtenus par inversion des observations en surface.

Dans ce cadre conceptuel, une connaissance fine de la distribution des propriétés frictionnelles le long des failles pourrait ainsi, en théorie, permettre aux modèles de prédire le comportement passé, présent et futur des failles, et ainsi de prédire les grandes ruptures. Une telle connaissance est toutefois tout-à-fait hors d'atteinte à partir des observations dont l'on dispose actuellement et il est peu probable que l'on ait un jour accès au degré d'information nécessaire à la prédiction à partir d'observations de surface. L'approche physique s'avère ainsi, en pratique,



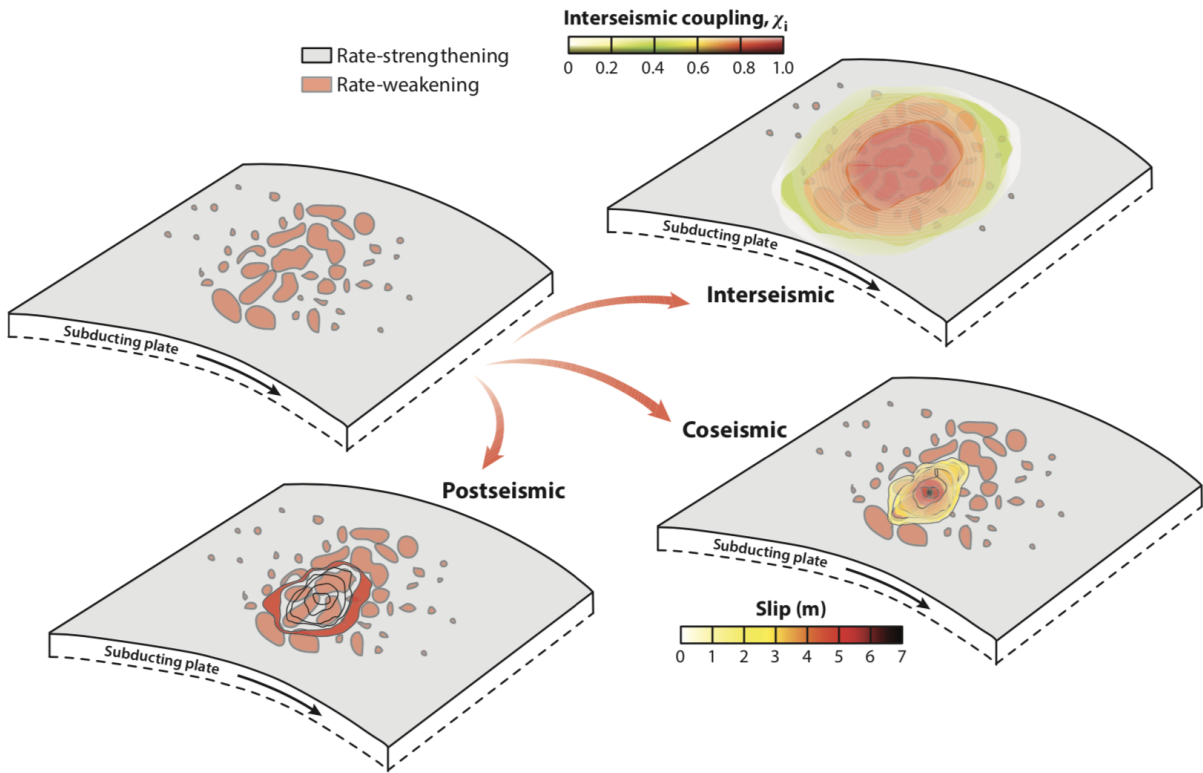


**Figure I.7** – Modèle conceptuel de comment la distribution des propriétés frictionnelles – en zones dites *rate-weakening* (i.e ou  $a - b < 0$ ) et en zones dites *rate-strengthening* (i.e ou  $a - b > 0$ ) – le long d’une faille contrôle le comportement de la faille lors des phases co-, post- et inter-sismique [Avouac, 2015].

incapable de prédire les séismes.

### 3.2 Approche statistique

Une autre approche naïve pour prévoir les séismes serait de décrire statistiquement la sismicité afin d’extrapoler l’occurrence de futurs évènements à partir de séquences sismiques passées. Une caractéristique évidente lorsque l’on observe la sismicité, est qu’après un grand évènement, un certain nombre de répliques se produisent. À partir d’observations suivant le séisme de Nobi (1891), *Omori* [1894] a décrit ce phénomène de manière empirique et conclu que le nombre de répliques décroît en  $\frac{K}{t+c}$ , où  $K$  et  $c$  sont des constantes [Utsu *et al.*, 1995]. *Utsu* [1961] a modifié cette célèbre loi d’Omori, observant que les séquences de répliques décroissent avec différents exposants. D’autres lois alternatives ont été proposées [Mignan, 2015, 2016]. Aujourd’hui, l’activité des répliques est généralement décrite comme un processus en cascade et le modèle ETAS (*Epidemic-Type Aftershock Sequence*) [Ogata, 1988, 1998] donne la meilleur description de l’ac-

### I.3 Est-il possible de prédire les séismes ?

---

tivité sismique [*Marzocchi et al.*, 2017]. Même si ces modèles sont purement empiriques, des explications physiques, souvent dérivées d'expériences en laboratoire [e.g., *Toda et al.*, 2005], ont été proposées pour expliquer des augmentations du taux de sismicité pouvant aller jusqu'à un facteur 1000 dans certaines régions ou même engendrer des diminution dans d'autres [*Wyss and Wiemer*, 2000; *Gerstenberger et al.*, 2005].

Une autre loi empirique célèbre, la loi de Gutenberg-Richter [*Gutenberg and Richter*, 1944] donne le nombre  $N$  de séismes de magnitude supérieure ou égale à  $M$  par la formule

$$\log N = a - bM, \quad (\text{I-5})$$

où  $a$  et  $b$  n'ont rien à voir avec les constantes du formalisme *rate-and-state* décrit dans le précédent paragraphe mais où  $a$  décrit le volume global de la sismicité d'un catalogue donné (i.e. le nombre d'évènements recensé dans une région donnée au cours d'une période donnée) et  $b$  décrit la proportion entre le nombre de grands séismes et de petits séismes. La valeur de  $b$  – connue sous le terme de *b-value* – est généralement proche de 1, ce qui veut dire que pour 1 séisme de magnitude 9, il y a 10 séismes de magnitude 8, 100 de magnitude 7 (etc.). Une valeur légèrement inférieure à 1 signifie qu'il y a une plus grande proportion de séismes de forte magnitude, une valeur légèrement supérieure à 1 signifie l'inverse. Des expériences en laboratoires ont montré un lien entre la *b-value* et l'état de contraintes; plus les contraintes différentielles appliquées ( $\sigma_1 - \sigma_3$ ) sont élevées plus la *b-value* est faible [*Scholz*, 1968; *Amitrano*, 2003; *Goebel et al.*, 2013]. Des observations faites dans divers contextes tectoniques semblent cohérentes avec un contrôle de l'état de contraintes sur  $b$  [*Schorlemmer et al.*, 2005], et suggèrent également des liens entre la valeur de  $b$  et le mécanisme au foyer [*Gulia and Wiemer*, 2010], la profondeur [*Spada et al.*, 2013] et la pression fluide [*Bachmann et al.*, 2012].

Les variations spatiales et temporelles de  $b$  ont suscité un grand intérêt dans la communauté car si celles-ci sont reliées à un changement d'état de contraintes, elles pourraient nous renseigner sur l'imminence d'un grand évènement. Une augmentation de la *b-value* a ainsi été observée après quelques grands séismes [*Wiemer and Katsumata*, 1999; *Wiemer et al.*, 2002; *Tormann et al.*, 2012; *Ogata and Katsura*, 2014; *Tormann et al.*, 2014, 2015; *Tamaribuchi et al.*, 2018], puis de manière plus systématique [*Gulia et al.*, 2018]. De manière intéressante, les quelques exceptions – i.e. des séismes suivis d'une diminution de la *b-value* – ont été suivis d'évènements de magnitude plus forte [*Gulia and Wiemer*, 2019]. Cette observation suggère qu'un monitoring en temps réel de la *b-value* pourrait aboutir à un système de prévention des grands évènements (dont le cadre d'application resterait à inventer). Pour être validé statistiquement, ce système devra toutefois être confronté à un grand nombre de données, lesquelles prendront des an-



nées à être acquises [*Gulia and Wiemer, 2019*]. Malgré des éléments encourageants, l'approche statistique s'avère ainsi, à l'heure actuelle, incapable de prévoir les séismes.

### 3.3 Approche observationnelle

Devant l'échec des approches physique et statistique à prédire les grands séismes, l'approche observationnelle apparaît comme une solution simple et peut-être plus prometteuse. Si l'on arrivait à observer un signal, quel qu'il soit, systématiquement avant un grand séisme, on pourrait se baser sur l'occurrence de ce signal pour prévoir l'activité sismique à venir. Cette idée simple est à l'origine de la quête des signaux précurseurs. L'existence de tels signaux est hypothétique et dépend de l'existence d'une phase précurserice. Il est possible que les séismes soient des phénomènes de nature chaotique [e.g., *Geller, 1997; Kagan, 1997*]. Dans ce cas, aucune phase précurserice n'existe et aucun signal précurseur non plus. Si, à l'inverse, les séismes sont des phénomènes de nature déterministe [e.g., *Dieterich, 1987; Rubin and Ampuero, 2005; Ampuero and Rubin, 2008*], alors les signaux précurseurs existent. Dans la deuxième hypothèse, tout l'enjeu est de les détecter.

Si aucune détection systématique de signaux précurseurs n'a jamais pu être démontrée, de nombreuses observations sur des séismes ponctuels ont été proposées [*Bouchon et al., 2011, 2013; Kato et al., 2012; Ruiz et al., 2014; Brodsky and Lay, 2014; Ellsworth and Bulut, 2018*]. Le cadre conceptuel sous-jacent est que les grands séismes s'initient avec une phase de glissement a-sismique lent sur la faille, associée à une augmentation de la micro-sismicité dans la zone qui en viendra à produire la rupture [*Bouchon et al., 2011, 2013; Kato et al., 2012; Ruiz et al., 2014*]. Ces études suggèrent que les précurseurs sismiques existent et que les grands séismes pourraient être anticipés des heures [*Bouchon et al., 2011*], des jours [*Kato et al., 2012*], des semaines [*Ruiz et al., 2014*] ou des mois [*Bouchon et al., 2013*] avant qu'ils ne se produisent.

Si ces observations sont intéressantes, elles se limitent à un petit nombre d'évènements. L'absence de généralisation à l'ensemble – ou à défaut à un grand nombre – des évènements connus rend impossible la mise en place d'un système de prévision, d'autant que des signaux similaires associés à des glissements a-sismiques transitoires se produisent couramment sans provoquer de grands séismes [e.g., *Schwartz and Rokosky, 2007; Gomberg et al., 2010; Obara and Kato, 2016; Wallace, 2020*].

## 4 Anticiper les séismes autrement : l’alerte précoce

Détecter des signaux précurseurs, i.e. des signaux précédant l’origine des séismes, est un objectif très (trop ?) ambitieux, qui n’a jamais mené à un système de prévention opérationnel. Des signaux précoces suivant directement l’origine des séismes – mais ne les précédant pas – peuvent en revanche être utilisés pour alerter les populations de manière concrète. L’exploitation de ces signaux précoces non-précurseurs permet en effet d’alimenter des systèmes d’alerte sismique. Les algorithmes dits d’alerte estiment la magnitude et la localisation des événements dès les premiers signaux recueillis sur les capteurs les plus proches de la source afin de lancer (ou non) l’alerte dans des régions habitées, plus éloignées, avant que les premières secousses n’y soient ressenties et avant qu’un éventuel tsunami ne frappe les côtes. L’alerte précoce est ainsi moins ambitieuse que la prédiction car elle ne cherche pas à connaître le futur, seulement à déduire très vite des signaux disponibles une information utile pour alerter les populations.

### 4.1 L’alerte sismique

Si énormément d’espoir a été mis dans la prédiction dans le début des années 1970 [[Scholz et al., 1973](#)], sa faisabilité a été sérieusement remise en question par des études théoriques suggérant que les séismes sont un processus non-linéaire sensibles à des variations non mesurables des conditions physiques en profondeur [[Geller, 1997](#); [Kagan, 1997](#)]. Les approches probabilistes (statistiques) développées par la suite n’ont jamais apporté suffisamment d’information pour être implémentées dans un système d’alerte opérationnel [[Jordan et al., 2011](#); [Zechar et al., 2016](#)]. Alors que l’espoir de la prédiction des tremblements de terre s’est progressivement estompé, le domaine de l’alerte sismique précoce a pris de plus en plus d’importance. Il a donné vie à une variété de techniques aujourd’hui implémentées dans des systèmes d’alerte opérationnels dans de nombreux pays exposés au risque sismique et tsunami. L’alerte sismique repose sur le fait que les ondes sismiques se propagent à une vitesse finie, très rapide (quelques km/s), mais beaucoup plus lente que les messages d’alerte, les systèmes de télécommunication transmettant à la vitesse de la lumière. On peut donc utiliser des signaux sismiques enregistrés par des stations sismiques situées proche de l’épicentre pour alerter des régions habitées situées plus loin de la source avant que les ondes sismiques n’arrivent. De plus, les plus forts mouvements du sol sont produits par les ondes S qui se propagent plus lentement que les premières ondes enregistrées, les ondes P, ce qui donne un peu plus de temps pour l’alerte (Figure [I.8](#)). On ne parle pour autant que de quelques secondes – dans le meilleur des cas quelques dizaines de secondes – de temps d’alerte avant les secousses.

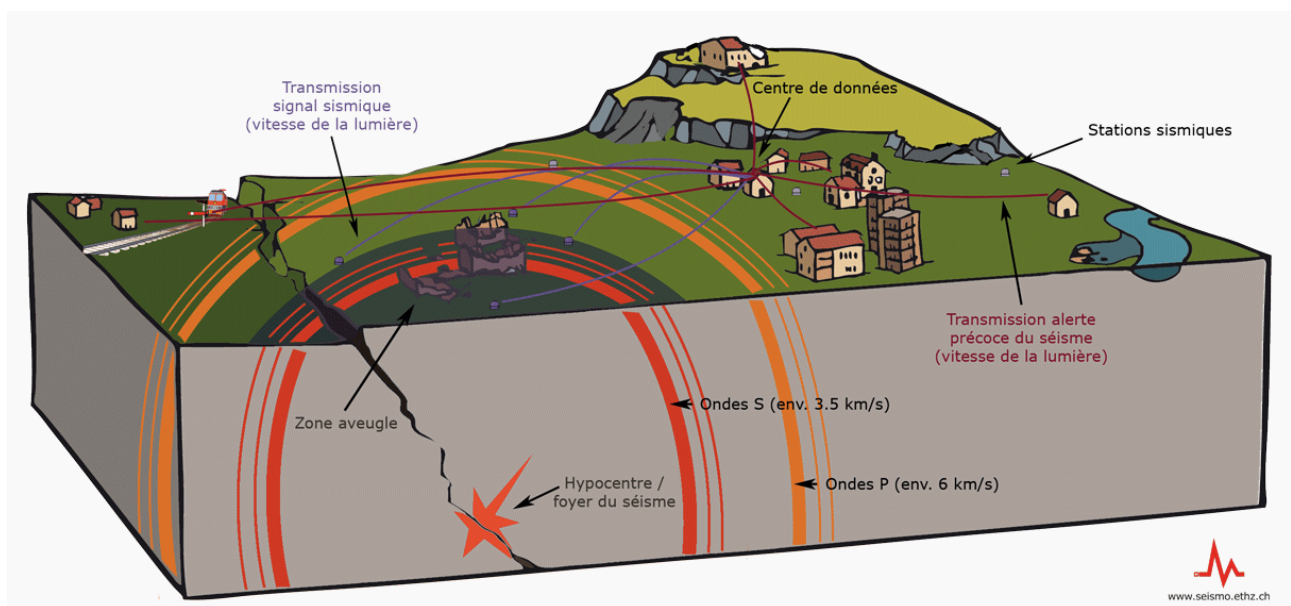


**Figure I.8** – Illustration des principes de l'alerte sismique (ETH Zurich)

L'alerte sismique peut se décomposer en 4 catégories d'approches.

(1) Les approches *in situ* utilisent un capteur à un endroit donné pour alerter directement la région alentour [Böse et al., 2009; Meier et al., 2015]. Ces approches peuvent s'avérer efficaces sur une région étendue si de nombreux capteurs sont disponibles, c'est l'ambition de l'application MyShake qui utilise les smartphones comme capteurs sismiques [Kong et al., 2016a,b].

(2) Les algorithmes « point-source », tels que PRESTo [Satriano et al., 2011] ou ElarmS [Serdar Kuyuk et al., 2014; Sheen et al., 2017; Chung et al., 2019], procurent des estimations plus rapides des caractéristiques du séisme (magnitude, localisation) en utilisant les toutes premières secondes d'ondes P enregistrées.

(3) Les algorithmes de modélisation des mouvements du sol, tels que FinDer [Böse et al., 2012, 2015, 2018] ou PLUM [Hoshiwa and Aoki, 2015], prédisent les mouvements du sol à venir à partir des mouvements du sol observés. Leurs performances sont meilleures que celles des algorithmes « point-source ».

Ces 3 familles d'algorithmes fonctionnent relativement bien dans des systèmes régionaux, et pour des séismes de magnitudes modérées, car ils sont assez rapides. Ils ont, en revanche, tendance à systématiquement sous-estimer la magnitude des grands séismes (magnitude  $M_w > 7$ ). En d'autres termes, l'estimation de la magnitude sature à  $M_w = 7$  : pour des séismes de magnitude supérieure l'estimation sera  $M_w = 7$ . Ce problème a pour origine principale la saturation des instruments ; l'amplitude des ondes P enregistrées proche de la source d'un séisme

de magnitude supérieure à 7 est supérieure à ce que les accéléromètres (instruments les plus performants pour enregistrer les mouvements forts du sol) sont capables de mesurer. S’ajoute à ce problème instrumental, un problème de modélisation : l’approximation « point-source » devient, en effet, largement fautive proche de la source pour des séismes d’une telle magnitude.

(4) Les algorithmes « faille-finie », comme G-larmS [*Grapenthin et al., 2014a,b*], G-FAST [*Crowell et al., 2016, 2018*], BEFORES [*Minson et al., 2014*] ou REGARD [*Kawamoto et al., 2016, 2017*], inversent le glissement sur la faille à partir des données GNSS. Ces algorithmes règlent en partie le problème de saturation de l’estimation de la magnitude mais sont significativement plus lents que les 3 autres types d’algorithmes [*Ruhl et al., 2019; Allen and Melgar, 2019*]. Il y a ainsi un compromis à trouver entre la rapidité de l’estimation et sa fiabilité [*Meier, 2017*].

### 4.2 L’alerte tsunami

Le problème de saturation de l’estimation de la magnitude est particulièrement problématique, dans le cas des grands séismes de subduction, pour évaluer l’amplitude du tsunami, lequel peut être beaucoup plus destructeur que les secousses dans le cas de séismes de magnitude supérieure à 9, ou inexistant pour des séismes de magnitude inférieure à 8. L’estimation de la magnitude des séismes est ainsi cruciale pour prévoir l’ampleur du tsunami, mais les algorithmes d’alerte sismique ont des difficultés à estimer rapidement et de manière fiable la magnitude des grands événements. Les tsunamis atteignent les côtes entre 30 min et 2 h après le séisme, ce qui laisse plus de temps pour l’alerte que pour les secousses. Cependant, réduire le temps d’alerte est essentiel pour arrêter les infrastructures sensibles, telles que les centrales nucléaires, et évacuer les régions côtières densément peuplées.

Le calcul de la magnitude d’un séisme est normalement réalisé à partir des ondes de surface enregistrées partout sur Terre [*Kanamori and Given, 1981*], mais ces ondes se propagent beaucoup plus lentement que les ondes P. Le calcul « classique » de la magnitude ne peut donc pas être effectué avant l’arrivée du tsunami. Les systèmes d’alerte tsunami modernes utilisent ainsi un autre type d’onde, de faible amplitude et de très longue période, appelé phase W [*Kanamori and Rivera, 2008*], qui peut être enregistré plus tôt que les ondes de surface (Figure I.9) et procure de meilleures estimations de la magnitude que les systèmes d’alerte basés sur les ondes P [*Duputel et al., 2011, 2012*]. Les algorithmes basés sur la phase W permettent ainsi une estimation plus fiable de la taille des tsunamis mais sont beaucoup plus lents ( $\approx 20$  min) que les algorithmes basés sur les ondes P [*Duputel et al., 2011*].

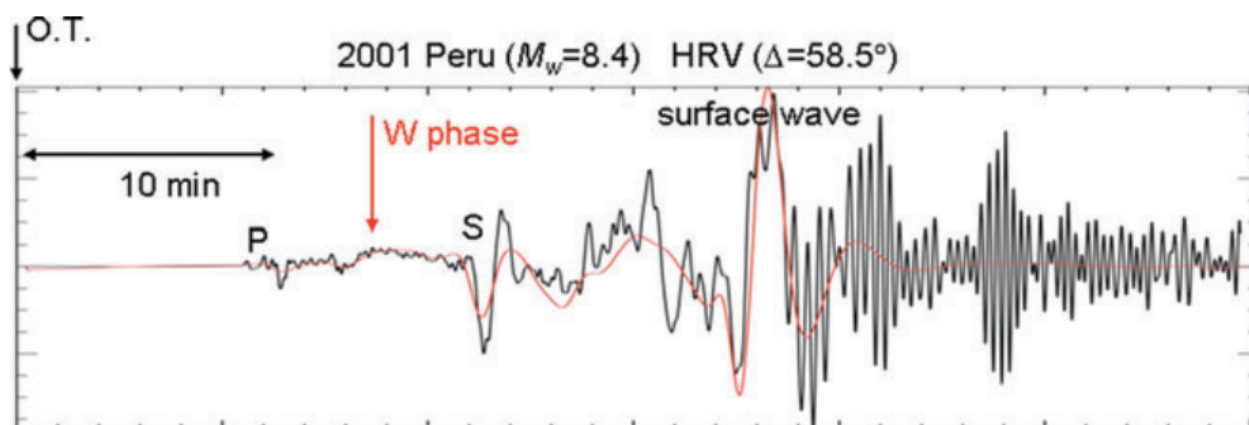


**Figure I.9** – Sismogramme du séisme péruvien de 2001 ( $M_w$  8.4) (black line) indiquant les temps d’arrivées des ondes P, S et des ondes de surface, enregistré à la station HRV, située à une distance épacentrale de  $58.5^\circ$ . La courbe rouge montre une forme d’onde synthétique de la phase W [Kanamori and Rivera, 2008].

### 4.3 La découverte prometteuse des PEGS

Les déformations statiques et transitoires générées par les séismes entraînent des perturbations de densité qui, à leur tour, provoquent des perturbations à grande échelle du champ de gravité terrestre de manière instantanée [Harms *et al.*, 2015; Harms, 2016]. Ainsi, les signaux les plus précoces générés par un séisme ne sont pas les ondes P mais les perturbations du champ de gravité terrestre – i.e. des variations infimes de l’accélération de la pesanteur  $g$  – qui se propagent à la vitesse de la lumière. Cependant, ces perturbations sont trop faibles pour être observées systématiquement sur tous les séismes, ce qui a, jusqu’ici, considérablement limité leur utilité pour l’alerte précoce.

La première observation d’un signal dans le champ de gravité terrestre induit par un séisme a été faite par un gravimètre superconducteur lors du séisme de Tohoku-Oki ( $M_w$  9.0) survenu en 2011 au large du Japon [Montagner *et al.*, 2016]. Cette découverte a été suivie de multiples observations sur des sismogrammes enregistrés lors du même séisme (Figure I.10) – la gravité étant une accélération, les variations de  $g$  peuvent être mesurées sur un accélérogramme ou un vélocigramme dérivé (plus sensible aux basses fréquences). Dans le détail, les signaux observés sur ces sismogrammes sont composés d’un terme direct, i.e. la perturbation de  $g$ , et d’un terme induit par la réponse élastique de la Terre à la perturbation gravitationnelle. Ce terme induit est de signe opposé et d’amplitude similaire au terme direct, « annulant » une grande partie du signal [Vallée *et al.*, 2017]. La résultante des 2 termes a été nommée *Prompt Elasto-Gravity Signal* (PEGS). Découpler les termes direct et induit rendrait le signal plus facilement

observable mais la technologie nécessaire à ce découplage n'est malheureusement pas encore disponible.

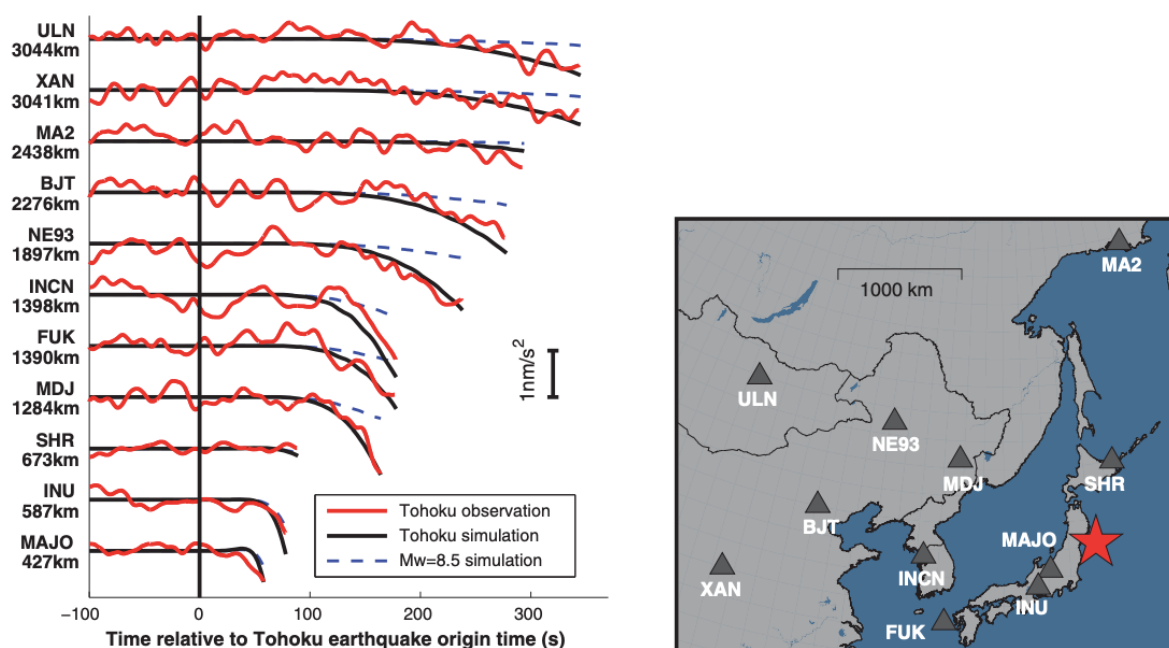


**Figure I.10** – PEGS observés (rouge) et prédits (noir) pour le séisme de Tohoku-Oki (étoile rouge) à différentes stations (triangles noirs sur la carte). Les formes d'ondes sont coupées à l'arrivée des ondes P. Les courbes pointillées bleues montrent le signal prédit pour un séisme de magnitude  $M_w$  8.5 [Vallée et al., 2017].

Les PEGS montrent toutefois un fort potentiel pour l'alerte précoce puisque ces signaux présentent des caractéristiques exceptionnelles : ils sont très sensibles à la magnitude, ils ne saturent pas (au contraire des ondes P dans les systèmes « classiques »), et surtout ils se propagent à la vitesse de la lumière. Cela veut dire que des signaux très précoces, de faible amplitude, contenant l'information de la magnitude des grands séismes – ce que les premières secondes des ondes P ne contiennent probablement pas [Meier et al., 2017] – existent dans les formes d'ondes sismiques, cachés dans le bruit. Extraire ces signaux du bruit sismique en temps réel est cependant un réel challenge. L'observation directe des PEGS lors du séisme de Tohoku n'a été rendue possible que par la magnitude exceptionnelle de l'évènement ( $M_w$  9.0) conjuguée à la qualité des instruments de mesure installés au Japon. Les séismes de magnitude 9 sont rares et ne se produisent pas toujours dans des régions aussi bien instrumentées. Un séisme de magnitude 8.5 aurait été difficilement observable par le même réseau sismique (Figure I.10). Une recherche systématique des PEGS générés par les grands séismes récents a été réalisée et n'a été concluante que pour 5 évènements [Vallée and Juhel, 2019].



La faisabilité de la détection rapide et systématique des PEGS n'est ainsi pas démontrée. Une piste prometteuse est le développement d'une nouvelle génération d'instruments spécifiquement conçus pour n'enregistrer que le terme gravitationnel direct des PEGS, découplé du terme induit [Juhel *et al.*, 2018]. Nous explorerons dans ce manuscrit une piste alternative : l'utilisation de la technologie émergente de l'Intelligence Artificielle (IA) pour rapidement détecter les PEGS et estimer la magnitude et la localisation des grands séismes. Cette technologie s'avère, en effet, être extrêmement efficace pour extraire du bruit des signaux de faible amplitude.

## 5 Possibilités offertes par l'émergence de l'IA

L'IA – ou plus exactement sa sous-branche appelée Apprentissage Machine (*Machine Learning*) – offre une variété d'outils pour extraire de l'information de n'importe quel type de données [Jordan and Mitchell, 2015]. Les algorithmes de *Machine Learning* – que l'on appellera improprement algorithmes d'IA par simplicité – sont conçus pour apprendre à reconnaître des structures dans les données à partir d'un grand nombre d'exemples. Ces algorithmes suivent une approche différente des techniques classiques d'analyse de données, une approche qui est robuste, rapide et permet l'exploration d'espaces de très grandes dimensions. Ces caractéristiques rendent l'IA particulièrement adaptée à la résolution de nombreux problèmes en Sciences de la Terre [Bergen *et al.*, 2019]. Les algorithmes d'IA sont utilisés en sismologie depuis plus de 30 ans [Dowla *et al.*, 1990; Dysart and Pulli, 1990; Dai and MacBeth, 1995] mais ont été accueillis avec peu d'enthousiasme par la communauté dans les années 1990. Le développement exponentiel des capacités de calcul a depuis révélé le potentiel l'IA.

### 5.1 Principes simplifiés de l'IA à l'usage des non-spécialistes

Si la théorie et le développement de schémas algorithmiques nouveaux sont des domaines encore réservés aux spécialistes, l'utilisation d'algorithmes d'IA « pré-implémentés » s'est considérablement démocratisée ces dernières années grâce au développement de bibliothèques d'algorithmes en libre d'accès (e.g., Tensorflow, Keras, PyTorch). Écrire un algorithme d'IA est aujourd'hui largement accessible à un non-spécialiste. Cette démocratisation ouvre la voie à des découvertes majeures dans tous les champs disciplinaires. Elle procure un nouvel outil que des spécialistes de tous les domaines peuvent s'approprier pour résoudre des problèmes qui n'ont, pour l'heure, pas pu être résolus par les techniques « standards ».

Si l'apprentissage non-supervisé est un domaine en développement, relativement abstrait, et encore peu accessible aux non-spécialistes, le principe des algorithmes d'apprentissage supervisé

(Supervised) Machine Learning

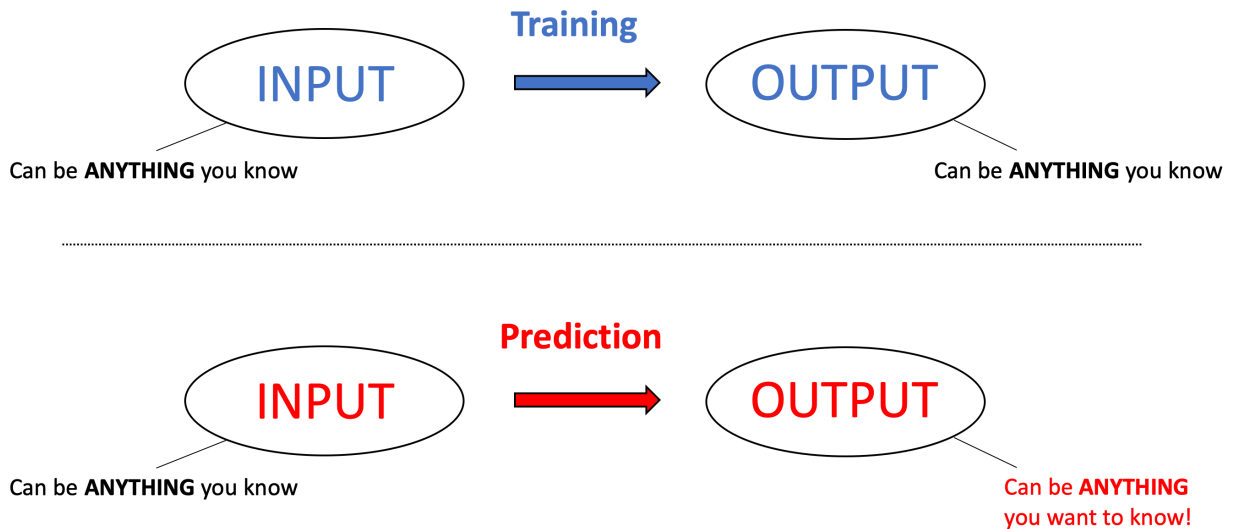


**Figure I.11** – Principes de l'apprentissage machine supervisé (*Supervised Machine Learning*).

– de loin les plus utilisés aujourd'hui – peut être résumé de manière assez simple : il permet de prédire n'importe quel type de sortie (scalaire, vecteur, matrice, image, son, vidéo...) à partir de n'importe quel type d'entrée, en apprenant les liens entre entrée et sortie sur un grand nombre d'exemples. Lors de la phase dite d'entraînement, l'algorithme va chercher dans un espace de grandes dimensions des « liens » entre les jeux de données en entrée et en sortie. Si l'apprentissage est concluant, l'algorithme sera capable lors de la phase de prédiction, de prédire la sortie à partir d'une entrée qu'il n'a jamais vue (Figure I.11). Les 2 seules conditions pour que l'apprentissage fonctionne sont (1) d'avoir suffisamment d'exemples (au moins plusieurs dizaines de milliers) non-redondants et (2) que les jeux de données en entrée et en sortie ne soient pas indépendants.

L'exemple le plus utilisé pour illustrer l'apprentissage supervisé est celui de la reconnaissance d'image. Les données en entrée sont dans l'exemple que l'on prendra des photographies de chiens et de chats. Les données en sortie associent à chaque photographie un scalaire, 0 pour les photographies de chiens, 1 pour celles de chats. Une fois entraîné sur des millions d'exemples, l'algorithme s'avère capable de « reconnaître » des chiens et des chats qu'il n'a jamais vus, i.e. il prédira 0 ou 1 de manière correcte à partir d'une donnée d'entrée absente du jeu d'entraînement. Cet exemple laisse entrevoir les possibilités immenses de l'IA. Celle-ci permet en effet de



répondre à n'importe quelle question formulée en des termes d'entrée et sortie si l'on dispose de suffisamment de données.

### 5.2 Accomplissements récents en sismologie

Les succès de l'IA dans de nombreuses applications couvrant des disciplines très différentes (reconnaissance d'image, traduction automatique, etc.) ont entraîné un regain d'intérêt dans la communauté sismologique. *Bergen et al.* [2019] ont classé les applications récentes de l'IA en Sciences de la Terre solide en 3 catégories.

(1) L'automatisation. L'IA peut, par exemple, être utilisée pour automatiser des tâches comme la détection de séismes [*Zhang et al.*, 2014; *Yoon et al.*, 2015; *Tibi et al.*, 2017; *Bergen and Beroza*, 2018; *Rong et al.*, 2018; *Perol et al.*, 2018; *Ross et al.*, 2018a], le pointé des temps d'arrivée des ondes P et S – une tâche toujours largement réalisée manuellement aujourd'hui – [*Ross et al.*, 2018b; *Zhu and Beroza*, 2019], l'association des phases sismiques [*Ross et al.*, 2019a], et a même été utilisée dans des algorithmes d'alerte précoce [*Reddy and Nair*, 2013; *Kong et al.*, 2016b; *Ochoa et al.*, 2018; *Yin et al.*, 2018; *Lin et al.*, 2021]. L'automatisation par IA donne des résultats plus rapides, plus robustes et moins biaisés que les outils standards, ce qui permet la constitution de catalogues de sismicité beaucoup plus complets [*Ross et al.*, 2019b].

(2) La modélisation. La modélisation par IA inclue des applications comme la prédiction des mouvements du sol à partir des paramètres de la source sismique [*Derras et al.*, 2014; *Trugman and Shearer*, 2018], l'accélération des calculs de simulations numériques [*DeVries et al.*, 2017; *Valera et al.*, 2018] ou encore des problèmes d'inversion [*Käufel et al.*, 2016; *McCann et al.*, 2017].

(3) La découverte. Si l'apprentissage machine procure des outils plus performants que les techniques standards d'automatisation et de modélisation, le plus gros potentiel de l'IA se situe probablement dans la *data-driven discovery*, i.e. la découverte orientée par la donnée. L'IA procure en effet un moyen unique d'extraire de l'information dans de gros volumes de données qu'aucune autre technique ne permet. L'IA peut ainsi permettre de découvrir des signaux ou des processus physiques inconnus [*Holtzman et al.*, 2018; *Rouet-Leduc et al.*, 2018, 2019; *Hulbert et al.*, 2019] et même prédire des séismes en laboratoire [*Rouet-Leduc et al.*, 2017]...

---

# Chapitre II

---

## Où se produisent les grands séismes ?

### 1 Liens entre failles et séismes

La magnitude d'un séisme dépend principalement de la surface de la faille rompue. Pour faire un grand séisme il faut donc une grande faille. La première réponse à la question « Où se produisent les grands séismes » est donc : sur les grandes failles (Figure II.1).

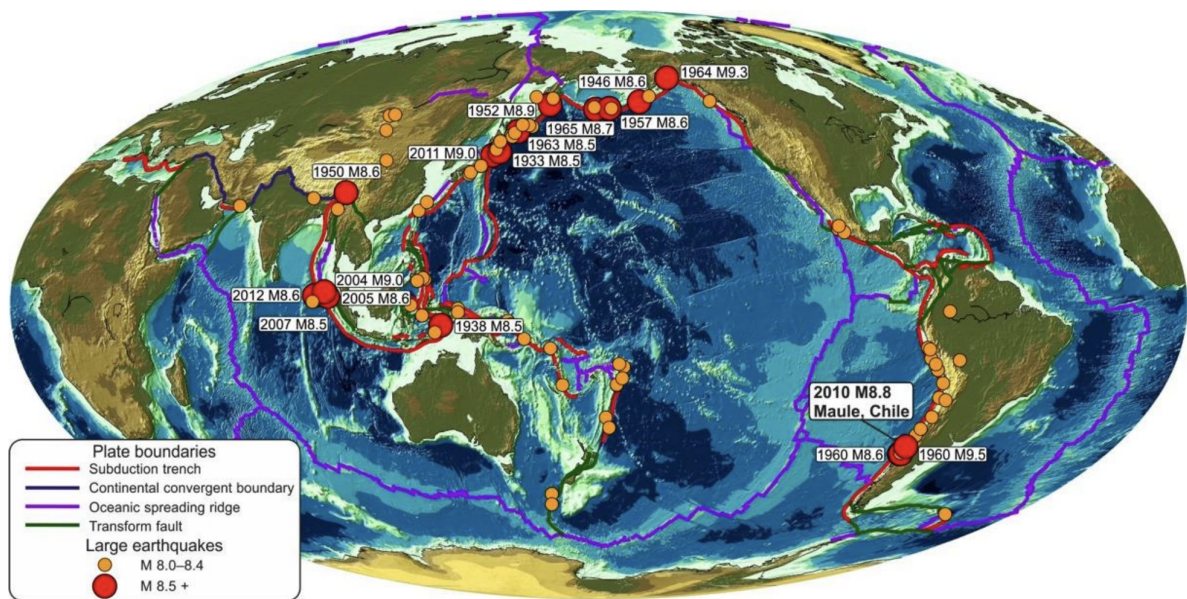


**Figure II.1** – Distribution des grandes failles et des grands séismes à travers le monde [Hicks, 2015].

Toutefois, la relation entre failles et séismes est plus profonde et complexe que cela. Un séisme n'est pas un objet physique hors sol mais l'un des modes de glissement entre deux blocs de Terre le long d'une faille. Les propriétés des failles conditionnent ainsi les propriétés fondamentales des séismes, comme la chute de contraintes [Cao and Aki, 1986; Choy and Kirby, 2004; Manighetti

*et al.*, 2007; *Hecker et al.*, 2010], la longueur de rupture et l’amplitude du glissement [*Manighetti et al.*, 2007], le nombre de segments rompus [*Wesnowsky*, 1988; *Manighetti et al.*, 2007, 2009], la vitesse de la rupture [*Perrin et al.*, 2016] et même les mouvements forts du sol [*Radiguet et al.*, 2009] ainsi que la *b*-value [*Stirling et al.*, 1996].

Peut-on alors déduire des propriétés des failles où les prochains grands séismes sont le plus susceptibles de se produire ? Quelles propriétés des failles ont-elles un contrôle significatif sur la magnitude des grands événements ? *Schellart and Rawlinson* [2013] ont passé en revue 24 paramètres physiques caractérisant les plus grandes failles de la planète – les failles de subduction – découpées pour l’occasion en 44 segments. Il n’ont trouvé que de faibles corrélations entre ces paramètres et la magnitude des séismes historiques, et pour seulement 6 des paramètres testés.

## 2 Les grands séismes se produisent sur les grandes failles planes

Toutes les expériences en laboratoire – à partir desquelles ont été développées les équations utilisées pour modéliser la rupture et le cycle sismique (voir Chapitre I.3.1) – ont été réalisées sur des échantillons de roche de quelques centimètres et présentant une faille pré-existante plane. Or les failles réelles – en particulier les plus grandes d’entre elles, les failles de subduction – sont longues de milliers de kilomètres et ne sont pas planes. Imaginez que l’on ajoute une petite aspérité géométrique dans la topographie d’une faille centimétrique en laboratoire. On intuitivement facilement que le comportement d’une telle micro-faille va être différent du comportement de la même faille plane. Comment cette intuition pourrait-elle se traduire sur des failles naturelles, longues de milliers de kilomètres ? J’ai voulu tester cette idée en calculant le gradient du pendage – une mesure de la topographie – le long des grandes failles de la planète. Il est apparu que les grands séismes historiques se sont produits sur des portions de failles particulièrement planes (à faible gradient de pendage). Notre interprétation de cette observation est que les différentes portions d’une faille ont plus de chances de rompre de manière synchrone, si celle-ci est plane, rendant ainsi le système plus homogène.

Cette étude a été réalisée à l’Université d’Oregon en collaboration avec Amanda M. Thomas, Alan W. Rempel, Leif Karlstrom, Anthony Sladen et Louis De Barros. Elle a été publiée en 2016 dans le journal *Science* [*Bletery et al.*, 2016b].

EXTENDED PDF FORMAT  
SPONSORED BY



### Mega-earthquakes rupture flat megathrusts

Quentin Bletery, Amanda M. Thomas, Alan W. Rempel, Leif Karlstrom, Anthony Sladen and Louis De Barros (November 24, 2016)

*Science* **354** (6315), 1027-1031. [doi: 10.1126/science.aag0482]

Editor's Summary

#### Mega-earthquakes go the flat way

Megathrust faults in subduction zones cause large and damaging earthquakes. Bletery *et al.* argue that certain geometric features of the subduction zones relate to earthquake size. The key parameter is the curvature of the megathrust. Larger earthquakes occur where the subducting slab is flatter, providing a rough metric for estimating where mega-earthquakes may occur in the future.

*Science*, this issue p. 1027

---

This copy is for your personal, non-commercial use only.

---

**Article Tools** Visit the online version of this article to access the personalization and article tools:

<http://science.sciencemag.org/content/354/6315/1027>

**Permissions** Obtain information about reproducing this article:

<http://www.sciencemag.org/about/permissions.dtl>

*Science* (print ISSN 0036-8075; online ISSN 1095-9203) is published weekly, except the last week in December, by the American Association for the Advancement of Science, 1200 New York Avenue NW, Washington, DC 20005. Copyright 2016 by the American Association for the Advancement of Science; all rights reserved. The title *Science* is a registered trademark of AAAS.

in combination with periodic reservoir reloading from a cold atom source (such as a MOT), could be used to maintain arrays indefinitely.

Atom-by-atom assembly of defect-free arrays forms a scalable platform with unique possibilities. It combines features that are typically associated with ion-trapping experiments, such as single-qubit addressability (32, 33) and fast cycling times, with the flexible optical trapping of neutral atoms in a scalable fashion. Furthermore, in contrast to solid-state platforms, such atomic arrays are highly homogeneous (31) and mostly decoupled from their environment. The homogeneity of our array should also allow for cooling of the atomic motion via simultaneous sideband cooling in all tweezers at once (34, 35).

These features provide an excellent starting point for multiqubit experiments, for studies of quantum many-body effects, and for exploring future applications. The required interactions between the atoms can be engineered using several approaches. Even without sideband cooling, exciting the atoms into high-lying Rydberg states would introduce strong dipole interactions that can be used for fast entangling gates (24, 25, 27). The parallelism afforded by our flexible atom rearrangement enables efficient diagnostics of such Rydberg-mediated entanglement. These interactions may also enable approaches to quantum simulations that involve both coherent coupling and engineered dissipation (26, 27), as well as large-scale entangled quantum states for applications in precision measurements (36).

An alternative approach to engineering interactions involves the integration of atom arrays with nanophotonic platforms as demonstrated previously (28, 29). These enable photon-mediated interactions that can be employed to couple the atoms within a local multiqubit register or for efficient communication between the registers using a modular quantum network architecture (3).

Finally, our platform could enable new bottom-up approaches to studying quantum many-body physics in Hubbard models (15, 16, 30), where atomic Mott insulators with fixed atom number and complex spin patterns could be directly assembled. This requires atom temperatures close to the ground state, coherent tunneling between the traps, and sizable on-site interactions. With side-band cooling, ground-state fractions in excess of 90% have already been demonstrated (34, 35) and can likely be improved via additional optical trapping along the longitudinal tweezer axes, which would also increase on-site interaction strengths. Coherent tunneling of Rb atoms between similarly sized tweezers has been observed before by reducing the tweezer distance (15, 16). The parametric heating, currently limiting the minimal distance between our traps, could be reduced by working with shallower traps, as needed for tunneling, and by employing fewer traps to increase the frequency separation between neighboring traps. Eventually, this approach could be applied to create ultracold quantum matter composed of exotic atomic species or complex molecules (37, 38) that are difficult to cool evaporatively.

## REFERENCES AND NOTES

1. S. Haroche, *Ann. Phys.* **525**, 753–776 (2013).
2. D. J. Wineland, *Rev. Mod. Phys.* **85**, 1103–1114 (2013).
3. C. Monroe, J. Kim, *Science* **339**, 1164–1169 (2013).
4. M. H. Devoret, R. J. Schoelkopf, *Science* **339**, 1169–1174 (2013).
5. W. S. Bakr *et al.*, *Science* **329**, 547–550 (2010).
6. J. F. Sherson *et al.*, *Nature* **467**, 68–72 (2010).
7. C. Weitenberg *et al.*, *Nature* **471**, 319–324 (2011).
8. D. S. Weiss *et al.*, *Phys. Rev. A* **70**, 040302 (2004).
9. J. Vala *et al.*, *Phys. Rev. A* **71**, 032324 (2005).
10. N. Schlosser, G. Reymond, I. Protsenko, P. Grangier, *Nature* **411**, 1024–1027 (2001).
11. M. Weber, J. Volz, K. Saucke, C. Kurtsiefer, H. Weinfurter, *Phys. Rev. A* **73**, 043406 (2006).
12. K. D. Nelson, X. Li, D. S. Weiss, *Nat. Phys.* **3**, 556–560 (2007).
13. M. J. Piotrowicz *et al.*, *Phys. Rev. A* **88**, 013420 (2013).
14. F. Nogrette *et al.*, *Phys. Rev. X* **4**, 021034 (2014).
15. A. M. Kaufman *et al.*, *Science* **345**, 306–309 (2014).
16. A. M. Kaufman *et al.*, *Nature* **527**, 208–211 (2015).
17. Y. Miroshnychenko *et al.*, *Nature* **442**, 151 (2006).
18. J. Beugnon *et al.*, *Nat. Phys.* **3**, 696–699 (2007).
19. M. Schlosser *et al.*, *New J. Phys.* **14**, 123034 (2012).
20. H. Kim, *et al.*, *Nat. Commun.* **7**, 13317 (2016).
21. T. Grünzweig, A. Hilliard, M. McGovern, M. F. Andersen, *Nat. Phys.* **6**, 951–954 (2010).
22. B. J. Lester, N. Luick, A. M. Kaufman, C. M. Reynolds, C. A. Regal, *Phys. Rev. Lett.* **115**, 073003 (2015).
23. Y. H. Fung, M. F. Andersen, *New J. Phys.* **17**, 073011 (2015).
24. D. Jaksch *et al.*, *Phys. Rev. Lett.* **85**, 2208–2211 (2000).
25. M. Saffman, T. G. Walker, K. Mølmer, *Rev. Mod. Phys.* **82**, 2313–2363 (2010).
26. H. Weimer, M. Müller, I. Lesanovsky, P. Zoller, H. P. Büchler, *Nat. Phys.* **6**, 382–388 (2010).
27. A. Browaeys, D. Barredo, T. Lahaye, *J. Phys. B* **49**, 152001 (2016).
28. J. D. Thompson *et al.*, *Science* **340**, 1202–1205 (2013).
29. A. Goban *et al.*, *Nat. Commun.* **5**, 3808 (2014).
30. S. Murrmann *et al.*, *Phys. Rev. Lett.* **115**, 215301 (2015).
31. See supplementary materials on Science Online.
32. T. Xia *et al.*, *Phys. Rev. Lett.* **114**, 100503 (2015).
33. Y. Wang, X. Zhang, T. A. Corcovilos, A. Kumar, D. S. Weiss, *Phys. Rev. Lett.* **115**, 043003 (2015).
34. A. M. Kaufman, B. J. Lester, C. A. Regal, *Phys. Rev. X* **2**, 041014 (2012).
35. J. D. Thompson, T. G. Tiecke, A. S. Zibrov, V. Vuletić, M. D. Lukin, *Phys. Rev. Lett.* **110**, 133001 (2013).
36. P. Kómár *et al.*, *Phys. Rev. Lett.* **117**, 060506 (2016).
37. J. F. Barry, D. J. McCarron, E. B. Norrgard, M. H. Steinecker, D. DeMille, *Nature* **512**, 286–289 (2014).
38. N. R. Hutzler, L. R. Liu, Y. Yu, K.-K. Ni, <https://arxiv.org/abs/1605.09422> (2016).
39. D. Barredo, S. de Léséleuc, V. Lienhard, T. Lahaye, A. Browaeys, *Science* **354**, 1021–1023 (2016).

## ACKNOWLEDGMENTS

We thank K.-K. Ni, N. Hutzler, A. Mazurenko, and A. Kaufman for insightful discussion. This work was supported by NSF, Center for Ultracold Atoms, National Security Science and Engineering Faculty Fellowship, and Harvard Quantum Optics Center. H.B. acknowledges support by a Rubicon Grant of the Netherlands Organization for Scientific Research (NWO). During the completion of this work, we became aware of a related approach (39).

## SUPPLEMENTARY MATERIALS

[www.sciencemag.org/content/354/6315/1024/suppl/DC1](http://www.sciencemag.org/content/354/6315/1024/suppl/DC1)  
Materials and Methods  
Figs. S1 to S5  
Movies S1 to S3  
References (40, 41)

17 June 2016; accepted 17 October 2016  
Published online 3 November 2016  
10.1126/science.aah3752

## GEOPHYSICS

# Mega-earthquakes rupture flat megathrusts

Quentin Bletery,<sup>1\*</sup> Amanda M. Thomas,<sup>1</sup> Alan W. Rempel,<sup>1</sup> Leif Karlstrom,<sup>1</sup> Anthony Sladen,<sup>2</sup> Louis De Barros<sup>2</sup>

The 2004 Sumatra-Andaman and 2011 Tohoku-Oki earthquakes highlighted gaps in our understanding of mega-earthquake rupture processes and the factors controlling their global distribution: A fast convergence rate and young buoyant lithosphere are not required to produce mega-earthquakes. We calculated the curvature along the major subduction zones of the world, showing that mega-earthquakes preferentially rupture flat (low-curvature) interfaces. A simplified analytic model demonstrates that heterogeneity in shear strength increases with curvature. Shear strength on flat megathrusts is more homogeneous, and hence more likely to be exceeded simultaneously over large areas, than on highly curved faults.

**P**ast mega-earthquakes, such as the magnitude ( $M$ ) 9.6 Chile earthquake in 1960 and the  $M$  9.3 Alaska earthquake in 1964, occurred in areas where the subducting lithosphere was relatively young (and buoyant) and the plate convergence rate was relatively high ( $I$ ). These observations led some authors to hypothesize that maximum earthquake

size is controlled by these two geological parameters (2, 3). The development of space-based geodesy enabled refined measurements of plate motion that challenged the role of convergence rate (4–6). Additionally, the moment magnitude ( $M_w$ ) 9.0 Tohoku-Oki earthquake (7) ruptured lithosphere that is over 120 million years old (8), ruling out lithospheric age as the dominant control. Weak correlations appear in recent data sets among a variety of parameters, including forearc structure (9, 10); age, density, and buoyancy of the slab (6); upper plate motion (11); upper plate strain (12); long-term trench migration (11); trench sediment thickness (12); and width of the seismogenic

<sup>1</sup>Department of Earth Sciences, University of Oregon, 1272 University of Oregon, Eugene, OR 97403, USA. <sup>2</sup>Université Côte d'Azur, CNRS, OCA, IRD, Géoazur, 250 rue Albert Einstein, Sophia Antipolis, 06560 Valbonne, France.

\*Corresponding author. Email: [qbletery@uoregon.edu](mailto:qbletery@uoregon.edu)



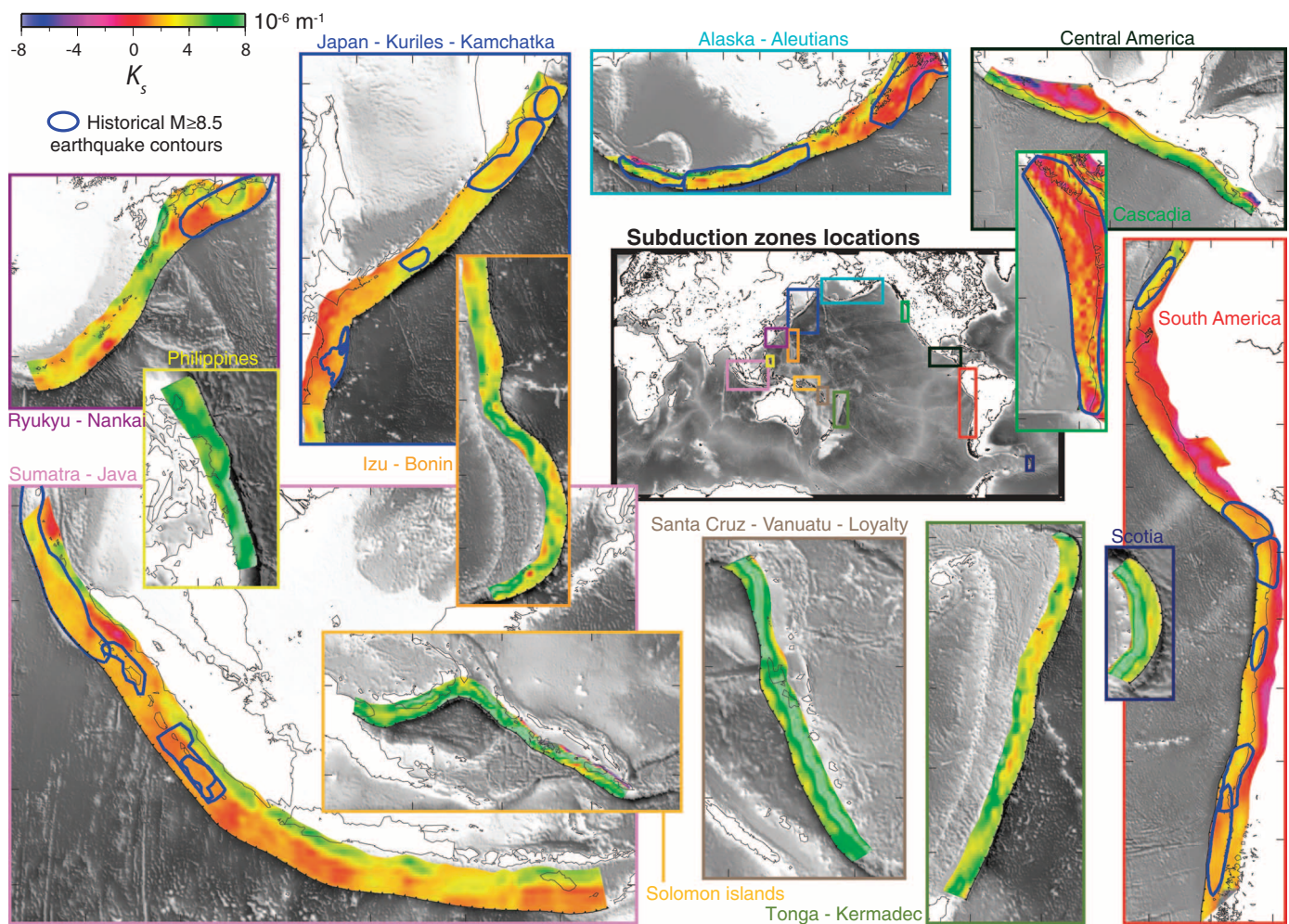


**Fig. 1. Variations in megathrust curvature and distribution of historical mega-earthquakes.** Along-dip curvature  $K_s = d\theta/ds$  on the megathrust is shown for the 13 main subduction zones of the world, overlaid with the estimated slip contours of known historical mega-earthquakes ( $M \geq 8.5$ ) (see table S1 for a list of events). Tick marks in each panel are spaced at  $5^\circ$  increments.

zone (11, 13, 14). However, aside from dip angle and seismogenic width [coefficient of correlation  $r = 0.61$  (14)], none of these parameters correlate strongly ( $|r| < 0.5$ ) with the maximum earthquake magnitude recorded in the different zones (11). Stronger correlations are found with fault properties such as thrust interface dip angle (11) and apparent friction derived from heat flow measurements (15).

Today, forecasts of potential large earthquakes focus mainly on imaging the slip deficit with respect to the relative plate motion, because such deficits are thought to result in stress loading that is ultimately released in earthquakes [e.g., (16)]. We followed a complementary approach by analyzing large-scale geometrical features of subduction faults and assessing their possible influence on the physical conditions favoring large earthquake ruptures. Seismic moment  $M_0 \propto \Delta\sigma S^{3/2}$  (17) depends mainly on the surface area  $S$  over which an earthquake ruptures, because the stress drop  $\Delta\sigma$  (the difference in stress before and after an earthquake) is roughly constant among earthquakes over a large range of magnitudes (18). Here we demonstrate that slab interface curvature

exerts a leading-order control on the spatial extent of potential ruptures in subduction zones and hence on the magnitude of the largest earthquakes.

Data sets from active- and passive-source seismology have been combined to constrain the slab1.0 model for the geometry of the world's major subduction zones (14) [details and limitations of the slab1.0 model are discussed in the supplementary materials (19)]. We computed maps of the along-dip interface curvature  $K_s = d\theta/ds$ , hereafter referred to as curvature [where  $\theta$  is the dip angle and  $s$  is the tangent to the interface pointing in the down-dip direction (19)], using the slab1.0 model (14, 20) (Fig. 1). Because  $K_s$  is almost always positive (Fig. 1), we hereafter interchangeably refer to low- $K_s$  fault regions as flat, low-curvature, or planar. Similarly, we computed the along-strike gradient of the dip angle  $K_t = d\theta/dt$  (fig. S1). Comparison with a catalog of historical events (19) reveals a tendency for mega-earthquakes to occur on relatively flat (low- $K_s$ ) megathrusts (Fig. 1). The curvature is particularly small in the Japan-Kuriles-Kamchatka, Alaska-Aleutians, Sumatra-Java, South America, and Cascadia subduction zones, which are known

to produce  $M \geq 9.0$  earthquakes. Subduction zones with large curvatures, such as the Philippines, Solomon Islands, Izu-Bonin, Santa Cruz-Vanuatu-Loyalty, and Tonga-Kermadec zones, lack historic mega-earthquakes. At a smaller scale, we also observe that the down-dip limit of mega-earthquakes offshore of Sumatra—and to a lesser extent, in the Aleutians, Alaska, Nankai, and Kamchatka—coincides with an abrupt change in the slope, suggesting that the conditions required to generate large earthquakes are directly related to the local curvature along the megathrust interface.

To further explore the role of subduction geometry, we calculated the average dip angle  $\bar{\theta}$  (Fig. 2A), the average curvature  $\bar{K}_s$  (Fig. 2B), and the average along-strike gradient of dip angle  $|\bar{K}_t|$  (fig. S2) from the trench to 60 km depth, and we compared these values with the magnitude of the largest megathrust earthquake  $M_{\max}$  recorded in each subduction zone. We found that  $M_{\max}$  anticorrelates ( $r = -0.72$ ) with  $\bar{\theta}$  (Fig. 2A) and anticorrelates even more strongly ( $r = -0.80$ ) with  $\bar{K}_s$  (Fig. 2B). The anticorrelation with  $|\bar{K}_t|$  is weaker ( $r = -0.64$ ) but still significant (fig.

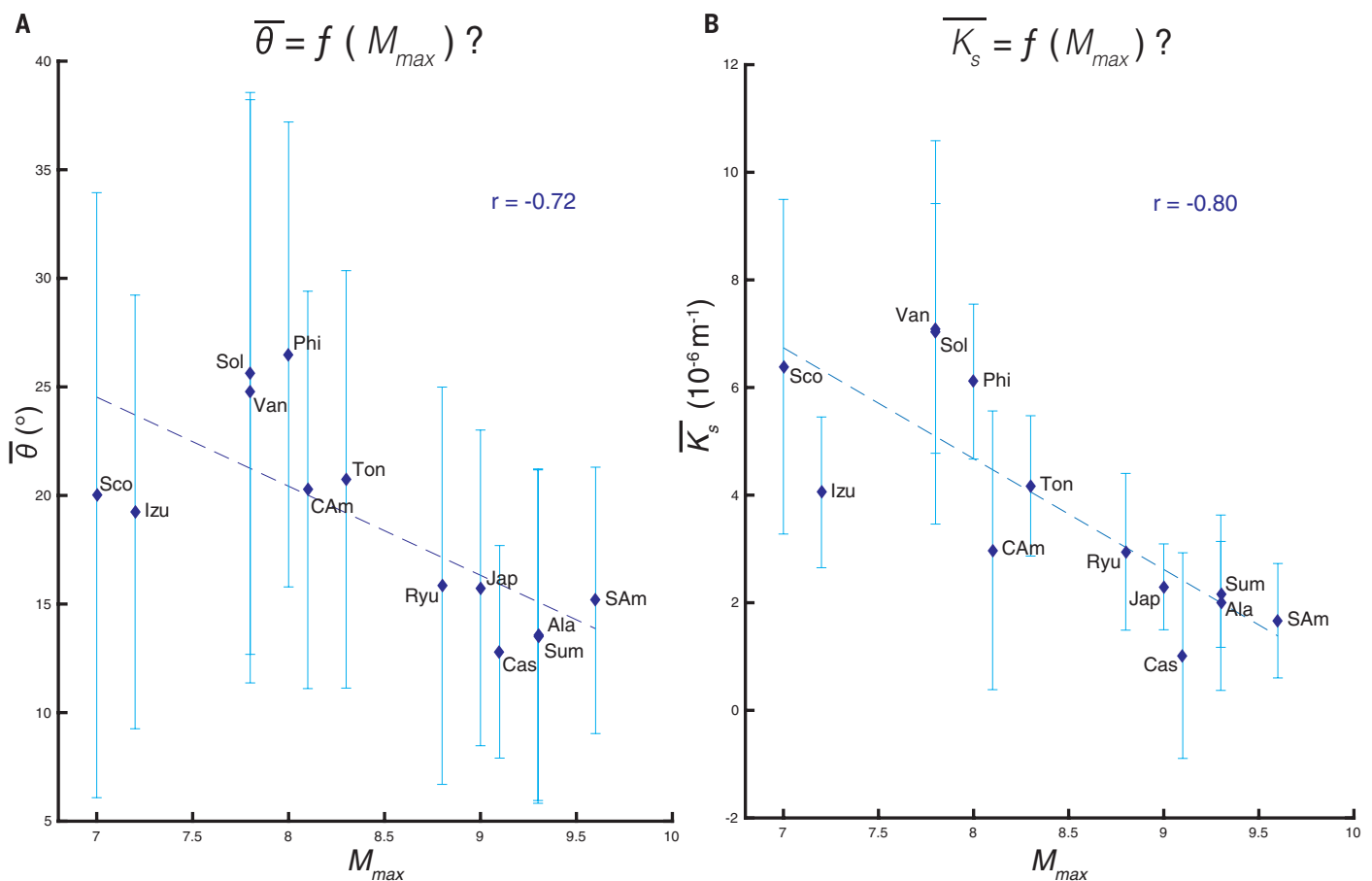


**Fig. 2. Correlation of average dip angle and curvature with maximum earthquake magnitude.** (A) Average dip angle  $\bar{\theta}$  of the 13 main subduction zones of the world as a function of the maximum event magnitude  $M_{max}$  recorded on the megathrust (see table S2 for a list of events). The coefficient of correlation  $r$  is  $-0.72$ . (B) Same as (A), but for the average along-dip curvature  $\bar{K}_s$  ( $r = -0.80$ ). Light blue bars show the standard deviation for the distribution of  $\bar{\theta}$  (A) and  $\bar{K}_s$  (B) in each subduction zone. These bars should

not be considered as error bars because we are reasoning with averages; they rather indicate how  $\theta$  and  $K_s$  are distributed along the different subduction zones. Blue dashed lines are the linear regressions. Ala, Alaska-Aleutians; CAm, Central America; Cas, Cascadia; Izu, Izu-Bonin; Jap, Japan-Kuriles-Kamchatka; Phi, Philippines; Ryu, Ryukyu-Nankai; SAm, South America; Sco, Scotia arc; Sol, Solomon Islands; Sum, Sumatra-Java; Ton, Tonga-Kermadec; Van, Santa Cruz-Vanuatu-Loyalty.

S2). We suggest, on the basis of our observations, that planar slab interfaces are prone to hosting larger earthquakes. Multiple factors, including the subducting (21) or overriding (22) plate thickness and viscosity contrast (23), have been invoked as controls on subduction curvature; these studies (21–23) provide a useful introduction to this field of research.

The average curvature within mega-earthquake slip contours is consistent with the linear regression in Fig. 2B, with observed values always smaller than  $3.76 \times 10^{-6} \text{ m}^{-1}$  (fig. S5B). Given the distribution of  $K_s$  across the different megathrusts of the world, the likelihood that all known mega-earthquakes occurred by chance on  $K_s \leq 3.76 \times 10^{-6} \text{ m}^{-1}$  areas is 0.8% (19), allowing us to affirm with >99% confidence that earthquake magnitude is related to megathrust curvature. The distribution of the average dip angle within mega-rupture contours is much broader (fig. S5A), confirming the stronger relationship of earthquake size with curvature than with dip angle (19). Nevertheless, known mega-earthquakes do not exhibit a strong tendency to rupture the lower-

curvature portions of their host subduction zones (19). This suggests that over the long term, mega-earthquakes might rupture any portion of a low-curvature subduction thrust, such as those of the Cascadia, South America, Alaska-Aleutians, Sumatra-Java, Japan-Kuriles-Kamchatka, Ryukyu-Nankai, and Central America subduction zones. Large earthquakes are preferentially hosted by megathrusts with low dip angles in part as a consequence of larger down-dip seismogenic extents making ruptures possible over wider fault areas (11, 13, 14). However, the stronger relationship of earthquake size with curvature than with dip angle noted above (Fig. 2B) warrants a more thorough description of fault loading.

The present understanding of seismic ruptures can be framed in terms of the asperity model: Earthquakes are caused by the sudden failure of locked macroscopic asperities that accumulate stress during interseismic periods (24). In this context, the extent of an earthquake has a leading-order dependence on the size of the rupturing asperity and the neighboring region that is pushed to failure by coseismic stress change.

Recent efforts aimed at characterizing the nature of asperities and their immediate surroundings have mostly focused on potential variations in friction along faults [e.g., (25–28)]. The capacity of a fault segment to accumulate stress is bounded by the Coulomb failure criterion

$$|\tau^c| = \mu(\sigma_n^c - p) \quad (1)$$

where  $\tau^c$  is the critical shear stress required to initiate a rupture (hereafter referred to as shear strength),  $\mu$  is the coefficient of friction,  $p$  is the pore pressure,  $\sigma_n^c$  is the normal stress when the rupture initiates, and cohesion is neglected. The Coulomb failure criterion is met when the accumulated shear stress reaches the frictional shear strength and an earthquake initiates. From Eq. 1, one can define an asperity as a fault area characterized by a particularly high friction coefficient  $\mu$ . Alternatively, one can also explain the time-dependent behavior of asperities by appealing to variations in pore pressure  $p$  that accompany fluid migration [e.g., (29)]. We explore here a different hypothesis, which is that the locations of



asperities can be determined by analyzing variations in normal stress  $\sigma_n$  that are governed by large-scale geometrical characteristics of megathrust interfaces. Assuming constant friction  $\mu$  and hydrostatic pore pressure  $p = \rho_w g h$  (with  $\rho_w$  being the water density,  $g$  the acceleration of gravity, and  $h$  the local interface depth), we illustrate the effect of variations in normal stress  $\sigma_n$  on variations in shear strength [this method is reminiscent of the consideration of normal force in (16) but invokes different causative factors, i.e., curvature instead of plate tectonic forces].

We considered a simple two-dimensional (2D) fault model: a fault interface subjected to the pressure of the upper plate mass and an unknown horizontal tectonic stress. We also treated the convergence direction as aligned with the horizontal projection of the local along-dip direction (i.e., pure dip-slip convergence). This latter simplification is justified by the dominantly dip-slip mechanisms of most megathrust earthquakes [e.g., figures 14, 15, and 16 of (30)]. Even though subduction zones present, to varying degrees, oblique convergences, this obliquity is usually accommodated for the most part by large strike-slip faults in the back arc. One notable exception is the Solomon Islands subduction zone, which presents a very strong oblique convergence and hosts megathrust earthquakes that typically exhibit large strike-slip components. Our idealized description of the convergence direction allows us to treat the 3D problem with a 2D model (fig. S6). Within this framework, the shear strength—defined as the critical shear stress required to initiate slip at a given location—can be expressed as a function of the crustal density  $\rho$ , the friction  $\mu$ , the depth  $h$ , the dip angle  $\theta$ , and the angle  $\psi$  between the maximum principal component of stress and the horizontal

$$\tau^c = \frac{g h \mu (\rho - \rho_w) (\sin 2\theta + \tan 2\psi \cos 2\theta)}{\sin 2\theta - \mu (1 - \cos 2\theta) + \tan 2\psi (\cos 2\theta - \mu \sin 2\theta)} \quad (2)$$

$\tau^c$  increases with  $\theta$  ( $\partial \tau^c / \partial \theta \geq 0$ ) (19) meaning that large dip angles imply greater shear strength. If the dominant control of earthquake magnitude were the amplitude of shear strength, we might expect a positive correlation between  $M_{\max}$  and  $\theta$ . The negative correlation that we observe (Fig. 2A) points to other factors.

Because the magnitude of an earthquake is primarily controlled by the area of rupture, homogeneous distributions of shear strength over large fault areas may favor the occurrence of mega-earthquakes. In this framework, the shear-strength gradient  $d\tau^c/ds$  is a critical parameter. Treating  $\mu$ ,  $\rho$ ,  $\rho_w$ , and  $g$  as constants, spatial variations of  $\tau^c$  obtained by differentiation of Eq. 2 satisfy

$$\frac{d\tau^c}{ds} = g \mu (\rho - \rho_w) \left( A_\mu(\theta, \psi) \sin \theta + B_\mu(\theta, \psi) h K_s + C_\mu(\theta, \psi) h \frac{d\psi}{ds} \right) \quad (3)$$

where  $\rho > \rho_w$  and the functions  $A_\mu(\theta, \psi)$ ,  $B_\mu(\theta, \psi)$ , and  $C_\mu(\theta, \psi)$  are positive for  $\mu = 0.6$  and values of  $\theta$  and  $\psi$  typically encountered in subduction zones (19). Therefore,  $|d\tau^c/ds|$  increases with  $K_s$  [a similar argument can be made to show that  $|d\tau^c/dt|$  increases, on average, with  $|K_t|$  (19)]. Shear-strength heterogeneity increases with curvature: The flatter the megathrust interface (lower  $K_s$ ), the more homogeneous the shear-strength distribution. Stress accumulation along faults is complex, and heterogeneities in driving stress can result from the effect of stress concentrations inherited from past events or changes in coupling associated with variations in the friction coefficient or pore fluid pressure. However, dynamic stress perturbations induced by earthquake propagation are more likely to overstep the resistance to failure over broad areas if shear strength is homogeneously distributed along a large fault surface. In contrast, barriers to earthquake propagation are more likely for heterogeneous shear-strength distributions, because the dynamic stress perturbations required to reach local values of shear strength will tend to be larger in some regions. The idea that geometrical heterogeneity may limit earthquake propagation has been previously invoked (15, 31) and is consistent with the observation that many large earthquake ruptures terminate near subducting seamounts or other structural heterogeneities (31, 32).

During an earthquake, fault slip will propagate as long as the dynamic stress perturbation induced by the earlier phase of the rupture,  $\delta\tau$ , is larger than the difference between shear strength and shear stress in the surrounding area,  $\Delta\tau$ . Hence, one way to generate mega-earthquakes is to initiate a large dynamic stress perturbation by the failure of a strongly locked asperity so that  $\delta\tau > \Delta\tau$  over a large surrounding fault area. In this scenario, mega-earthquakes are characterized by the rupture of one or several asperities where shear strength is particularly high. Our finding that large earthquakes rupture flat megathrusts suggests that another way to generate mega-earthquakes is if  $\Delta\tau$  is small in a large area surrounding rupture nucleation, and thus even relatively small dynamic stress perturbations  $\delta\tau$  can continue to propagate rupture. The 2004 Sumatra-Andaman earthquake, a unilaterally propagating 1600-km-long rupture without evidence of a localized high stress drop (33), exemplifies this second scenario, because it is unlikely that the energy released during the early phases of rupture could have initiated slip on fault portions as far as 1600 km away if the entire ruptured area was not already close to failure. In this situation, mega-earthquakes are not characterized by the rupture of asperities in regions where strength is much greater than in the surrounding area but, on the contrary, by the absence of strong variations in strength. The limiting case of homogeneous null shear strength results in constant creep and the absence of earthquakes of any magnitude. Hence, although the amplitude of  $\tau^c$  is an important parameter, the observation that mega-earthquakes preferentially occur on flat subduction zones (Fig. 2) seems to indicate that the homogeneity of the

shear-strength distribution is among the most critical factors in enabling the generation of mega-earthquakes.

It has recently been proposed that any subduction zone may produce a  $M \geq 9$  earthquake (34). Our results suggest that earthquake size is limited by curvature and, if our interpretation is correct, mega-earthquakes might be physically incapable of rupturing highly curved subduction zones with large shear-strength gradients, such as the Philippines, the Solomon Islands, Scotia arc, and Santa Cruz-Vanuatu-Loyalty; heterogeneous shear strength creates natural barriers that stop earthquake propagation. It is possible that heterogeneous shear stress could build to match a heterogeneous shear-strength distribution and allow rare large events, but such scenarios are expected to be less likely, and therefore more infrequent, than on megathrusts with more homogeneous shear strength. As indicated by Fig. 2B, some subduction zones, such as Izu-Bonin or Central America, may yet host earthquakes larger than previously recorded. Cascadia is noteworthy because the last mega-earthquake that it hosted is thought to have ruptured the entire subduction fault and therefore reached the maximum possible magnitude for this subduction zone (35). At a smaller scale, some areas, such as Peru, Java, or the large low-to-negative  $K_s$  fault region in Central America (Fig. 1), which includes the Guerrero gap but extends much farther, show favorable features for a possible very large rupture—implying in the Guerrero case the potential for an even larger earthquake than that inferred from the extent of the gap. Moreover, large flat portions of subduction faults may sometimes rupture as one mega-earthquake and sometimes as several smaller earthquakes. Such behavior is documented, for instance, in Nankai (36), where two nearby asperities sometimes break as two separate consecutive earthquakes (as in 1854 and 1944–1946) and sometimes as one larger earthquake (1707; blue contour in the Ryukyu-Nankai box). This suggests that high-curvature regions of generally flat subduction zones may act as barriers to rupture most of the time and still sometimes be overcome by coseismic stress changes. Planar fault areas may thus host moderate-sized earthquakes for a long time and still have the potential to generate mega-earthquakes in the future.

It is possible that frictional properties and geometry are related. Such mechanical relationships are well described in accretionary wedges (37) and are certainly expected, though more difficult to constrain, along the deeper portions of megathrusts. Slab curvature has also been proposed to promote higher permeability (38–41) and thus to have an impact on the pore fluid pressure as well. Nevertheless, we have shown that spatial variations in friction and pore fluid pressure are not required to explain the gross distribution of mega-earthquakes. The observation that mega-earthquakes preferentially rupture flat megathrusts (Figs. 1 and 2B) is consistent with the inference that shear strength tends to be more homogeneously distributed along such subduction interfaces (Eq. 3), facilitating synchronized



failure over large areas. This implies that the critical feature at play in the generation of mega-earthquakes is not the amplitude of shear strength but its spatial variations. Thus, the absence of asperities on large faults may counterintuitively be a source of higher hazard. Though our study focused on subduction earthquakes, flatness may favor large earthquakes on long strike-slip faults as well.

## REFERENCES AND NOTES

- H. Kanamori, *Philos. Trans. R. Soc. A* **364**, 1927–1945 (2006).
- L. Ruff, H. Kanamori, *Phys. Earth Planet. Inter.* **23**, 240–252 (1980).
- L. Ruff, H. Kanamori, *Tectonophysics* **99**, 99–117 (1983).
- R. McCaffrey, *Geophys. Res. Lett.* **21**, 2327–2330 (1994).
- S. Stein, E. A. Okal, *Bull. Seismol. Soc. Am.* **97**, S279–S295 (2007).
- T. Nishikawa, S. Ide, *Nat. Geosci.* **7**, 904–908 (2014).
- Q. Bletery et al., *J. Geophys. Res. Solid Earth* **119**, 7636–7653 (2014).
- R. D. Müller, M. Sdrolias, C. Gaina, W. R. Roest, *Geochim. Geophys. Geosyst.* **9**, Q04006 (2008).
- T.-R. A. Song, M. Simons, *Science* **301**, 630–633 (2003).
- R. E. Wells, R. J. Blakely, Y. Sugiyama, D. W. Scholl, P. A. Dinterman, *J. Geophys. Res. Solid Earth* **108**, 2507 (2003).
- W. Schellart, N. Rawlinson, *Phys. Earth Planet. Inter.* **225**, 41–67 (2013).
- A. Heuret, C. Conrad, F. Funicello, S. Lallemand, L. Sandri, *Geophys. Res. Lett.* **39**, L05304 (2012).
- J. F. Pacheco, L. R. Sykes, *Bull. Seismol. Soc. Am.* **82**, 1306 (1992).
- G. P. Hayes, D. J. Wald, R. L. Johnson, *J. Geophys. Res. Solid Earth* **117**, B01302 (2012).
- X. Gao, K. Wang, *Science* **345**, 1038–1041 (2014).
- C. H. Scholz, J. Campos, *J. Geophys. Res. Solid Earth* **117**, B05310 (2012).
- R. Madariaga, *J. Geophys. Res.* **84**, 2243 (1979).
- H. Kanamori, D. L. Anderson, *J. Geophys. Res.* **80**, 1075–1078 (1975).
- Materials and methods are available as supplementary materials on Science Online.
- P. A. McCrory, J. L. Blair, F. Waldhauser, D. H. Oppenheimer, *J. Geophys. Res. Solid Earth* **117**, n/a (2012).
- W. P. Schellart, J. Freeman, D. R. Stegman, L. Moresi, D. May, *Nature* **446**, 308–311 (2007).
- A. F. Holt, B. A. Buffett, T. W. Becker, *Geophys. Res. Lett.* **42**, 3802–3810 (2015).
- W. Schellart, *J. Geophys. Res. Solid Earth* **115**, B11406 (2010).
- T. Lay, H. Kanamori, L. Ruff, *Earthq. Predict. Res.* **1**, 3 (1982).
- S. T. Tse, J. R. Rice, *J. Geophys. Res.* **91**, 9452 (1986).
- J. Dieterich, *J. Geophys. Res. Solid Earth* **99**, 2601–2618 (1994).
- C. H. Scholz, *Nature* **391**, 37–42 (1998).
- C. Marone, *Nature* **391**, 69–72 (1998).
- Y. Guglielmi, F. Cappa, J.-P. Avouac, P. Henry, D. Elsworth, *Science* **348**, 1224–1226 (2015).
- B. P. Allmann, P. M. Shearer, *J. Geophys. Res. Solid Earth* **114**, B01310 (2009).
- K. Wang, S. L. Bilek, *Tectonophysics* **610**, 1–24 (2014).
- K. Wang, S. L. Bilek, *Geology* **39**, 819–822 (2011).
- Q. Bletery, A. Sladen, J. Jiang, M. Simons, *J. Geophys. Res. Solid Earth* **121**, 5116–5135 (2016).
- R. McCaffrey, *Geology* **36**, 263 (2008).
- K. Satake, K. Wang, B. F. Atwater, *J. Geophys. Res. Solid Earth* **108**, 2535 (2003).
- T. Furumura, K. Imai, T. Maeda, *J. Geophys. Res. Solid Earth* **116**, B02308 (2011).
- F. Dahlen, *Annu. Rev. Earth Planet. Sci.* **18**, 55–99 (1990).
- R. J. Lisle, J. M. Robinson, *J. Struct. Geol.* **17**, 739–750 (1995).
- C. R. Ranero, J. Phipps Morgan, K. McIntosh, C. Reichert, *Nature* **425**, 367–373 (2003).
- M. Faccenda, T. V. Gerya, L. Burlini, *Nat. Geosci.* **2**, 790–793 (2009).
- T. Nishikawa, S. Ide, *Geophys. Res. Lett.* **42**, 7081–7089 (2015).

## ACKNOWLEDGMENTS

We thank R. Bürgmann for his valuable comments on the manuscript. The slab1.0 model is available online at [earthquake.usgs.gov/data/slab/](http://earthquake.usgs.gov/data/slab/). The U.S. Geological Survey catalog of historical earthquakes ( $M \geq 8.0$  since 1900) that we used in this

study can be found at <http://earthquake.usgs.gov/earthquakes/world/historical.php>. For the subduction zones that have not experienced any  $M \geq 8.0$  earthquakes since 1900, this catalog was complemented by the Global Centroid Moment Tensor catalog ([www.globalcmt.org/](http://www.globalcmt.org/)). We used Generic Mapping Tools to compute the distributions of dip-angle gradients ([gmt.soest.hawaii.edu/](http://gmt.soest.hawaii.edu/)). This work was supported by NSF grant EAR-1520238, ANR project TO-EOS, and the French Ministry of Research and Education.

## SUPPLEMENTARY MATERIALS

[www.sciencemag.org/content/354/6315/1027/suppl/DC1](http://www.sciencemag.org/content/354/6315/1027/suppl/DC1)  
Materials and Methods  
Figs. S1 to S8  
Tables S1 to S2  
References (42–53)

6 May 2016; accepted 19 October 2016  
10.1126/science.aag0482

## CATALYSIS

# Direct and continuous strain control of catalysts with tunable battery electrode materials

Haotian Wang,<sup>1</sup> Shicheng Xu,<sup>2</sup> Charlie Tsai,<sup>3,4</sup> Yuzhang Li,<sup>5</sup> Chong Liu,<sup>5</sup> Jie Zhao,<sup>5</sup> Yayuan Liu,<sup>5</sup> Hongyuan Yuan,<sup>6</sup> Frank Abild-Pedersen,<sup>4</sup> Fritz B. Prinz,<sup>2,5</sup> Jens K. Nørskov,<sup>3,4</sup> Yi Cui<sup>5,7\*</sup>

We report a method for using battery electrode materials to directly and continuously control the lattice strain of platinum (Pt) catalyst and thus tune its catalytic activity for the oxygen reduction reaction (ORR). Whereas the common approach of using metal overlayers introduces ligand effects in addition to strain, by electrochemically switching between the charging and discharging status of battery electrodes the change in volume can be precisely controlled to induce either compressive or tensile strain on supported catalysts. Lattice compression and tension induced by the lithium cobalt oxide substrate of ~5% were directly observed in individual Pt nanoparticles with aberration-corrected transmission electron microscopy. We observed 90% enhancement or 40% suppression in Pt ORR activity under compression or tension, respectively, which is consistent with theoretical predictions.

Highly efficient electrocatalysts for renewable energy conversion processes, such as in H<sub>2</sub> fuel cells and water-splitting electrocatalysis, is becoming increasingly important (1–3). One strategy for systematically improving the activities of known catalysts is to modify their electronic structure (4–6). Numerous examples have been demonstrated in H<sub>2</sub>O–O<sub>2</sub>–H<sub>2</sub> electrocatalysis, such as the changing of d band filling in perovskite oxides for oxygen evolution (7), transition-metal alloying for the oxygen reduction reaction (ORR) (4, 8–11), and our recent studies of using lithium (Li)-ion intercalation and extraction in layered materials for water-splitting (12, 13).

Lattice strain, either compressive or tensile, can alter the surface electronic structure by mod-

ifying the distances between surface atoms and in turn catalytic activity (14–17). For platinum (Pt), previous studies have suggested that the 5d-band center of Pt can be shifted by ~0.1 eV with only 1% lattice strain (18), which can appreciably strengthen or weaken bonding of reaction intermediates to the surface (14, 18). Lattice-mismatch between metals can be generated by directly synthesizing core-shell structures (19–23) or by selectively removing atoms from an alloy (for example, stripping away Cu from a Pt-Cu alloy) (8, 14, 24–26). However, because of the larger lattice of Pt as compared with that of most metal cores, this method is typically restricted to compressive strain (14, 27). Additionally, both electronic charge transfer between the different metal atoms (ligand effects) and changes in the surface stability—and thus surface area—are present, making it difficult to identify and control the effects of strain alone (14, 25). Another strategy is to deposit catalysts onto flat substrates that undergo physical transformations as external forces are applied or the temperatures varied (28, 29). Those flat and tunable substrates present great importance to fundamental analysis, but only a few of them have been successfully demonstrated effective in electrocatalysis (28). Thus, new methods that can flexibly and effectively control both tensile and compressive lattice strain in catalysts without introducing additional effects are needed.

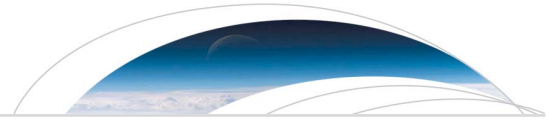
<sup>1</sup>Department of Applied Physics, Stanford University, Stanford, CA 93205, USA. <sup>2</sup>Department of Mechanical Engineering, Stanford University, Stanford, CA 93205, USA. <sup>3</sup>SUNCAT Center for Interface Science and Catalysis, Department of Chemical Engineering, Stanford University, Stanford, CA 94305, USA. <sup>4</sup>SUNCAT Center for Interface Science and Catalysis, SLAC National Accelerator Laboratory, 2575 Sand Hill Road, Menlo Park, CA 94025, USA. <sup>5</sup>Department of Material Science and Engineering, Stanford University, Stanford, CA 94305, USA. <sup>6</sup>Department of Physics, Stanford University, Stanford, CA 94305, USA. <sup>7</sup>Stanford Institute for Materials and Energy Sciences, SLAC National Accelerator Laboratory, 2575 Sand Hill Road, Menlo Park, CA 94025, USA.

\*Corresponding author. Email: [yicui@stanford.edu](mailto:yicui@stanford.edu)

### 3 Imager le seuil de rupture le long des grandes failles

Nous avons proposé dans l'étude précédente que les grandes ruptures sismiques sont plus probables le long d'une faille aux conditions physiques homogènes, rendant le comportement du « système faille » plus propice à des ruptures synchrones. Cette idée peut se traduire en des termes plus physiques. Une façon de modéliser le comportement des failles est de considérer que chaque point de la faille a une valeur de contraintes cisailantes  $\tau$ . Dans ce cadre conceptuel, chaque point de la faille est susceptible de rompre lorsque  $\tau$  attend une valeur critique  $\tau^c$ . Nous avons, dans l'étude qui suit, trouvé un moyen d'estimer la distribution spatiale de  $\tau^c$  le long des grandes failles. Après avoir décrit le cadre théorique et dérivé l'équation donnant  $\tau^c$  en fonction d'un certain nombre de paramètres physiques – incluant notamment des paramètres décrivant la géométrie de la faille mais aussi l'orientation des contraintes – nous avons « imagé » les variations spatiales de  $\tau^c$  le long des failles de subduction japonaises et observé que les deux plus grands séismes historiques sur ces failles s'étaient produits sur des zones présentant une distribution spatiale de  $\tau^c$  particulièrement homogène. Cette observation renforce notre intuition que plus le seuil de rupture est similaire d'un bout à l'autre d'une faille, plus il est probable qu'une grande portion de cette faille puisse rompre de manière synchrone, générant ainsi un très grand séisme.

Cette étude a été réalisée à l'Université d'Oregon en collaboration avec Amanda M. Thomas, Alan W. Rempel et Jeanne L. Hardebeck. Elle a été publiée en 2017 dans le journal *Geophysical Research Letters* [[Bletery et al., 2017a](#)].



RESEARCH LETTER

10.1002/2017GL075501

Imaging Shear Strength Along Subduction Faults

Quentin Bletery<sup>1</sup>, Amanda M. Thomas<sup>1</sup>, Alan W. Rempel<sup>1</sup>, and Jeanne L. Hardebeck<sup>2</sup>

<sup>1</sup>Department of Earth Science, University of Oregon, Eugene, OR, USA, <sup>2</sup>U.S. Geological Survey, Menlo Park, CA, USA

Key Points:

- We relate earthquake rupture threshold to physical parameters
- We estimate the variation of the rupture threshold along an actual subduction fault
- We relate estimates of rupture threshold variations to earthquake magnitude

Supporting Information:

- Supporting Information S1

Correspondence to:

Q. Bletery,  
qbletery@uoregon.edu

Citation:

Bletery, Q., Thomas, A. M., Rempel, A. W., & Hardebeck, J. L. (2017), Imaging shear strength along subduction faults. *Geophysical Research Letters*, 44. <https://doi.org/10.1002/2017GL075501>

Received 1 SEP 2017

Accepted 22 OCT 2017

Accepted article online 26 OCT 2017

**Abstract** Subduction faults accumulate stress during long periods of time and release this stress suddenly, during earthquakes, when it reaches a threshold. This threshold, the shear strength, controls the occurrence and magnitude of earthquakes. We consider a 3-D model to derive an analytical expression for how the shear strength depends on the fault geometry, the convergence obliquity, frictional properties, and the stress field orientation. We then use estimates of these different parameters in Japan to infer the distribution of shear strength along a subduction fault. We show that the 2011  $M_w$ 9.0 Tohoku earthquake ruptured a fault portion characterized by unusually small variations in static shear strength. This observation is consistent with the hypothesis that large earthquakes preferentially rupture regions with relatively homogeneous shear strength. With increasing constraints on the different parameters at play, our approach could, in the future, help identify favorable locations for large earthquakes.

**Plain Language Summary** Subduction faults accumulate stress during hundreds of years until this stress reaches a threshold. When this threshold is reached, an earthquake occurs. We derive an expression of the rupture threshold depending on different physical parameters, which vary along subduction faults. We then use estimates of the spacial variations of these different parameters in Japan to infer the distribution of the rupture threshold along the Japanese subduction faults. Our results suggest that very large earthquakes, such as the 2011  $M_w$ 9.0 Tohoku earthquake, occur on fault portions of particularly homogeneous rupture thresholds. Our interpretation is that the rupture threshold is more likely to be reached simultaneously on broad fault portions if it does not vary much from one point of the fault to another. Imaging spatial variations of the rupture threshold along large faults may then reveal the location of possible future large earthquakes.

1. Introduction

Earthquakes are the result of relative motion between elastic blocks that is accommodated by slip on active faults. On convergent margins, during prolonged time periods, the contacts between crustal rocks are strong enough to prevent significant slip in the first 40–70 km beneath Earth’s surface. As a result, stress gradually accumulates along these “locked” portions of subduction faults. The accumulated stress is ultimately released when it reaches a threshold that overcomes the shear strength along a fault segment of sufficient extent for an earthquake to nucleate. Once initiated, an earthquake can propagate as long as the dynamic stress perturbation  $\delta\tau$  inherited from earlier phases of the rupture is larger than the difference between the local shear strength  $\tau^c$ —defined as the critical shear stress required to slip at a given location—and the background shear stress  $\tau$ , so that

$$\delta\tau \geq \tau^c - \tau. \tag{1}$$

We see from equation (1) that rupture propagation past any given point is favored by large dynamic stress perturbations  $\delta\tau$  and/or small values of  $\tau^c - \tau$ . Large  $\delta\tau$  is expected from the sudden release of large stress concentrations that were able to build up in regions where the local shear strength  $\tau^c$  was higher than that of surrounding fault segments. On the other hand, high  $\tau^c$  fault segments also produce barriers to rupture propagation by making  $\tau^c - \tau$  larger than in the surroundings so that it can potentially exceed  $\delta\tau$ . Unfortunately, despite this established conceptual understanding, few detailed constraints are available to quantify the terms in equation (1), particularly over the short length scales known to govern earthquake nucleation (e.g., Dieterich, 1981; Li & Rice, 1983; Rice, 1983). Nevertheless, the observation that the largest earthquakes can only occur when equation (1) is satisfied over large areas suggests that a viable strategy for identifying those regions most prone to hosting such events might be based on an approximate analysis

of the mechanical conditions over long wavelengths. Fortunately, the available data on plate geometries, convergence directions, and stress field orientations make it possible to estimate subduction shear strengths  $\tau^c$  and their variations over length scales relevant to mega-earthquake propagation ( $\geq 100$  km). Accordingly, here we pursue the hypothesis that insights on key features of fault behavior—in particular on the maximum earthquake magnitude—may be inferred from the distribution of shear strength.

In an earlier paper we presented a simplified 2-D formulation, assuming hydrostatic pore pressure and neglecting cohesion, of the shear strength as a function of the friction coefficient  $\mu$ , bulk densities of the crust  $\rho$  and water  $\rho_w$ , depth  $h$ , dip angle  $\theta$ , and the angle  $\psi$  between the maximum principal component of stress and the horizontal (Bletery et al., 2016)

$$\tau^c = \frac{gh\mu(\rho - \rho_w)(\sin 2\theta + \tan 2\psi \cos 2\theta)}{\sin 2\theta - \mu(1 - \cos 2\theta) + \tan 2\psi(\cos 2\theta - \mu \sin 2\theta)}. \quad (2)$$

Here we derive a similar expression for the shear strength on any point of a subduction fault in a more general 3-D case that takes into account the obliquity of plate convergence. Our expression for  $\tau^c$  (equation (11)) depends on geometrical ( $h, \theta$ ) and constitutive ( $\mu$ ) parameters, in addition to other factors needed to describe the local state. After outlining our model formulation, we illustrate its implications by evaluating  $\tau^c$  and its spatial variations along the Japanese subduction faults for which the controlling parameters are best constrained. We ultimately show that the 2011  $M_w$  9.0 Tohoku-Oki earthquake ruptured an area of particularly low shear strength gradient, supporting the idea that shear strength is more likely to be exceeded simultaneously over large areas if its spatial distribution is homogeneous (Bletery et al., 2016).

## 2. Model

We consider the stress field that acts upon a fault increment on a subduction megathrust. In the  $(\mathbf{x}, \mathbf{y}, \mathbf{z})$  coordinate system, where  $\mathbf{x}$  coincides with the convergence direction,  $\mathbf{y}$  is perpendicular to  $\mathbf{x}$  in the horizontal plane and  $\mathbf{z}$  points up (Figure 1), the stress tensor  $\sigma$  can be written as

$$\sigma = \begin{pmatrix} \sigma_{zz} + \Delta\sigma & \sigma_{xy} & \sigma_{xz} \\ \sigma_{xy} & \sigma_{yy} & \sigma_{yz} \\ \sigma_{xz} & \sigma_{yz} & \sigma_{zz} \end{pmatrix}, \quad (3)$$

where  $\Delta\sigma = \sigma_{xx} - \sigma_{zz}$  is a stress difference. Let  $\psi$  be the angle between the first principal component axis and the horizontal. Assuming, based on symmetry considerations, that  $\mathbf{y}$  is a principal component, the stress tensor can be rewritten as (Appendix A)

$$\sigma = \begin{pmatrix} \sigma_{zz} + \Delta\sigma & 0 & \frac{\Delta\sigma}{2} \tan 2\psi \\ 0 & \sigma_{yy} & 0 \\ \frac{\Delta\sigma}{2} \tan 2\psi & 0 & \sigma_{zz} \end{pmatrix}. \quad (4)$$

Let  $\mathbf{n}$  be a unit vector normal to the megathrust and  $\mathbf{s}$  a unit vector in the direction of the plate convergence projected onto the megathrust (Figure 1). In the  $(\mathbf{x}, \mathbf{y}, \mathbf{z})$  reference frame,  $\mathbf{n} = (-\sin \delta, 0, -\cos \delta)^T$  and  $\mathbf{s} = (\cos \delta, 0, -\sin \delta)^T$ , with  $\delta$  the apparent dip angle in the direction of the convergence (Figure 1). Based on simple geometrical considerations,  $\delta$  may be expressed as a function of the strike angle  $\phi$ , the azimuth of the convergence direction  $\lambda$ , and the actual dip angle  $\theta$  (Appendix B)

$$\delta = \arctan(\sin(\phi - \lambda) \tan \theta). \quad (5)$$

The normal and shear stress  $\sigma_n$  and  $\tau$  are then

$$\sigma_n = (\sigma \cdot \mathbf{n}) \cdot \mathbf{n} = \sigma_{zz} + \frac{\Delta\sigma}{2}(1 - \cos 2\delta + \tan 2\psi \sin 2\delta), \quad (6)$$

$$\tau = \sqrt{(\sigma \cdot \mathbf{n}) \cdot (\sigma \cdot \mathbf{n}) - \sigma_n^2} = \frac{\Delta\sigma}{2}(\sin 2\delta + \tan 2\psi \cos 2\delta). \quad (7)$$

The Coulomb failure criterion gives the relationship between shear and normal stress at which the rupture initiates

$$\tau = \mu(\sigma_n - p). \quad (8)$$

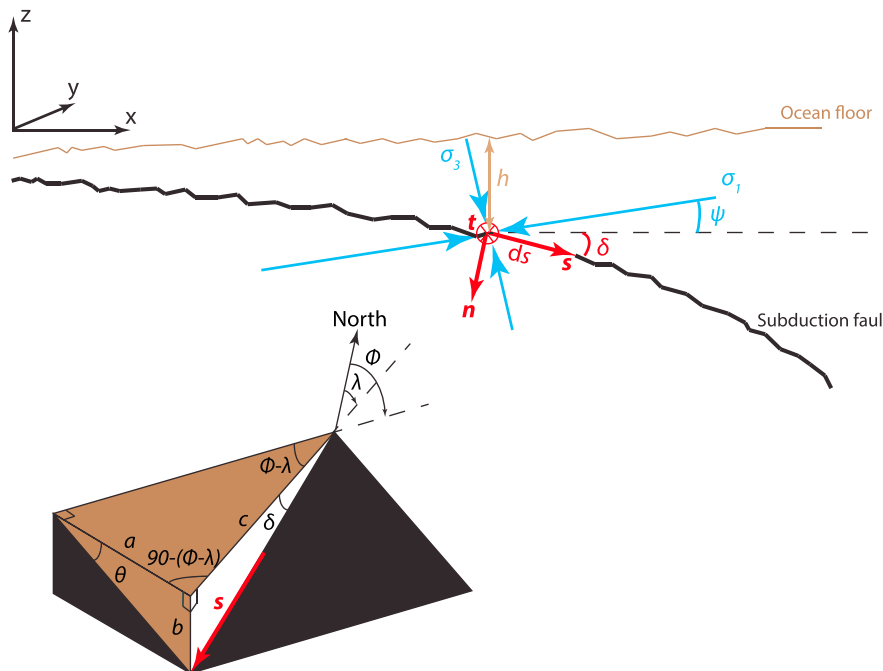


**Figure 1.** Sketch of the problem configuration. An incremental fault surface (of depth  $h$ , dip angle  $\theta$ , and strike angle  $\phi$ ) is oriented with an apparent angle  $\delta$  from the horizontal in the convergence direction of azimuth  $\lambda$ . The first principal component of the stress field  $\sigma_1$  applied to this incremental fault surface forms an angle  $\psi$  with the horizontal. Inset: relationship between the apparent dip angle  $\delta$ , the actual dip angle  $\theta$ , the strike angle  $\phi$ , and the horizontal convergence direction  $\lambda$ .

where  $\mu$  is the coefficient of friction and  $p$  is the pore fluid pressure, and we neglect cohesion for simplicity. Equations (6)–(8) enable us to express the critical stress difference required to initiate a rupture  $\Delta\sigma^c$  as a function of  $\mu$ ,  $\sigma_{zz}$ ,  $p$ ,  $\delta$ , and  $\psi$ :

$$\Delta\sigma^c = \frac{2\mu(\sigma_{zz} - p)}{\sin 2\delta - \mu(1 - \cos 2\delta) + \tan 2\psi(\cos 2\delta - \mu \sin 2\delta)}. \quad (9)$$

We can then derive from equation (7) (or equivalently equations (6) + (8)) an expression for the critical shear stress  $\tau^c$  at which a rupture initiates

$$\tau^c = \frac{\mu(\sigma_{zz} - p) \sin(2\delta + 2\psi)}{\sin(2\delta + 2\psi) + \mu(\cos(2\delta + 2\psi) - \cos 2\psi)}. \quad (10)$$

### 3. Numerical Computation

Equation (10) is quite general. The only assumptions are that the fault strength is govern by the Mohr-Coulomb failure criterion (equation (8)) and that  $\mathbf{y}$  is a principal component axis. In order to compute the distribution of shear strength, however, we need to make some stronger assumptions. A natural approximation for  $\sigma_{zz}$  is to treat it as equal to the pressure due to the mass of the upper plate; that is,  $\sigma_{zz} = \rho gh$ , with  $\rho$  the bulk density of the crust,  $g$  the acceleration of gravity, and  $h$  the depth. This case is valid as long as the gravitational loading dominates the vertical state of stress, implying that any contribution of tectonic origin to the vertical stress is negligible compared to the lithostatic pressure. A hydrostatic fluid pressure distribution could produce  $p = \rho_w gh$ , with  $\rho_w$  the bulk density of water. Although commonly assumed and useful as a starting point for exploring the controls on strength variations, the distribution of fluid pressure is relatively poorly constrained and potential deviations of  $p$  from  $\rho_w gh$  will be discussed the later sections. These two assumptions lead to

$$\tau^c = \frac{\mu(\rho - \rho_w)gh \sin(2\delta + 2\psi)}{\sin(2\delta + 2\psi) + \mu(\cos(2\delta + 2\psi) - \cos 2\psi)}, \quad (11)$$

where  $\delta = \arctan(\sin(\phi - \lambda) \tan \theta)$  (equation (5)).

We compute the distribution of shear strength using equations (11) and (5) and the Generic Mapping Tools (GMT) software. We use the distributions of dip ( $\theta$ ) and strike ( $\phi$ ) angles along the Japanese megathrusts from the SLAB1.0 model (Hayes et al., 2012), the distribution of the convergence direction  $\lambda$  given by the NNR-MORVEL56 model (Argus et al., 2011), and the distribution of the stress field orientation  $\psi$  from Hardebeck (2015). To estimate  $h$ , we use the depth of the interface given by the SLAB1.0 model (Hayes et al., 2012) corrected from the 1 arc min bathymetry given by the ETOPO1 model. Other variables are treated as constant:  $g = 9.8 \text{ m/s}^2$ ,  $\rho = 2700 \text{ kg/m}^3$ ,  $\rho_w = 1000 \text{ kg/m}^3$ , and  $\mu = 0.6$ .

Though we recognize the contribution of the preconditioned dynamic stress perturbation ( $\delta\tau$ ) and the background shear stress ( $\tau$ ) highlighted in equation (1), we proposed that the spatial variations of shear strength might be a key parameter in controlling the global distribution of mega-earthquakes because shear strength is more likely to be exceeded simultaneously over large areas if its spatial distribution is homogeneous (Bletery et al., 2016). To support this hypothesis, we further calculate the gradient of shear strength. We use the GMT software to differentiate our map of shear strength along east ( $x_E$ ) and along north ( $x_N$ ) and project the shear strength gradient in the rake-parallel ( $\frac{d\tau^c}{ds}$ ) and rake-perpendicular ( $\frac{d\tau^c}{dt}$ ) directions (with  $\mathbf{t}$  ( $= \mathbf{y}$ ) the normal to  $\mathbf{s}$  in the fault plane (Figure 1)),

$$\frac{d\tau^c}{ds} = \left( \frac{d\tau^c}{dx_E} \sin \lambda + \frac{d\tau^c}{dx_N} \cos \lambda \right) \cos \delta, \quad (12)$$

$$\frac{d\tau^c}{dt} = \frac{d\tau^c}{dx_E} \cos \lambda - \frac{d\tau^c}{dx_N} \sin \lambda. \quad (13)$$

#### 4. Results

Assuming  $\sigma_{zz} - p = (\rho - \rho_w)gh$  leads to a linear dependence of the shear strength on depth (equation (11)). This depth dependence is modified by variations in the stress field orientation with depth. Numerical computation of equation (11) using the stress field orientation of Hardebeck (2015) is shown in Figure 2. The pattern of variations in  $\tau^c$  that we determine is qualitatively consistent with the dependence of stress drop on depth observed among small earthquakes in the Tohoku rupture area (Oth, 2013; Uchide et al., 2014): higher stress drops are favored at depth where the shear stress rupture threshold is larger. It is worth noting, however, that the observed stress drops are a factor of 15 smaller than the calculated shear strengths (inset of Figure 2). A significant part of this difference could be attributed to inaccuracies in assumed pore pressures and other parameter values. For instance, assuming a coefficient of friction  $\mu$  of 0.1—such as reported by Fulton et al. (2013) in the shallow part of the Tohoku megathrust and in agreement with heat flow measurements (Gao & Wang, 2014)—instead of 0.6 reduces the difference to a factor of 2.5 (Figure S1 in the supporting information). Nevertheless, these offsets are consistent with the commonly accepted view that shear stress does not drop to zero following an earthquake; stress drops and shear strength clearly differ. In what follows, we use  $\mu = 0.6$ , but we show all equivalent figures for  $\mu = 0.1$  in the supporting information.

The distributions of the rake-parallel  $\frac{d\tau^c}{ds}$  and rake-perpendicular  $|\frac{d\tau^c}{dt}|$  components of the shear strength gradient along the Japanese megathrusts are shown in Figures 3a and 3b.  $\frac{d\tau^c}{ds}$  has a larger amplitude than  $\frac{d\tau^c}{dt}$  and is positive as long as  $\tau^c$  increases monotonically with depth (equation (11)). The norm of the shear strength gradient is dominated by the rake-parallel component, which has a higher amplitude (Figure 3c). The rake-parallel component  $\frac{d\tau^c}{ds}$  indicates particularly low gradient offshore Nankai (red patch in the south of Japan in Figure 3a). On the other hand, the rake-perpendicular component  $|\frac{d\tau^c}{dt}|$  indicates areas where the convergence direction  $\lambda$  relative to the fault orientation  $\phi$  generates heterogeneities in the shear strength distribution. Such heterogeneities seem to be minimal in the Tohoku rupture area (red patch east of the main island) and south of Nankai (Figure 3b). Even though  $|\frac{d\tau^c}{dt}|$  is of much smaller amplitude than  $\frac{d\tau^c}{ds}$ , the distributions of the two components may be of similar importance as one ( $\frac{d\tau^c}{ds}$ ) influences along-dip rupture propagation, while the other ( $|\frac{d\tau^c}{dt}|$ ) influences the lateral propagation. The amplitude of the rake-parallel and rake-perpendicular components of the shear strength gradient, as well as the norm, is reduced by a factor of  $\sim 6$  when computed with  $\mu = 0.1$  instead of  $\mu = 0.6$ , but the relative distributions are rather insensitive to the choice of  $\mu$  (Figure S2).



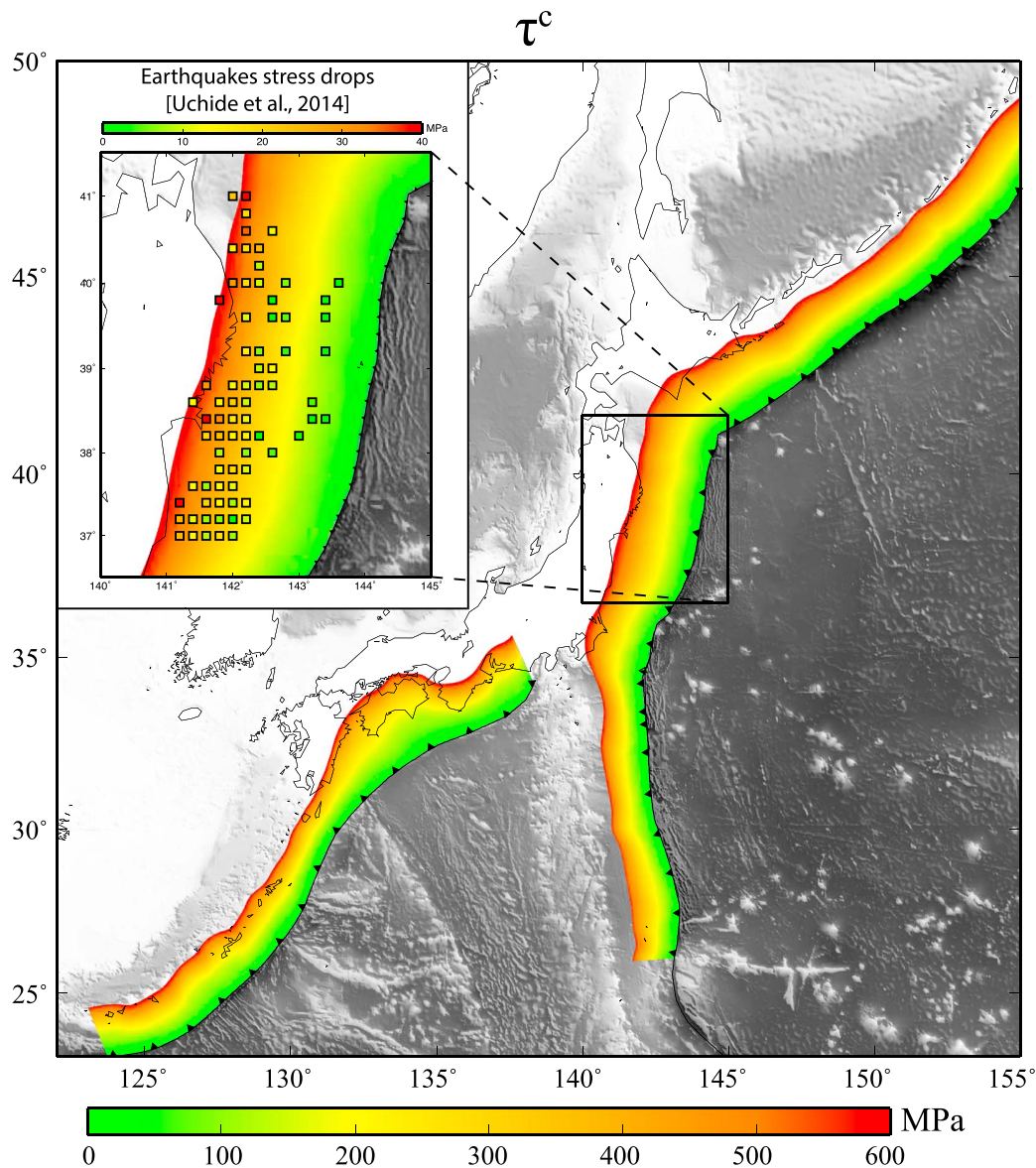


**Figure 2.** Shear strength  $\tau^c$  along the Japanese megathrusts computed from equation (11). Inset: Median stress drops (colored squares) of small earthquakes in the Tohoku-Oki area (Uchide et al., 2014) superimposed on top of the shear strength distribution.

The gradient maps are sensitive to the resolution of the different parameters in equation (11). The smaller wavelength features in Figure 3 reflect changes in the bathymetry, which is by far the best constrained parameter, with a resolution of 1 arc min. The slab1.0 model (constraining the dip and strike angles as well as the fault depth relative to sea level) has a nominal resolution of 0.5° but relies on uneven sampling in multiple data sets interpolated using Hermite splines of polynomial orders from 2 to 3, depending on depth (Hayes et al., 2012). The stress orientation is also interpolated from 0.5° wide pixels (Hardebeck, 2015). These uneven resolution limitations make our shear strength gradient maps overly sensitive to the spatial variations of the most well-resolved parameters. Though of comparable resolution, geometry dominates stress orientation effects because it varies more dramatically at the resolved scale (Figures 3a and 3c). Nevertheless, stress orientation and fault geometry may vary in different manners at much smaller scales and produce barriers at scales relevant to rupture nucleation that our long-wavelength imaging cannot capture. The rake-perpendicular component of the shear strength gradient is most sensitive to the obliquity term  $\phi - \lambda$  because

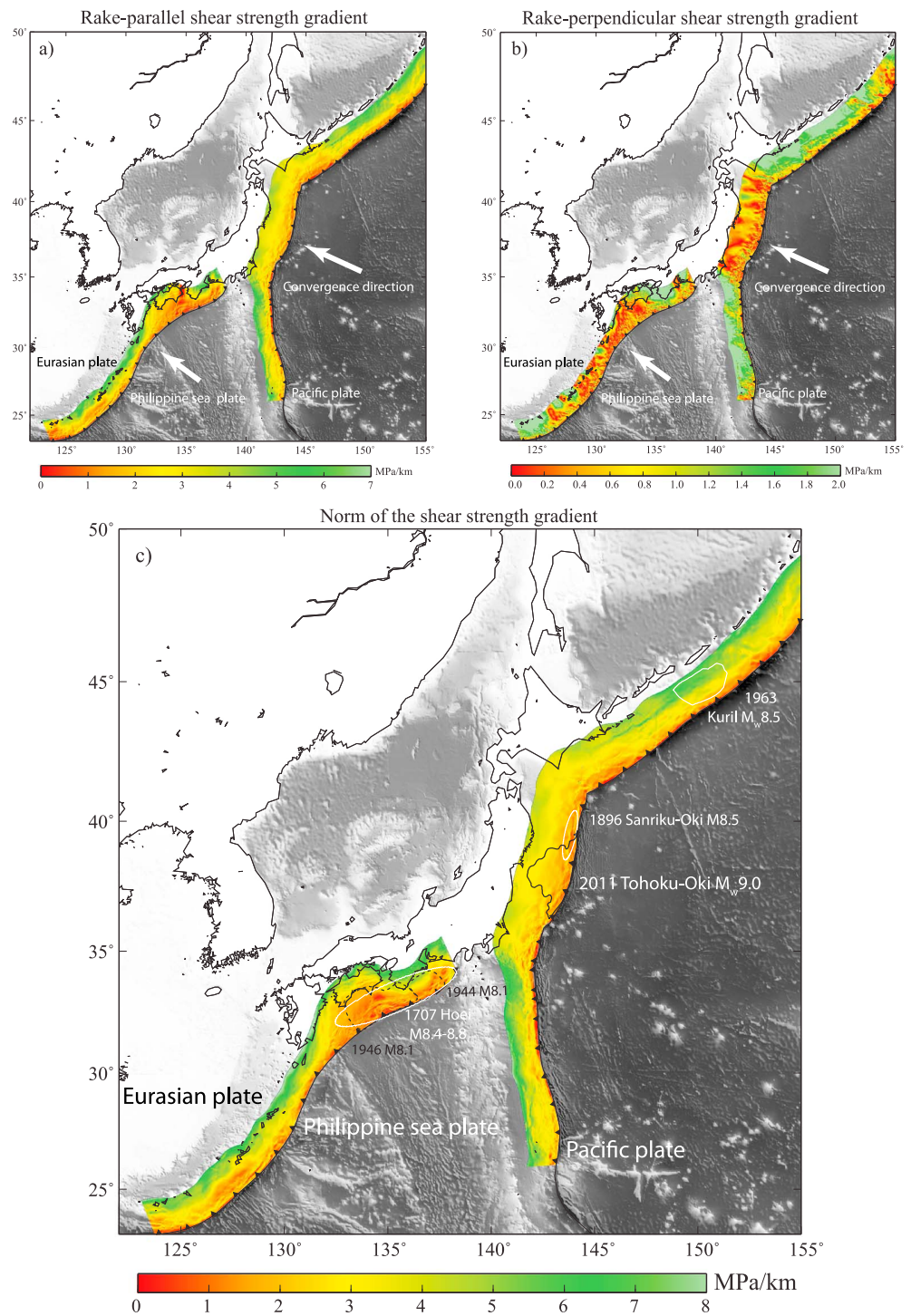


**Figure 3.** (a) Rake-parallel  $\frac{dr^c}{ds}$  and (b) absolute value of the rake-perpendicular  $|\frac{dr^c}{dt}|$  components of the shear strength gradient along the Japanese megathrusts. White arrows show the directions of plate convergences relative to the Eurasian plate. (c) Norm of the shear strength gradient. The black contour shows the location of the largest historical rupture along the Japanese megathrusts: the 2011  $M_w$  9.0 Tohoku-Oki earthquake (Bletery et al., 2014). White contours show  $M \sim 8.5$  historical earthquakes (Rhea et al., 2010; Simons et al., 2011; Furumura et al., 2011). Black dashed contours show recurrent  $M8.1-8.4$  earthquakes that ruptured simultaneously during the 1707  $M8.4-8.8$  Hoi earthquake (Furumura et al., 2011; Stein & Okal, 2007). Note that slip contours of historical earthquakes are much less well constrained than for the Tohoku-Oki earthquake.



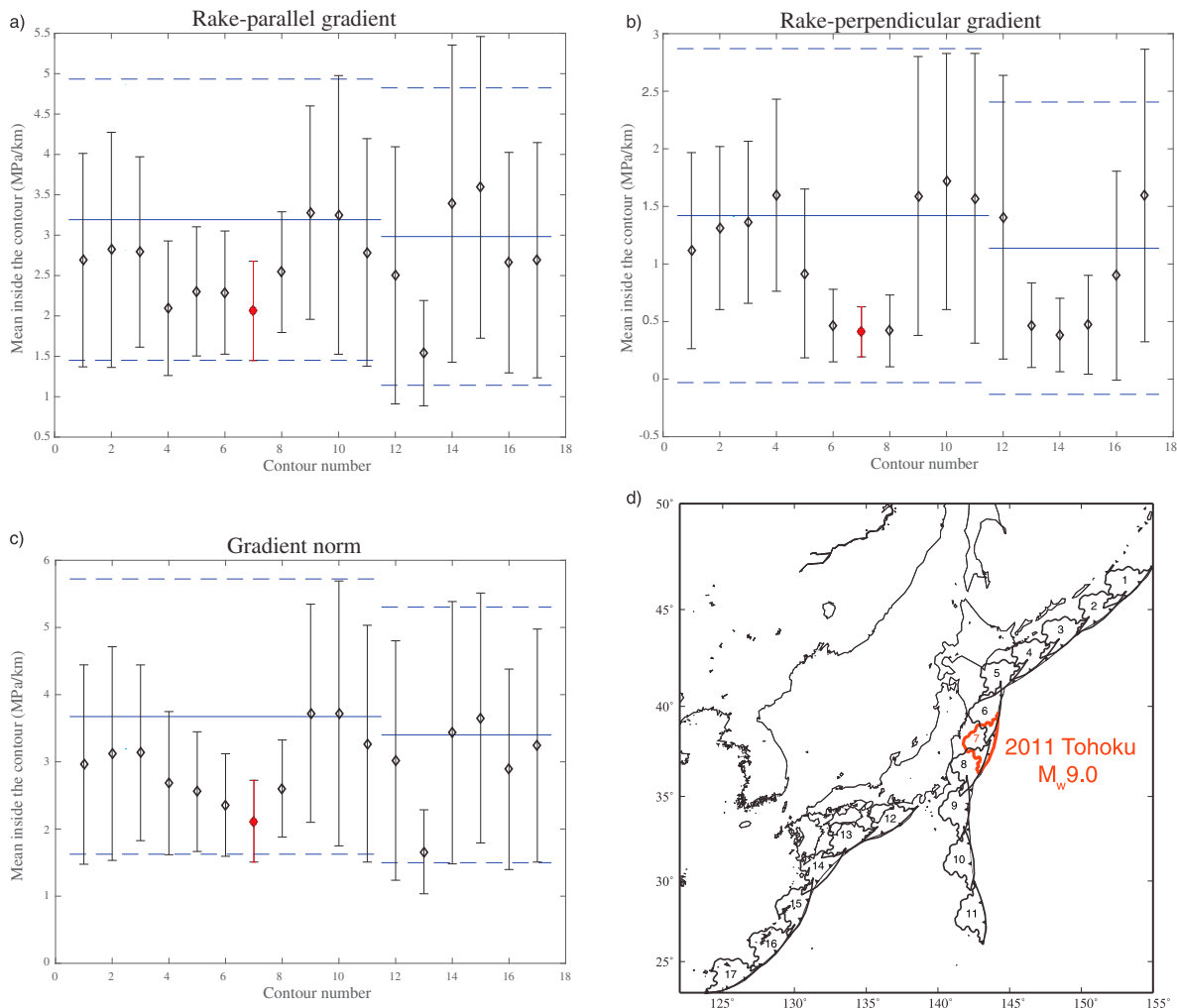


**Figure 4.** Average (black diamonds) and standard deviation (black vertical intervals) of the (a) rake parallel, (b) rake perpendicular, and (c) norm of shear strength gradient inside 17 slip contours corresponding to the (d) rupture area of the 2011 Tohoku earthquake ( $M_w$  9.0) distributed along the megathrusts. The red contour ( $n=7$ ) corresponds to the actual slip contour of the Tohoku earthquake (Bletery et al., 2014). The other 16 black contours have the same shape and area than the Tohoku earthquake but are shifted along the megathrusts. The horizontal blue solid and dashed lines show the averages and standard deviations along the seismogenic zone ( $\leq 60$  km) of the entire megathrusts.

the obliquity of the convergence makes the depth change along rake-perpendicular paths, inducing changes in strength along such paths (Figure 3b).

We proposed in an earlier paper that mega-earthquakes are favored by low shear strength gradients (Bletery et al., 2016) because homogeneous shear strength distributions facilitate synchronized failure over large fault portions. Though limited by the different parameter resolutions, Figure 3 provides material to further investigate this hypothesis. We therefore consider the slip contour of the 2011  $M_w$  9.0 Tohoku-Oki earthquake (Bletery et al., 2014), which is by far the largest rupture ever recorded in the region, and calculate the average shear strength gradient inside the rupture area (for both components and the norm). We then shift the Tohoku slip contour all along the Japanese megathrusts and compare the average shear strength gradient of Tohoku-sized areas. Our results indicate that the actual location of the Tohoku earthquake presents particularly homogeneous shear strength distributions (i.e., low shear strength gradient in all components) (Figure 4). As expected from Figure S2 relative to Figure 3, these results are insensitive to the choice of  $\mu$  (Figure S3).

Though it seems difficult to find a Tohoku-sized area of more homogeneous shear strength distribution than the actual area in which it took place, the smaller (still very large) 1963  $M_w$  8.5 Kuril earthquake seems to have ruptured a more heterogeneous fault portion (Figure 3c). Given the nature of our data sets, we are likely

insensitive to geometrical heterogeneities smaller than several tens of kilometers and frictional heterogeneities of any size, meaning that our shear strength gradient estimates essentially constitute lower bound constraints on the spatial variability of the static shear strength. In the case of the Kuril earthquake, this means that an average gradient in static shear strength of at least 4.4 MPa/km did not effectively halt a 245 km long rupture. In detail, this earthquake was actually composed of three distinct 40–60 km long subevents that ruptured successively (Beck & Ruff, 1987), consistent with a likely heterogeneous  $\tau^c$  distribution at a scale we are not able to resolve and resulting in relatively high integrated gradients at the scale to which we are sensitive (Figure 3).

The other  $M \sim 8.5$  historical earthquakes ruptured more favorable fault areas. The 1707 Hoei  $M8.4$ – $8.8$  earthquake ruptured the previously discussed red patch offshore Nankai in Figure 3a. Interestingly, this earthquake is thought to correspond to the simultaneous rupture of two patches that ruptured distinctively in 1944 and 1946 and before in 1854 (Furumura et al., 2011). The two patches seem to coincide with low shear strength gradient separated by a geometrical heterogeneity (Figure 3c).

## 5. Discussion and Conclusions

The rupture threshold  $\tau^c$  depends upon geometry ( $h, \theta, \phi$ ), rheology ( $\mu$ ), hydrology ( $p$ ), the orientation of the convergence ( $\lambda$ ), and the orientation of the stress field ( $\psi$ ), which is inherited from all the other parameters and past events (equations (10) and (5)). When the pore pressure and vertical normal stress both increase linearly with depth, the increase of  $\tau^c$  with  $h$  (equation (11) and Figure 2) suggests that larger values of  $\delta\tau$  are to be expected when an earthquake initiates at depth. Remembering that a rupture propagates as long as  $\delta\tau \geq \tau^c - \tau$  (equation (1)), it also suggests that it is much easier for a rupture to propagate in the updip direction than in the downdip direction. Indeed,  $\tau^c$ —and therefore likely  $(\tau^c - \tau)$ —decreases in the updip direction, meaning that the dynamic stress perturbation required to keep the propagation going is progressively reduced along an upwardly oriented rupture path. In special circumstances, this tendency may be counterbalanced by variations of the stress field orientation (equation (11)). However, the estimates of the stress field orientation (Hardebeck, 2015) included in our calculation of  $\tau^c$  for Japanese subduction zones do not compensate for the expected linear increase of  $\sigma_{zz} - p$  with depth (Figure 2).

The expected increase in  $\tau^c$  with depth may also be counterbalanced by nonhydrostatic distributions of pore fluid pressure. It is likely that in some areas, the distribution of pore fluid pressures is close to lithostatic (e.g., Byerlee, 1990; Faulkner & Rutter, 2001; Rice, 1992; Streit & Cox, 2001), taking the form  $p = \rho gh + C$  and breaking with the linear depth dependency of  $\tau^c$  predicted by equation (11). Near-lithostatic pore fluid pressure appears, for instance, to be required to explain the characteristics of slow earthquakes (e.g., Audet & Bürgmann, 2014; Liu & Rice, 2007; Segall et al., 2010) and other slow-slip phenomena (e.g., Bletery et al., 2017; Shelly et al., 2006), in particular their sensitivity to extremely small tidal stress perturbations (Thomas et al., 2009). Such phenomena are well documented in Nankai both at depth and in the wedge (e.g., Nakajima & Hasegawa, 2016; Obara & Kato, 2016; Shelly et al., 2006), implying that the actual shear strength in the Nankai section (contours n°12 and n°13 in Figure 4) is probably locally much smaller than suggested in Figure 4. More generally, pore pressure is expected to follow complex variations that evolve with fluid flow along the megathrust and depend upon such poorly constrained variables as the permeability of the overriding plate (e.g., Nakajima & Hasegawa, 2016; Skarbak & Rempel, 2016). In the absence of firm constraints to the contrary, the assumption of hydrostatic pore pressures should be viewed as a strong limitation of our analysis.

The present numerical computation is exploring the influence of nonfrictional parameters—nominally seafloor bathymetry, fault geometry, stress orientation, and convergence direction—on the spatial distribution of the static shear strength along the Japanese megathrusts. Though we treat  $\mu$  as constant, our approach does not require the assumption of constant friction and possible future constraints on the spatial distribution of  $\mu$  could be included in the numerical computation.  $\mu$  is also known to vary temporally as a function of the slip velocity and one or more state variables (e.g., review paper by Marone, 1998, and references therein). Although temporal variations in the friction coefficient due to rate-and-state effects are critical for our modern understanding of earthquake nucleation among other phenomena, the absolute magnitude of such changes is typically quite small ( $\leq 10\%$ ) and would be expected to have a correspondingly modest influence on our calculations of  $\tau^c$ . Dynamic weakening mechanisms, such as thermal pressurization (Lachenbruch, 1980), flash heating (Rice, 2006), or other material-dependent effects (e.g., Di Toro et al., 2011; Han et al., 2007), might

influence the evolution of shear strength more dramatically during the rupture process (e.g., Viesca & Garagash, 2015), possibly facilitating the propagation of rare large ruptures into domains that were strong enough (or rate strengthening) to withstand smaller seismic disturbances. Though beyond the scope of this study, our expression of  $\tau^c$  could be coupled with time-dependent equations governing these different mechanisms in numerical simulations of the seismic cycle and/or earthquake rupture to introduce effects of geometry, stress orientation, and convergence obliquity in these approaches. Spatial variations of the upper plate density ( $\rho$ ) could also, in future work, be included in the calculation of  $\tau^c$  (equation (11)). Bassett et al. (2016) observed a correlation between contrasts in residual density anomaly and the rupture termination of the Tohoku-Oki earthquake. They proposed that the residual density anomaly reflects changes in frictional properties. As the dependency of shear strength on density is linear (equation (11)), Bassett et al.'s (2016) observation could be reinterpreted in terms of gradients in shear strength stopping rupture propagation.

In any case, the larger shear strength at depth predicted by equation (11) is counterbalanced by larger shear strength gradient (Figures 3a and 3c). This implies that earthquakes at depth are energetic (large  $\delta\tau$ ) but spatially confined because their propagation is limited by the heterogeneity of the strength distribution. Such a mechanism would explain the high frequencies—thought to be radiated by small on-fault asperities (Madariaga, 1983)—detected at the downdip edge of the rupture of the Tohoku (Ide et al., 2011; Koper et al., 2011; Meng et al., 2011; Simons et al., 2011) and other large subduction earthquakes (Koper et al., 2012; Lay et al., 2012; Yao et al., 2013). Small-scale geometrical irregularities are themselves expected to influence rupture initiation and propagation (e.g., Dunham et al., 2011; Fang & Dunham, 2013) to the extent that such fault “bumps” are superimposed without a systematic dependence upon the large-scale geometry that we examine here. The variations in  $\tau^c$  that determine which fault segments are most prone to large earthquakes are expected to be well represented by equation (10).

The shear strength formulation we present here expresses the rupture threshold as a function of parameters for which we have some estimates along actual faults. Present estimates of stress field orientation are still rather crude, but the development of seismic instrumentation should allow for more refined studies in the future. More generally, the small-scale variations on most parameters in equations (11) and (5) (e.g.,  $h$ ,  $\theta$ ,  $\phi$ , and  $\psi$ ) are not reflected in the broad-scale estimates we used and could generate small-scale heterogeneities relevant to the nucleation and propagation of small to moderate earthquakes. Though local variations of the background shear stress are also relevant to rupture propagation (equation (1)), we showed that insights on the maximum earthquake magnitude may be deduced from the shear strength distribution alone. Though this study focused on the Japanese megathrusts, the approach may be applied to any subduction zone and the idea may be transposed to other fault systems. In particular, in the case of strike-slip faults, several studies have shown that strong variations in azimuth ( $\phi$ ) and lateral discontinuities coincide with brakes or stops in earthquake propagations (Biasi & Wesnousky, 2016; Lettis et al., 2002; Perrin et al., 2016; Wesnousky, 2006). Such variations in  $\phi$  could be interpreted as the source of large gradients in shear strength producing barriers to ruptures. Finally, we note that improved constraints on the depth dependence of pore fluid pressure and variations in the coefficient of friction may, in future work, be introduced in equation (10) to explore their influences on the distribution of shear strength along large faults.

## Appendix A: Determination of the Nondiagonal Components of the Stress Tensor

If  $\mathbf{y}$  is aligned with one of the principal components of the stress field, then the stress tensor can be expressed in the principal component reference frame as

$$\begin{pmatrix} \sigma_1 & 0 & 0 \\ 0 & \sigma_2 & 0 \\ 0 & 0 & \sigma_3 \end{pmatrix} = \begin{pmatrix} \cos \psi & 0 & \sin \psi \\ 0 & 1 & 0 \\ -\sin \psi & 0 & \cos \psi \end{pmatrix} \cdot \begin{pmatrix} \sigma_{zz} + \Delta\sigma & \sigma_{xy} & \sigma_{xz} \\ \sigma_{xy} & \sigma_{yy} & \sigma_{yz} \\ \sigma_{xz} & \sigma_{yz} & \sigma_{zz} \end{pmatrix} \cdot \begin{pmatrix} \cos \psi & 0 & -\sin \psi \\ 0 & 1 & 0 \\ \sin \psi & 0 & \cos \psi \end{pmatrix}. \quad (\text{A1})$$

The off-diagonal terms give a system of three equations that depend on  $\sigma_{xy}$ ,  $\sigma_{xz}$ , and  $\sigma_{yz}$

$$0 = \sigma_{xy} \cos \psi - \sigma_{yz} \sin \psi, \quad (\text{A2})$$

$$0 = -(\sigma_{zz} + \Delta\sigma) \sin \psi \cos \psi + \sigma_{xz} \cos^2 \psi - \sigma_{xz} \sin^2 \psi + \sigma_{zz} \cos \psi \sin \psi, \quad (\text{A3})$$

$$0 = \sigma_{xy} \sin \psi - \sigma_{yz} \cos \psi. \quad (\text{A4})$$

Solving this system gives

$$\sigma_{xy} = 0, \quad (\text{A5})$$

$$\sigma_{xz} = \frac{\Delta\sigma}{2} \tan 2\psi, \quad (\text{A6})$$

$$\sigma_{yz} = 0. \quad (\text{A7})$$

The stress tensor can then be rewritten in the  $(x, y, z)$  reference frame as equation (4).

## Appendix B: Apparent Dip Angle

Considering the inset of Figure 1, we have

$$a = c \sin(\phi - \lambda), \quad (\text{B1})$$

$$b = a \tan \theta, \quad (\text{B2})$$

$$b = c \tan \delta. \quad (\text{B3})$$

Combining (B2) and (B3) gives

$$c \tan \delta = a \tan \theta. \quad (\text{B4})$$

Using (B1), we obtain

$$\tan \delta = \sin(\phi - \lambda) \tan \theta, \quad (\text{B5})$$

from which we can derive equation (5).

### Acknowledgments

This work was supported by the National Science Foundation (NSF) project EAR-1520238. We thank Takahiko Uchide for providing his stress drop estimates shown in Figures 2 and S1 and Joan Gomberg and Nicholas M. Beeler for thoughtful comments on the manuscript. The SLAB1.0 and ETOPO1 models are available online at the following addresses [earthquake.usgs.gov/data/slab/](http://earthquake.usgs.gov/data/slab/) and [ngdc.noaa.gov/mgg/global/](http://ngdc.noaa.gov/mgg/global/), respectively. The convergence direction at the different points of the faults was calculated by the online motion calculator at this address: [geoscience.wisc.edu/~chuck/MORVEL/](http://geoscience.wisc.edu/~chuck/MORVEL/). We used the Generic Mapping Tools to compute the distributions of shear strength and their gradients ([gmt.soest.hawaii.edu/](http://gmt.soest.hawaii.edu/)).

### References

- Argus, D. F., Gordon, R. G., & DeMets, C. (2011). Geologically current motion of 56 plates relative to the no-net-rotation reference frame. *Geochemistry, Geophysics, Geosystems*, 12, Q11001. <https://doi.org/10.1029/2011GC003751>
- Audet, P., & Bürgmann, R. (2014). Possible control of subduction zone slow-earthquake periodicity by silica enrichment. *Nature*, 510(7505), 389–392.
- Bassett, D., Sandwell, D. T., Fialko, Y., & Watts, A. B. (2016). Upper-plate controls on co-seismic slip in the 2011 magnitude 9.0 Tohoku-Oki earthquake. *Nature*, 531(7592), 92–96.
- Beck, S. L., & Ruff, L. J. (1987). Rupture process of the Great 1963 Kurile Islands Earthquake Sequence: Asperity interaction and multiple event rupture. *Journal of Geophysical Research*, 92(B13), 14,123–14,138.
- Biasi, G. P., & Wesnousky, S. G. (2016). Steps and gaps in ground ruptures: Empirical bounds on rupture propagation. *Bulletin of the Seismological Society of America*, 106, 1110–1124.
- Bletery, Q., Sladen, A., Delouis, B., Vallée, M., Nocquet, J.-M., Rolland, L., & Jiang, J. (2014). A detailed source model for the  $M_w$  9.0 Tohoku-Oki earthquake reconciling geodesy, seismology, and tsunami records. *Journal of Geophysical Research: Solid Earth*, 119, 7636–7653. <https://doi.org/10.1002/2014JB011261>
- Bletery, Q., Thomas, A. M., Rempel, A. W., Karlstrom, L., Sladen, A., & De Barros, L. (2016). Mega-earthquakes rupture flat megathrusts. *Science*, 354(6315), 1027–1031.
- Bletery, Q., Thomas, A. M., Hawthorne, J. C., Skarbek, R. M., Rempel, A. W., & Krogstad, R. D. (2017). Characteristics of secondary slip fronts associated with slow earthquakes in Cascadia. *Earth and Planetary Science Letters*, 463, 212–220.
- Byerlee, J. (1990). Friction, overpressure and fault normal compression. *Geophysical Research Letters*, 17(12), 2109–2112.
- Di Toro, G., Han, R., Hirose, T., De Paola, N., Nielsen, S., Mizoguchi, K., ... Shimamoto, T. (2011). Fault lubrication during earthquakes. *Nature*, 471(7339), 494–8.
- Dieterich, J. H. (1981). Constitutive properties of faults with simulated gouge. In N. L. Carter et al. (Eds.), *Mechanical behavior of crustal rocks: The Handin volume* (Vol. 24, pp. 103–120). Washington, DC: American Geophysical Union.
- Dunham, E. M., Belanger, D., Cong, L., & Kozdon, J. E. (2011). Earthquake ruptures with strongly rate-weakening friction and off-fault plasticity. Part 2: Nonplanar faults. *Bulletin of the Seismological Society of America*, 101(5), 2308–2322.
- Fang, Z., & Dunham, E. M. (2013). Additional shear resistance from fault roughness and stress levels on geometrically complex faults. *Journal of Geophysical Research: Solid Earth*, 118, 3642–3654. <https://doi.org/10.1002/jgrb.50262>
- Faulkner, D. R., & Rutter, E. H. (2001). Can the maintenance of overpressured fluids in large strike-slip fault zones explain their apparent weakness? *Geology*, 29(6), 503–506.
- Fulton, P., Brodsky, E. E., Kano, Y., Mori, J., Chester, F., Ishikawa, T., ... Toczko, S. (2013). Low coseismic friction on the Tohoku-Oki fault determined from temperature measurements. *Science*, 342(6163), 1214–1217.
- Furumura, T., Imai, K., & Maeda, T. (2011). A revised tsunami source model for the 1707 Hōei earthquake and simulation of tsunami inundation of Ryujin Lake, Kyushu, Japan. *Journal of Geophysical Research*, 116, B02308. <https://doi.org/10.1029/2010JB007918>

- Gao, X., & Wang, K. (2014). Strength of stick-slip and creeping subduction megathrusts from heat flow observations. *Science*, *345*(6200), 1038–1041.
- Han, R., Shimamoto, T., Hirose, T., Ree, J.-H., & Ando, J.-i. (2007). Ultralow friction of carbonate faults caused by thermal decomposition. *Science*, *316*(5826), 878–881.
- Hardebeck, J. L. (2015). Stress orientations in subduction zones and the strength of subduction megathrust faults. *Science*, *349*(6253), 1213–1216.
- Hayes, G. P., Wald, D. J., & Johnson, R. L. (2012). Slab1.0: A three-dimensional model of global subduction zone geometries. *Journal of Geophysical Research: Solid Earth*, *117*, B01302. <https://doi.org/10.1029/2011JB008524>
- Ide, S., Baltay, A., & Beroza, G. C. (2011). Shallow dynamic overshoot and energetic deep rupture in the 2011  $M_w$  9.0 Tohoku-Oki earthquake. *Science*, *332*(6036), 1426–1429.
- Koper, K. D., Hutko, A. R., Lay, T., Ammon, C. J., & Kanamori, H. (2011). Frequency-dependent rupture process of the 2011  $M_w$  9.0 Tohoku earthquake: Comparison of short-period p wave backprojection images and broadband seismic rupture models. *Earth, Planets and Space*, *63*(7), 16.
- Koper, K. D., Hutko, A. R., Lay, T., & Sufri, O. (2012). Imaging short-period seismic radiation from the 27 February 2010 Chile ( $M_w$  8.8) earthquake by back-projection of P, PP, and PKIKP waves. *Journal of Geophysical Research: Solid Earth*, *117*, B02308. <https://doi.org/10.1029/2011JB008576>
- Lachenbruch, A. H. (1980). Frictional heating, fluid pressure, and the resistance to fault motion. *Journal of Geophysical Research*, *85*(B11), 6097–6112.
- Lay, T., Kanamori, H., Ammon, C. J., Koper, K. D., Hutko, A. R., Ye, L., ... Rushing, T. M. (2012). Depth-varying rupture properties of subduction zone megathrust faults. *Journal of Geophysical Research*, *117*, B04311. <https://doi.org/10.1029/2011JB009133>
- Lettis, W., Bachhuber, J., Witter, R., Brankman, C., Randolph, C., Barka, A., ... Kaya, A. (2002). Influence of releasing step-overs on surface fault rupture and fault segmentation: Examples from the 17 August 1999 Izmit earthquake on the North Anatolian Fault, Turkey. *Bulletin of the Seismological Society of America*, *92*(1), 19–42.
- Li, V. C., & Rice, J. R. (1983). Preseismic rupture progression and great earthquake instabilities at plate boundaries. *Journal of Geophysical Research*, *88*(B5), 4231–4246.
- Liu, Y., & Rice, J. R. (2007). Spontaneous and triggered aseismic deformation transients in a subduction fault model. *Journal of Geophysical Research*, *112*, B09404. <https://doi.org/10.1029/2007JB004930>
- Madariaga, R. (1983). High frequency radiation from dynamic earthquake. *Annales Geophysicae*, *1*, 17–23.
- Marone, C. (1998). Laboratory-derived friction laws and their application to seismic faulting. *Annual Review of Earth and Planetary Sciences*, *26*(1), 643–696.
- Meng, L., Inbal, A., & Ampuero, J.-P. (2011). A window into the complexity of the dynamic rupture of the 2011  $M_w$  9 Tohoku-Oki earthquake. *Geophysical Research Letters*, *38*, L00G07. <https://doi.org/10.1029/2011GL048118>
- Nakajima, J., & Hasegawa, A. (2016). Tremor activity inhibited by well-drained conditions above a megathrust. *Nature Communications*, *7*, 13863.
- Obara, K., & Kato, A. (2016). Connecting slow earthquakes to huge earthquakes. *Science*, *353*(6296), 253–257.
- Oth, A. (2013). On the characteristics of earthquake stress release variations in Japan. *Earth and Planetary Science Letters*, *377*, 132–141.
- Perrin, C., Manighetti, I., Ampuero, J.-P., Cappa, F., & Gaudemer, Y. (2016). Location of largest earthquake slip and fast rupture controlled by along-strike change in fault structural maturity due to fault growth. *Journal of Geophysical Research: Solid Earth*, *121*, 3666–3685. <https://doi.org/10.1002/2015JB012671>
- Rhea, S., Tarr, A. C., Hayes, G. P., Villaseñor, A., Furlong, K. P., & Benz, H. (2010). Seismicity of the Earth 1900–2007, Kuril-Kamchatka arc and vicinity: US Geological Survey.
- Rice, J. R. (1983). Constitutive relations for fault slip and earthquake instabilities. *Pure and Applied Geophysics*, *121*(3), 443–475.
- Rice, J. R. (1992). Fault stress states, pore pressure distributions, and the weakness of the San Andreas Fault. *International Geophysics*, *51*, 475–503.
- Rice, J. R. (2006). Heating and weakening of faults during earthquake slip. *Journal of Geophysical Research*, *111*, B05311. <https://doi.org/10.1029/2005JB004006>
- Segall, P., Rubin, A. M., Bradley, A. M., & Rice, J. R. (2010). Dilatant strengthening as a mechanism for slow slip events. *Journal of Geophysical Research*, *115*, B12305. <https://doi.org/10.1029/2010JB007449>
- Shelly, D. R., Beroza, G. C., Ide, S., & Nakamura, S. (2006). Low-frequency earthquakes in Shikoku, Japan, and their relationship to episodic tremor and slip. *Nature*, *442*(7099), 188–191.
- Simons, M., Minson, S. E., Sladen, A., Ortega, F., Jiang, J., ... Webb, F. H. (2011). The 2011 magnitude 9.0 Tohoku-Oki earthquake: Mosaicking the megathrust from seconds to centuries. *Science*, *332*(6036), 1421–1425.
- Skarbek, R. M., & Rempel, A. W. (2016). Dehydration-induced porosity waves and episodic tremor and slip. *Geochemistry, Geophysics, Geosystems*, *17*, 442–469. <https://doi.org/10.1002/2015GC006155>
- Stein, S., & Okal, E. A. (2007). Ultralong period seismic study of the December 2004 Indian Ocean earthquake and implications for regional tectonics and the subduction process. *Bulletin of the Seismological Society of America*, *97*(1A), S279–S295.
- Streit, J. E., & Cox, S. F. (2001). Fluid pressures at hypocenters of moderate to large earthquakes. *Journal of Geophysical Research*, *106*(B2), 2235–2243.
- Thomas, A. M., Nadeau, R. M., & Bürgmann, R. (2009). Tremor-tide correlations and near-lithostatic pore pressure on the deep San Andreas Fault. *Nature*, *462*(7276), 1048–1051.
- Uchide, T., Shearer, P. M., & Imanishi, K. (2014). Stress drop variations among small earthquakes before the 2011 Tohoku-Oki, Japan, earthquake and implications for the main shock. *Journal of Geophysical Research: Solid Earth*, *119*, 7164–7174. <https://doi.org/10.1002/2014JB010943>
- Viesca, R. C., & Garagash, D. I. (2015). Ubiquitous weakening of faults due to thermal pressurization. *Nature Geoscience*, *8*(11), 875–879.
- Wesnousky, S. G. (2006). Predicting the endpoints of earthquake ruptures. *Nature*, *444*(7117), 358–360.
- Yao, H., Shearer, P. M., & Gerstoft, P. (2013). Compressive sensing of frequency-dependent seismic radiation from subduction zone megathrust ruptures. *Proceedings of the National Academy of Sciences*, *110*(12), 4512–4517.

### 4 Imager la distribution du couplage le long des grandes failles

Une approche plus classique pour identifier les zones de faille sur lesquelles de grands séismes sont susceptibles de se produire est d'estimer la distribution spatiale du couplage le long des grandes failles (voir Chapitre I.2.2). Pour cela, on inverse des données géodésiques long terme (GNSS ou InSAR) à la manière des inversions co-sismiques. Comme indiquée dans le Chapitre I.1.3, une faiblesse fondamentale de telles inversions est la non-unicité de leur solution. Dans l'étude qui suit, nous avons réalisé, à partir de données InSAR et GNSS, une inversion Bayésienne conjointe du couplage le long des failles Nord- et Est-Anatolienne ainsi que de la vitesse relative des plaques tectoniques Eurasienne, Anatolienne et Arabique. Cette approche nous permet d'estimer l'ensemble des solutions compatibles avec les observations. Nous avons ainsi pu estimer des incertitudes sur la distribution du couplage obtenue – et sur la vitesse long terme des plaques tectoniques – nous procurant une quantification probabiliste d'où s'accumulent les contraintes sur les failles.

Cette étude a été réalisée à Géoazur en collaboration avec Olivier Cavalié, Jean-Mathieu Nocquet et Théa Ragon. Elle a été publiée en 2020 dans le journal *Geophysical Research Letters* [[Bletery et al., 2020](#)].



# Geophysical Research Letters

## RESEARCH LETTER

10.1029/2020GL087775

### Key Points:

- Distribution of interseismic coupling on the North and East Anatolian Faults
- Bayesian quantification of uncertainties on coupling and Euler poles
- The 2020  $M_w$  6.8 Elazığ earthquake released 221.5 years ( $\pm 26$ ) of accumulated moment

### Supporting Information:

- Supporting Information S1

### Correspondence to:

Q. Bletery,  
bletery@geoazur.unice.fr

### Citation:

Bletery, Q., Cavalié, O., Nocquet, J. M., & Ragon, T. (2020). Distribution of interseismic coupling along the North and East Anatolian Faults inferred from InSAR and GPS data. *Geophysical Research Letters*, 47, e2020GL087775. <https://doi.org/10.1029/2020GL087775>

Received 4 MAR 2020

Accepted 5 AUG 2020

Accepted article online 17 AUG 2020

## Distribution of Interseismic Coupling Along the North and East Anatolian Faults Inferred From InSAR and GPS Data

Quentin Bletery<sup>1</sup>, Olivier Cavalié<sup>1</sup>, Jean-Mathieu Nocquet<sup>1,2</sup>, and Théa Ragon<sup>3</sup>

<sup>1</sup>Université Côte d'Azur, IRD, CNRS, Observatoire de la Côte d'Azur, Géoazur, France, <sup>2</sup>Institut de Physique du Globe de Paris, Université de Paris, CNRS, Paris, France, <sup>3</sup>Seismological Laboratory, California Institute of Technology, Pasadena, CA, USA

**Abstract** The North Anatolian Fault (NAF) has produced numerous major earthquakes. After decades of quiescence, the  $M_w$  6.8 Elazığ earthquake (24 January 2020) has recently reminded us that the East Anatolian Fault (EAF) is also capable of producing significant earthquakes. To better estimate the seismic hazard associated with these two faults, we jointly invert interferometric synthetic aperture radar (InSAR) and GPS data to image the spatial distribution of interseismic coupling along the eastern part of both the NAF and EAF. We perform the inversion in a Bayesian framework, enabling to estimate uncertainties on both long-term relative plate motion and coupling. We find that coupling is high and deep (0–20 km) on the NAF and heterogeneous and superficial (0–5 km) on the EAF. Our model predicts that the Elazığ earthquake released between 200 and 250 years of accumulated moment, suggesting a bicentennial recurrence time.

**Plain Language Summary** Earthquakes are thought to occur on coupled fault portions, which are “locked” during the time separating two earthquakes, while tectonic plates are steadily moving. The spatial distribution of coupling has been imaged along numerous large faults in the world, but despite its considerable associated seismic hazard, not on the North Anatolian Fault (NAF). The recent  $M_w$  6.8 Elazığ earthquake (24 January 2020) has reminded us that the East Anatolian Fault (EAF) is also capable of producing large earthquakes. To better assess the seismic hazard associated with both the NAF and the EAF, we image the distribution of interseismic coupling along these faults. We find that the NAF is strongly coupled along most of the studied section. On the opposite, coupling is shallow and heterogeneous along the EAF. The initiation of the Elazığ earthquake coincides with a strongly locked but narrow ( $5 \times 14$  km) and superficial patch. The rest of the rupture extends over moderately coupled fault portions. We estimate that it took between 200 and 250 years to accumulate the moment released by the Elazığ event. Several fault segments along the EAF present similar coupling distributions, suggesting that, provided enough time, they could host earthquakes of similar magnitude.

## 1. Introduction

Earthquakes are thought to rupture fault portions that have previously accumulated a deficit of slip over tens to thousands of years (e.g., Avouac, 2015). Quantifying the spatial distribution of interseismic coupling—that is, the percentage of slip deficit with respect to the long-term drift of tectonic plates—along large faults is therefore crucial to anticipate earthquakes and better assess seismic hazard (e.g., Kaneko et al., 2010). The emergence of space geodetic techniques has allowed to infer interseismic coupling along a number of large faults during long quiescent periods of time separating one large earthquake to the next (e.g., Bürgmann et al., 2005; Jolivet et al., 2015; Loveless & Meade, 2011; Metois et al., 2016; Moreno et al., 2010; Nocquet et al., 2017; Protti et al., 2014). Though interseismic coupling models have been proposed to estimate the locking depth of the North Anatolian Fault (NAF) and East Anatolian Fault (EAF) (e.g., Aktug et al., 2013, 2016; Cavalié & Jónsson, 2014; Mahmoud et al., 2013; Tatar et al., 2012), none have quantified the lateral variations of coupling along these faults, which has limited the possibilities to study the spatial relationship between coupling and large earthquakes. The density of interferometric synthetic aperture radar (InSAR) observations (Cavalié & Jónsson, 2014) combined with sparser GPS measurements allows to infer these lateral variations of coupling on the eastern part of the NAF-EAF system (Figure 1).

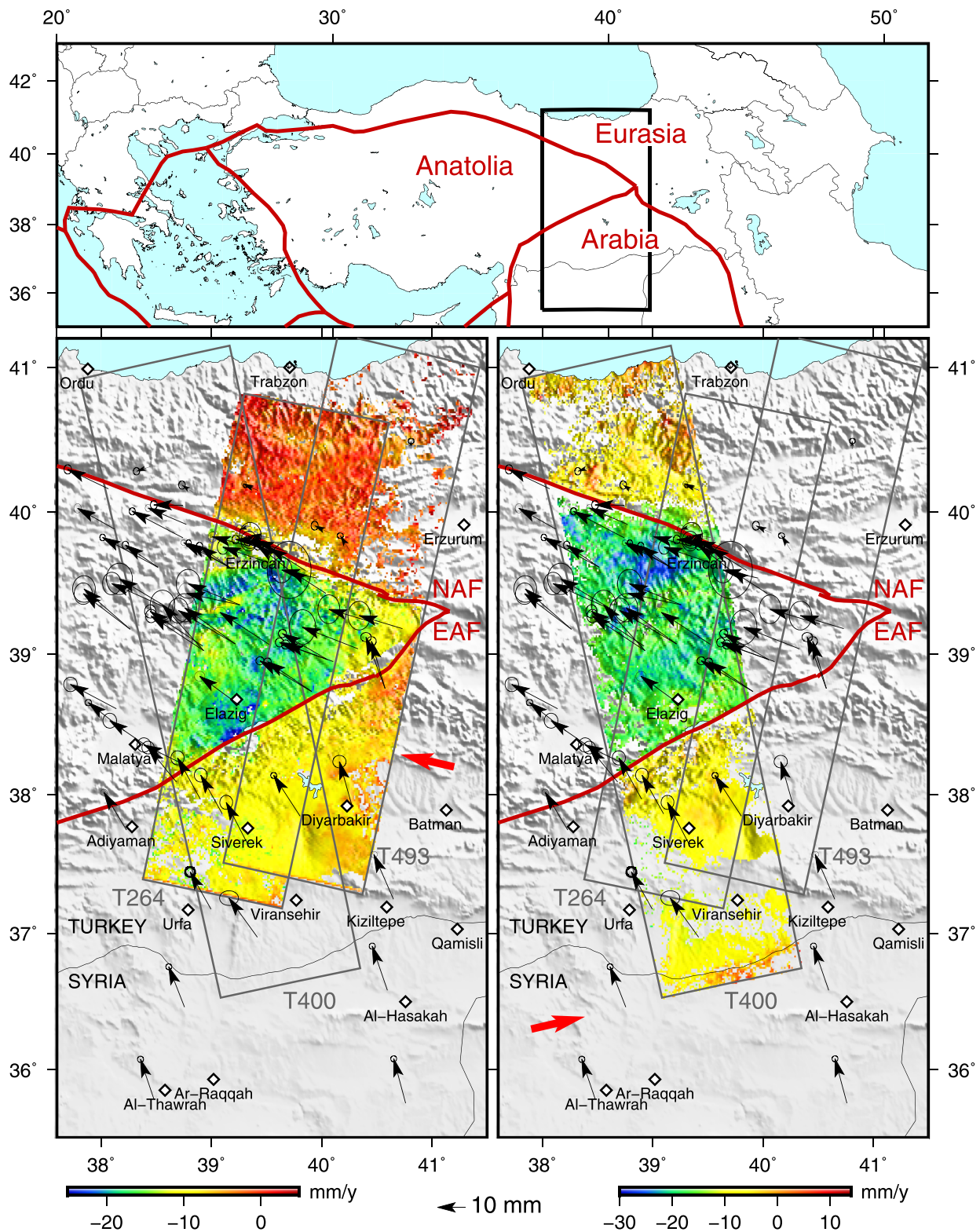


**Figure 1.** (top) Tectonic setting of the NAF-EAF system (red lines) and study area (black rectangle). (bottom) Color maps show InSAR horizontal velocities (in a Eurasiafixed reference frame) in the satellite line-of-sight (LOS) direction (thick red arrows),  $\sim 103^\circ\text{N}$  for Descending Tracks T264 and T493 (left) and  $\sim 77^\circ\text{N}$  for Ascending Track T400 (right) (Cavalié & Jónsson, 2014). Black arrows show GPS measurements and their 95% ellipses of uncertainty (Nocquet, 2012; Ozener et al., 2010; Tatar et al., 2012). White diamonds indicate large (>100,000 people) cities.



The eastern part of the NAF is known to produce large earthquakes (e.g., Ambraseys, 1971, 1989; Barka, 1996) and thought to be coupled from 0 to 15 km depth (Cavalié & Jónsson, 2014; Reilinger et al., 2006). On the other hand, simple back slip models showed that the EAF is weakly coupled and only in the first kilometers of the upper crust, from 0 to 5 km (Cavalié & Jónsson, 2014). This observation was in good agreement with the relative scarcity of large earthquakes recorded during the twentieth century (Burton et al., 1984; Jackson & McKenzie, 1988). For those reasons, the 24 January 2020  $M_w$  6.8 Elazığ earthquake came as a surprise, on a segment that does not exhibit signs of past rupture (Duman & Emre, 2013) and in an area where the last earthquake of comparable magnitude ( $M_s$  6.8) occurred in 1905 (Nalbant et al., 2002). To understand this unexpected event, and more generally the seismicity in the region, we infer here the spatial distribution of interseismic coupling along the eastern part of the NAF-EAF system using InSAR (Cavalié & Jónsson, 2014) and GPS measurements (Nocquet, 2012; Ozener et al., 2010; Tatar et al., 2012) of the interseismic surface deformation.

Inferring spatially variable interseismic coupling along faults from geodetic observations—such as InSAR and GPS—of the Earth surface deformation requires solving an inverse problem that usually does not admit a unique solution (Nocquet, 2018; Tarantola & Valette, 1982). Most inversion techniques deal with this nonuniqueness by finding the solution that best fits the observations in a least squares sense, together with some roughness and/or damping penalty function. As a result, typical published coupling (or slip) models are the smoothest best fitting solutions among an infinity of possible models. We adopt here a Bayesian approach, which does not invert for a specific “ambiguously defined best solution” but explores the entire solution space, sampled with respect to the likelihood of each model. This approach—originally developed to invert for coseismic slip models (Minson et al., 2013)—also enables to reliably estimate uncertainties on coupling distributions (Jolivet et al., 2015, 2020).

## 2. Data

Our data set is composed of InSAR and GPS measurements in eastern Anatolia, all calculated in a stable Eurasia reference frame (Figure 1). Our InSAR data set is composed of two descending and one ascending tracks—all crossing both the NAF and EAF near their junction in eastern Turkey—processed by Cavalié and Jónsson (2014). Our GPS data set is composed of the horizontal components of 72 GPS stations located in the area (Nocquet, 2012; Ozener et al., 2010; Tatar et al., 2012).

InSAR data were derived from multiframe Envisat synthetic aperture radar (SAR) images provided by the European Space Agency. Each track includes between 16 and 19 SAR images acquired between 2003 and 2010. Interferograms were generated using the New Small Baseline Subset (NSBAS) processing chain (Doin et al., 2011). They were corrected for a ramp mostly due to a drift in the local oscillator on board the Envisat satellite (Marinkovic & Larsen, 2013). To avoid removing tectonic signals related to the motion of the Anatolian and Arabian plates, the ramps were estimated only on their Eurasian part that is considered as stable and orthogonal to the flight direction. All calculations were made considering stable Eurasia as a reference by setting the mean displacement of this area to 0, in the least squares sense. Surface displacement rates from the interferograms were derived using a small baseline time series approach, which maximizes coherence and the number of pixels to use in the analysis. A smoothing operator was applied to limit phase variations due to turbulent atmospheric delays. Finally, the linear component of the time series was extracted for each pixel in order to obtain the steady ground velocities. For a more detailed description of the InSAR processing, we refer the reader to the original study of Cavalié and Jónsson (2014).

Additionally, we compiled GPS data located between longitudes 38°E and 41°E and latitudes 35°N and 43°N from three independent studies. Velocity for 19 points were published by Tatar et al. (2012) derived from three surveys performed between 2006 and 2008. Another set of 19 points were published by Ozener et al. (2010) from three campaigns with 12-month interval. The remaining 34 points were originally published by Reilinger et al. (2006) and Reilinger and McClusky (2011) but recalculated in the continental-scale combination solution described in Nocquet (2012). The three data sets are expressed in a Eurasia-fixed reference frame. The lack of enough common sites shared among the three solutions prevents to properly combine them, but the few common sites and analysis of models residuals do not show any systematic pattern, suggesting that the three velocity fields are consistent within their uncertainties.

### 3. Bayesian Inversion of Rotation Poles and Interseismic Slip Deficit Rate Along Two Faults From InSAR and GPS Data

We invert the aforementioned InSAR and GPS measurements of the eastern Anatolia surface deformation to infer the distribution of interseismic slip deficit rate along the NAF-EAF system using a Bayesian sampling approach implemented in the AlTar1 package, originally developed by Minson et al. (2013) under the name of CATMIP. AlTar associates Markov chain Monte Carlo methods with a tempering process to explore the solution space, each step of the tempering being followed by a resampling to select only the most probable models. The probability density function (pdf)  $p(\mathbf{m}|\mathbf{d})$  of a large number of likely models  $\mathbf{m}$  given our data  $\mathbf{d}$  is evaluated based on the ability of a model  $\mathbf{m}$  to predict the data  $\mathbf{d}$  (Minson et al., 2013):

$$p(\mathbf{m}|\mathbf{d}) \propto p(\mathbf{m}) \exp \left[ -\frac{1}{2} (\mathbf{d} - \mathbf{G}\mathbf{m})^T \mathbf{C}_\chi^{-1} (\mathbf{d} - \mathbf{G}\mathbf{m}) \right], \quad (1)$$

where  $\mathbf{G}$  is the matrix of the Green's functions and  $\mathbf{C}_\chi$  is the misfit covariance matrix. Vector  $\mathbf{d}$  is composed of 144 GPS measurements ( $72 \times 2$  components) and a subset of InSAR pixels on the three tracks downsampled using the Quadtree algorithm (Jónsson et al., 2002).

Because the inferred distribution of coupling is presumably highly sensitive to the (usually) predetermined tectonic block motion, especially in a case involving three plates, we do not impose precalculated plate rotations but invert for them simultaneously with the interseismic slip deficit rate—similarly to the approach proposed by Meade and Loveless (2009) but adapted to a Bayesian framework. We discretize the eastern part of the NAF and EAF into 110 subfaults of depth-dependent sizes (Tables S1 and S2 in the supporting information) and invert for the model vector:

$$\mathbf{m} = \begin{pmatrix} \mathbf{w}^1 \\ \mathbf{w}^2 \\ \mathbf{S} \end{pmatrix}, \quad (2)$$

where  $\mathbf{w}$  is the plate rotation vector expressed in Cartesian geocentric coordinates with unit of rad/year,<sup>1</sup> stands for Anatolia with respect to Eurasia,<sup>2</sup> for Arabia with respect to Eurasia, and  $\mathbf{S}$  is the back slip on each subfault. Accordingly, we build  $\mathbf{G}$  so that

$$\mathbf{G} = (\mathbf{A}, -\mathbf{G}_S), \quad (3)$$

where  $\mathbf{A}$  is the matrix relating the plate rotation vectors to the horizontal velocities (see Appendix A) and  $\mathbf{G}_S$  is the classical matrix of the Green's functions computed using the analytical solution of a shear finite fault embedded in an elastic half-space (Mansinha & Smylie, 1971; Okada, 1985).

$\mathbf{C}_\chi$  is the misfit covariance matrix, which translates data and epistemic uncertainties into uncertainties on the inverted model  $\mathbf{m}$  (Bletery et al., 2016; Duputel et al., 2014; Ragon et al., 2018, 2019a, 2019b). Here, we only account for data uncertainties. For GPS records, we fill  $\mathbf{C}_\chi$  with the (squared) standard deviations and covariances between the east and north components of a given station provided in the GPS solutions. For InSAR pixels, we first remove the tectonic signal from the unsampled interferograms using a preliminary model and calculate the covariance across the pixels of the residual interferograms as a function of their distances. We fit an exponential function (Figure S1) to the obtained cloud of points and express the covariance  $C_{i,j}$  between two pixels as a function of their distance  $D_{i,j}$ :

$$C_{i,j} = a^2 \exp \left( \frac{-D_{i,j}}{b} \right), \quad (4)$$

by applying a regression to the parameters  $a$  and  $b$  independently on the three tracks (Jolivet et al., 2012, 2015, Sudhaus & Sigurjón, 2009). We then use Equation 4 to evaluate the covariance on the subsampled interferograms.

$p(\mathbf{m})$  is the pdf describing the prior information assumed on the different model parameters. We choose the less informative distributions for back slip parameters  $\mathbf{S}$ , that is, uniform distributions between 0 and the a priori long-term interplate velocities: 19.5 mm/year for the North Anatolian and 13 mm/year for the EAF (Cavalié & Jónsson, 2014). For the plate rotation vectors, we use the Euler poles and their associated

**Table 1**  
*A Priori (Le Pichon & Kreemer, 2010) and A Posteriori Euler Pole Coordinates and Angular Velocities With Respect to Eurasia*

	Plate	Longitude (° E)	Latitude (° N)	Angular velocity (°/My)
A priori	Anatolia	31.96 ± 0.10	32.02 ± 0.10	1.307 ± 0.083
	Arabia	15.21 ± 0.10	28.31 ± 0.10	0.396 ± 0.010
A posteriori	Anatolia	34.22 ± 0.35	30.96 ± 0.60	1.087 ± 0.078
	Arabia	16.13 ± 0.52	27.08 ± 0.37	0.386 ± 0.008

*Note.* A posteriori parameters are the mean and 2- $\sigma$  standard deviation (95% confidence) of the posterior pdfs (Figure S6).

uncertainty from Le Pichon and Kreemer (2010) to derive a prior pdf. Plate rotation vectors (in Cartesian geocentric coordinates)  $\mathbf{w}^p$  are related to Euler pole parameters through

$$\mathbf{w}^p = \Omega^p \begin{pmatrix} \cos \phi^p \cos \lambda^p \\ \cos \phi^p \sin \lambda^p \\ \sin \phi^p \end{pmatrix}, \quad (5)$$

where  $\lambda^p$  and  $\phi^p$  are the longitude and latitude of the Euler pole of a plate  $p$  and  $\Omega^p$  is its angular velocity (Bowring, 1985). Note that this change of coordinate system makes the problem linear (e.g., Maurer & Johnson, 2014; Meade & Loveless, 2009; Nocquet et al., 2001). We draw 100,000 sets of parameters ( $\lambda^1, \phi^1, \Omega^1, \lambda^2, \phi^2, \Omega^2$ ) from normal distributions defined by means and standard deviations taken from previously published solutions (Le Pichon & Kreemer, 2010, summarized in Table 1). For each drawn set of parameters, we calculate the corresponding  $\mathbf{w}^1$  and  $\mathbf{w}^2$ . We obtain Gaussian-like distributions for each component of  $\mathbf{w}^1$  (Figure S2) and  $\mathbf{w}^2$  (Figure S3). We extract the mean and standard deviation of these distributions and use them to define normal prior pdfs on  $w_{x,y,z}^{1,2}$  in AlTar.

#### 4. Results

We obtain a posterior marginal pdf for every inverted parameter in  $\mathbf{m}$ , 110 fault slip parameters and 6 parameters describing the plate rotation vectors ( $w_{x,y,z}^{1,2}$ ). The posterior pdfs on  $\mathbf{w}^1$  and  $\mathbf{w}^2$  parameters (Figure S4) appear uncorrelated (coefficients of correlation <0.013) with each other and—to a lesser extent—with fault slip parameters (coefficients of correlation <0.13) (Figure S5). Moderate anticorrelations are noticeable between fault slip parameters of patches located one beneath another (i.e., at the same location but different depth) (Figure S5a).

We convert the inverted pdfs on the rotation vectors ( $\mathbf{w}^1, \mathbf{w}^2$ ) (Figure S4) into pdfs on the Euler pole coordinates and angular velocities (Figure S6). The means and 2- $\sigma$  standard deviations of the inverted pdfs are summarized in Table 1. They are close to the previously published values we used as a prior (Le Pichon & Kreemer, 2010) but not equal (Figure S7). A possible explanation for this small discrepancy is that the plates are not strictly rigid (Aktug et al., 2013; England et al., 2016; Le Pichon & Kreemer, 2010; Nocquet, 2012), and thus, the rotations we invert from data in eastern Anatolia are slightly different from those obtained from data sampling on a larger area of the plate. Figure S8a shows the velocities corrected from plate motion using the Euler poles from Le Pichon and Kreemer (2010). It clearly shows a pattern of a residual rotation and unlikely large (5 mm/year) fault normal relative motion across both faults. Using our poles, residuals velocities appear to be consistent with the interseismic pattern (back slip) expected for strike-slip faults (Figure S8b). Our goal here is to infer the coupling distribution, and for that aim a refined estimate of the rotation parameters close to the fault is preferable to a plate-average solution, but one should be careful in using values in Table 1 for other purposes.

For each posterior Euler pole, we calculate the rotation predicted at the center of each patch and project the obtained vector along the fault strike direction to obtain posterior pdfs of the long-term slip rate along the faults (Figure S9). These pdfs are consistent with steady long-term slip rates of ~20 mm/year along the NAF and ~10 mm/year along the EAF (Figures 2 and S9 and Tables S1 and S2).

For each sampled model  $\mathbf{m}_k = (\mathbf{w}_k^1, \mathbf{w}_k^2, \mathbf{S}_k)^T$ , we divide the back slip parameters  $\mathbf{S}_k$  by the long-term fault rate calculated at the center of each patch using the corresponding sampled Euler poles  $\mathbf{w}_k^1$  and  $\mathbf{w}_k^2$  to obtain

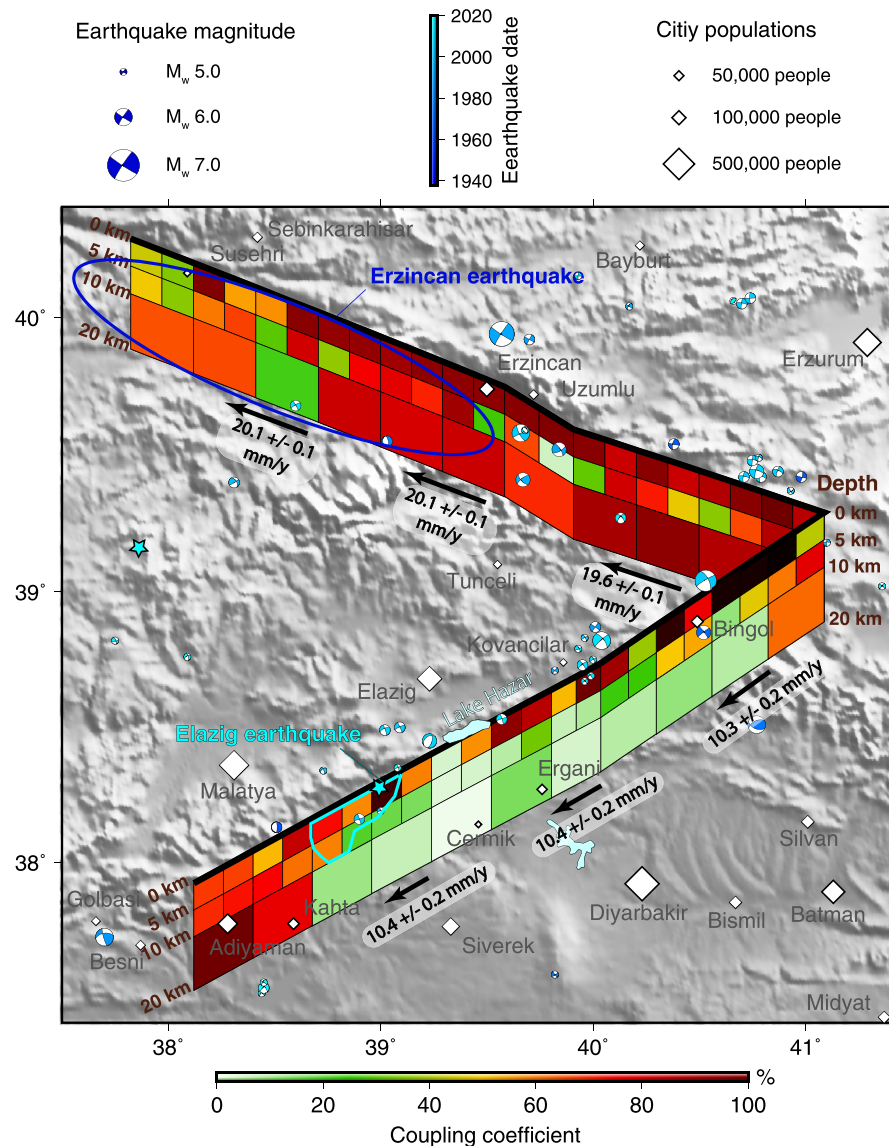


**Figure 2.** Interseismic coupling distribution inverted from InSAR and GPS data (mean of posterior pdfs in Figures S10 and S11). Black thick arrows indicate the long-term slip rate at depth derived from the inversion (mean and standard deviation of posterior pdfs in Figure S9). Focal mechanisms show  $M > 4.8$  earthquakes (colors indicate event dates). Contours delineate the approximate rupture extent of the 1939  $M_S$  8.0 Erzincan earthquake and of the 2020  $M_w$  6.8 Elazığ earthquake (USGS finite fault solution). The light blue star indicates the epicenter of the Elazığ earthquake.

the posterior marginal pdfs on the coupling coefficients (Figures S10 and S11). We show these pdfs in the form of their means (Figure 2) and standard deviations (Figure 3). Although restrictive, this representation gives an approximate view of the coupling spatial distribution and its associated uncertainties. Uncertainty is high ( $>25\%$ ) on the extreme west and—to a lesser extent—the extreme east parts of the fault system that are located outside of the InSAR tracks (Figure 1). The standard deviation on most parts of the faults is  $<20\%$ , much lower on many subfaults (Figure 3). Note that standard deviation values are likely underestimated since we did not consider epistemic uncertainties here. The Earth structure is likely not homogeneous and the fault geometry not as simple as we modeled it, generating more uncertainties that we do not account for.

We calculate the GPS and InSAR measurements predicted for every posterior sampled model. We plot the predicted GPS means (red arrows) and  $2\sigma$  standard deviations (red ellipses) on Figure S12 and the residuals on Figure S13. For InSAR, we plot the mean predicted line-of-sight (LOS) displacements (Figures S14–S16)

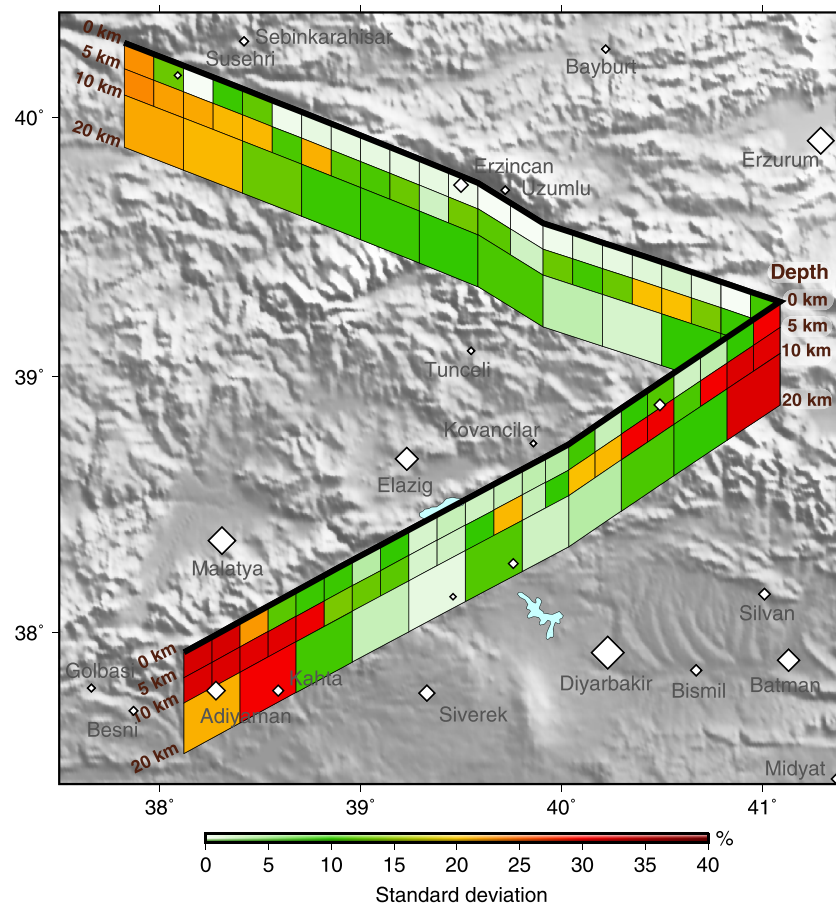


**Figure 3.** Standard deviation of the coupling posterior pdfs. The extreme west and—to a lesser extent—the extreme east parts of the NAF-EAF system, presenting high (>25%) standard deviations, are located outside of the InSAR tracks.

and standard deviations (Figure S17). The range of likely models that we found (Figures S10 and S11) is in very good agreement with both GPS and InSAR data. One way to quantify the relative amplitudes of residuals with respect to the observations is to calculate the ratio  $r$  of the mean of the absolute value of the residuals with the mean of the absolute value of the observations,

$$r = \frac{\langle |\mathbf{d} - \mathbf{d}_{\text{pred}}| \rangle}{\langle |\mathbf{d}| \rangle}. \quad (6)$$

This ratio is 15.9% for T264, 36.1% for T400, 24.3% for T493, and 21.6% for GPS. We attribute these reasonably small residuals—which do not exhibit coherent pattern (Figures S13 and S17)—to nontectonic sources. Furthermore, we find that every posterior sampled model predict very similar GPS and InSAR displacements; red ellipses are hardly visible on Figure S12, and the standard deviations of the predicted InSAR LOS displacements are very small (Figure S17). This highlights the limited resolution on the coupling model: If different models predict the same observations, discriminating between them is difficult.

## 5. Discussion

We show focal mechanisms of  $M > 4.8$  earthquakes in the studied area from the Global Centroid Moment Tensor (GCMT) catalog (Dziewonski et al., 1981; Ekström et al., 2012) for events posterior to 1976 and from a compilation of historical earthquakes (Tan et al., 2008) for earlier events (1938–1976) (Figure 2). Focal mechanisms are represented at the location of their surface projections (i.e., at depth = 0). Colors indicate the dates of the events. The largest earthquake in the studied area is the 1939  $M_s$  8.0 Erzurum earthquake, which initiated near Erzurum and extended over the entire NAF segment west of Erzurum represented in

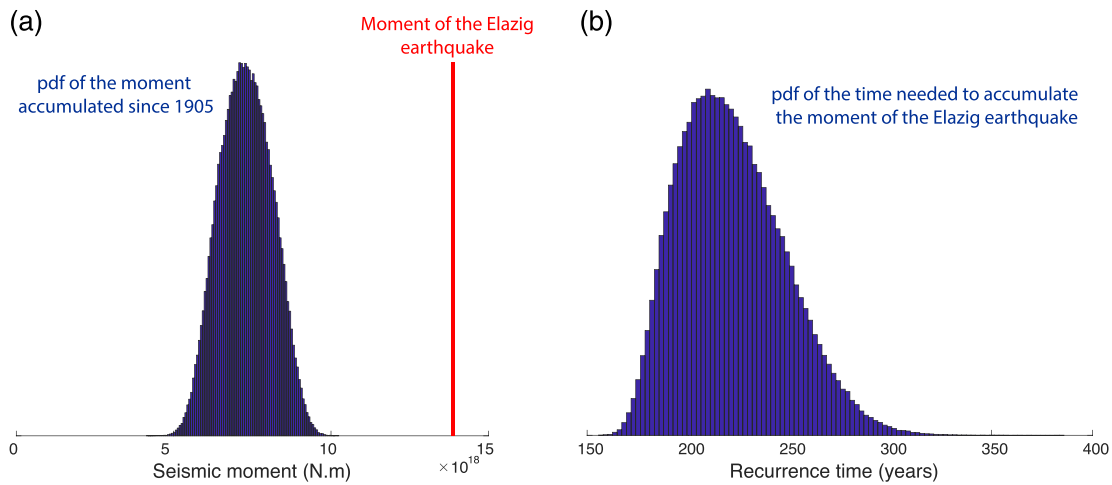


Figure 2 (Barka, 1996; Stein et al., 1997). We find that almost all of this section is strongly coupled, such as the rest of the studied NAF segment east of Erzincan. This easternmost segment of the NAF presents a moderate seismicity compared to the rest of the NAF. Our interseismic slip distribution suggests that it is as prone to generate large earthquakes as the rest of the NAF and as the Erzincan rupture segment in particular. In the middle of this overall strongly coupled (>75%) fault, we identify a few low-to-moderate coupling (10–50%) patches at depths between 5 and 10 km (Figure 2). These patches are associated with standard deviations between 5% and 25%, suggesting that these uncoupled patches are robust features. Interestingly, the most uncoupled patch coincides with the main step over of this section of the NAF. Step overs are thought to act as geometrical barriers that stop earthquake ruptures (e.g., Wesnousky, 2006). Although limited to one example, our results suggest that these geometrical features may also influence—or be influenced by—the interseismic behavior of the faults.

We find that locking on the EAF is much shallower with coupling values >50% limited to the first 5 km, consistently with previous studies (Cavalié & Jónsson, 2014). High coupling found at depth on the westernmost part of the fault is associated with standard deviations >20%, meaning that they are not reliable (Figure 3). Furthermore, we find that coupling also varies within the shallowest portion of the fault, alternating strongly coupled segments with weakly-to-moderately (0–60%) coupled ones (Figure 2). The most uncoupled shallow fault portion of the central EAF is located near Elazığ and coincides with the pull apart basin of Lake Hazar, as also observed on the Haiyuan fault (Jolivet et al., 2013). Different stress orientations around the basin could favor low coupling (Bertoluzza & Perotti, 1997; Wang et al., 2017; Van Wijk et al., 2017). This large reservoir of water may also provide the shallow part of the fault with fluids (although low resistivity associated to fluids is rather observed below 10 km depth, Türkoğlu et al., 2015) and locally weaken its mechanical friction, favoring aseismic slip. Such a behavior is observed both in laboratory and in situ (at the decametric scale) (Cappa et al., 2019). The mechanism invoked by the authors—consisting in an increase in nucleation length due to an increase in pore fluid pressure—may be at play at much larger scale here. On the other hand, the few earthquakes recorded on the EAF coincide with relatively high coupling. Before the recent Elazığ earthquake, the two largest events occurred near the localities of Bingöl ( $M_w$  6.3, 2003) and Kovancilar ( $M_w$  6.1, 2010). The second one was followed by numerous aftershocks with magnitudes up to 5.6. All of these earthquakes occurred on >65% coupled fault portions, while fault segments with coupling <50% do not appear to have hosted  $M > 4.8$  earthquakes.

According to the U.S. Geological Survey (USGS) finite-fault model (USGS, 2020), the Elazığ earthquake initiated between Elazığ and Malatya (light blue star in Figure 2) and propagated unilaterally westward (light blue contour in Figure 2). The early part coincides with a strongly locked (coupling coefficient: 100%) but narrow ( $13.7 \times 5$  km) patch. The rupture seems to have then propagated throughout moderately coupled (coupling coefficient: 50–80%) fault segments. Although the USGS model is preliminary, its contours correlate fairly well with the coupling distribution, suggesting that the rupture stopped when reaching <25% coupled fault portions (Figure 2).

The last  $M > 6.6$  earthquake in the approximate region dates back to 1905 ( $M_S = 6.7$ ) (Nalbant et al., 2002). This event was located west of the recent Elazığ earthquake ( $38.6^\circ\text{E}$ ,  $38.1^\circ\text{N}$ ) (Nalbant et al., 2002) but, given location uncertainties, could have ruptured the same fault portion. We calculate, for each sampled coupling model, the accumulated moment inside the rupture contour of the Elazığ earthquake since 1905. To simplify the problem, we assume that the earthquake ruptured the entire surface of the four main subfaults inside the rupture contour and not more, that is, the three shallowest subfaults plus the westernmost intermediate-depth one (Figure 3). We obtain a pdf of the seismic moment accumulated since 1905 (Figure 4a). The pdf mean is  $7.3 \times 10^{18}$  N m, its standard deviation  $0.8 \times 10^{18}$  N m. According to the USGS solution, the seismic moment released during the Elazığ earthquake is  $13.87 \times 10^{18}$  N m—other solutions find even larger seismic moments (e.g., GCMT, Pousse-Beltran et al., 2020)—which is much larger than the  $7.3 \pm 0.8 \times 10^{18}$  N m of moment deficit that we estimated since 1905. This seems to indicate that the recent Elazığ earthquake did not rupture the same fault portion than the 1905 earthquake. We further calculate the pdf of the time necessary to accumulate the seismic moment, which was released during the 2020 Elazığ earthquake (Figure 4b). The mean and standard deviation of the obtained pdf give a recurrence time for an Elazığ-type earthquake of  $221.5 \pm 26$  years.



**Figure 4.** (a) Pdf of the accumulated seismic moment on the four patches inside the Elazığ rupture since 1905. The red vertical line indicates the seismic moment of the Elazığ earthquake according to the USGS solution ( $13.87 \times 10^{18}$  N.m). (b) Pdf of the time necessary to accumulate the seismic moment that was released during the Elazığ earthquake.

## 6. Conclusion

We inverted InSAR and GPS observations to image interseismic coupling along the NAF and EAF in eastern Turkey. We adopted a Bayesian sampling approach in order to estimate posterior uncertainties on the coupling distributions and on the long-term fault rate. We did not impose a precalculated plate motion but inverted for the rotation of both the Anatolian and Arabian plates with respect to Eurasia, ensuring that the inferred coupling distribution is not biased in a systematic way by an inaccurate plate motion model. We found that the NAF is strongly coupled from 0 to 20 km depth, while the EAF is weakly coupled for the most part with high (>50%) coupling values limited to the shallowest part of the fault (0 to 5 km). Furthermore, we find that coupling is heterogeneous within this shallow portion, alternating seemingly creeping sections with strongly locked patches. Comparison between our interseismic coupling distribution and the preliminary finite-fault model of the USGS for the 2020  $M_w$  6.8 Elazığ earthquake reveals that this event likely initiated on one of this strongly locked (coupling coefficient: 100%) fault patches and then propagated into moderately coupled fault segments (coupling coefficient: 50–80%). Overall, we estimate that the Elazığ earthquake released  $221.5 (\pm 26)$  years of accumulated moment, suggesting a recurrence time ranging from 200 to 250 years.

## Appendix A: Rotation Matrix $\mathbf{A}$

We build the rotation matrix  $\mathbf{A}$  so that the motion due to the rotation of both the Anatolian and Arabian plates with respect to Eurasia equals  $\mathbf{A} \cdot \mathbf{W}$ , where

$$\mathbf{W} = \begin{pmatrix} \mathbf{w}^1 \\ \mathbf{w}^2 \end{pmatrix}. \quad (\text{A1})$$

Sorting all data points located on the Eurasian plate at the beginning of  $\mathbf{d}$ , all data points located on the Anatolian plate in the middle and all data points located on the Arabian plate at the end, that is, writing  $\mathbf{d}$  as

$$\mathbf{d} = \begin{pmatrix} \mathbf{d}_0 \\ \mathbf{d}_1 \\ \mathbf{d}_2 \end{pmatrix}, \quad (\text{A2})$$

with  $\mathbf{d}_0$ ,  $\mathbf{d}_1$ , and  $\mathbf{d}_2$  data points located on the Eurasian, Anatolian, and Arabian plates respectively, we can write  $\mathbf{A}$  as a block matrix

$$\mathbf{A} = \begin{pmatrix} \mathbf{0} & \mathbf{0} \\ \mathbf{A}' & \mathbf{0} \\ \mathbf{0} & \mathbf{A}' \end{pmatrix}, \quad (\text{A3})$$

so that  $\mathbf{A} \cdot \mathbf{W}$  equals  $\mathbf{0}$  for data points in Eurasia,  $\mathbf{A}' \cdot \mathbf{w}^1$  in Anatolia, and  $\mathbf{A}' \cdot \mathbf{w}^2$  in Arabia.  $\mathbf{A}'$  is a transfer matrix relating the rotation vector in Cartesian geocentric coordinates  $\mathbf{W}$  to the rotation block motion at each data point. It can be expressed at the location of an InSAR pixel or GPS station of longitude  $\lambda$  and latitude  $\phi$  as

$$\mathbf{A}'_{\lambda,\phi} = \begin{pmatrix} -\sin \lambda & \cos \lambda & 0 \\ -\sin \phi \cos \lambda & -\sin \phi \sin \lambda & \cos \phi \\ \cos \phi \cos \lambda & \cos \phi \sin \lambda & \sin \phi \end{pmatrix} \cdot \begin{pmatrix} 0 & z & -y \\ -z & 0 & x \\ y & -x & 0 \end{pmatrix}, \quad (\text{A4})$$

where

$$\begin{pmatrix} x \\ y \\ z \end{pmatrix} = R_e(1 - \epsilon \sin^2 \phi)^{-1/2} \begin{pmatrix} \cos \phi \cos \lambda \\ \cos \phi \sin \lambda \\ (1 - \epsilon) \sin \phi \end{pmatrix}, \quad (\text{A5})$$

with  $R_e = 6,378.137$  km the Earth equatorial radius and  $\epsilon = 0.00669438003$  the Earth eccentricity (Bowring, 1985).

#### Acknowledgments

The SAR data were provided by the European Space Agency through category1 project 6703, accessible at the following address (<https://earth.esa.int/web/guest/data-access/>). The inversion was performed using the AlTar software developed by Sarah Minson, Junle Jiang, Hailiang Zhang, Romain Jolivet, Zacharie Duputel, Michael Aivazis, James Beck, and Mark Simons at Caltech. We thank the Editor and Romain Jolivet and A. Ozgun Konca for thorough reviews.

#### References

- Aktug, B., Dikmen, U., Dogru, A., & Ozener, H. (2013). Seismicity and strain accumulation around Karliova Triple Junction (Turkey). *Journal of Geodynamics*, *67*, 21–29.
- Aktug, B., Ozener, H., Dogru, A., Sabuncu, A., Turgut, B., Halicioğlu, K., et al. (2016). Slip rates and seismic potential on the East Anatolian Fault System using an improved GPS velocity field. *Journal of Geodynamics*, *94*, 1–12.
- Ambraseys, N. (1971). Value of historical records of earthquakes. *Nature*, *232*(5310), 375–379.
- Ambraseys, N. (1989). Temporary seismic quiescence: SE Turkey. *Geophysical Journal International*, *96*(2), 311–331.
- Avouac, J.-P. (2015). From geodetic imaging of seismic and aseismic fault slip to dynamic modeling of the seismic cycle. *Annual Review of Earth and Planetary Sciences*, *43*, 233–271.
- Barka, A. (1996). Slip distribution along the North Anatolian Fault associated with the large earthquakes of the period 1939 to 1967. *Bulletin of the Seismological Society of America*, *86*(5), 1238–1254.
- Bertoluzza, L., & Perotti, C. R. (1997). A finite-element model of the stress field in strike-slip basins: Implications for the Permian tectonics of the Southern Alps (Italy). *Tectonophysics*, *280*(1-2), 185–197.
- Bletery, Q., Sladen, A., Jiang, J., & Simons, M. (2016). A Bayesian source model for the 2004 great Sumatra-Andaman earthquake. *Journal of Geophysical Research: Solid Earth*, *121*, 5116–5135. <https://doi.org/10.1002/2016JB012911>
- Bowring, B. R. (1985). The accuracy of geodetic latitude and height equations. *Survey Review*, *28*(218), 202–206.
- Bürgmann, R., Kogan, M. G., Steblov, G. M., Hilley, G., Levin, V. E., & Apel, E. (2005). Interseismic coupling and asperity distribution along the Kamchatka subduction zone. *Journal of Geophysical Research*, *110*, B07405. <https://doi.org/10.1029/2005JB003648>
- Burton, P. W., McGonigle, R., Makropoulos, K. C., & Üçer, S. B. (1984). Seismic risk in Turkey, the Aegean and the eastern Mediterranean: The occurrence of large magnitude earthquakes. *Geophysical Journal International*, *78*(2), 475–506.
- Cappa, F., Scuderi, M. M., Collettini, C., Guglielmi, Y., & Avouac, J.-P. (2019). Stabilization of fault slip by fluid injection in the laboratory and in situ. *Science Advances*, *5*(3), eaau4065.
- Cavalié, O., & Jónsson, S. (2014). Block-like plate movements in Eastern Anatolia observed by InSAR. *Geophysical Research Letters*, *41*, 26–31. <https://doi.org/10.1002/2013GL058170>
- Doin, M.-P., Guillaso, S., Jolivet, R., Lasserre, C., Lodge, F., Ducret, G., & Grandin, R. (2011). Presentation of the small baseline NSBAS processing chain on a case example: The Etna deformation monitoring from 2003 to 2010 using Envisat data. In *Proceedings of the Fringe symposium*, pp. 3434–3437.
- Duman, T. Y., & Emre, O. (2013). The East Anatolian Fault: Geometry, segmentation and jog characteristics. *Geological Society, London, Special Publications*, *372*(1), 495–529.
- Duputel, Z., Agram, P. S., Simons, M., Minson, S. E., & Beck, J. L. (2014). Accounting for prediction uncertainty when inferring subsurface fault slip. *Geophysical Journal International*, *197*(1), 464–482.
- Dziewonski, A. M., Chou, T.-A., & Woodhouse, J. H. (1981). Determination of earthquake source parameters from waveform data for studies of global and regional seismicity. *Journal of Geophysical Research*, *86*(B4), 2825–2852.
- Ekström, G., Nettles, M., & Dziewoński, A. M. (2012). The global CMT project 2004–2010: Centroid-moment tensors for 13,017 earthquakes. *Physics of the Earth and Planetary Interiors*, *200*, 1–9.
- England, P., Houseman, G., & Nocquet, J.-M. (2016). Constraints from GPS measurements on the dynamics of deformation in Anatolia and the Aegean. *Journal of Geophysical Research: Solid Earth*, *121*, 8888–8916.
- Jackson, J., & McKenzie, D. (1988). The relationship between plate motions and seismic moment tensors, and the rates of active deformation in the Mediterranean and Middle East. *Geophysical Journal International*, *93*(1), 45–73.
- Jolivet, R., Lasserre, C., Doin, M.-P., Guillaso, S., Peltzer, G., Dailu, R., et al. (2012). Shallow creep on the Haiyuan Fault (Gansu, China) revealed by SAR interferometry. *Journal of Geophysical Research: Solid Earth*, *117*, B06401. <https://doi.org/10.1029/2011JB008732>
- Jolivet, R., Lasserre, C., Doin, M.-P., Peltzer, G., Avouac, J.-P., Sun, J., & Dailu, R. (2013). Spatio-temporal evolution of aseismic slip along the Haiyuan Fault, China: Implications for fault frictional properties. *Earth and Planetary Science Letters*, *377*, 23–33.
- Jolivet, R., Simons, M., Agram, P. S., Duputel, Z., & Shen, Z.-K. (2015). Aseismic slip and seismogenic coupling along the central San Andreas Fault. *Geophysical Research Letters*, *42*, 297–306. <https://doi.org/10.1002/2014GL062222>
- Jolivet, R., Simons, M., Duputel, Z., Olive, J.-A., Bhat, H. S., & Bletery, Q. (2020). Interseismic loading of subduction megathrust drives long term uplift in northern Chile. *Geophysical Research Letters*, *47*, e2019GL085377. <https://doi.org/10.1029/2019GL085377>
- Jónsson, S., Zebker, H., Segall, P., & Amelung, F. (2002). Fault slip distribution of the 1999 Mw 7.1 Hector Mine, California, earthquake, estimated from satellite radar and GPS measurements. *Bulletin of the Seismological Society of America*, *92*(4), 1377–1389.
- Kaneko, Y., Avouac, J.-P., & Lapusta, N. (2010). Towards inferring earthquake patterns from geodetic observations of interseismic coupling. *Nature Geoscience*, *3*(5), 363–369.



- Le Pichon, X., & Kreemer, C. (2010). The Miocene-to-Present kinematic evolution of the eastern Mediterranean and Middle East and its implications for dynamics. *Annual Review of Earth and Planetary Sciences*, *38*, 323–351.
- Loveless, J. P., & Meade, B. J. (2011). Spatial correlation of interseismic coupling and coseismic rupture extent of the 2011  $M_w = 9.0$  Tohoku-oki earthquake. *Geophysical Research Letters*, *38*, L17306. <https://doi.org/10.1029/2011GL048561>
- Mahmoud, Y., Masson, F., Meghraoui, M., Cakir, Z., Alchalbi, A., Yavasoglu, H., et al. (2013). Kinematic study at the junction of the East Anatolian fault and the Dead Sea Fault from GPS measurements. *Journal of Geodynamics*, *67*, 30–39.
- Mansinha, L., & Smylie, D. E. (1971). The displacement fields of inclined faults. *Bulletin of the Seismological Society of America*, *61*(5), 1433–1440.
- Marinkovic, P., & Larsen, Y. (2013). Consequences of long-term ASAR local oscillator frequency decay—An empirical study of 10 years of data. In *Living Planet Symposium*, European Space Agency Edinburgh, Frascati.
- Maurer, J., & Johnson, K. (2014). Fault coupling and potential for earthquakes on the creeping section of the central San Andreas fault. *Journal of Geophysical Research: Solid Earth*, *119*, 4414–4428. <https://doi.org/10.1002/2013JB010741>
- Meade, B. J., & Loveless, J. P. (2009). Block modeling with connected fault-network geometries and a linear elastic coupling estimator in spherical coordinates. *Bulletin of the Seismological Society of America*, *99*(6), 3124–3139.
- Metois, M., Vigny, C., & Socquet, A. (2016). Interseismic coupling, megathrust earthquakes and seismic swarms along the Chilean subduction zone (38–18 s). *Pure and Applied Geophysics*, *173*(5), 1431–1449.
- Minson, S. E., Simons, M., & Beck, J. L. (2013). Bayesian inversion for finite fault earthquake source models I—Theory and algorithm. *Geophysical Journal International*, *194*(3), 1701–1726.
- Moreno, M., Rosenau, M., & Oncken, O. (2010). 2010 Maule earthquake slip correlates with pre-seismic locking of Andean subduction zone. *Nature*, *467*(7312), 198–202.
- Nalbant, S. S., McCloskey, J., Steacy, S., & Barka, A. A. (2002). Stress accumulation and increased seismic risk in eastern Turkey. *Earth and Planetary Science Letters*, *195*(3–4), 291–298.
- Nocquet, J.-M. (2012). Present-day kinematics of the mediterranean: A comprehensive overview of GPS results. *Tectonophysics*, *579*, 220–242.
- Nocquet, J.-M. (2018). Stochastic static fault slip inversion from geodetic data with non-negativity and bound constraints. *Geophysical Journal International*, *214*(1), 366–385.
- Nocquet, J.-M., Calais, E., Altamimi, Z., Sillard, P., & Boucher, C. (2001). Intraplate deformation in western Europe deduced from an analysis of the international terrestrial reference frame 1997 (ITRF97) velocity field. *Journal of Geophysical Research*, *106*(B6), 11,239–11,257.
- Nocquet, J.-M., Jarrin, P., Vallée, M., Mothes, P. A., Grandin, R., Rolandone, F., et al. (2017). Supercycle at the Ecuadorian subduction zone revealed after the 2016 Pedernales earthquake. *Nature Geoscience*, *10*(2), 145–149.
- Okada, Y. (1985). Surface deformation due to shear and tensile faults in a half-space. *Bulletin of the seismological society of America*, *75*(4), 1135–1154.
- Ozener, H., Arpat, E., Ergintav, S., Dogru, A., Cakmak, R., Turgut, B., & Dogan, U. (2010). Kinematics of the eastern part of the North Anatolian Fault Zone. *Journal of Geodynamics*, *49*(3–4), 141–150.
- Pousse-Beltran, L., Nissen, E., Bergman, E. A., Cambaz, M. D., Gaudreau, E., Karasözen, E., & Tan, F. (2020). The 2020  $M_w$  6.8 Elazığ (Turkey) earthquake reveals rupture behavior of the East Anatolian Fault. *Geophysical Research Letters*, *47*, e2020GL088136. <https://doi.org/10.1029/2020GL088136>
- Protti, M., González, V., Newman, A. V., Dixon, T. H., Schwartz, S. Y., Marshall, J. S., et al. (2014). Nicoya earthquake rupture anticipated by geodetic measurement of the locked plate interface. *Nature Geoscience*, *7*(2), 117–121.
- Ragon, T., Sladen, A., Bletery, Q., Vergnolle, M., Cavalié, O., Avallone, A., et al. (2019b). Joint inversion of coseismic and early postseismic slip to optimize the information content in geodetic data: Application to the 2009  $M_w$  6.3 L'Aquila earthquake, central Italy. *Journal of Geophysical Research: Solid Earth*, *124*, 10,522–10,543. <https://doi.org/10.1029/2018JB017053>
- Ragon, T., Sladen, A., & Simons, M. (2018). Accounting for uncertain fault geometry in earthquake source inversions—I: Theory and simplified application. *Geophysical Journal International*, *214*(2), 1174–1190.
- Ragon, T., Sladen, A., & Simons, M. (2019a). Accounting for uncertain fault geometry in earthquake source inversions—II: Application to the  $M_w$  6.2 Amatrice earthquake, central Italy. *Geophysical Journal International*, *218*(1), 689–707.
- Reilinger, R., & McClusky, S. (2011). Nubia-Arabia-Eurasia plate motions and the dynamics of Mediterranean and Middle East tectonics. *Geophysical Journal International*, *186*(3), 971–979.
- Reilinger, R., McClusky, S., Vernant, P., Lawrence, S., Ergintav, S., Cakmak, R., et al. (2006). GPS constraints on continental deformation in the Africa-Arabia-Eurasia continental collision zone and implications for the dynamics of plate interactions. *Journal of Geophysical Research*, *111*, B05411. <https://doi.org/10.1029/2005JB004051>
- Stein, R. S., Barka, A. A., & Dieterich, J. H. (1997). Progressive failure on the north anatolian fault since 1939 by earthquake stress triggering. *Geophysical Journal International*, *128*(3), 594–604.
- Sudhaus, H., & Sigurjón, J. (2009). Improved source modelling through combined use of InSAR and GPS under consideration of correlated data errors: Application to the June 2000 Kleifarvatn earthquake, Iceland. *Geophysical Journal International*, *176*(2), 389–404.
- Tan, O., Tapirdamaz, M. C., & Yörük, A. (2008). The earthquake catalogues for Turkey. *Turkish Journal of Earth Sciences*, *17*(2), 405–418.
- Tarantola, A., & Valette, B. (1982). Inverse problems = Quest for information. *Journal of Geophysics*, *50*(1), 159–170.
- Tatar, O., Poyraz, F., Gürsoy, H., Cakir, Z., Ergintav, S., Akpınar, Z., et al. (2012). Crustal deformation and kinematics of the eastern part of the north anatolian fault zone (Turkey) from GPS measurements. *Tectonophysics*, *518*, 55–62.
- Türkoğlu, E., Unsworth, M., Bulut, F., & Çağlar, I. (2015). Crustal structure of the North Anatolian and East Anatolian Fault Systems from magnetotelluric data. *Physics of the Earth and Planetary Interiors*, *241*, 1–14.
- USGS (2020). Finite fault model for the 01 24 2020  $M$  6.7 earthquake, Turkey. USGS finite-fault solution.
- Van Wijk, J., Axen, G., & Abera, R. (2017). Initiation, evolution and extinction of pull-apart basins: Implications for opening of the Gulf of California. *Tectonophysics*, *719*, 37–50.
- Wang, H., Liu, M., Ye, J., Cao, J., & Jing, Y. (2017). Strain partitioning and stress perturbation around stepovers and bends of strike-slip faults: Numerical results. *Tectonophysics*, *721*, 211–226.
- Wesnousky, S. G. (2006). Predicting the endpoints of earthquake ruptures. *Nature*, *444*(7117), 358–360.

## 5 Perspectives

À la suite des études présentées dans les paragraphes II.2 et II.3, j'ai soumis un projet ERC Starting Grant (EarthS<sup>3</sup>Fault) à l'appel d'offre 2018 dans lequel je projetais d'utiliser les équations présentées dans ces deux études pour estimer, le long de l'ensemble des grandes de failles de la planète, la distribution de  $\tau^c$ , mais également de  $\tau$ . On peut en effet combiner les équations (7) et (A6) de l'article du paragraphe II.3 pour obtenir l'expression du taux de chargement en contraintes  $\dot{\tau}$  suivante :

$$\dot{\tau} = \frac{\sin 2\delta + \tan 2\psi \cos 2\delta}{\tan 2\psi} \dot{\sigma}_{xz}. \quad (\text{II-1})$$

La loi de Hooke donne

$$\dot{\sigma}_{xz} = 2G\dot{\epsilon}_{xz}. \quad (\text{II-2})$$

$\dot{\epsilon}_{xz}$  étant une fonction du couplage, on peut exprimer  $\dot{\tau}$  en fonction du couplage, du pendage apparent  $\delta$  (lui-même fonction du pendage, de l'azimut et du rake, équation (5) de la partie II.3) et de l'orientation des contraintes  $\psi$  [Hardebeck, 2015]. L'idée était ensuite de collecter un maximum d'informations sur la sismicité historique mondiale (temps depuis le dernier séisme  $\Delta t$  et chute de contraintes  $\Delta\sigma$  associée en chaque point de chaque faille) pour tenter d'estimer

$$\tau \approx \tau^c - \Delta\sigma + \dot{\tau}\Delta t, \quad (\text{II-3})$$

puis d'introduire toutes ces contraintes dans des codes de simulations numériques pour tenter de prédire le comportement futur de chaque faille.

Le projet a été bien perçu et franchi la première phase. À l'issue de l'audition, le Jury a toutefois décidé de ne pas financer EarthS<sup>3</sup>Fault car il a jugé improbable que l'on puisse connaître assez bien les paramètres physiques en profondeur pour pouvoir utiliser des modèles à des fins prédictives. Après réception de cette décision, j'ai souscrit à ce point de vue. En particulier, la valeur de  $\psi$  est d'une importance capitale dans les calculs et son estimation n'est pas résolue très finement spatialement [Hardebeck, 2015]. J'ai ainsi abandonné cette piste de recherche pour me focaliser sur d'autres, en particulier sur l'utilisation de l'IA pour l'alerte rapide et la détection de signaux précurseurs, pistes qui m'ont mené à soumettre un second projet ERC Starting Grant (EARLI) à l'appel d'offre 2020, second projet qui a lui été financé et dont les premiers résultats seront présentés dans le Chapitre IV (quelques idées du projet seront également esquissées dans la partie III.4).

Je continue, en revanche, à travailler sur des problèmes d'inversion – notamment à partir de

## Chapitre II. Où se produisent les grands séismes ?

---

l'approche Bayésienne – pour imager le glissement lors des phases inter-sismique [[Jolivet et al., 2020](#)], mais également co-sismique [[Ragon et al., 2021](#)], post-sismique [[Ragon et al., 2019b](#)] et au cours d'épisodes transitoires [[Bletery and Nocquet, 2020](#)].

---

---

# Chapitre III

---

## Quand se produisent les grands séismes ?

### 1 Comment étudier la dynamique des grandes failles ?

Bien que nous ayons exploré des pistes intéressantes, nous avons vu qu'estimer où les grands séismes sont susceptibles de se produire est complexe. La question du « Où ? » est, toutefois, relativement accessible en comparaison de la question du « Quand ? ». Comment prédire quand vont se produire les prochains grands évènements ? Toutes les tentatives de réponse à cette question ont notoirement échoué.

La découverte des séismes lents – et de la micro-sismicité qui leur est associée – a ouvert la voie, à partir des années 2000 à un certain *monitoring* de l'activité des failles. L'étude de ces phénomènes permet en effet d'accéder à de l'information sur la dynamique des grandes failles. Lors de la phase inter-sismique, les failles ne sont pas « statiques », ou « figées » dans un état de couplage permanent. Elles présentent une dynamique complexe, observable par la géodésie (voir Chapitre I.2.3). Les propriétés des séismes lents renferment des informations sur les conditions physiques en profondeur. Les changements éventuels de ces propriétés au cours du temps indiquent une évolution des propriétés physiques en profondeur et pourraient potentiellement nous renseigner sur l'imminence d'un évènement. La micro-sismicité associée aux séismes lents apporte une information très riche, à haute résolution temporelle (les évènements micro-sismiques étant extrêmement nombreux). L'analyse de cette micro-sismicité peut ainsi servir à « mesurer » le glissement sur la faille en profondeur [Thomas *et al.*, 2018]. Plusieurs études ont même proposé que des séismes lents ont précédé des grands séismes (voir Chapitre I.3.3).

Les séismes lents et la micro-sismicité associée constituent ainsi une grande opportunité d'étudier la dynamique des grandes failles. Depuis leur découverte, des séismes lents ont été identifiés dans de nombreuses régions du monde [Obara and Kato, 2016]. Qu'est-ce qu'un séisme lent ? Comment le glissement évolue lors de l'évènement qui peut durer plusieurs semaines ?

Dans les deux études suivantes, nous avons cherché à observer les détails de la dynamique d'un séisme lent dans la région des Cascades pour répondre à ces questions.

## 2 Les fronts secondaires de glissement associés aux séismes lents

Le glissement lent sur la faille est généralement imagé par inversion de données GNSS. La résolution de ces données et les limites des techniques d'inversion conduisent à imager des distributions de glissement très lisses spatialement et temporellement. La micro-sismicité qui leur est associée présente, au contraire, une très bonne résolution temporelle et une assez bonne résolution spatiale. Si l'on fait l'hypothèse que tremors et LFEs sont les manifestations passives de la rupture de micro-aspérités déstabilisées par le glissement lent sous-jacent [*Shelly et al., 2007*], on peut considérer que là où l'on observe tremors et LFEs, il y a glissement lent, et ainsi avoir indirectement accès à une vision du glissement beaucoup mieux résolue que par inversion de données GNSS. Pour analyser la dynamique des séismes lents, nous avons ainsi, dans l'étude qui suit, identifié, de manière automatique, un grand nombre de migrations de tremors/LFEs le long de la faille de subduction des Cascades. Nous avons interprété ces migrations d'événements micro-sismiques comme les témoins de fronts de glissement lent secondaires – que nous avons nommé *Secondary Slip Fronts* (SSFs) – au sein des séismes lents. Nous avons ainsi mis en évidence que les séismes lents ont une dynamique spatio-temporelle très complexe, composée de nombreux sous-événements. Ces sous-événements, les SSFs, semblent par ailleurs – même si les approximations faites pour estimer leurs magnitudes sont susceptibles de biaiser les estimations vers ce résultat – obéir à la loi d'échelle proposée par *Ide et al. [2007]* (magnitude proportionnelle à la durée) pour les SSEs, les LFEs et les VLFEs (Figure I.6) dans une gamme de magnitude et de durée inaccessible à la géodésie et à la sismologie conventionnelles.

Cette étude a été réalisée à l'Université d'Oregon, en collaboration avec Amanda M. Thomas, Jessica C. Hawthorne, Robert M. Skarbak, Alan W. Rempel and Randy D. Krogstad. Elle a été publiée en 2017 dans le journal *Earth and Planetary Science Letters* [*Bletery et al., 2017b*].



# Characteristics of secondary slip fronts associated with slow earthquakes in Cascadia



Quentin Bletery<sup>a,\*</sup>, Amanda M. Thomas<sup>a</sup>, Jessica C. Hawthorne<sup>b</sup>, Robert M. Skarbak<sup>c</sup>, Alan W. Rempel<sup>a</sup>, Randy D. Krogstad<sup>a</sup>

<sup>a</sup> Department of Earth Sciences, University of Oregon, 1272 University of Oregon, Eugene, OR 97403, USA

<sup>b</sup> University of Leeds, School of Earth and Environment, Leeds, United Kingdom

<sup>c</sup> Lamont–Doherty Earth Observatory, Columbia University, Palisades, NY, USA

## ARTICLE INFO

### Article history:

Received 10 November 2016

Received in revised form 30 January 2017

Accepted 31 January 2017

Editor: P. Shearer

### Keywords:

slow slip  
low-frequency earthquakes  
nonvolcanic tremor  
secondary slip fronts  
Cascadia

## ABSTRACT

We implement an algorithm to automatically detect migrations of low frequency earthquakes at time scales between 30 min and 32 h during the 2003, 2004 and 2005 slow slip events in Cascadia. We interpret these migrations of seismicity as a passive manifestation of secondary slip fronts (SSFs) that propagate faster than the main front. We identify the dominant features of 383 SSFs, including time, location, duration, area, propagation velocity and estimate: their moment, stress drop, slip, and slip rate. We apply the same algorithm to continuous tremor detection in Cascadia between 2009 and 2015 and characterize 693 SSFs at time scales between 4 h and 32 h. We identify – to our knowledge for the first time – numerous 11–22.5 h long SSFs that propagate at velocities intermediate between slow slip events and previously reported SSFs. The systematic detection of SSFs fills a gap between seismically and geodetically detectable slow earthquake processes. Analysis of SSF basic features indicates a wide range of stress drops and slip rates (with medians of 5.8 kPa and 1.1 mm/h) as well as an intriguing relationship between SSF direction and duration that was observed in other contexts and could potentially help discriminate between the different physical models proposed to explain slow slip phenomena.

© 2017 Elsevier B.V. All rights reserved.

## 1. Introduction

Slow slip events (SSEs) in subduction zones propagate along the plate interface at velocities of 5–10 km/day and are largely confined to the region known as the transition zone, located down-dip of the seismogenically locked zone (Dragert et al., 2001; Bartlow et al., 2011). As SSEs propagate, small on-fault asperities capable of generating seismic radiation fail in earthquake-like events known as low-frequency earthquakes (LFEs) and nonvolcanic tremor (Obara, 2002; Kao et al., 2006; Ide, 2010; Ueno et al., 2010; Houston et al., 2011). Multiple lines of evidence indicate that LFEs and tremor – which has been interpreted as a superposition of LFEs (Shelly et al., 2007b) – are a passive manifestation of surrounding aseismic slow slip (Shelly et al., 2007b). The occurrence of LFEs and tremor during SSEs are not random. Instead, spatially and temporally coherent migrations of LFEs and tremor can often be identified within the actively slipping portion of the fault after the main slip front associated with the SSE has passed. These

migration patterns are thought to represent secondary slip fronts (SSFs) occurring over several different lengths and timescales. For example, Houston et al. (2011) and Royer et al. (2015) used tremor and LFEs to image approximately 40 km long slip fronts – known as rapid tremor reversals (RTRs) – that propagate back in the opposite direction but 10 to 40 times faster than the main slip front. Ghosh et al. (2010) used tremor in Cascadia to image seismic migrations – known as streaks – that propagate back and forth along the main slip front (i.e., perpendicular to its propagation direction) but approximately 100 times faster. Rubin and Armbruster (2013) reported tremor migrations at the kilometer scale that propagate along strike either towards or away from the main front, but approximately ten times faster. Finally, Peng et al. (2015a) and Peng and Rubin (2016) found evidence for complex tremor migration patterns that evolve as the main front propagates. While all of the aforementioned studies were conducted in Cascadia, similar observations have been reported in Japan (Shelly et al., 2007a; Ueno et al., 2010; Obara et al., 2012), Mexico (Radiguet et al., 2012; Frank et al., 2014; Peng and Rubin, 2017) and along the San Andreas fault (Ryberg et al., 2010; Shelly, 2009, 2010; Peng et al., 2015b), suggesting that SSFs may be a ubiquitous feature of slow slip.

\* Corresponding author.

E-mail address: qbletery@uoregon.edu (Q. Bletery).



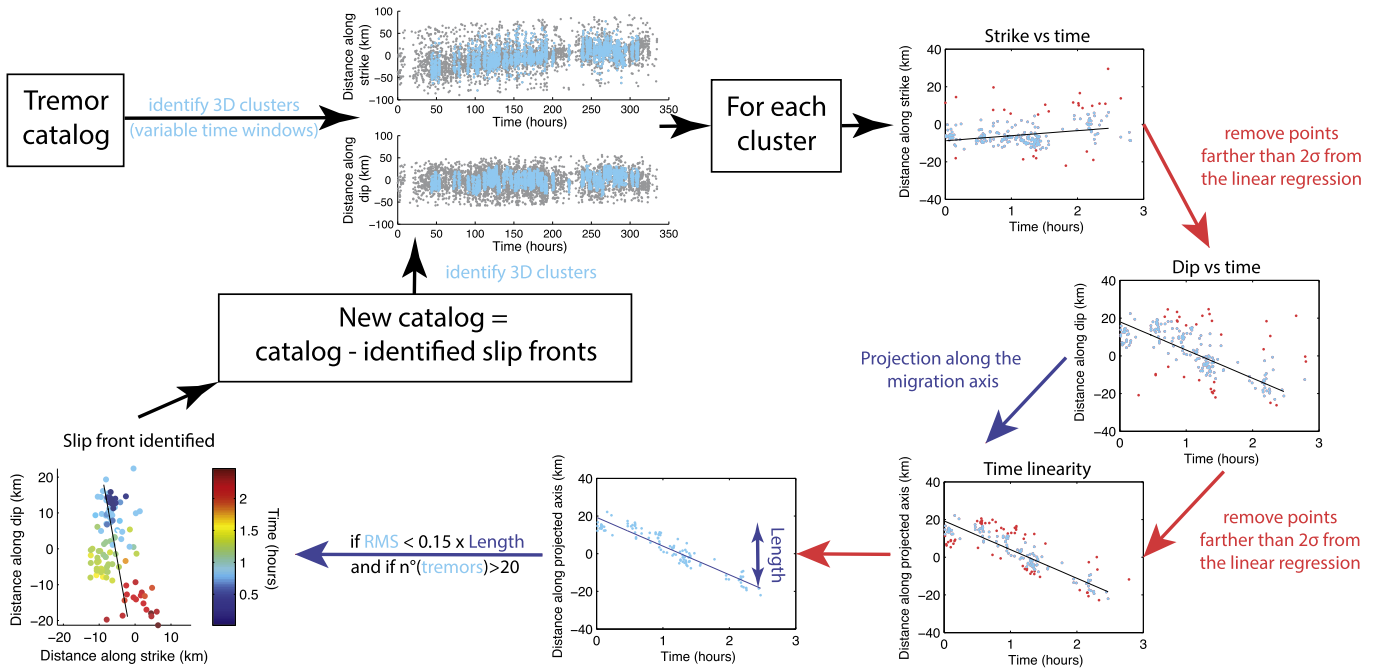


Fig. 1. Algorithm scheme. See main text for description.

Slow-slip phenomena require the fault slip rate to increase to observed speeds, typically 10 to 100 times the plate rate, but abstain from accelerating to typical earthquake slip rates. The specific physical mechanisms responsible for imposing this speed limit are still debated. SSFs generally propagate at least an order of magnitude faster than the main front associated with the SSE, and estimates of the ratio of the SSF stress drop to that of the main front range between one tenth and one (Rubin and Armbruster, 2013; Royer et al., 2015; Hawthorne et al., 2016). These stress drop estimates combined with the propagation speeds mentioned above imply that SSFs must be slipping either as fast as or faster than the main front. Hence, reproducing stress drops, slip and propagation speeds of both the main and secondary fronts requires a rheology that limits the speed of the main front while allowing the SSFs to slip one to two orders of magnitude faster. Such behavior is difficult to reproduce with a single state variable friction law (Rubin, 2011). Additionally, SSFs appear to be sensitive to very small ( $\approx 1$  kPa) tidal stress perturbations (Thomas et al., 2013; Royer et al., 2015; Houston, 2015) allowing them to be used to probe in situ conditions in deep faults. Observations of SSFs, in addition to SSEs, may provide useful constraints on physical models of slow slip processes (Rubin, 2011; Hawthorne and Rubin, 2013).

To date, most studies that have documented SSFs have relied on subjective identification methods such as visual identification, often using only one dimension of space and time (Shelly et al., 2007a; Ueno et al., 2010; Ghosh et al., 2010; Houston et al., 2011; Rubin and Armbruster, 2013; Royer et al., 2015; Peng et al., 2015a; Savard and Bostock, 2015). While these approaches successfully find some SSFs, such subjective identification makes it possible and even likely that many SSFs go undetected. Here we develop an algorithm that systematically identifies SSFs based on spatial and temporal migration of tremor/LFEs and discuss its advantages compared to the similar method developed by Obara et al. (2012). We apply our algorithm to both tremor and LFE datasets resulting from SSEs that occurred between 2003 and 2015 in Cascadia. We detect over 1000 SSFs, determine their locations, duration, directions, and estimate some of their physical properties, such as moment, average slip, stress drop and slip rate.

## 2. Data and algorithm

We use two types of data: a catalog of LFEs located near Vancouver Island during the 2003, 2004 and 2005 SSEs (Savard and Bostock, 2015) and a catalog of continuous tremor detections from August 2009 to December 2015 that occur throughout the Cascadia subduction zone (Wech and Creager, 2008; Wech, 2010). The LFE catalog was obtained using cross-station waveform correlation; thanks to a dense campaign seismic network, it has very good spatial (location errors of  $< 1$  km) and temporal resolution (Savard and Bostock, 2015). The tremor catalog contains locations and detection times of tremor events determined using waveform envelope correlation and clustering (Wech and Creager, 2008; Wech, 2010). Detections correspond to 5-minute seismogram windows that likely represent a superposition of LFEs (Shelly et al., 2007b). Therefore, resolution of both time (each detection is separated by at least 2.5 min) and location (5–10 km) is worse than for the LFE catalog. Because the tremor detection algorithm is independently implemented on several adjacent seismic networks, some tremor detections appear twice in the final catalog (Wech, 2010). To eliminate duplicate detections, when two tremors are detected at the same time within 25 km, we exclude one (Wech, 2010).

These two catalogs provide a large number of identified LFE and tremor events. To identify possible SSFs, we analyze LFE and tremor migration patterns in 3 dimensions: distance along strike, distance along dip, and time. The algorithm is illustrated in Fig. 1. As in the approach of Obara et al. (2012), we look for SSFs in time windows of various durations. The different time windows considered in our analysis are 30 min, 1 h, 2 h, 4 h, 8 h, 16 h, 32 h for the LFE catalog and 4 h, 8 h, 16 h, 32 h for the tremor catalog. As individual detections in the tremor catalog are all separated by at least 2.5 min (Wech and Creager, 2008), the number of potential detections in a  $\leq 2$  h time window is too small to analyze their potential migration. The analysis is performed independently on the different time windows. Therefore, tremor/LFE detections may theoretically be part of more than one SSF in different time windows; thus a short duration SSF may be a part of a longer duration SSF.

We first identify clusters of LFE and tremor detections in the individual catalogs. We use the `subclust` Matlab routine to identify

LFE/tremor clusters of different durations. The subclust routine estimates the centers of subclusters of a given duration in a data set using subtractive clustering (Chiu, 1994; Yager and Filev, 1994). We set the duration of the subclusters to correspond to the different time windows. The subclust routine then returns the tremor/LFE clusters of 30 min to 32 h duration with the highest concentration of events. For each identified cluster, we then calculate the linear regression of the distance along strike as a function of time and exclude points farther than two standard deviations ( $2\sigma$ ) from the regression line. After removing those points, we do the same linear regression but for the distance along dip as a function of time and remove events farther than  $2\sigma$  from the linear regression. Finally, we project the remaining points along the best-fitting migration axis and remove again events that lie outside  $2\sigma$  from the linear regression of the distance along the migration axis as a function of time. The remaining points are then tested: if the cluster still contains more than 20 LFE or tremor detections and if the root mean square (RMS) of their distance to the last regression is smaller than 15% of the migration length, then the cluster is identified as an SSF. For a given time window, if the SSF length is small, then the front is not moving quickly (the signal is low). Thus we require the deviation from the propagation axis (the noise) to be very low (to ensure a decent signal to noise ratio). If the SSF length is larger, then the front is clearly moving (the signal is larger) and we can be more tolerant with the deviation from the propagation axis (as we have a clear signal). We repeat the process for all the clusters. We then remove the LFE or tremor detections identified as part of an SSF from the catalog and rerun the clustering routine on the new catalog with identified SSFs removed. We iterate until the catalog no longer contains any LFE or tremor. If no SSF is identified on one iteration, we remove all the tested clusters from the catalog and iterate once more in the truncated catalog. All the detected SSFs are then tested to ensure that each SSF is continuous rather than composed of two distinct SSFs. We subdivide the successfully identified SSFs into 4 equal portions along their best-fitting migration axis and 3 equal periods and if one of the parts or periods contains less than 1/20th of the number of LFE/tremor detections that compose the SSF, the SSF is rejected.

Our approach is inspired by Obara et al. (2012) (who implemented an automatic SSF detection based on principal component analysis of tremor in Japan), but has some significant differences. Obara et al. (2012) identified SSFs using moving time windows shifted by discrete increments. As it is unlikely that SSFs all start and end at the specific times of arbitrary time windows, this may result in detecting SSFs that either are just a part of a larger undetected SSFs or include LFE/tremor that should not be associated with the SSF, potentially affecting the apparent migration velocities. The use of a clustering subroutine allows for flexibility in the start and end time of the explored SSFs – as tested time windows are not shifted by discrete increments but determined in respect of high concentrations of tremor/LFEs – substantially increasing the number of SSF detections. Another significant difference is the detection thresholds. In the work of Obara et al. (2012), SSF acceptance is based on linearity, angular difference and in the number of tremor detections, all of which vary with the given time window. We apply only two thresholds, which are the same for all time windows: the number of LFE/tremor detections (20 for all time windows) and a deviation criteria based on the ratio of the misfit to the SSF length (required to be  $\leq 15\%$ ), which can be interpreted as a signal to noise ratio. Our choices of 20 LFE/tremor detections and 15% are arbitrary – as are the thresholds used by Obara et al. (2012) – but these values do provide visually coherent patterns in all the detected SSFs (Figs. 2, 3).

To ensure that our algorithm does not interpret noise as SSF, we test it on synthetic catalogs. To produce the synthetic catalogs,

we use the actual catalog locations and randomize the time of occurrence. We run the algorithm for all the time windows of our analysis and detect no SSF in the synthetic catalogs.

### 3. Spatial distribution of secondary slip fronts

We identified 383 SSFs in the LFE catalog of the 2003, 2004, and 2005 SSEs beneath Vancouver Island and 693 SSFs in the tremor catalog between August 2009 and December 2015 in Cascadia. While SSFs lasting from 10 min to 11 h have been documented in multiple subduction zones (Ghosh et al., 2010; Houston et al., 2011; Obara et al., 2012; Rubin and Armbruster, 2013; Royer et al., 2015; Peng et al., 2015a; Savard and Bostock, 2015), we identified – to our knowledge for the first time – numerous SSFs lasting between 11 and 22.5 h in both catalogs (243 in the tremor catalog, 57 in LFEs catalog). They propagate at intermediate speeds ( $\approx 3$  km/h) between those of the main front ( $\approx 0.2$ – $0.5$  km/h) and previously documented SSFs ( $\approx 40$  km/h) (Ghosh et al., 2010; Houston et al., 2011; Obara et al., 2012; Rubin and Armbruster, 2013; Royer et al., 2015; Peng et al., 2015a; Savard and Bostock, 2015).

The spatial distribution of SSFs is of particular interest because it can reveal atypical behaviors of some fault areas and may highlight spatial variations of fault properties. Fig. 4 shows the distribution of tremor derived SSFs during the 2009–2015 period along the Cascadia megathrust by time window. Note that some long duration tremor derived SSFs may correspond to the main front of short duration SSEs. In the inset diagrams we plot the number of SSFs as a function of their propagation directions. Some areas show a clear tendency to host numerous SSFs (for instance at latitude  $40^\circ\text{N}$ – $41.5^\circ\text{N}$ ,  $42^\circ\text{N}$ – $42.5^\circ\text{N}$ , or  $44.5^\circ\text{N}$ – $45.5^\circ\text{N}$ ) whereas other regions had no detectable SSFs. Additionally, there is a clear preference for along-strike propagation for the majority of the tremor derived SSFs. Both the spatial distribution and propagation directions are consistent from SSE to SSE, suggesting that the physical mechanism responsible for generating SSFs does not change over a timescale of several years.

Because both the temporal and spatial resolution are much better in the LFE catalog, we are able to detect short timescale SSFs beneath Vancouver island (Fig. 5). Since the 3 SSEs that drove LFEs in this area all roughly propagated in the same direction (blue arrow in Fig. 5), this catalog is also more convenient to analyze the direction of SSFs with respect to the direction of SSEs. SSFs propagate in all directions and encompass phenomena previously described as RTRs or streaks. They also encompass slip fronts that propagate in the direction of the SSE (Fig. 5). Such forward-propagating SSFs are hard to distinguish by eye from LFE or tremor migration associated with the main front. They typically initiate after the main front has passed and migrate towards the tip of the main front. Interestingly, we observe a clear relationship between the direction and the duration of SSFs. The vast majority of short duration (i.e. 30 min and 1 h) SSFs propagate along dip. As the SSF duration increases, the proportion of SSFs propagating along strike gradually increases (see Rose diagrams in Fig. 5) resulting in the longest duration LFE derived SSFs propagating almost solely along strike. Similar relationships were observed by Ghosh et al. (2010) and Houston et al. (2011) in Cascadia and by Obara et al. (2012) beneath the Kii peninsula in the Nankai subduction zone. Potential physical mechanisms responsible for SSFs will have to explain this enigmatic dependence between duration and direction (Rubin, 2011). The ratio of along-strike SSFs propagating in the SSE direction to along-strike SSFs propagating in the opposite direction also seems to depend on the duration. While reversal SSFs are predominant in the 8 h time window, almost all SSFs propagate forward in the 32 h time window.

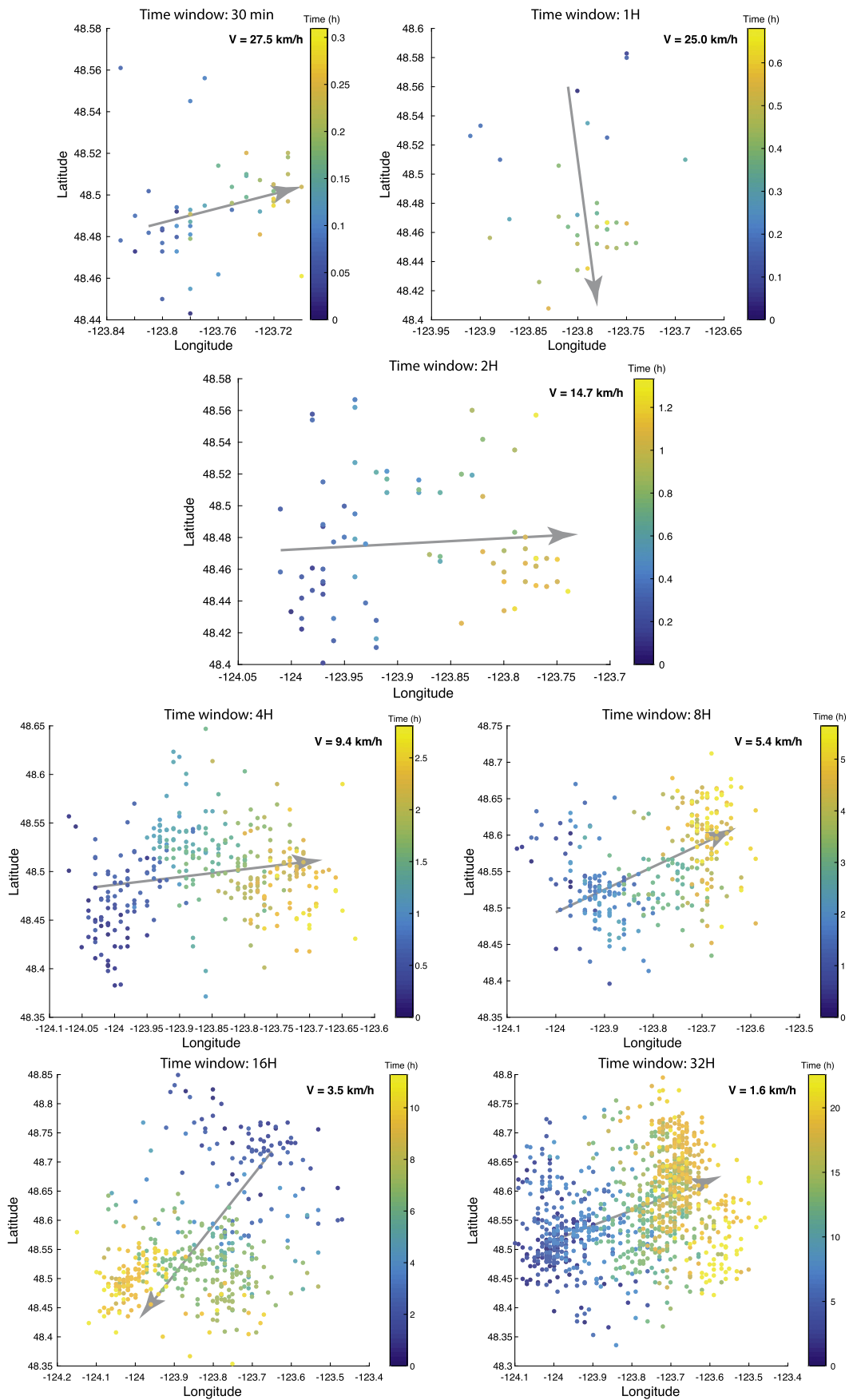
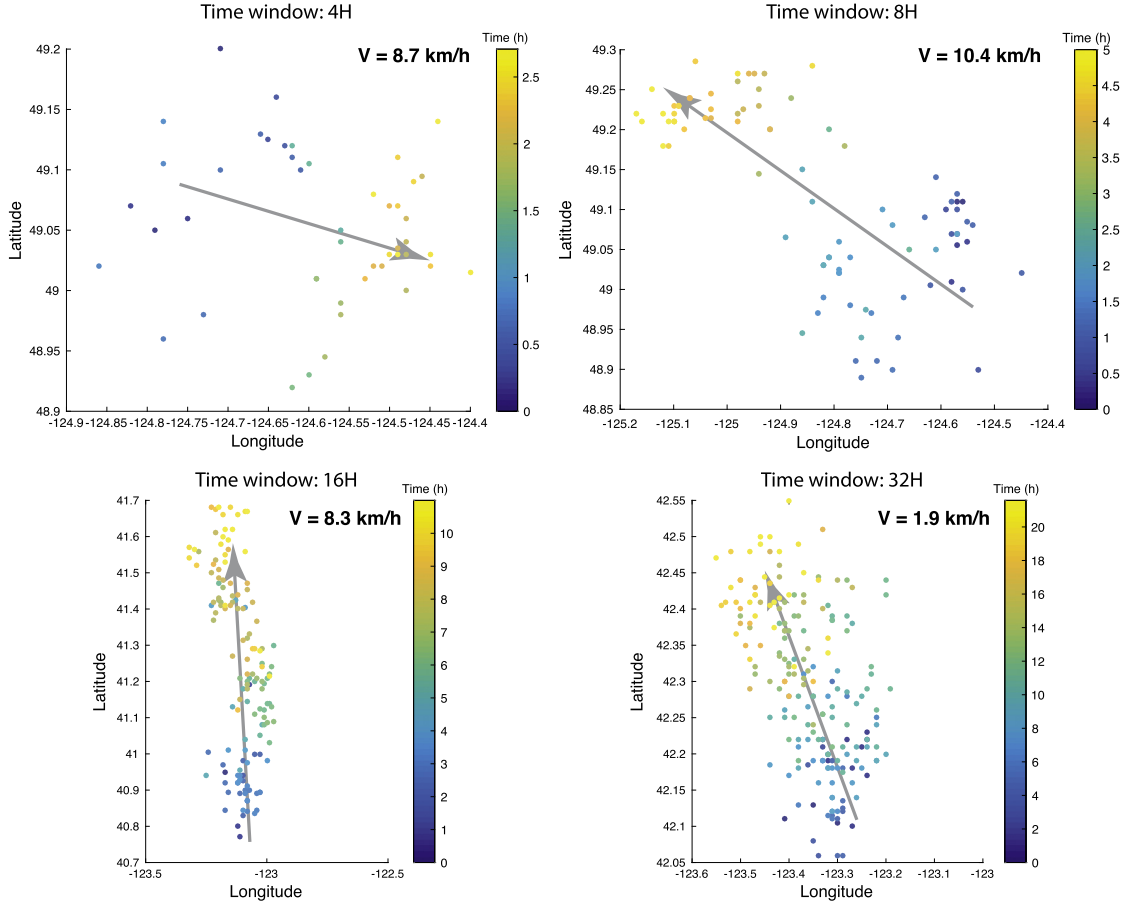


Fig. 2. Examples of SSFs detected in the LFE catalog for the different time windows of our analysis. Grey arrows show SSF direction determined by the algorithm.



**Fig. 3.** Examples of SSFs detected in the tremor catalog for the different time windows of our analysis. Grey arrows show SSF direction determined by the algorithm.

The distribution of propagation velocity  $V_{prop}$  is shown at the bottom of each subfigure in Figs. 4 and 5. In individual time windows, along-dip SSFs do not appear faster than along-strike SSFs. However, as the length  $L$  of SSFs is limited by the extent of the fault, the average propagation velocity decreases with the duration  $T$  (because  $V_{prop} = L/T$ ). Accordingly, the limited number of distinct time windows in the analysis of the tremor catalog results in little difference in the propagation velocity (Fig. S1f).

#### 4. Physical characteristics of secondary slip fronts

Our detection algorithm provides a number of direct observations characterizing each SSF including start time, location, direction (Figs. 4, 5), duration  $T$ , length  $L$ , width  $W$ , pulse (i.e. actively slipping) length  $l$  (Fig. 6), propagation velocity  $V_{prop}$  (defined as  $L/T$ ), and number of LFE or tremor detections  $n_e$ . The distributions of these SSF properties are shown in Fig. S1 (catalogs are available in the supplementary materials). Assessing other physical characteristics of SSFs, such as moment or stress drop, is challenging because these quantities require an estimate of the total slip associated with each SSF.

Individual SSFs are too small to generate a surface deformation signal detectable with GPS and hence most studies that have estimated slip for individual SSFs have relied on the total SSE moment and the fraction of LFE detections or bursts that occurred as part of the SSF (Rubin and Armbruster, 2013; Royer et al., 2015). Here, we adopt a similar approach and assume that the total moment  $M_e$  associated with each LFE or tremor detection is the same (although different for LFEs and tremor). This assumption is demonstrably false for individual LFE repeats, which have been shown to have very different moments (Bostock et al.,

2015), and for individual tremor events, as their definition (i.e. the 2.5 min timescale used to separate individual events) is arbitrary and includes no contribution from waveform amplitudes (Wech and Creager, 2008). However, since moment estimates for each SSF include a minimum of 20 LFEs or tremors, it is likely that the average moment will be a more accurate measure of total SSF moment. Nevertheless, our estimates of the physical characteristic of SSFs (such as moment, slip, stress drop, slip rate) are tentative and caution should be exercised when interpreting them.

We obtain  $M_e$ , the average moment associated with each LFE or tremor, by dividing the moment  $M_0$  (assessed by geodetic studies Schmidt and Gao, 2010; Krogstad and Schmidt, 2015) associated with an SSE by the number of events  $N_e$  detected during the event:

$$M_e = \frac{M_0}{N_e}. \quad (1)$$

An implicit assumption behind equation (1) is that moment associated with aseismic slip that does not generate LFE or tremor detections is negligible. The moment,  $M_{SSF}$ , associated with one SSF, is defined as the sum of the moment associated with all the LFE or tremor detections that are part of that SSF,

$$M_{SSF} = \sum_{i=1}^{n_e} M_e(i), \quad (2)$$

where  $n_e$  is the number of LFE/tremor detections part of the given SSF. As we assumed that for all  $i$ ,  $M_e(i) = \frac{M_0}{N_e}$ ,

$$M_{SSF} = \frac{n_e}{N_e} M_0. \quad (3)$$



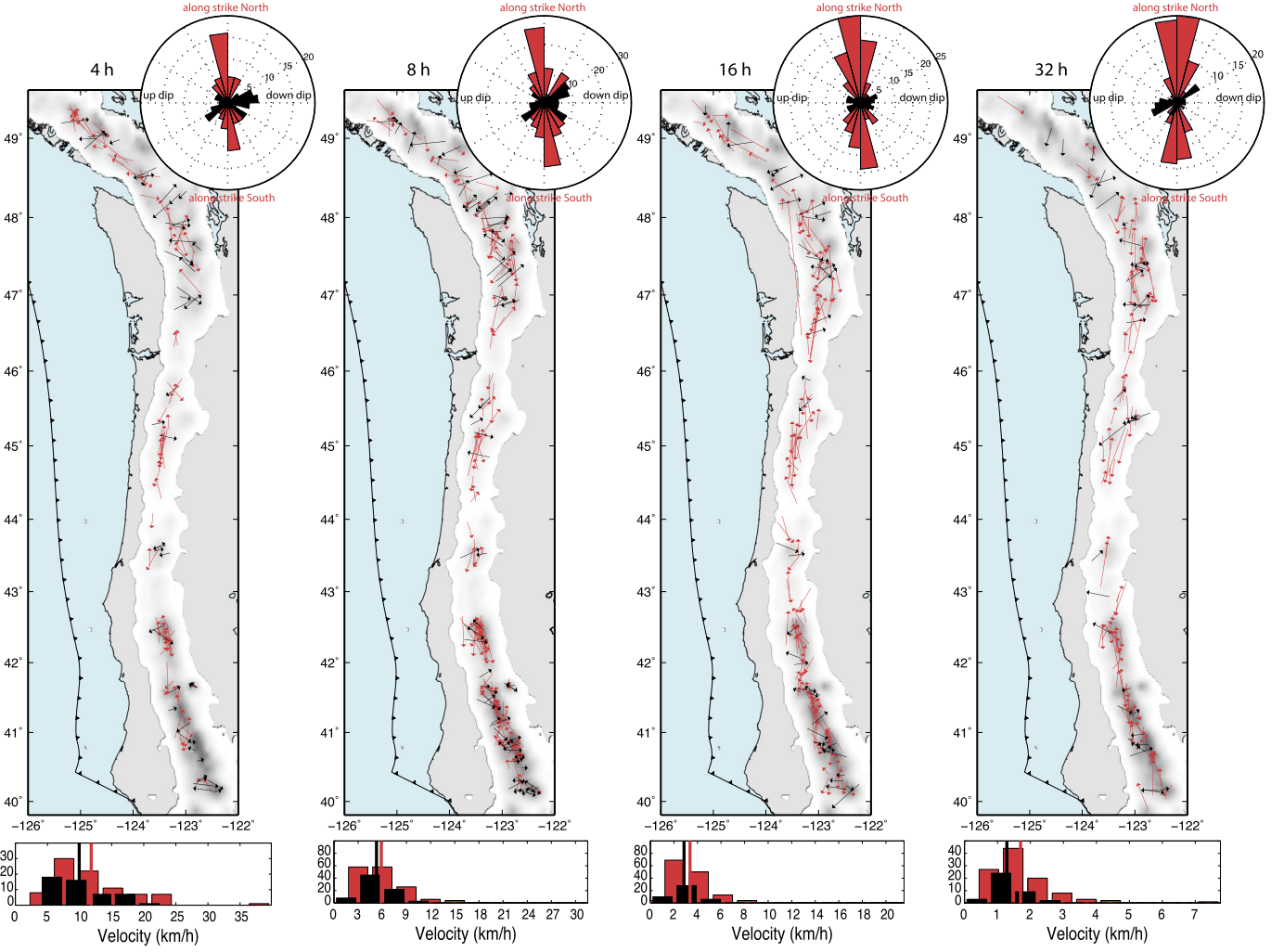


**Fig. 4.** Detected secondary slip fronts in Cascadia from August 2009 to December 2015 for time windows of 4 h, 8 h, 16 h and 32 h (tremor catalog). White to gray color scale indicates the density of tremor detections. Arrows show lengths and directions of the SSFs propagating along strike (red) and along dip (black). Rose diagrams show the number of SSFs in the different directions. Histograms show velocity distributions for SSFs propagating along strike (red) and along dip (black). Red and black vertical lines superimposed on histograms show average velocity for SSFs propagating along strike and along dip, respectively.

Note that possible deviations from constant  $M_e(i)$  would tend to be averaged out over the number of events in equation (3) because  $M_e(i)$  is sometimes larger and sometimes smaller than the assumed average  $M_e = \frac{M_0}{N_e}$ . We further estimate an average slip  $d$  for each SSF,

$$d = \frac{M_{SSF}}{\mu A}, \quad (4)$$

where  $\mu$  is the shear modulus and  $A = WL$  is the SSF slip area, with the SSF width  $W$  and length  $L$  both estimated from our analysis (Fig. 6). To be consistent with geodetic inversions, we use  $\mu = 40$  GPa (Schmidt and Gao, 2010; Krogstad and Schmidt, 2015). The stress drop  $\Delta\sigma$  is then given by

$$\Delta\sigma = \frac{4(\lambda + \mu)}{\pi(\lambda + 2\mu)} \mu \frac{d}{W}, \quad (5)$$

where  $\lambda$  is Lamé’s parameter (Lay and Wallace, 1995), which we set to  $\lambda = 40$  GPa. The total slip  $d$  accumulates in the time the front propagates the distance  $l$ . Thus, we can deduce the slip rate  $V_{slip}$  from the propagation velocity  $V_{prop}$  as

$$V_{slip} = \frac{d}{l} V_{prop}. \quad (6)$$

The distributions of assessed physical characteristics (moment, slip, stress drop and slip rate) are shown in Figs. S2 and S3 (catalogs in the supplementary materials). Because we did not estimate these parameters independently, their distributions are correlated with each other (Fig. S4). However, most of the correlation coefficients between the different parameters are relatively weak (i.e. below 0.6 in magnitude, see Fig. S4). As expected, high correlation coefficients are found for slip and stress drop, since the stress drop is estimated from slip (eq. (5)), and between the different spatial dimensions ( $L$ ,  $W$  and  $l$ ), implying that the aspect ratios of SSFs do not vary appreciably. Significant anticorrelations are observed between propagation rate  $V_{prop}$  and duration  $T$ , as well as between the spatial dimensions and both slip  $d$  and slip rate  $V_{slip}$ . It is also noteworthy that stress drop  $\Delta\sigma$  appears to be independent of moment  $M$  in both catalogs (Fig. S4).

The median stress drop among all SSFs is 5.8 kPa, which is very consistent with stress drop estimates obtained for RTRs using strainmeters (8 kPa) (Hawthorne et al., 2016). These values of stress drop are several times smaller than typical stress drops in SSEs (10–100 kPa), and over 2 orders of magnitude smaller than regular earthquakes (Gao et al., 2012). The estimated stress drops are also all consistently smaller than effective normal stress (0.2–3 MPa) inferred in LFE source regions (Liu and Rice, 2007; Hawthorne and Rubin, 2013; Royer et al., 2015). The median slip

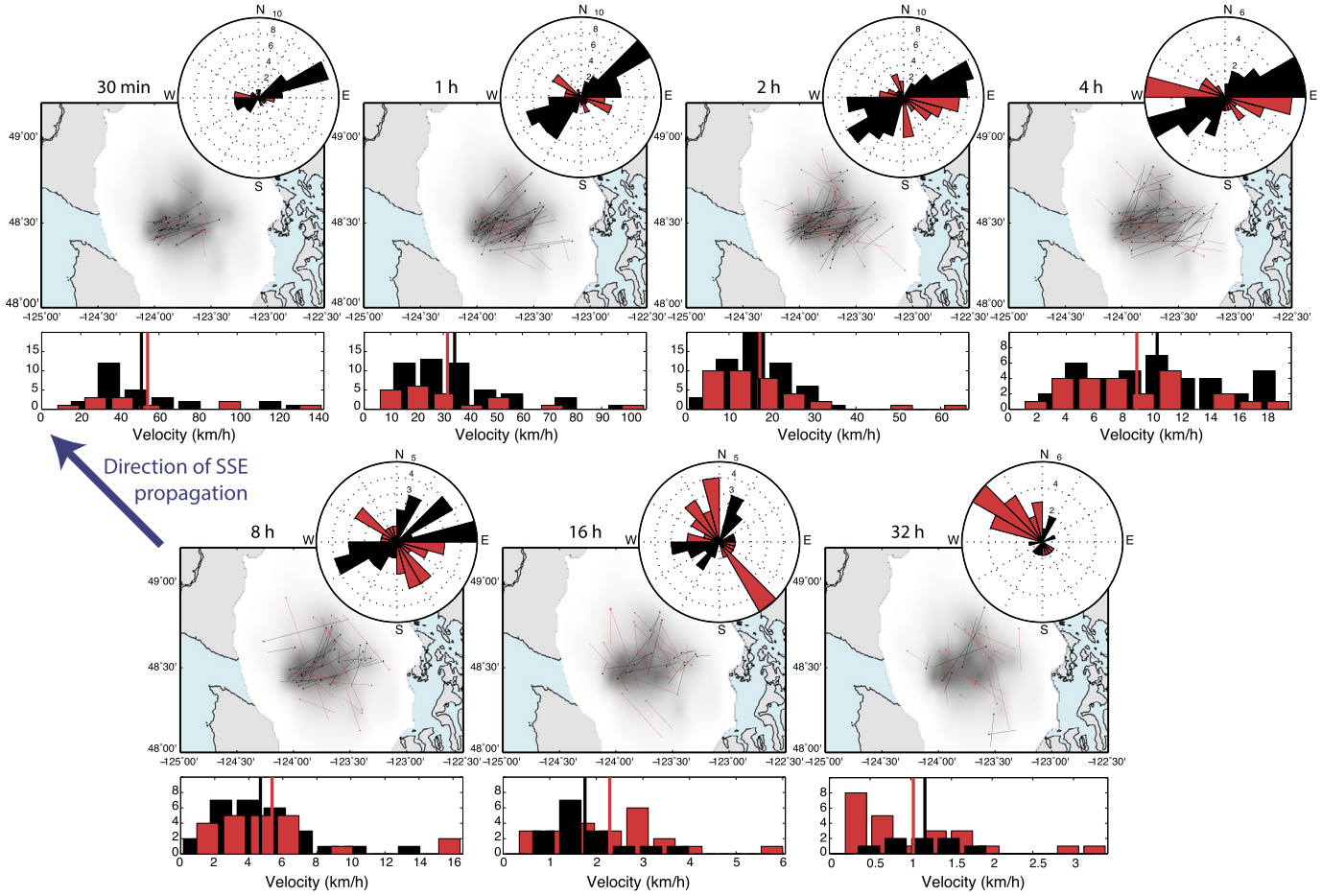


**Fig. 5.** Detected secondary slip fronts during the 2003, 2004 and 2005 SSEs for time windows of 30 min, 1 h, 2 h, 4 h, 8 h, 16 h and 32 h (LFE catalog). White to gray color scale indicates the relative density of LFEs. Blue thick arrow shows the approximate direction of the three SSEs ( $45^\circ$  west from north). Red arrows show lengths and directions of SSFs propagating in the direction of SSE propagation  $\pm 45^\circ$  (along strike). Black arrows show lengths and directions of SSFs propagating perpendicular to the direction of SSE propagation  $\pm 45^\circ$  (along dip). Rose diagrams show the number of SSFs in the different directions. Histograms show velocity distributions for SSFs propagating along strike (red) and along dip (black). Red and black vertical lines superimposed on histograms show average velocity for SSFs propagating along strike and along dip, respectively. (For interpretation of the references to color in this figure legend, the reader is referred to the web version of this article.)

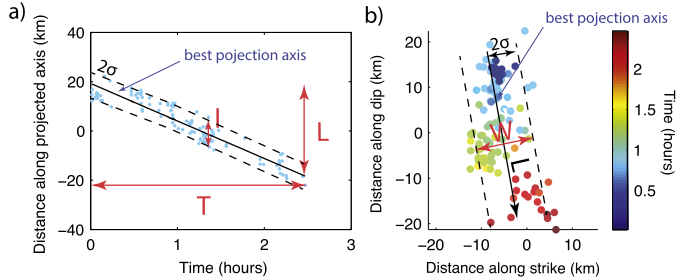


**Fig. 6.** Scheme illustrating how SSF length ( $L$ ), width ( $W$ ), and pulse length ( $l$ ) are deduced from the analysis.  $L$  is defined as the length of the best projection axis (parallel to the propagation direction) (a and b).  $l$  is defined as the  $2\sigma$  dispersion from the linear regression of the distance along the best projection axis as a function of time (a).  $W$  is defined as the  $2\sigma$  spatial dispersion (perpendicular to the propagation direction) from the best projection axis (b).

is 3 mm and the median slip rate is 1.1 mm/h, which is much faster than slip rates inferred for SSEs (on the order of 1–2 mm/day Wech and Bartlow, 2014). The observation that SSF slip rates are significantly faster than SSE slip rates is consistent with previous studies (Rubin and Armbruster, 2013; Royer et al., 2015; Hawthorne et al., 2016) and implies that the fault rheology limits the main front speed and then allows secondary fronts to slip faster. As acknowledged in the introduction, such a time dependent behavior is not easy to reproduce with a single state variable

friction law (Rubin, 2011). SSF slip rates may then be used to constrain physical models of slow slip phenomena.

Though variations in the moments and slip distributions of SSFs range within a single order of magnitude ( $4.10^{16}$  to  $4.10^{17}$  N.m and 0.1 to 40 mm) for all SSFs, stress drop varies by over 3 orders of magnitude (from 0.1 to 300 kPa), as does slip rate (between 0.02 and 30 mm/h) (Figs. S2 and S3). We recall here that our estimates of stress drop are based on the original assumption that SSF moment scales with the number of LFE/tremor detections, which could be inaccurate for some SSFs. Large scatter in slip, stress drop and slip rate is also expected from equations (4), (5) and (6) as a result of multiplying quantities ( $M_{SSF}$ ,  $L$ ,  $W$ ,  $l$  and  $V_{prop}$ ) that have large variability. Therefore a large part of the scatter in slip rate and stress drop might be attributed to assumption inaccuracy and propagation of uncertainties, but some of this scatter could also be sourced to changes in fault properties. As SSF areas widely overlap – this is particularly clear in the LFE catalog (Fig. 5) – the varying SSF properties might suggest that, in addition to being able to slip at different rates, the same fault area is also able to release very different amounts of stress.

## 5. Moment–duration scaling

Ide et al. (2007) suggested that slow slip phenomena – including LFEs, very low frequency earthquakes (VLFEs) and SSEs – follow a moment–duration scaling law distinct from regu-



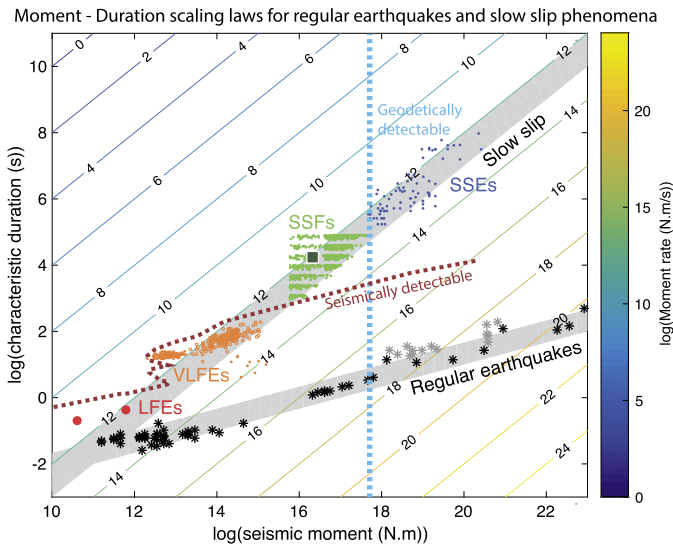


**Fig. 7.** Moment–duration scaling law for regular earthquakes and slow slip phenomena (gray shaded areas). Colored solid lines are isolines of equal moment rate. Black stars indicate regular earthquakes over a large range of magnitude (compilation of Peng and Gomberg, 2010 augmented with M4.8–5.8 events from the GCMT catalog and recent mega-earthquakes, Delouis et al., 2010; Bletery et al., 2014; Bletery et al., 2016). Gray stars indicate tsunami earthquakes (compilation from Peng and Gomberg, 2010). Orange dots are VLFES (Ito and Obara, 2006; Matsuzawa et al., 2009; Ide and Yabe, 2014). Orange circles are unnamed 20–200 s long duration earthquakes assimilated to VLFES (Ide et al., 2008). Red circles are LFE moment and duration averaged over 100 (Thomas et al., 2016) and >100,000 events (Bostock et al., 2015). Cyan dashed line shows an approximate moment threshold ( $M_w \approx 5.7$ – $6.0$ ) for geodetically detectable events. Red dashed line shows the limit of seismically detectable events (see text). In agreement with moment of large SSFs determined from strain meters (green square, Hawthorne et al., 2016), SSFs detected in this study (green dots) span a moment–duration region that cannot be directly recorded either by common seismic or geodetic instrumentation. (For interpretation of the references to color in this figure legend, the reader is referred to the web version of this article.)

lar earthquakes. While regular (fast) earthquakes have moment proportional to the cube of their duration, slow slip phenomena would have moment proportional to duration (with  $M/T = 10^{12}$ – $10^{13}$  N.m/s) (Fig. 7). In this representation, important gaps separate the various slow slip phenomena (Ide et al., 2007). The question of whether these gaps result from detection limitations or from the inherent behavior of fault slip is of importance because it could provide us with physical constraints on earthquake processes (Ide et al., 2007; Ide, 2008; Ide et al., 2008; Peng and Gomberg, 2010; Gao et al., 2012; Ide and Yabe, 2014; Liu, 2014; Gomberg et al., 2016).

In the far field, seismic amplitudes scale with moment rate (Aki and Richards, 2002). Thus, the threshold for seismically detectable signals follows the noise level in the different frequency bands. We use the USGS low noise model (Peterson et al., 1993; Ide, 2014) and empirically calibrate it on the smallest moment rate events that have been seismically detected (VLFES from Ide and Yabe, 2014) to determine a threshold for seismically detectable events (red dashed line in Fig. 7). Existing geodetic instrumentation has proven capable of detecting magnitude 5.7–6.0 events and above regardless of their duration (Peng and Gomberg, 2010) (blue dashed line in Fig. 7). The gap between LFEs and VLFES (Fig. 7) may be attributed to particularly large noise in the frequency band corresponding to the gap (Ide et al., 2008) while the gap between the VLFES and SSEs corresponds to moments too low to be detected by geodesy (Peng and Gomberg, 2010) and characteristic periods too long to be detected in seismograms (Ide et al., 2008).

The large range of duration and moment among the SSFs we detected follows the slow slip scaling law and fills the gap between

VLFES and SSEs, where signal is not directly detectable either from seismic or geodetic records (Fig. 7). The vertical (moment) threshold in SSFs corresponds to the minimum number of LFE/tremor detections (20) in one SSF times  $M_e$  and the distinct horizontal lines in SSF duration correspond to our different time windows. These two noncontinuous characteristics are consequences of our approach. Interestingly, SSFs appear to follow the same threshold of constant moment rate – on the order of  $10^{13}$  N.m/s – as the other slow slip phenomena (Fig. 7). The fact that SSFs follow the slow slip phenomena scaling law may be a consequence of estimating SSF moment from moment of SSEs (eq. (3)), as SSEs follow this law. Nevertheless, it is worth noting that our moment estimates are in agreement with SSF moments estimated from strain meters (Hawthorne et al., 2016) (green square in Fig. 7).

While individual slow slip phenomena do not appear to have moment proportional to duration (e.g. Ide et al., 2008; Bostock et al., 2015; Gomberg et al., 2016), they all fit a constant moment rate scaling law (within less than 2 orders of magnitude variation) when considered together on a 10 orders of magnitude scale (Fig. 7). More generally, fast and slow slip phenomena appear to be well distinguished in Fig. 7. Fault slip processes that would range between the two scaling laws are, in theory, detectable – and should therefore have been detected – by seismology, geodesy or both (Fig. 7). The large gap in detection of fault slip processes between the two scaling laws suggests that earthquakes and slow slip phenomena are two very distinct fault slip processes.

## 6. Conclusion

We identified a total of 1076 SSFs in Cascadia at timescales between 30 min and 32 h. We cataloged their duration, width, length, pulse length and time of occurrence and provided estimates for some of their physical properties such as moment, slip, slip rate, and stress drop. The median moment is  $5.3 \times 10^{16}$  N.m (corresponding to a moment magnitude of 5.1), the median slip is 3 mm, the median slip rate is 1.1 mm/h and the median stress drop is 5.8 kPa. Moment estimates suggest that SSFs bridge a major gap between seismically and geodetically detectable events in the slow slip phenomena scaling law (Ide et al., 2007). As previously observed with different approaches (Ghosh et al., 2010; Houston et al., 2011; Obara et al., 2012), we found that short duration SSFs dominantly propagate along dip while long duration SSFs dominantly propagate along strike. We also found that inferred SSF stress drops and slip rates range over 3 orders of magnitude, suggesting that the same fault region could be able to slip at very different rates and to release very different stresses. These findings may be used to constrain models of slow earthquake processes.

## Acknowledgements

This work was funded by the NSF grant EAR-1520238. The tremor catalog was made available online by A. Wech and K. Creager ([tunk.ess.washington.edu/map\\_display/](http://tunk.ess.washington.edu/map_display/)). We thank G. Savard and M. Bostock for providing the LFE catalog.

## Appendix A. Supplementary material

Supplementary material related to this article can be found online at <http://dx.doi.org/10.1016/j.epsl.2017.01.046>.

## References

- Aki, K., Richards, P.G., 2002. *Quantitative Seismology*. Vol. 1.
- Bartlow, N.M., Miyazaki, S., Bradley, A.M., Segall, P., 2011. Space–time correlation of slip and tremor during the 2009 Cascadia slow slip event. *Geophys. Res. Lett.* 38 (18).

- Bletery, Q., Sladen, A., Delouis, B., Vallée, M., Nocquet, J.-M., Rolland, L., Jiang, J., 2014. A detailed source model for the Mw9.0 Tohoku-Oki earthquake reconciling geodesy, seismology, and tsunami records. *J. Geophys. Res., Solid Earth* 119 (10), 7636–7653.
- Bletery, Q., Sladen, A., Jiang, J., Simons, M., 2016. A Bayesian source model for the 2004 great Sumatra–Andaman earthquake. *J. Geophys. Res., Solid Earth* 121 (7), 5116–5135.
- Bostock, M., Thomas, A., Savard, G., Chuang, L., Rubin, A., 2015. Magnitudes and moment–duration scaling of low-frequency earthquakes beneath southern Vancouver island. *J. Geophys. Res., Solid Earth* 120 (9), 6329–6350.
- Chiu, S.L., 1994. Fuzzy model identification based on cluster estimation. *J. Intell. Fuzzy Syst.* 2 (3), 267–278.
- Delouis, B., Nocquet, J.-M., Vallée, M., 2010. Slip distribution of the February 27, 2010 Mw = 8.8 Maule Earthquake, central Chile, from static and high-rate GPS, InSAR, and broadband teleseismic data. *Geophys. Res. Lett.* 37 (17).
- Dragert, H., Wang, K., James, T.S., 2001. A silent slip event on the deeper Cascadia subduction interface. *Science* 292 (5521), 1525–1528.
- Frank, W.B., Shapiro, N.M., Husker, A.L., Kostoglodov, V., Romanenko, A., Campillo, M., 2014. Using systematically characterized low-frequency earthquakes as a fault probe in Guerrero, Mexico. *J. Geophys. Res., Solid Earth* 119 (10), 7686–7700.
- Gao, H., Schmidt, D.A., Weldon, R.J., 2012. Scaling relationships of source parameters for slow slip events. *Bull. Seismol. Soc. Am.* 102 (1), 352–360.
- Ghosh, A., Vidale, J.E., Sweet, J.R., Creager, K.C., Wech, A.G., Houston, H., Brodsky, E.E., 2010. Rapid, continuous streaking of tremor in Cascadia. *Geochem. Geophys. Geosyst.* 11 (12).
- Gomberg, J., Wech, A., Creager, K., Obara, K., Agnew, D., 2016. Reconsidering earthquake scaling. *Geophys. Res. Lett.* 43 (12), 6243–6251.
- Hawthorne, J.C., Bostock, M.G., Royer, A.A., Thomas, A.M., 2016. Variations in slow slip moment rate associated with rapid tremor reversals in Cascadia. *Geochem. Geophys. Geosyst.* 17 (12), 4899–4919.
- Hawthorne, J., Rubin, A., 2013. Tidal modulation and back-propagating fronts in slow slip events simulated with a velocity-weakening to velocity-strengthening friction law. *J. Geophys. Res., Solid Earth* 118 (3), 1216–1239.
- Houston, H., 2015. Low friction and fault weakening revealed by rising sensitivity of tremor to tidal stress. *Nat. Geosci.* 8 (5), 409–415.
- Houston, H., Delbridge, B.G., Wech, A.G., Creager, K.C., 2011. Rapid tremor reversals in Cascadia generated by a weakened plate interface. *Nat. Geosci.* 4 (6), 404–409.
- Ide, S., 2008. A Brownian walk model for slow earthquakes. *Geophys. Res. Lett.* 35 (17).
- Ide, S., 2010. Striations, duration, migration and tidal response in deep tremor. *Nature* 466 (7304), 356–359.
- Ide, S., 2014. Modeling fast and slow earthquakes at various scales. *Proc. Jpn. Acad., Ser. B* 90 (8), 259–277.
- Ide, S., Beroza, G.C., Shelly, D.R., Uchide, T., 2007. A scaling law for slow earthquakes. *Nature* 447 (7140), 76–79.
- Ide, S., Imanishi, K., Yoshida, Y., Beroza, G.C., Shelly, D.R., 2008. Bridging the gap between seismically and geodetically detected slow earthquakes. *Geophys. Res. Lett.* 35 (10).
- Ide, S., Yabe, S., 2014. Universality of slow earthquakes in the very low frequency band. *Geophys. Res. Lett.* 41 (8), 2786–2793.
- Ito, Y., Obara, K., 2006. Very low frequency earthquakes within accretionary prisms are very low stress-drop earthquakes. *Geophys. Res. Lett.* 33 (9).
- Kao, H., Shan, S.-J., Dragert, H., Rogers, G., Cassidy, J.F., Wang, K., James, T.S., Ramachandran, K., 2006. Spatial-temporal patterns of seismic tremors in northern Cascadia. *J. Geophys. Res., Solid Earth* 111 (B3).
- Krogstad, R.D., Schmidt, D.A., 2015. Assessing the updip spatial offset of tremor and slip during ETS events in Cascadia. In: 2015 AGU Fall Meeting. AGU.
- Lay, T., Wallace, T.C., 1995. *Modern Global Seismology*. International Geophysics Series, vol. 58. Academic Press.
- Liu, Y., 2014. Source scaling relations and along-strike segmentation of slow slip events in a 3-d subduction fault model. *J. Geophys. Res., Solid Earth* 119 (8), 6512–6533.
- Liu, Y., Rice, J.R., 2007. Spontaneous and triggered aseismic deformation transients in a subduction fault model. *J. Geophys. Res., Solid Earth* 112 (B9).
- Matsuzawa, T., Obara, K., Maeda, T., 2009. Source duration of deep very low frequency earthquakes in western Shikoku, Japan. *J. Geophys. Res., Solid Earth* 114 (B11).
- Obara, K., 2002. Nonvolcanic deep tremor associated with subduction in southwest Japan. *Science* 296 (5573), 1679–1681.
- Obara, K., Matsuzawa, T., Tanaka, S., Maeda, T., 2012. Depth-dependent mode of tremor migration beneath Kii peninsula, Nankai subduction zone. *Geophys. Res. Lett.* 39 (10).
- Peng, Z., Gomberg, J., 2010. An integrated perspective of the continuum between earthquakes and slow-slip phenomena. *Nat. Geosci.* 3 (9), 599–607.
- Peng, Y., Rubin, A.M., 2016. High-resolution images of tremor migrations beneath the Olympic Peninsula from stacked array of arrays seismic data. *Geochem. Geophys. Geosyst.* 17, 587–601.
- Peng, Y., Rubin, A.M., 2017. Intermittent tremor migrations beneath Guerrero, Mexico and implications for fault healing within the slow slip zone. *Geophys. Res. Lett.*
- Peng, Y., Rubin, A.M., Bostock, M.G., Armbruster, J.G., 2015a. High-resolution imaging of rapid tremor migrations beneath southern Vancouver island using cross-station cross correlations. *J. Geophys. Res., Solid Earth* 120 (6), 4317–4332.
- Peng, Z., Shelly, D.R., Ellsworth, W.L., 2015b. Delayed dynamic triggering of deep tremor along the Parkfield–Cholame section of the San Andreas Fault following the 2014 M6.0 South Napa earthquake. *Geophys. Res. Lett.* 42 (19), 7916–7922.
- Peterson, J., et al., 1993. *Observations and Modeling of Seismic Background Noise*. US Geological Survey, Albuquerque, New Mexico.
- Radiguet, M., Cotton, F., Vergnolle, M., Campillo, M., Walpersdorf, A., Cotte, N., Kostoglodov, V., 2012. Slow slip events and strain accumulation in the Guerrero gap, Mexico. *J. Geophys. Res., Solid Earth* 117 (B4).
- Royer, A., Thomas, A., Bostock, M., 2015. Tidal modulation and triggering of low-frequency earthquakes in northern Cascadia. *J. Geophys. Res., Solid Earth* 120 (1), 384–405.
- Rubin, A.M., 2011. Designer friction laws for bimodal slow slip propagation speeds. *Geochem. Geophys. Geosyst.* 12 (4).
- Rubin, A.M., Armbruster, J.G., 2013. Imaging slow slip fronts in Cascadia with high precision cross-station tremor locations. *Geochem. Geophys. Geosyst.* 14 (12), 5371–5392.
- Ryberg, T., Haberland, C., Fuis, G., Ellsworth, W., Shelly, D., 2010. Locating non-volcanic tremor along the San Andreas Fault using a multiple array source imaging technique. *Geophys. J. Int.* 183 (3), 1485–1500.
- Savard, G., Bostock, M.G., 2015. Detection and location of low-frequency earthquakes using cross-station correlation. *Bull. Seismol. Soc. Am.*
- Schmidt, D., Gao, H., 2010. Source parameters and time-dependent slip distributions of slow slip events on the Cascadia subduction zone from 1998 to 2008. *J. Geophys. Res., Solid Earth* 115 (B4).
- Shelly, D.R., 2009. Possible deep fault slip preceding the 2004 Parkfield earthquake, inferred from detailed observations of tectonic tremor. *Geophys. Res. Lett.* 36 (17).
- Shelly, D.R., 2010. Migrating tremors illuminate complex deformation beneath the seismogenic San Andreas Fault. *Nature* 463 (7281), 648–652.
- Shelly, D.R., Beroza, G.C., Ide, S., 2007a. Complex evolution of transient slip derived from precise tremor locations in western Shikoku, Japan. *Geochem. Geophys. Geosyst.* 8 (10).
- Shelly, D.R., Beroza, G.C., Ide, S., 2007b. Non-volcanic tremor and low-frequency earthquake swarms. *Nature* 446 (7133), 305–307.
- Thomas, A.M., Beroza, G.C., Shelly, D.R., 2016. Constraints on the source parameters of low-frequency earthquakes on the San Andreas Fault. *Geophys. Res. Lett.*
- Thomas, T.W., Vidale, J.E., Houston, H., Creager, K.C., Sweet, J.R., Ghosh, A., 2013. Evidence for tidal triggering of high-amplitude rapid tremor reversals and tremor streaks in northern Cascadia. *Geophys. Res. Lett.* 40 (16), 4254–4259.
- Ueno, T., Maeda, T., Obara, K., Asano, Y., Takeda, T., 2010. Migration of low-frequency tremors revealed from multiple-array analyses in western Shikoku, Japan. *J. Geophys. Res., Solid Earth* 115 (B9).
- Wech, A.G., 2010. Interactive tremor monitoring. *Seismol. Res. Lett.* 81 (4), 664–669.
- Wech, A.G., Bartlow, N.M., 2014. Slip rate and tremor genesis in Cascadia. *Geophys. Res. Lett.* 41 (2), 392–398.
- Wech, A.G., Creager, K.C., 2008. Automated detection and location of Cascadia tremor. *Geophys. Res. Lett.* 35 (20).
- Yager, R.R., Filev, D.P., 1994. Generation of fuzzy rules by mountain clustering. *J. Intell. Fuzzy Syst.* 2 (3), 209–219.

### 3 La coalescence de séismes lents comme possible mécanisme d'initiation des grands séismes

Lors de mes travaux sur les tremors à l'Université d'Oregon, j'ai été frappé par la distribution des tremors associés à un séisme lent particulier, survenu en 2013 au Nord de la faille des Cascades (événement entouré en noir sur la Figure III.1). Alors que les séismes lents se propagent normalement, soit unilatéralement, soit bilatéralement, formant dans la distribution des tremors représentée dans un diagramme latitude-temps, soit une droite, soit un éventail ouvert vers la droite, les tremors associés à cet événement forment un éventail vers la gauche, comme si ce dernier défiait la causalité (Figure III.1).

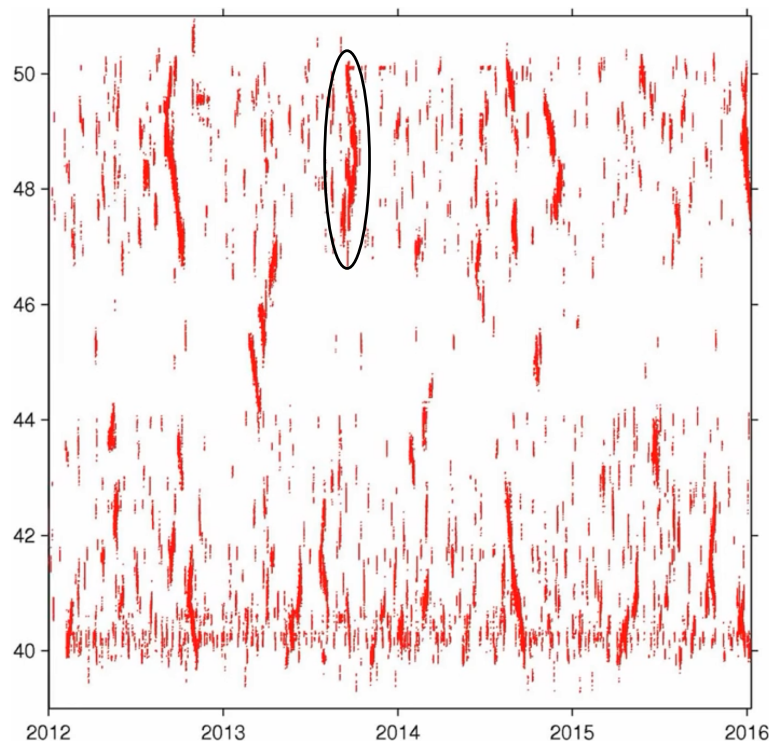


**Figure III.1** – Latitude des tremors en fonction du temps le long de la faille des Cascades [*Wech and Creager, 2008; Wech, 2010*]. L'ellipse noire indique l'évènement particulier de 2013.

Après mon recrutement à Géoazur, j'ai voulu savoir si le glissement lent associé à cet épisode de tremors présentait également cette étrange distribution. J'ai, pour cela, utilisé les outils développés par Jean-Mathieu Nocquet pour inverser le glissement journalier le long de la faille. Nous avons trouvé, dans l'étude qui suit, que le glissement lent présentait effectivement une distribution exceptionnelle, originant non pas en 2 mais en 3 sous-événements distincts coalesçant



### III.3 La coalescence de séismes lents comme possible mécanisme d'initiation des grands séismes

---

en 1 seul. De manière encore plus intéressante, nous avons observé que lors des 2 coalescences successives de ces sous-événements (observées de manière concordante dans l'inversion GNSS et dans la distribution des tremors), l'énergie (le moment) relâchée a significativement augmenté, suggérant que la coalescence de séismes lents puisse être un mécanisme d'initiation des grands séismes.

Cette étude a été réalisée à Géoazur, en collaboration avec Jean-Mathieu Nocquet. Elle a été publiée en 2020 dans le journal Nature Communications [[Bletery and Nocquet, 2020](#)].

# Slip bursts during coalescence of slow slip events in Cascadia

Quentin Bletery <sup>1</sup>✉ & Jean-Mathieu Nocquet <sup>1,2</sup>

Both laboratory experiments and dynamic simulations suggest that earthquakes can be preceded by a precursory phase of slow slip. Observing processes leading to an acceleration or spreading of slow slip along faults is therefore key to understand the dynamics potentially leading to seismic ruptures. Here, we use continuous GPS measurements of the ground displacement to image the daily slip along the fault beneath Vancouver Island during a slow slip event in 2013. We image the coalescence of three originally distinct slow slip fronts merging together. We show that during coalescence phases lasting for 2 to 5 days, the rate of energy (moment) release significantly increases. This observation supports the view proposed by theoretical and experimental studies that the coalescence of slow slip fronts is a possible mechanism for initiating earthquakes.

<sup>1</sup> Université Côte d'Azur, IRD, CNRS, Observatoire de la Côte d'Azur, Géoazur, 250 rue Albert Einstein, 06560 Valbonne, France. <sup>2</sup> Institut de Physique du Globe de Paris, Université de Paris, CNRS, 75238 Paris, France. ✉email: [bletery@geoazur.unice.fr](mailto:bletery@geoazur.unice.fr)



In western North America, the northern Cascadia subduction fault experiences slow slip events (SSEs) approximately every 14 months<sup>1</sup>. As slow slip develops, it generates a particular type of micro-earthquakes, known as low-frequency earthquakes that superpose as tectonic tremors<sup>1–3</sup>. The space–time correlation between slow slip and tremors<sup>4,5</sup> gives the opportunity to study the details of the evolution of SSEs, taking advantage of independent measurements of the ground displacement and tremor activity<sup>6–12</sup>. Here we focus on a complex SSE that occurred beneath Vancouver Island in September–October 2013. We use Global Positioning System (GPS) time series of the ground displacement to image the daily evolution of slip along the Cascadia subduction fault (Figs. 1 and 2) in relation to the daily distribution of tremors cataloged by the Pacific Northwest Seismic Network (PNSN)<sup>13,14</sup>.

## Results

**Two coalescence episodes.** We find that slow slip initiates in the area of Seattle on September 7, 2013, associated with intense tremor activity (Supplementary Fig. 3). During the first 2 weeks, most of the slip and tremors remain confined to the same  $60 \times 30 \text{ km}^2$  area, with a maximum activity on September 22 (Supplementary Figs. 3 and 4). Starting on September 15, tremors also emerge  $\sim 250 \text{ km}$  from that area at latitude  $50^\circ$  under Vancouver Island with low-amplitude slip sparsely detected from September 19 onward (Supplementary Fig. 4). Tremor locations indicate a southeastward, along-strike, and constant depth migration at  $\sim 10 \text{ km}$  per day. On September 26, slip catches up with tremors and extends southeastward. On September 24, an additional area of tremors arises between the two SSE areas, in the southern part of Vancouver island, soon followed by slow slip. On September

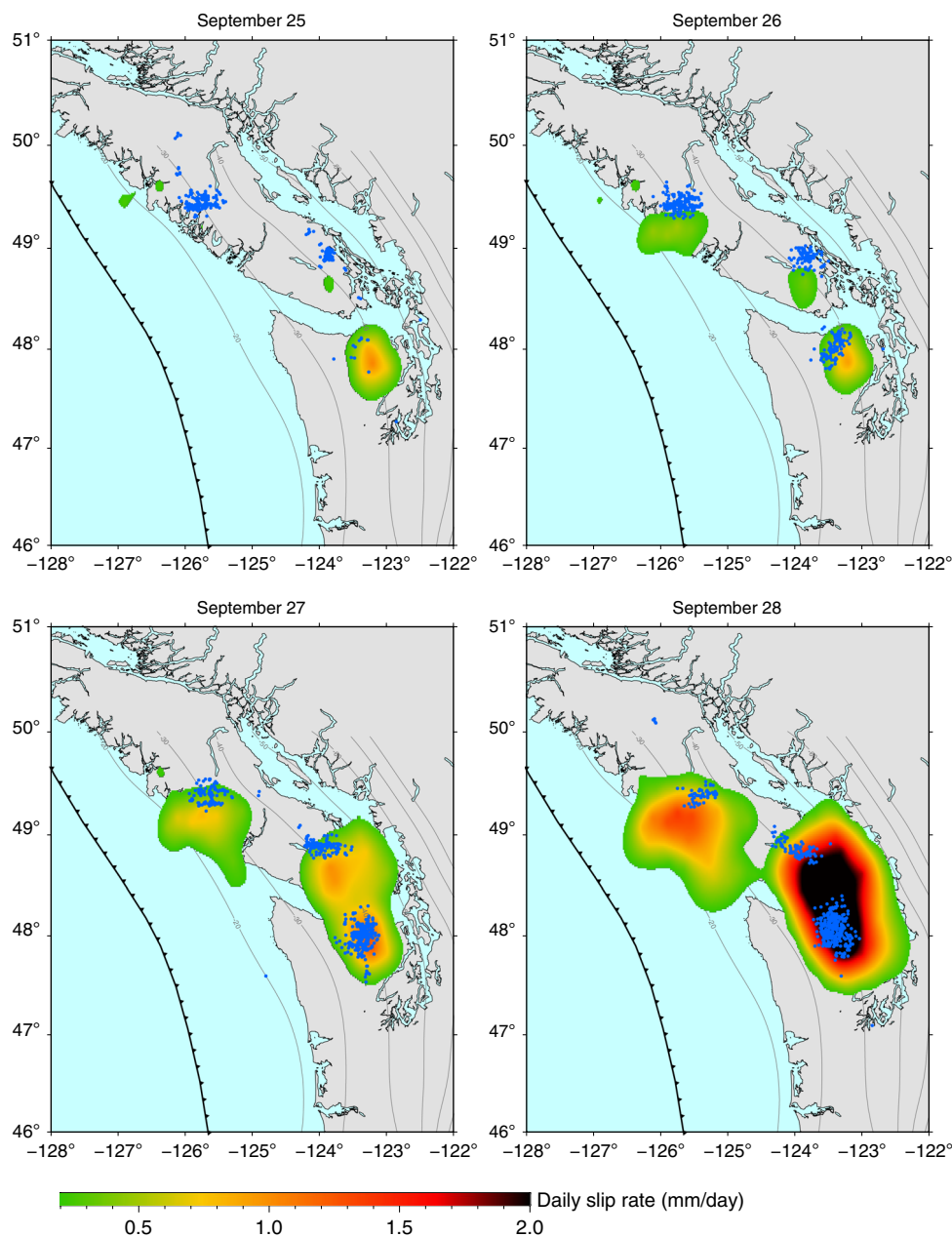


**Fig. 1 First coalescence episode.** Color maps show the slow slip rate inverted along the fault on each day from September 25 to September 28, 2013. Blue dots show the location of tremors recorded on the corresponding day. Isolines indicate the fault depth from 20 to 80 km.



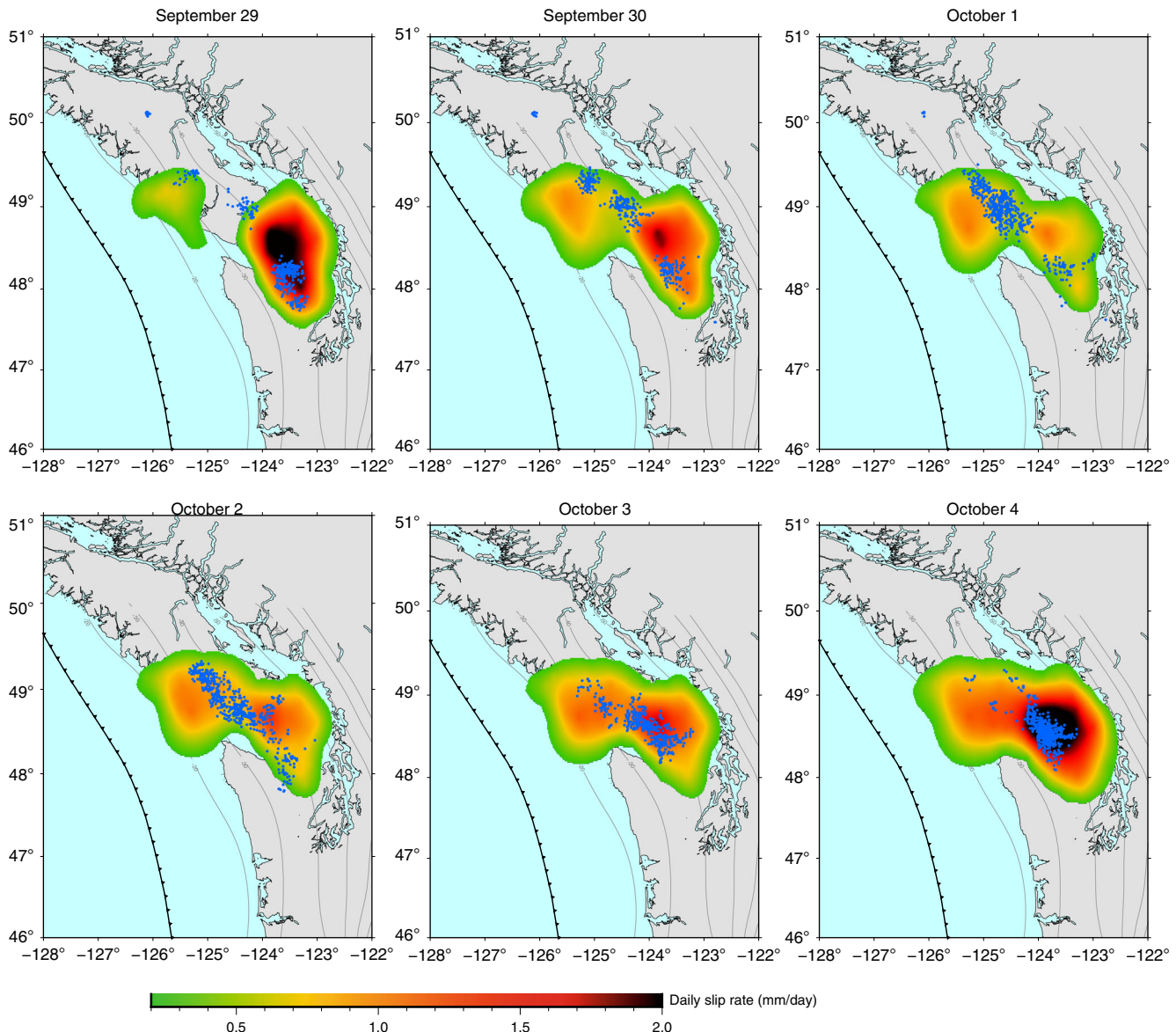


**Fig. 2 Second coalescence episode.** Color maps show the slow slip rate inverted along the fault on each day from September 29 to October 4, 2013. Blue dots show the location of tremors recorded on the corresponding day. Isolines indicate the fault depth from 20 to 80 km.

26, we see three clearly distinct patches of slip, each of them associated with a tremor swarm (Fig. 1). From September 27, the region located in between the southern and central patches starts slipping. On September 28, the two southern patches are indistinguishable one from the other (Fig. 1). During this merging phase, the moment rate release raises by a factor 10 in 3 days and the daily maximum slip increases by a factor 3 in 2 days (Fig. 3a). As an independent check for this acceleration, we find that the average daily incremental displacement recorded by the GPS stations close to the merging area is multiplied by a factor 8 (Fig. 3b) (see “Methods—Edge filter”). An interesting aspect is that, before the merging phase, the slow slip at the southern patch was fading out (see decrease in moment rate release after September 22, Fig. 3a), suggesting that the coalescence of the two previously distinct slipping areas is the actual cause for the observed increase in moment rate release. Following the first merging, the moment release slightly diminishes (Figs. 2 and 3a). A second merging phase occurs quickly afterwards (Fig. 2). This latter merging phase is also associated with a significant pulse in the moment release rate (2× between October 1 and October 4),

which eventually decreases to end the sequence on October 12 (Fig. 3, Supplementary Fig. 5).

**Interaction between distant slip fronts?** The 2013 Fall sequence highlights two successive coalescence episodes of pre-existing distinct slipping areas. Though jumping and halting are common in SSEs<sup>6</sup>, merging episodes similar to this sequence have not been observed during other SSEs in Cascadia or elsewhere. Nevertheless, the coalescence of nearby slipping areas might not be uncommon. In a rate-and-state framework<sup>15,16</sup>, as slip propagates from one area toward another, it progressively meets increasing positive shear stress generated by the counterpart patch, which in turn enhances its slip and promotes further propagation, until both slipping areas coalesce. For both merging phases during the 2013 sequence, our inversion suggests that coalescence initiates when the distance between the two SSE areas is on the order of one length-scale of their size. However, interaction at larger distance cannot be ruled out since tremors—and by extension SSEs—are known to be sensitive to extremely small stress

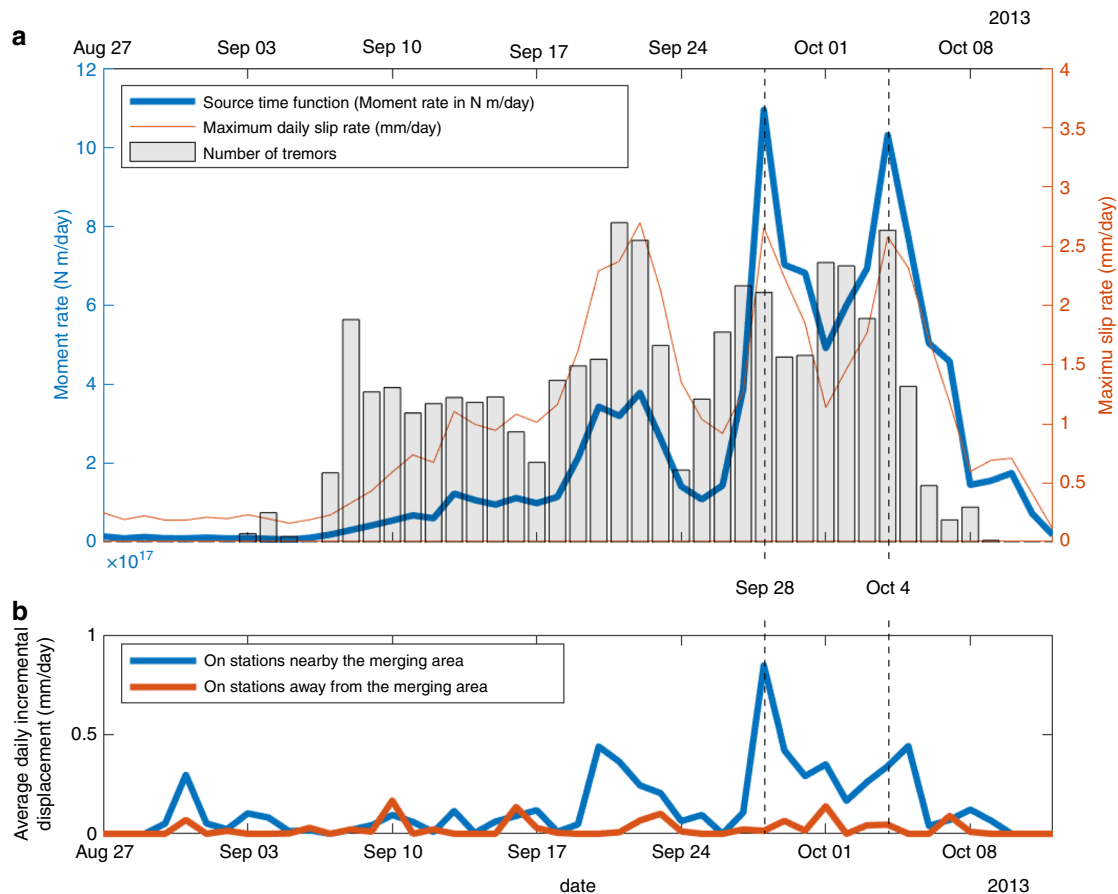


**Fig. 3 Increase in moment release during both coalescence episodes.** **a** Evolution of the moment rate release during the entire sequence. Gray histograms indicate the relative number of tremors on each day. The red thin curve shows the maximum daily slip on the fault every day. The blue thick curve shows the moment rate release. **b** Average daily displacement recorded on GPS stations close to (blue curve) and away from (red curve) the merging area after application of an edge filter, highlighting an increase in GPS data amplitude within the stations located close to the coalescence episodes. Stations used in both stacks are shown in Supplementary Fig. 1 (blue and red stations close to and away from the merging area, respectively).

perturbations, such as those generated by tides<sup>17</sup>. The southern migration of the northern slip front or the onset of the center one possibly reflects such long-distance interaction.

**Enhanced slip during coalescence episodes.** Both merging phases are associated with a burst in moment rate release resulting from a combination of a growth of the slipping area filling the space between the two patches and an increase in daily slip velocity (Fig. 3a). Moment release bursts result in an acceleration of the daily incremental displacement at GPS sites located above the merging area, directly seen in the GPS data (Fig. 3b). The period of merging between September 27 and October 5 (9 days) contributes to more than half (59%) of the total moment released during the entire sequence (47 days). Furthermore, peak moment rates on September 28 and October 4 represent a third (33%) of the moment released during the merging period. These ratios suggest a merging-induced burst-like behavior of slip at a daily time scale. Slip might, however, experience sub-daily variations. Indeed, analyses of seismic data indicate that microseismic activity, presumably driven by slow slip, is clustered in minute-to-hour-long bursts<sup>18,19</sup>. The daily incremental slip inferred here is likely an average of multiple shorter episodic events, with the implication that slip rates may punctually be significantly faster than the daily slip velocities inferred from our inversion.

## Discussion

Laboratory-derived constitutive friction laws predict that, for certain combinations of parameters referred to as velocity-weakening regimes, when sliding initiates, the friction drops proportionally to the logarithm of the sliding velocity, which in turn leads to enhanced sliding velocity<sup>15,16</sup>. Applied to the earthquake initiation problem, dynamic simulations have shown that the conditions required for slip to become unstable are functions—among other parameters—of the slip rate or stress perturbation in the nucleation area<sup>15,16</sup>. The coalescence of slow slip fronts therefore provides a mechanism counteracting the usual damping of slip observed during SSEs. This mechanism promotes instability on the fault through a slip acceleration and a stress increase at the tip of the locked area, which is larger than the summed contribution of individual fronts.

Based on laboratory experiments and numerical simulation, Dieterich intuited 40 years ago that slip velocity must increase if two previously independent zones of slip approach and coalesce to form a single zone<sup>20</sup>. His reasoning was that, because stress on a dislocation is controlled by the ratio of slip over the length of the slipping area, the rate of slip must accelerate to double the displacement as the segments merge to form a single zone. Dieterich<sup>20</sup> and more recent studies<sup>21,22</sup> proposed the coalescence of slow slip fronts as a possible mechanism to initiate earthquakes. While not the case here, the mechanism might have been at play during SSEs that have been proposed to trigger earthquakes.

Among the examples of recent large earthquakes that have been preceded by SSEs<sup>23–25</sup>, multiple slow slips accompanied by intense seismicity have been documented from months to days before the  $M_w$  8.1 April 1, 2014 Iquique earthquake<sup>26,27</sup>. Although the merging of SSEs has not been geodetically identified, the sequence shows some similarities with the 2013 Cascadia sequence. The migration of small earthquakes and activity of repeating earthquakes both suggest the existence of two slow slip areas separated by ~120 km in January and February 2014 north and south of the epicenter. While the northern area appears to be stationary and shows repeating earthquake activity until March 23, clustered and intense seismicity following the March 16  $M_w$  6.7 earthquake migrates from south to north<sup>27</sup>, leaving the possibility for the two slow slip areas to have merged near the future epicenter.

The 2013 Cascadia sequence provides an observational evidence of a phenomenon previously proposed by physical models<sup>20–22</sup>. It demonstrates that periods of SSE merging are key periods during which slip is enhanced, possibly bringing the fault closer to seismic failure. In the quest for earthquake precursors, it provides a clue on where to pay attention.

## Methods

**GPS data.** We use 59 GPS daily time series from the final Geodesy Advancing Geosciences and EarthScope combined solution<sup>28</sup> available from the UNAVCO data center and added 3 stations (ELIZ, WOST, GLDR) from the Pacific Northwest Geodetic Array of the Central Washington University, north of Vancouver island where coverage is sparse. The location of the 62 used stations is shown in Supplementary Fig. 1. We remove outliers and seasonal signals over the whole time series. We detrend the time series, so that the velocity during the weeks before and after the 2013 event is zero. This procedure ensures that the transient displacement recorded at the GPS sites reflects positive reverse slip at the plate interface. Regional common mode motion evaluated by stacking time series for 10 sites with complete data and good repeatability located 100–300 km away for the slip area was found to be negligible. The obtained time series are shown in Supplementary Figs. 7–17 and discussed in Supplementary Note 1.

**Green's functions.** We use a curved geometry for the subduction interface based on the slab2.0 model for Cascadia<sup>29</sup> discretized into 307 quasi-equilateral triangular subfaults, ranging from 46°N to 50°N in latitude and from the trench down to 50 km. The rake is calculated on each subfault accounting for the rotation of the North American plate with respect to the Juan de Fuca plate (Euler rotation pole: –111.7°E, 32.0°N<sup>30</sup>). We calculate the transfer matrix  $g$  relating unit slip in the rake direction at each triangular subfault to the displacement components at the GPS sites using the solution for triangular dislocation elements in a uniform elastic half space<sup>31</sup>.

**Slip time-dependent inversion.** We invert for daily incremental slip from August 27, 2013 to October 12, 2013 using only the horizontal components. Our approach relates the vector of cumulative displacements  $d_k$  at GPS sites since August 27 at date  $k$  to the sum of all daily incremental slip  $\delta s_i$  before date  $k$  multiplied by the Green's function  $g$ :

$$\sum_{i=1}^k g\delta s_i = d_k \quad (1)$$

Repeated for all dates  $k$ , Eq. (1) leads to a linear system  $G\delta s = d$ , where  $G$  is a block-triangular matrix made of  $g$ ,  $d$  and  $\delta s$  are the displacement vector and modeled daily slip resulting from concatenating all  $d_k$  and  $\delta s_i$ , respectively. The chosen formulation allows to solve consistently for the daily slip at every subfault in a single inversion. Two important aspects of our inversion procedure are a non-negativity constraint<sup>32</sup> that proscribes backward slip increment at all time steps, strongly reducing the solution space<sup>33</sup> and the absence of temporal smoothing that allows a better restitution of slip acceleration. Spatial regularization constraints are imposed by the mean of a model covariance matrix controlling the level of damping and smoothing with respect to an a priori model<sup>8,34,35</sup> here taken as 0. The model covariance matrix is taken as an isotropic decreasing exponential<sup>8</sup>:

$$C_{m_{i,j}} = \left( \sigma \frac{d_0}{D_c} \right)^2 \exp(-d_{i,j}/D_c) \quad (2)$$

where  $C_{m_{i,j}}$  are the model covariance matrix elements corresponding to the  $i$ th and  $j$ th subfaults,  $\sigma$  a constant (unit in  $\text{mm day}^{-1/2}$ ) controlling the weight of the regularization,  $d_{i,j}$  the distance between the center of subfaults  $i$  and  $j$ , and  $D_c$  is a correlation length controlling the level of spatial smoothing<sup>36</sup>.  $d_0$  is a reference

distance taken as the mean length of the triangles. No temporal smoothing is added here aside from the non-negativity constraint imposing that slip must grow through time. We used  $D_c = 50$  km, a value on the order of the distance between the center of two adjacent subfaults. We tested different values of  $\sigma$  and plotted the gain in misfit reduction as a function of regularization ( $\sigma$ ). We obtained a figure commonly known as an L-curve (Supplementary Fig. 2). We chose  $\sigma = 3 \text{ mm day}^{-1/2}$ , the point at the corner of the L-curve for which the misfit minimization becomes marginal when regularization increases.

**Tremor data.** We analyze the obtained slip distribution in light of the tremor activity (Figs. 1–3, Supplementary Figs. 3–6). We use the tremor catalog from the PNSN<sup>13,14</sup>. Because GPS data are daily averages of the positions measured from 00:00:00 to 23:59:30 UTC, they can be seen as the positions at 12:00:00 UTC every day. Therefore, the daily slip on the fault we image on day  $i$  should be seen as the slip from day  $(i-1)$  at 12:00:00 to day  $i$  at 11:59:59 (Figs. 1 and 2, Supplementary Figs. 3–5). Accordingly, the tremors represented on the subfigure of day  $i$  are tremors recorded from day  $(i-1)$  at 12:00:00 to day  $i$  at 11:59:59 (Figs. 1–3, Supplementary Figs. 3–5).

**Moment rate release.** The moment rate release (Fig. 3a) is calculated by summing the contributions of all subfaults assuming a uniform elastic Earth with an elastic shear modulus of 30 GPa. The cumulative moment is  $1.10 \times 10^{19}$  N m, equivalent to a maximum magnitude  $M_w = 6.6$ , the maximum cumulative slip is 35.3 mm, the maximum slip rate  $2.7 \text{ mm day}^{-1}$ . Because the dimensions of all the subfaults are equal, the moment rate release is strictly proportional to the average slip rate integrated over the ruptured surface. The daily number of tremors correlates fairly well with the moment rate release (coefficient of correlation: 0.63) and even better with daily maximum slip rate (coefficient of correlation: 0.76) (Fig. 3a). Furthermore, the two merging phases are associated with spikes in tremor activity (Figs. 1–3) and the day-to-day spatial correlation between slow slip and the independently inferred distribution of tremors (Figs. 1 and 2, Supplementary Figs. 3–5, Supplementary Movie 1) suggests that the main features of our inverted slip distribution are robust. Additional resolution tests can be found in Supplementary Information in the online version of the article (Supplementary Note 2, Supplementary Figs. 18–22).

**Edge filter.** In order to verify that the moment rate increase found in our inversion does not arise from fitting noise, we investigate the high-frequency properties of our time series. We apply a one-dimensional edge filter<sup>37</sup> to the north and east components of the GPS displacement time series. Edge filtering is a technique widely used in image processing that allows to retrieve sharp gradients in noisy data. We differentiate the filtered time series, take the norm, stack the obtained time series, and normalize it by the number of sites. The obtained time series reflect the average displacement over 1 day. We apply this procedure independently to a selection of 16 sites located in the area of the mergings (stations represented in blue in Supplementary Fig. 1) and to 10 sites away from the merging area in order to assess the level of noise (stations represented in red in Supplementary Fig. 1). We verify that sites located away from the SSE show spatially averaged daily velocity  $<0.2 \text{ mm day}^{-1}$  (Fig. 3b, red curve). On the contrary, sites located near the merging area show a clear increase in recorded slip displacement during the periods of enhanced tremor activity. In particular, the late-September merging phase is associated with a sharp (8×) increase in daily displacement (Fig. 3b, blue curve). This analysis demonstrates, independently from the inversion, that the 2013 sequence had several periods of coherent displacement acceleration, the largest one corresponding to the period of SSE merging around September 28 as found in our inversion.

## Data availability

The GPS time series and tremor catalog we used are respectively available on the UNAVCO (<https://www.unavco.org>) and PNSN websites (<https://tremor.pnsn.org>).

## Code availability

The pyacs library we used for data processing and for the kinematic slip inversion is available upon request to J.-M.N. (email: [nocquet@geoazur.unice.fr](mailto:nocquet@geoazur.unice.fr)).

Received: 13 July 2019; Accepted: 27 February 2020;

Published online: 01 May 2020

## References

- Rogers, G. & Dragert, H. Episodic tremor and slip on the cascadia subduction zone: the chatter of silent slip. *Science* **300**, 1942–1943 (2003).
- Obara, K. Nonvolcanic deep tremor associated with subduction in southwest Japan. *Science* **296**, 1679–1681 (2002).
- Shelly, D. R., Beroza, G. C. & Ide, S. Non-volcanic tremor and low-frequency earthquake swarms. *Nature* **446**, 305 (2007).



4. Bartlow, N. M., Miyazaki, S., Bradley, A. M. & Segall, P. Space-time correlation of slip and tremor during the 2009 cascadia slow slip event. *Geophys. Res. Lett.* <https://doi.org/10.1029/2011GL048714> (2011).
5. Wech, A. G. & Bartlow, N. M. Slip rate and tremor genesis in cascadia. *Geophys. Res. Lett.* **41**, 392–398 (2014).
6. Kao, H., Shan, S.-J., Dragert, H. & Rogers, G. Northern cascadia episodic tremor and slip: a decade of tremor observations from 1997 to 2007. *J. Geophys. Res. Solid Earth* <https://doi.org/10.1029/2008JB006046> (2009).
7. Schmidt, D. & Gao, H. Source parameters and time-dependent slip distributions of slow slip events on the cascadia subduction zone from 1998 to 2008. *J. Geophys. Res. Solid Earth* <https://doi.org/10.1029/2008JB006045> (2010).
8. Radiguet, M. et al. Spatial and temporal evolution of a long term slow slip event: the 2006 Guerrero slow slip event. *Geophys. J. Int.* **184**, 816–828 (2011).
9. Bartlow, N. M., Wallace, L. M., Beavan, R. J., Bannister, S. & Segall, P. Time-dependent modeling of slow slip events and associated seismicity and tremor at the Hikurangi subduction zone, New Zealand. *J. Geophys. Res. Solid Earth* **119**, 734–753 (2014).
10. Bletery, Q. et al. Characteristics of secondary slip fronts associated with slow earthquakes in cascadia. *Earth Planet. Sci. Lett.* **463**, 212–220 (2017).
11. Michel, S., Gualandi, A. & Avouac, J.-P. Interseismic coupling and slow slip events on the cascadia megathrust. *Pure Appl. Geophys.* **176**, 3867–3891 (2019).
12. Michel, S., Gualandi, A. & Avouac, J.-P. Similar scaling laws for earthquakes and cascadia slow-slip events. *Nature* **574**, 522–526 (2019).
13. Wech, A. G. & Creager, K. C. Automated detection and location of cascadia tremor. *Geophys. Res. Lett.* **35**, L20302 (2008).
14. Wech, A. G. Interactive tremor monitoring. *Seismol. Res. Lett.* **81**, 664–669 (2010).
15. Scholz, C. H. Earthquakes and friction laws. *Nature* **391**, 37 (1998).
16. Marone, C. Laboratory-derived friction laws and their application to seismic faulting. *Annu. Rev. Earth Planet. Sci.* **26**, 643–696 (1998).
17. Thomas, A. M., Nadeau, R. M. & Bürgmann, R. Tremor-tide correlations and near-lithostatic pore pressure on the deep San Andreas fault. *Nature* **462**, 1048 (2009).
18. Frank, W. B., Rousset, B., Lasserre, C. & Campillo, M. Revealing the cluster of slow transients behind a large slow slip event. *Sci. Adv.* **4**, eaat0661 (2018).
19. Thomas, A., Beeler, N., Bletery, Q., Burgmann, R. & Shelly, D. Using low-frequency earthquake families on the San Andreas fault as deep creepmeters. *J. Geophys. Res. Solid Earth* **123**, 457–475 (2018).
20. Dieterich, J. H. Modeling of rock friction: 2. Simulation of preseismic slip. *J. Geophys. Res. Solid Earth* **84**, 2169–2175 (1979).
21. Kaneko, Y. & Ampuero, J.-P. A mechanism for preseismic steady rupture fronts observed in laboratory experiments. *Geophys. Res. Lett.* **38**, L21307 (2011).
22. Fukuyama, E. et al. Spatiotemporal complexity of 2-d rupture nucleation process observed by direct monitoring during large-scale biaxial rock friction experiments. *Tectonophysics* **733**, 182–192 (2018).
23. Kato, A. et al. Propagation of slow slip leading up to the 2011 Mw 9.0 Tohoku-oki earthquake. *Science* **335**, 705–708 (2012).
24. Radiguet, M. et al. Triggering of the 2014 Mw 7.3 Papanoa earthquake by a slow slip event in Guerrero, Mexico. *Nat. Geosci.* **9**, 829 (2016).
25. Voss, N. et al. Do slow slip events trigger large and great megathrust earthquakes. *Sci. Adv.* **4**, eaat8472 (2018).
26. Ruiz, S. et al. Intense foreshocks and a slow slip event preceded the 2014 Iquique Mw 8.1 earthquake. *Science* **345**, 1165–1169 (2014).
27. Kato, A. & Nakagawa, S. Multiple slow-slip events during a foreshock sequence of the 2014 Iquique, Chile Mw 8.1 earthquake. *Geophys. Res. Lett.* **41**, 5420–5427 (2014).
28. Herring, T. A. et al. Plate boundary observatory and related networks: GPS data analysis methods and geodetic products. *Rev. Geophys.* **54**, 759–808 (2016).
29. Hayes, G. P. et al. Slab2, a comprehensive subduction zone geometry model. *Science* **362**, 58–61 (2018).
30. DeMets, C., Gordon, R. G. & Argus, D. F. Geologically current plate motions. *Geophys. J. Int.* **181**, 1–80 (2010).
31. Meade, B. J. Algorithms for the calculation of exact displacements, strains, and stresses for triangular dislocation elements in a uniform elastic half space. *Comput. Geosci.* **33**, 1064–1075 (2007).
32. Stark, P. B. & Parker, R. L. Bounded-variable least-squares: an algorithm and applications. *Comput. Stat.* **10**, 129–129 (1995).
33. Nocquet, J.-M. Stochastic static fault slip inversion from geodetic data with non-negativity and bound constraints. *Geophys. J. Int.* **214**, 366–385 (2018).
34. Tarantola, A. *Inverse Problem Theory and Methods for Model Parameter Estimation*, Vol. 89 (Siam, 2005).
35. Nocquet, J.-M. et al. Motion of continental slivers and creeping subduction in the Northern Andes. *Nat. Geosci.* **7**, 287 (2014).
36. Vaca, S., Vallée, M., Nocquet, J.-M., Battaglia, J. & Régnier, M. Recurrent slow slip events as a barrier to the northward rupture propagation of the 2016 Pedernales earthquake (Central Ecuador). *Tectonophysics* **724**, 80–92 (2018).
37. Barbero, A. & Sra, S. Modular proximal optimization for multidimensional total-variation regularization. *J. Mach. Learn. Res.* **19**, 1–82 (2018).

### Acknowledgements

We built our fault geometry based on the slab2.0 model available online at the following address: <https://www.sciencebase.gov/catalog/item/5aa1b00ee4b0b1c392e86467/>. We thank A. Wech, K. Creager, and PNSN for letting their tremor catalog available (<https://tremor.pnsn.org>). We downloaded the GPS time series from the UNAVCO website (<https://www.unavco.org>). We used the Generic Mapping Tools GMT5 (<https://gmt.soest.hawaii.edu/>). We thank Jean-Paul Ampuero and Martin Vallée for helpful discussion. This work has been supported by the French government, through the UCAJEDI Investments in the Future project managed by the National Research Agency (ANR) ANR-15-IDEX-01 and by the ANR research grants E-POST, REMAKE, and S5.

### Author contributions

Q.B. had the original idea. J.-M.N. provided numerical tools (PYACS python library) and expertise. Both authors contributed to the analysis, interpretation and to the manuscript preparation.

### Competing interests

The authors declare no competing interests.

### Additional information

**Supplementary information** is available for this paper at <https://doi.org/10.1038/s41467-020-15494-4>.

**Correspondence** and requests for materials should be addressed to Q.B.

**Peer review information** *Nature Communications* thanks Aitaro Kato and the other anonymous reviewer(s) for their contribution to the peer review of this work. Peer reviewer reports are available.

**Reprints and permission information** is available at <http://www.nature.com/reprints>

**Publisher's note** Springer Nature remains neutral with regard to jurisdictional claims in published maps and institutional affiliations.



**Open Access** This article is licensed under a Creative Commons Attribution 4.0 International License, which permits use, sharing, adaptation, distribution and reproduction in any medium or format, as long as you give appropriate credit to the original author(s) and the source, provide a link to the Creative Commons license, and indicate if changes were made. The images or other third party material in this article are included in the article's Creative Commons license, unless indicated otherwise in a credit line to the material. If material is not included in the article's Creative Commons license and your intended use is not permitted by statutory regulation or exceeds the permitted use, you will need to obtain permission directly from the copyright holder. To view a copy of this license, visit <http://creativecommons.org/licenses/by/4.0/>.

© The Author(s) 2020

## 4 Perspectives

Bien que l'étude des séismes lents est une piste intéressante en vue de la prédiction des séismes, nous sommes très loin d'une possible application opérationnelle. L'émergence de l'IA en sismologie apporte des possibilités nouvelles, peut-être plus prometteuses (voir Chapitre I.5). Le projet ERC EARLI, que je porte depuis Janvier 2021, comporte un volet très exploratoire sur les possibilités d'utilisation de l'IA à des fins prédictives. L'idée est d'exploiter une information de taille que nous avons à notre disposition que l'IA peut potentiellement utiliser efficacement : nous savons quand les séismes passés se sont produits. Cette information nous permet de définir la présence d'un signal précurseur dans les données selon l'occurrence postérieure d'un tremblement de terre. On peut théoriquement, à partir de là, entraîner un algorithme à reconnaître un précurseur dans le bruit sismique sans avoir besoin de l'identifier formellement (Figure III.2).

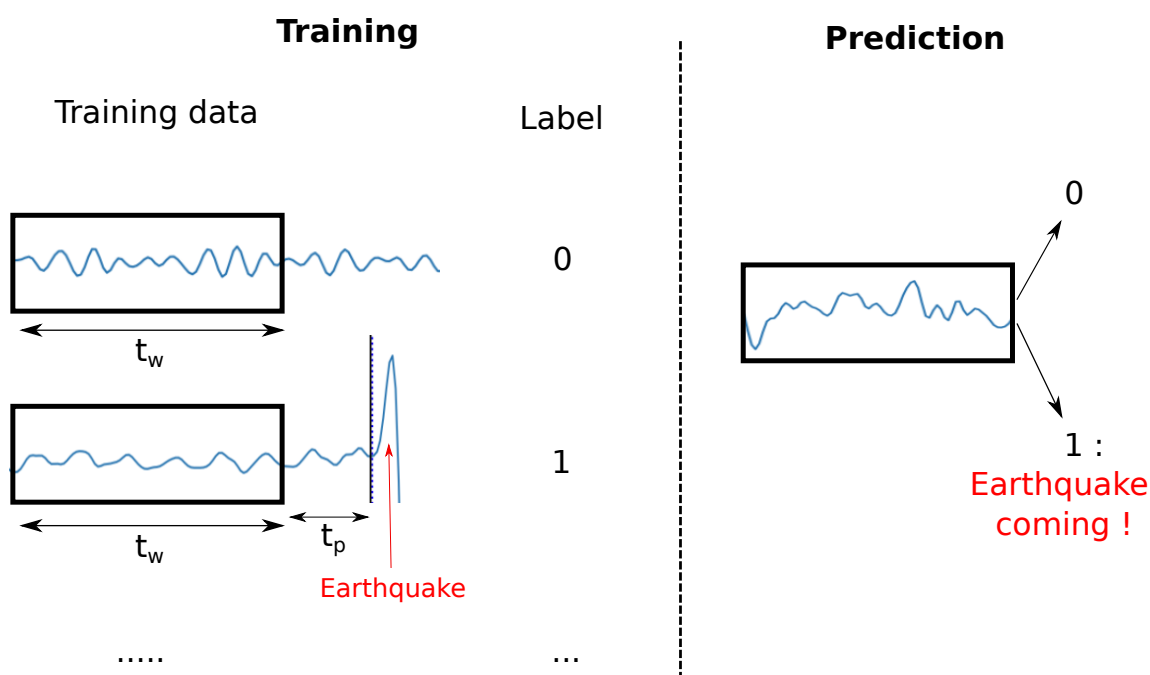


**Figure III.2** – Schéma illustratif du principe de la détection de précurseurs par apprentissage supervisé (voir Chapitre I.5.1). Les données d'entraînement sont composées de sismogrammes (3 composantes) de durées égales  $t_w$ . La moitié du jeu de données d'entraînement contient du bruit enregistré sur une station quelconque à un moment quelconque ; le label correspondant à ces données est 0. L'autre moitié du jeu de données est composée de sismogrammes précédant un séisme d'un temps  $t_p$  ; le label correspondant à ces données est 1. Une fois entraîné, l'algorithme prédira 0 ou 1 pour des sismogrammes sur lesquels il n'a pas été entraîné, 0 signifiant « rien à signaler », 1 signifiant « séisme attendu dans  $t_p$  ».

Quelque soit l'origine des signaux précurseurs, on s'attend à ce qu'ils dépendent, au premier

ordre, de la distance  $d_{i,k}$  entre la source  $S^i$  et la station  $ST^k$  et de la magnitude  $M_w^i$ . Comme on connaît la localisation des séismes passés, on peut facilement calculer  $d_{i,k}$ , et l'utiliser comme label avec  $M_w^i$  (Figure III.3).

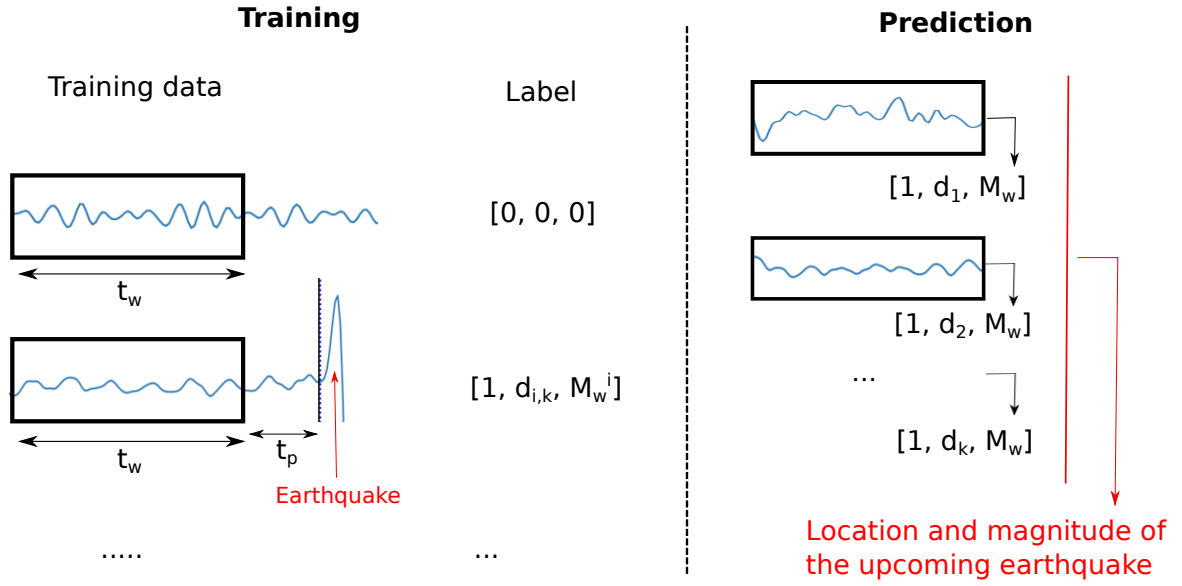


**Figure III.3** – Schéma illustratif de la modification du protocole d'entraînement par rapport à la version simplifiée (Figure III.2). Le label binaire est augmenté avec les informations sur la magnitude  $M_w^i$  de l'évènement et sa distance  $d_{i,k}$  à la station  $ST^k$ . Lors de la phase prédictive, l'algorithme pourrait alors procurer des informations sur la magnitude et la distance de l'évènement à venir, permettant ainsi de prédire la localisation (en croisant les informations données par différentes stations) et la magnitude.

L'étape suivante serait alors d'inclure  $t_p$  dans le label, afin d'avoir également accès au temps avant l'évènement lors de la phase prédictive. L'approche proposée ici est clairement exploratoire et repose sur (1) l'hypothèse de l'existence des précurseurs et (2) sur le fait que l'on dispose de suffisamment de données pour extraire ces signaux. Notez, toutefois, qu'une grande force de cette approche est de pouvoir, en théorie, fonctionner quelque soit l'origine des signaux précurseurs. Qu'ils soient générés par une phase de glissement lent précurserice, par une coalescence de séismes lents, par un changement des paramètres physiques du milieu ou quelque autre phénomène physique qu'il soit, nous n'avons besoin ici de ne faire aucune hypothèse sur l'origine des précurseurs.





---

---

# Chapitre IV

---

## Comment anticiper les grands séismes ?

### 1 L’alerte sismique/tsunami, une course contre le temps

Nous avons vu dans les chapitres précédents que, si quelques pistes existent, la prévision opérationnelle des séismes est difficilement envisageable à moyen terme. Néanmoins, il n’est pas forcément nécessaire de prédire le futur pour anticiper les catastrophes. Les systèmes d’alerte sismique détectent et caractérisent rapidement les séismes en cours en temps réel dans le but d’alerter les populations alentours de l’imminence de secousses. Ils utilisent l’information contenue dans les premières secondes d’enregistrement de l’évènement, qui sont généralement d’assez faible amplitude, pour estimer de potentielles secousses de plus forte amplitude. Les messages d’alerte se transmettant plus vite que les ondes sismiques ne se propagent, ils peuvent atteindre les populations concernées avant les premières secousses, offrant un temps précieux aux personnes et aux systèmes automatisés pour prendre des mesures afin de réduire les pertes humaines et matérielles. Les mesures vont de simples procédures invitant la population à rejoindre un lieu sûr à des procédures automatisées complexes comme interrompre le décollage et l’atterrissage des avions [*Wu et al., 2013*].

Des systèmes d’alerte opèrent dans de nombreuses régions du monde exposées aux tremblements de terre. Le Mexique a un système d’alerte opérationnel depuis 1991 [*Espinosa-Aranda et al., 2009*]. L’Agence Météorologique du Japon (JMA) opère un système depuis 2007 [*Hoshiba et al., 2011*]. Comme le système japonais, le système ShakeAlert développé pour la Côte Ouest des États-Unis [*Kohler et al., 2018*] estime la localisation et la magnitude des séismes. Ces estimations sont alors utilisées dans des équations de prédiction des mouvements du sol pour estimer l’amplitude des secousses ainsi que le risque de tsunami ; une alerte est lancée – ou non – sur la base de ces dernières estimations. Le système JMA a lancé des centaines d’alertes, dont certaines ont concerné des millions de personnes, comme pour le séisme de Tohoku-Oki ( $M_w$  9.0) en 2011 [*Fujinawa and Noda, 2013*].

## Chapitre IV. Comment anticiper les grands séismes ?

Les systèmes d'alerte ont été conçus dans l'hypothèse que la taille et l'étendue de la rupture pouvaient être connues immédiatement [Heaton, 1985; Meier, 2017] ou que la magnitude finale d'un séisme pouvait être déterminée à partir des premières secondes d'enregistrement des ondes P [Allen, 2006; Zollo et al., 2006]. Or, des études indiquent que la magnitude finale d'un séisme n'est pas déterminée au début de la rupture [Kanamori, 2005; Rydelek and Horiuchi, 2006; Rydelek et al., 2007; Yamamoto et al., 2008]. Des arguments théoriques vont dans ce sens [Sato and Kanamori, 1999] ainsi que des études observationnelles qui suggèrent que les premières secondes des sismogrammes des grands et des petits séismes sont indissociables [Mori and Kanamori, 1996; Ellsworth and Beroza, 1998; Kilb and Gomberg, 1999; Uchide and Ide, 2010; Meier et al., 2017].

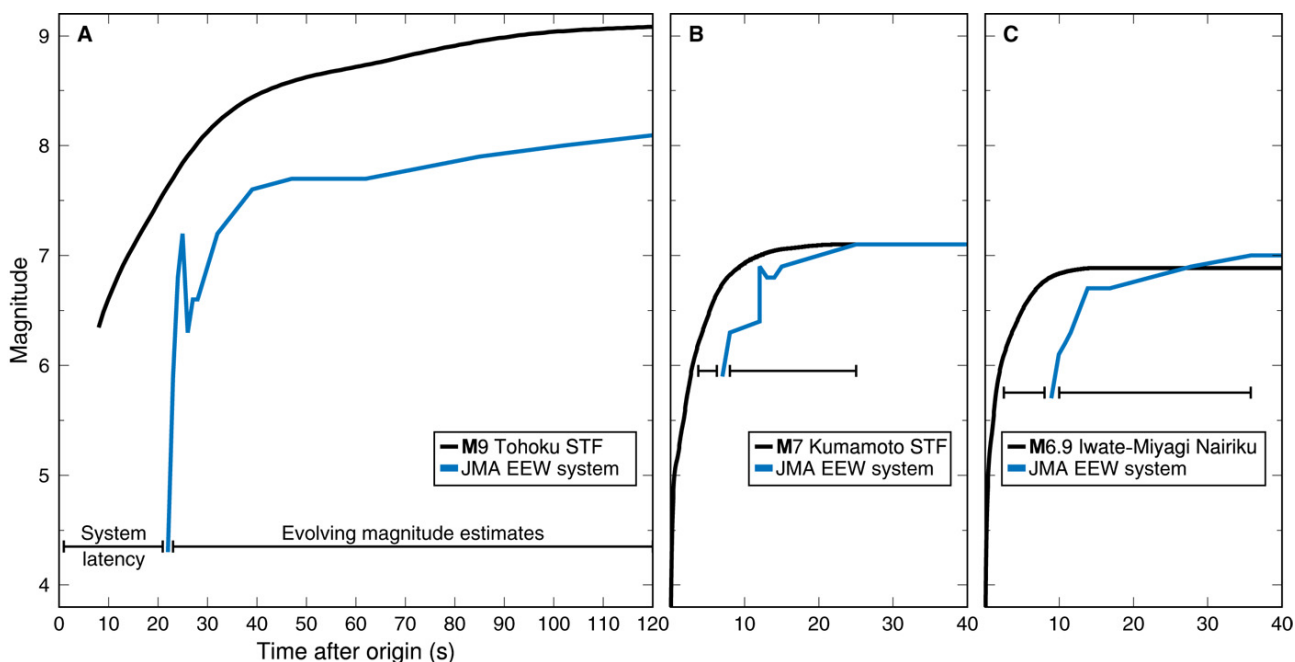


**Figure IV.1** – Estimation de la magnitude par le système JMA (bleu) en fonction du temps après l'origine des séismes de (A) Tohoku-OKi ( $M_w$  9.0, 2011), (B) Kumamoto ( $M_w$  7.0, 2016) et (C) Iwate-Miyagi Nairiku ( $M_w$  6.9, 2008) [Minson et al., 2018]. Les courbes noires donnent les fonctions sources des séismes (évolution réelle de la magnitude en fonction du temps).

L'observation de la performance des systèmes d'alerte opérationnels va également dans ce sens (Figure IV.1). L'estimation de la magnitude de séismes récents, tels que les 3 présentés dans la Figure IV.1, suggère que l'estimation suit l'évolution du moment relâché par le séisme avec un délai dû à l'attente de l'arrivée des premières ondes sismiques. On note également que le système JMA sature au delà de  $M_w = 8.1$ . L'étude présentée ci-après a pour objectif de réduire le délai de latence (dû à l'attente de l'arrivée des ondes sismiques) et de résoudre le problème

de saturation, problématique en particulier pour l'estimation du tsunami, comme dans le cas du séisme de Tohoku-Oki.

## 2 Estimation instantanée de la croissance des très grands séismes

L'étude qui suit est venue de l'idée de tester l'approche décrite dans les perspectives du Chapitre précédent (section III.4) sur des signaux intermédiaires, non précurseurs puisqu'ils sont générés par le séisme, mais précédant les ondes sismiques puisqu'ils présentent la particularité de se propager à la vitesse de la lumière : les PEGS (voir Chapitre I.4.3). Nous avons ainsi conçu un algorithme d'IA, PEGSnet, capable d'estimer la magnitude et la localisation de très grands séismes à partir des PEGS enregistrés sur un réseau de stations sismiques. Cet algorithme, entraîné sur un très grand nombre de données synthétiques augmentées de bruit empirique, s'avère capable d'estimer la magnitude des très grands séismes de manière instantanée – i.e. sans le délai dû à l'attente des ondes sismiques – à partir du moment où cette magnitude atteint  $M_w = 8.3$ . S'il n'est pas performant pour des événements de magnitude inférieure à 8.3, PEGSnet résout le problème de saturation des très grandes magnitudes. Ses performances sont d'autant plus impressionnantes que PEGSnet n'utilise que des données précédant les premières ondes sismiques, i.e. exclusivement des formes d'onde communément traitées comme du bruit.

Cette étude a été réalisée à Géoazur dans le cadre du postdoctorat d'Andrea Licciardi, en collaboration avec Bertrand Rouet-Leduc, Jean-Paul Ampuero et Kévin Juhel. Elle a été publiée en 2022 dans le journal Nature [[Licciardi et al., 2022](#)].

# Instantaneous tracking of earthquake growth with elastogravity signals

<https://doi.org/10.1038/s41586-022-04672-7>

Received: 14 June 2021

Accepted: 22 March 2022

Published online: 11 May 2022

Open access

 Check for updates

Andrea Licciardi<sup>1</sup>, Quentin Bletery<sup>1</sup>, Bertrand Rouet-Leduc<sup>2,3</sup>, Jean-Paul Ampuero<sup>1</sup> & Kévin Juhel<sup>1,4</sup>

Rapid and reliable estimation of large earthquake magnitude (above 8) is key to mitigating the risks associated with strong shaking and tsunamis<sup>1</sup>. Standard early warning systems based on seismic waves fail to rapidly estimate the size of such large earthquakes<sup>2–5</sup>. Geodesy-based approaches provide better estimations, but are also subject to large uncertainties and latency associated with the slowness of seismic waves. Recently discovered speed-of-light prompt elastogravity signals (PEGS) have raised hopes that these limitations may be overcome<sup>6,7</sup>, but have not been tested for operational early warning. Here we show that PEGS can be used in real time to track earthquake growth instantaneously after the event reaches a certain magnitude. We develop a deep learning model that leverages the information carried by PEGS recorded by regional broadband seismometers in Japan before the arrival of seismic waves. After training on a database of synthetic waveforms augmented with empirical noise, we show that the algorithm can instantaneously track an earthquake source time function on real data. Our model unlocks ‘true real-time’ access to the rupture evolution of large earthquakes using a portion of seismograms that is routinely treated as noise, and can be immediately transformative for tsunami early warning.

The sudden displacement of rock mass induced by an earthquake generates density variations that, in turn, modify the Earth’s gravity field. The signal associated with these transient gravity perturbations propagates at the speed of light, much faster than the fastest elastic waves (P-waves)<sup>8–10</sup>. Recent theoretical studies have shown the potential for earthquake early warning systems (EWS) that are based on the gravity signals that would be measured by a future generation of gravity-gradient sensors<sup>11,12</sup>, yet to be developed. In practice, existing inertial sensors (for example, seismometers) measure a combination of the direct gravity perturbations and their induced elastic response, named prompt elastogravity signals (PEGS)<sup>13,14</sup>. PEGS detection on real data is difficult for two reasons. First, the amplitude of the direct gravity perturbations is very small. Second, the induced elastic response tends to cancel out the gravity effects on seismometer recordings, especially in the early portion of the signal. The combination of these effects results in detectability limited to a time window preceding the P-wave arrival, which depends on epicentral distance (between a few seconds to a few tens of seconds), where PEGS reach their maximum amplitudes (a few  $\text{nm s}^{-2}$  at most)<sup>14,15</sup>. Nevertheless, PEGS could prove beneficial for EWS. First, they travel at the speed of light and might provide extra time for alert. Second, PEGS do not saturate, as opposed to P-waves recorded by near-field seismometers that may clip during large earthquakes. Finally, given the wavelength of the signal and the smoothness of the generated wavefield<sup>14</sup>, the spatial complexity of the rupture does not substantially affect PEGS amplitudes<sup>15</sup>. For this reason, PEGS dependence on earthquake magnitude, focal mechanism

and source time function (STF) has the potential to improve early characterization of earthquake size and source parameters, under a simple point-source approximation<sup>15,16</sup>. In this work we show that PEGS can efficiently be used to improve operational EWS.

Given the expected level of background noise, previous works have suggested a limit for PEGS detectability to earthquakes with magnitude ( $M_w$ ) above 8 (refs. <sup>15,16</sup>). The occurrence of  $M_w > 8$  earthquakes poses a difficult challenge for conventional EWS. On the one hand, subduction megathrust earthquakes require accurate and fast estimates of final magnitude to mitigate the risk associated with strong shaking and to forecast the potential size of tsunami waves<sup>17–19</sup>. On the other hand, EWS based on point-source algorithms that rely on the first few seconds of P-waves tend to produce saturated magnitude estimation for such large earthquakes. One reason is that instruments saturate for very large events. Another more fundamental reason is that the early portion of seismograms simply does not contain enough information to distinguish between small and large earthquakes (which have longer duration) at the very early stage of rupture<sup>5</sup>. An example of this paradigm is the performance of the EWS of the Japan Meteorological Agency (JMA) during the 2011  $M_w = 9.0$  Tohoku-Oki earthquake, which underestimated the final  $M_w$  of the event to around 8.1 (ref. <sup>20</sup>). Although the deterministic nature of earthquake rupture is still debated, a growing amount of evidence suggests that earthquake ruptures are not deterministic<sup>21</sup>. Therefore, EWS should be designed to track the moment release as the rupture unfolds instead of forecast the final earthquake magnitude<sup>3,22</sup>. Over the last decade, finite-fault EWS based on global navigation satellite

<sup>1</sup>Université Côte d’Azur, IRD, CNRS, Observatoire de la Côte d’Azur, Géoazur, Sophia Antipolis, France. <sup>2</sup>Disaster Prevention Research Institute, Kyoto University, Kyoto, Japan.

<sup>3</sup>Los Alamos National Laboratory, Geophysics Group, Los Alamos, NM, USA. <sup>4</sup>Laboratoire de Planétologie et Géodynamique, UMR 6112, Nantes University, CNRS, Nantes, France.

<sup>✉</sup>e-mail: andrea.licciardi@geoazur.unice.fr

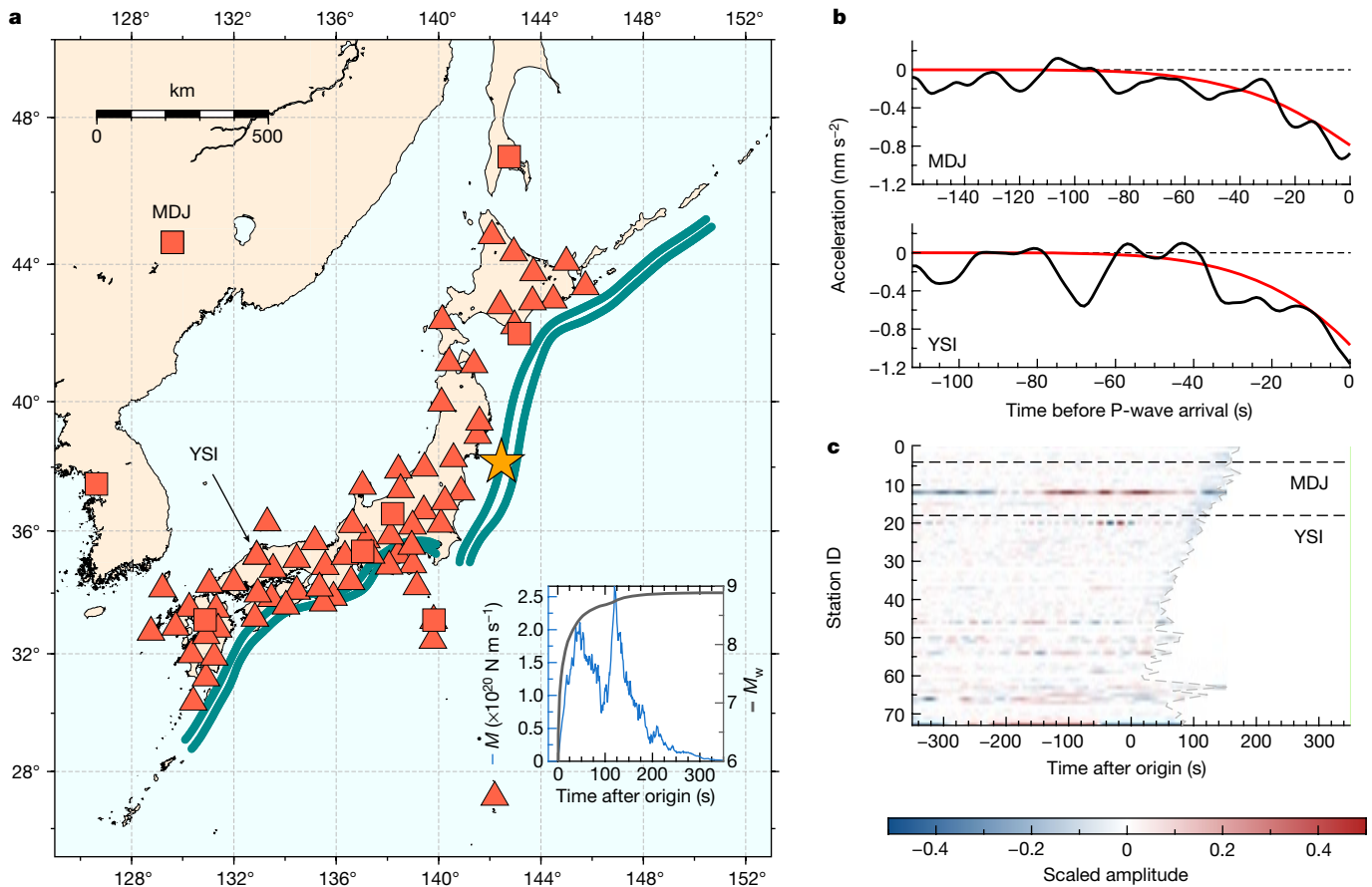


**Fig. 1 | Experimental set-up and input data examples from the synthetic database.** **a**, Locations of the stations in our network are indicated by light red symbols. Triangles are stations belonging to the F-Net seismic network and squares are stations from various networks obtained through the IRIS data centre. Dark green lines are made of 1,400 discrete locations of the synthetic earthquakes considered in our training database (see text). The orange star indicates the source location for one random synthetic example ( $M_w = 8.9$ ) extracted from the database whose moment rate (blue) and  $M_w$  evolution (grey)

are shown in the inset. **b**, The corresponding vertical waveforms at stations MDJ and YSI, where the red trace is the noise-free synthetic PEGS and the black trace is the same, with empirical noise added. Only the pre-P-wave time window is shown. **c**, Synthetic vertical waveforms plus noise associated with the selected event for each station in the seismic network. The grey dashed line indicates the P-wave arrival time. Stations are sorted by their longitude. The positions of MDJ and YSI are indicated by black horizontal dashed lines.

system (GNSS) data have emerged as a new tool with which to overcome the magnitude saturation problem<sup>23–28</sup>. Nevertheless, subjective choices required in GNSS data selection and/or preprocessing<sup>24,25</sup> may result in large uncertainties. Moreover, the fast responses achieved for megathrust earthquakes<sup>26</sup> have recently been questioned and attributed not to the predictive power of GNSS data—which would enable the estimation of an earthquake’s final magnitude before the rupture is over—but to prior constraints and regularization-induced artefacts<sup>22</sup>. A deep learning model based on GNSS data has recently been proposed to overcome these limitations<sup>29</sup>. Although it proved promising, as for other finite-fault approaches, it requires a priori assumptions on slip distribution. Finally, all existing EWS suffer from unavoidable latency, owing to the speed at which the information is carried by P-waves, and therefore produce a time-shifted version of the earthquake STF.

In this context, we show that a convolutional neural network (CNN)<sup>30</sup> approach can leverage the information carried by PEGS at the speed of light to overcome these limitations for large earthquakes. Successful applications of deep learning in seismology have provided new tools for pushing the detection limit of small seismic signals<sup>31,32</sup> and for the characterization of earthquake source parameters (magnitude and location)<sup>33–35</sup> with EWS applications<sup>29,36,37</sup>. Here we present a deep learning model, PEGSNet, trained to estimate earthquake location and track the time-dependent magnitude,  $M_w(t)$ , from PEGS data before P-wave arrivals.

### The training database

We focus on the Japanese subduction zone because: (1) it has experienced one of the largest and most destructive subduction events (the 2011  $M_w = 9.0$  Tohoku-Oki earthquake), and (2) we can rely on a large and dense network of good-quality broadband seismic stations (Fig. 1a).

Because of the paucity of PEGS observations<sup>16</sup>, we train PEGSNet on a database of synthetic PEGS waveforms generated with a normal-mode summation code<sup>14</sup> and add real noise recorded at each station in the seismic network. The training database is made of 500,000 synthetic earthquake sources distributed along the Japanese megathrust, with location, strike and dip angles following the Slab2.0 model<sup>38</sup>. We draw random magnitude and rake angles following uniform (from 5.5 to 10) and Gaussian ( $\mu = 90^\circ$ ,  $\sigma = 10^\circ$ ) distributions, respectively. In this work, we consider only the most simplistic rupture spatial descriptions: point sources. The difference in PEGS predictions associated with the source finiteness was shown to be within data uncertainties during the 2011 Tohoku earthquake<sup>15</sup>. The validity of this assumption is further corroborated by the detection of PEGS generated by multiple events considering a simple point-source model<sup>16</sup>. However, simple triangular STFs might not suffice for modelling PEGS for realistic earthquake ruptures<sup>16</sup>. For this reason, we generate random STFs using a model designed to mimic empirical laws and statistical observations<sup>5</sup> (Fig. 1a, inset, and Extended Data Fig. 1a) to produce



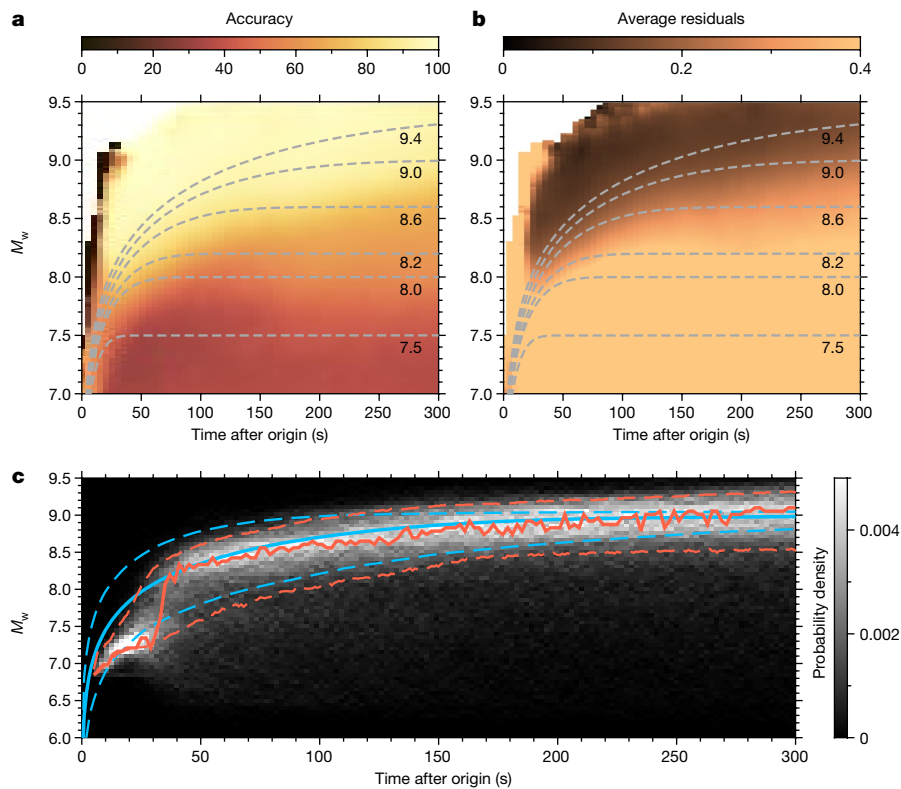


**Fig. 2 | Tracking  $M_w(t)$  from PEGS data.** Results of predictions on the test set. **a**, Predictions accuracy as a function of time and  $M_w$ . For each pixel in the image, accuracy is calculated as the number of successful predictions divided by the total number of samples. A prediction is defined as successful if the distance with its corresponding label is within  $\pm 0.4$  magnitude units. Dashed lines indicate the average values of the true  $M_w(t)$  for events with different final

magnitudes. **b**, As in **a**, but showing the average residuals ( $|M_{w[\text{true}]} - M_{w[\text{pred}]}|$ ) for each pixel. **c**, Probability density of  $M_w$  predictions for all the events in the test set with true final  $M_w$  of  $9 \pm 0.05$ . The solid red line is the mode of the distribution. The red dashed lines bound the 25th–95th percentile range. The blue lines are the median (solid) and the 5th–95th percentile range (dashed) of the labels.

three-component (east, north, vertical) waveforms representing the source characteristics of all expected large megathrust earthquakes. In this STF model the smaller and larger earthquakes start in the same way. We then add empirical noise recorded at each station (Fig. 1b) to the generated waveforms. Both synthetics and noise seismograms are decimated to 1 Hz and bandpass-filtered between 2 mHz (high-pass Butterworth, two poles, causal) and 30 mHz (low-pass Butterworth, six poles, causal), to enhance long-period PEGS amplitudes by suppressing higher-frequency noise<sup>7</sup>. Traces are clipped to a threshold value of  $\pm 10 \text{ nm s}^{-2}$  (the maximum expected amplitude for PEGS in our database) and scaled by the same value to facilitate convergence of the optimizer, and at the same time to preserve information about PEGS radiation patterns across the seismic network. Finally, we store each example as 700-s-long traces centred at the origin time of the earthquake (Fig. 1c), with its three labels corresponding to the latitude ( $\varphi$ ), longitude ( $\lambda$ ) and the time-integrated STF of the event converted to the time-dependent magnitude  $M_w(t)$ .

### Building PEGSNet, labelling and training

PEGSNet is a deep CNN that combines convolutional layers and fully connected layers in sequence (Extended Data Fig. 2; details in Methods). There exists a wealth of literature on deep learning architectures, but our goal here is to show the feasibility of PEGS-based EWS using deep learning, and we therefore use a simple and classic Le-NET-like CNN architecture<sup>39</sup>. Similar architectures have been used for magnitude and location estimation using P and S-waves with a single-station approach to increase the number of training examples<sup>33,34</sup>. Here we take advantage of our large synthetic database and adopt a multi-station approach.

CNNs work best with image-like inputs, and we arrange our data as an image, sorting stations by their longitude (Fig. 1c).

Our aim is to track the time-dependent magnitude,  $M_w(t)$ , which corresponds to the time-integrated STF at a given time. For PEGSNet to learn  $M_w(t)$ , we design a specific strategy: we randomly select the starting time ( $T_1$ ) of the analysed data during training. For each input example, we extract 315 s of data from  $T_1$  to  $T_2 = T_1 + 315$  s and assign the value of  $M_w(T_2)$  as the corresponding label. This allows the model to learn patterns in the data as the STF evolves with time.

We exclusively use the information carried by PEGS by setting to zero the amplitude of the seismograms for  $t \geq T_p$ , where  $T_p$  is the P-wave arrival time at each station for a given event. Therefore, P-wave arrival times are assumed to be known—in practice, any existing triggering algorithms (whether based on deep learning or not) could be used to obtain them before feeding the data to the model. The final input data for each example consists of a three-channel image (one for each seismic component), and the output layer of PEGSNet predicts three real values for  $M_w(T_2)$ ,  $\varphi$  and  $\lambda$ .

The synthetic database described above is randomly split into 70% training, 20% validation and 10% test sets, with a given synthetic STF and a given empirical noise measurement going to only one of the datasets. Training is performed by minimizing the Huber loss between the labels (the true values of  $M_w(t)$ ,  $\varphi$  and  $\lambda$  are known) and the predicted values. The model with the lowest error on the validation set is chosen as the final model.

### Instantaneous tracking of $M_w$

Figure 2 summarizes the results on the synthetic test set for  $M_w(t)$ , and those for  $\varphi$  and  $\lambda$  are displayed in Extended Data Fig. 3. Results

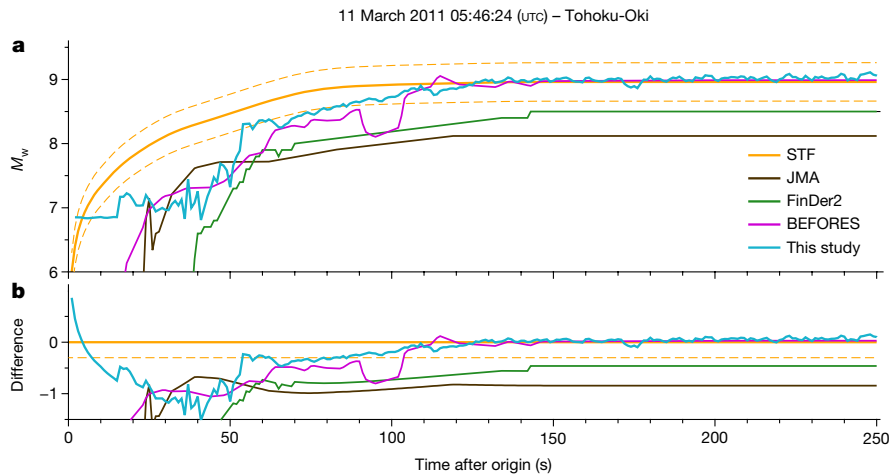


**Fig. 3 | Moment tracking of the 2011  $M_w$  9.0 Tohoku-Oki earthquake. a**, Comparison of PEGSNet  $M_w(t)$  predictions (blue) with the source time function (STF) of the Tohoku-Oki earthquake<sup>40</sup> (orange) and with the results of three existing EWS (JMA<sup>20</sup>, FinDer2<sup>41</sup> and BEFORES<sup>24</sup>). Dashed orange lines indicate

$\pm 0.3$  magnitude units. **b**, Difference between the predicted  $M_w$  of various algorithms (PEGSNet in blue) and the ‘true’ STF as shown in **a**. The solid orange line indicates a difference of zero, the dashed orange line a difference of  $-0.3$   $M_w$  units (underestimation).

for location rely on the P-wave arrival times (which are assumed to be known) and show errors around 25 to 30 km starting at about 50 s after origin. In the following, we will exclusively discuss the results for  $M_w(t)$ . These results represent the main contribution of this work as they are obtained using only the pre P-wave portion of the seismograms, which is routinely treated as pure noise. For each example in the test set, we simulate a real-time scenario by parsing the data with a running time window of 315 s. Each data window is fed to PEGSNet, which makes an  $M_w$  estimate for the end of the window, and the window is shifted in steps of 1 s as PEGSNet attempts to progressively reconstruct the STF (Extended Data Fig. 4). We define a successful prediction if the estimated  $M_w(t)$  lies within  $\pm 0.4$  magnitude units from the true value.

PEGSNet can track the moment released by earthquakes with final  $M_w$  above 8.6 with good accuracy (above 90%, Fig. 2a) and low errors ( $M_w$  error below 0.25, Fig. 2b), starting at about 40 s after origin time. For earthquakes with final  $M_w$  between 8.2 and 8.6, early tracking of the moment release is more difficult and only the final  $M_w$  can be estimated (with accuracy between 60% and 70% and errors above 0.25) after 150 s from origin time. Any predicted  $M_w$  below 8.2 is poorly constrained by the data and we place a conservative lower limit on PEGSNet sensitivity to  $M_w$  at 8.3. However, this limit depends on the noise amplitudes across the seismic network. Under favourable noise conditions (standard deviation of the noise for the whole seismic network below around  $0.5 \text{ nm s}^{-2}$ ), it can be reduced to about 7.9 or 8.0 (Extended Data Fig. 5).

To examine the time-dependent performance of PEGSNet more closely, Fig. 2c shows all the predictions (on the test set) associated with events with a final  $M_w$  of  $9.0 \pm 0.05$ . In the first 30–40 s after origin, predictions are strongly underestimated. This arises from a combination of two effects: the lack of sensitivity below 8.3 (in the first 30–40 s after origin the current magnitude is below 8.3 in our STF database) and the fact that, at stations located close to the source, P-waves can mask PEGS, owing to their small time separation. A test performed on noise-free synthetics shows that at least 15 s after origin are needed by the model to reliably predict  $M_w$  (Extended Data Fig. 6). Starting at about 40 s (when the true  $M_w$  is generally above 8.2 in our STF database), PEGSNet can track the evolution of the moment release instantaneously, that is, without time shift between estimated and true  $M_w(t)$ , as indicated by the mode of the distribution of the predictions. Our results show that PEGSNet can exploit the key features of PEGS: (1) PEGS sensitivity to magnitude for large earthquakes allows the model to distinguish, for example, between an  $M_w = 8$  and an  $M_w = 9$  earthquake and (2) the information about  $M_w$  is effectively propagated at the speed of light,

which results in instantaneous tracking of the moment release, from about 40 s into the rupture until its end. Although P-wave triggering is needed at each station, the instantaneous information about the source carried by PEGS is readily available in the data that precede P-wave arrivals. This allows PEGSNet to estimate  $M_w(t)$  with zero delay once the magnitude exceeds approximately 8.3.

### Playback of the Tohoku-Oki earthquake

We tested PEGSNet on real data from the 2011  $M_w$  9.0 Tohoku-Oki earthquake. The raw seismograms are processed as described in Methods and fed to PEGSNet. We simulated a data playback scenario and made an  $M_w$  prediction at each second starting at the earthquake origin time and using only the previous 315 s of data (details in Methods). Figure 3 shows the results of this retrospective analysis compared with a ‘true’ STF calibrated against various different data types<sup>40</sup>, the historical JMA EWS performance<sup>20</sup>, and the best-performing finite-fault EWS based on seismic (FinDer2)<sup>41</sup> and GNSS data (BEFORES)<sup>24</sup>. Further comparisons with additional algorithms are shown in Extended Data Fig. 7. After around 55 s, PEGSNet is always closer to the ‘true’ STF than the other algorithms (Fig. 3a). The predicted  $M_w$  between 55 and 100 s is underestimated by about 0.3 magnitude units compared to the ground truth. PEGSNet reaches a correct prediction of the final  $M_w$  after about 120 s, when the rupture is almost over. Despite the slight underprediction, the predicted  $M_w(t)$  values between 55 and 100 s show a clear increasing trend and suggest that the rupture is still in progress. Therefore, we argue that PEGS can be used in real time to track the evolving rupture as it unfolds. Consistently with our synthetic tests (Fig. 2), our predictions after about 55 s (corresponding to the time the earthquake reaches  $M_w \approx 8.3$ ) provide a snapshot of the evolution of the earthquake rupture at that exact time because PEGS carry information about the source at the speed of light. This is further corroborated by a test on synthetic data generated using the ‘true’ Tohoku-Oki earthquake STF and noise seismograms extracted from the test set (Extended Data Fig. 8).

Notably, PEGSNet does not suffer from the magnitude saturation issue that instead affects the seismic-based EWS. Both in terms of latency and accuracy, the performance of the GNSS-based algorithm BEFORES is the closest to PEGSNet. However, the response of PEGSNet is faster: for an arbitrary threshold at  $M_w = 8.0$ , PEGSNet would issue an alert 53 s after origin, BEFORES about 8 s later. PEGSNet is more accurate: the difference with the ‘true’ STF is always equal to or less than 0.3  $M_w$  units starting at 55 s, whereas BEFORES reaches that level

of precision only after 100 s from origin (Fig. 3b). More importantly, in contrast to GNSS-based EEWS, PEGSNet does not require prior assumptions on the data, because it is trained to learn features from the entire network of stations regardless of their data quality. In addition, no-slip distributions are assumed or modelled in our approach as PEGS are only sensitive to smooth variations of the released moment and, therefore, less likely to be influenced by the spatial complexity of the rupture.

To further assess the robustness of PEGSNet predictions on the Tohoku data, we performed a test in which we keep the P-wave arrival information but substitute the actual recorded waveforms in the pre-P-wave time window with noise. The resulting prediction of  $M_w(t)$  never exceeds the lower sensitivity limit of PEGSNet (that is, 8.3) and remains constant at about 6.5, which provides a baseline value for noise (Extended Data Fig. 9). We also tested PEGSNet on all the subduction earthquakes (dip-slip mechanism within 40 km from the megathrust) with  $M_w \geq 7$  that have occurred since January 2003, without considering aftershocks (Methods and Extended Data Fig. 10). For  $M_w < 8$  earthquakes, PEGSNet predictions converge toward the noise baseline, confirming that these events are essentially not distinguishable from noise.

## Implications for early warning

We have demonstrated instantaneous tracking of moment release for large earthquakes (Fig. 3). Our results promote PEGS as a new class of observables, easily accessible from the recordings of currently deployed broadband seismometers worldwide, for practical application in early warning systems that are currently limited by the speed of P-waves. In the context of EEWS, PEGSNet can complement any existing algorithm (either seismic- or GNSS-based), to improve  $M_w$  latency estimation and accuracy for  $M_w > 8.3$  megathrust earthquakes. For example, PEGSNet could be combined with a recent deep learning model based on GNSS data<sup>29</sup> to eliminate intrinsic latency due to P-wave speed.

At the same time, PEGSNet can immediately prove critical for tsunami early warning for which  $M_w$  estimation within a few minutes is vital. Continuous updates of current  $M_w$  can be fed to predictive models of tsunami waves height, helping mitigate the associated risk.

Our results suggest that PEGS can play a key part in the early characterization of rupture evolution for large earthquakes. For such events, PEGS data represent a new and independent source of information to constrain the magnitude in real time.

PEGSNet requires only a few modifications to be implemented in real time. Once trained, PEGSNet predictions are quasi-instantaneous, although some latency could be introduced by the preprocessing step. Although tailored here to earthquakes from the Japanese subduction zone, PEGSNet can be easily adapted to other seismic networks and regions and source mechanisms. In particular, PEGSNet portability to other regions only requires the availability of noise recordings for the seismic network of interest.

## Online content

Any methods, additional references, Nature Research reporting summaries, source data, extended data, supplementary information, acknowledgements, peer review information; details of author contributions and competing interests; and statements of data and code availability are available at <https://doi.org/10.1038/s41586-022-04672-7>.

- Allen, R. M. & Melgar, D. Earthquake early warning: advances, scientific challenges, and societal needs. *Annu. Rev. Earth. Planet. Sci.* **47**, 361–388 (2019).
- Wald, D. J. Practical limitations of earthquake early warning. *Earthq. Spectra* **36**, 1412–1447 (2020).
- Minson, S. E., Meier, M. A., Baltay, A. S., Hanks, T. C. & Cochran, E. S. The limits of earthquake early warning: timeliness of ground motion estimates. *Sci. Adv.* **4**, eaa0504 (2018).

- Meier, M. A. How “good” are real-time ground motion predictions from earthquake early warning systems? *J. Geophys. Res. Solid Earth* **122**, 5561–5577 (2017).
- Meier, M. A., Ampuero, J.-P. & Heaton, T. H. The hidden simplicity of subduction megathrust earthquakes. *Science* **357**, 1277–1281 (2017).
- Montagner, J.-P. et al. Prompt gravity signal induced by the 2011 Tohoku-Oki earthquake. *Nat. Commun.* **7**, 13349 (2016).
- Vallée, M. et al. Observations and modeling of the elastogravity signals preceding direct seismic waves. *Science* **358**, 1164–1168 (2017).
- Dahlen, F. & Tromp, J. *Theoretical Global Seismology* (Princeton Univ. Press, 1998).
- Harms, J. et al. Transient gravity perturbations induced by earthquake rupture. *Geophys. J. Int.* **201**, 1416–1425 (2015).
- Harms, J. Transient gravity perturbations from a double-couple in a homogeneous half-space. *Geophys. J. Int.* **205**, 1153–1164 (2016).
- Juhel, K. et al. Earthquake early warning using future generation gravity strainmeters. *J. Geophys. Res. Solid Earth* **123**, 10889–10902 (2018).
- Shimoda, T., Juhel, K., Ampuero, J.-P., Montagner, J.-P. & Barsuglia, M. Early earthquake detection capabilities of different types of future-generation gravity gradiometers. *Geophys. J. Int.* **224**, 533–542 (2021).
- Heaton, T. H. Correspondence: response of a gravimeter to an instantaneous step in gravity. *Nat. Commun.* **8**, 966 (2017).
- Juhel, K. et al. Normal mode simulation of prompt elasto-gravity signals induced by an earthquake rupture. *Geophys. J. Int.* **216**, 935–947 (2019).
- Zhang, S., Wang, R., Dahm, T., Zhou, S. & Heimann, S. Prompt elasto-gravity signals (PEGS) and their potential use in modern seismology. *Earth Planet. Sci. Lett.* **536**, 116150 (2020).
- Vallée, M. & Juhel, K. Multiple observations of the prompt elastogravity signals heralding direct seismic waves. *J. Geophys. Res. Solid Earth* **124**, 2970–2989 (2019).
- Melgar, D. & Bock, Y. Near-field tsunami models with rapid earthquake source inversions from land- and ocean-based observations: the potential for forecast and warning. *J. Geophys. Res. Solid Earth* **118**, 5939–5955 (2013).
- Melgar, D. et al. Local tsunami warnings: perspectives from recent large events. *Geophys. Res. Lett.* **43**, 1109–1117 (2016).
- Setiyono, U., Gusman, A. R., Satake, K. & Fujii, Y. Pre-computed tsunami inundation database and forecast simulation in Pelabuhan Ratu, Indonesia. *Pure Appl. Geophys.* **174**, 3219–3235 (2017).
- Hoshiba, M. & Ozaki, T. Earthquake early warning and tsunami warning of the Japan Meteorological Agency, and their performance in the 2011 off the Pacific Coast of Tohoku Earthquake ( $M_w$  9.0). In *Early Warning for Geological Disasters* (eds Wenzel, F. & Zschau, J.) 1–28 (Springer, 2014).
- Meier, M.-A., Ampuero, J.-P., Cochran, E. & Page, M. Apparent earthquake rupture predictability. *Geophys. J. Int.* **225**, 657–663 (2020).
- McGuire, J. J., Minson, S. E., Murray, J. R. & Brooks, B. A. The role of geodetic algorithms for earthquake early warning in Cascadia. *Geophys. Res. Lett.* **48**, e2020GL029324 (2021).
- Grapenthin, R., Johanson, I. A. & Allen, R. M. Operational real-time GPS-enhanced earthquake early warning. *J. Geophys. Res. Solid Earth* **119**, 7944–7965 (2014).
- Minson, S. E., Murray, J. R., Langbein, J. O. & Gombert, J. S. Real-time inversions for finite fault slip models and rupture geometry based on high-rate GPS data. *J. Geophys. Res. Solid Earth* **119**, 3201–3231 (2014).
- Melgar, D. et al. Earthquake magnitude calculation without saturation from the scaling of peak ground displacement. *Geophys. Res. Lett.* **42**, 5197–5205 (2015).
- Ruhl, C. J., Melgar, D., Grapenthin, R. & Allen, R. M. The value of real-time GNSS to earthquake early warning. *Geophys. Res. Lett.* **44**, 8311–8319 (2017).
- Crowell, B. W. et al. G-FAST earthquake early warning potential for great earthquakes in Chile. *Seismol. Res. Lett.* **89**, 542–556 (2018).
- Ruhl, C. J., Melgar, D., Chung, A. I., Grapenthin, R. & Allen, R. M. Quantifying the value of real-time geodetic constraints for earthquake early warning using a global seismic and geodetic data set. *J. Geophys. Res. Solid Earth* **124**, 3819–3837 (2019).
- Lin, J. T., Melgar, D., Thomas, A. M. & Searcy, J. Early warning for great earthquakes from characterization of crustal deformation patterns with deep learning. *J. Geophys. Res. Solid Earth* **126**, e2021JB022703 (2021).
- LeCun, Y., Bengio, Y. & Hinton, G. Deep learning. *Nature* **521**, 436–444 (2015).
- Ross, Z. E., Meier, M.-A. & Hauksson, E. P wave arrival picking and first-motion polarity determination with deep learning. *J. Geophys. Res. Solid Earth* **123**, 5120–5129 (2018).
- Rouet-Leduc, B., Hulbert, C., McBrearty, I. W. & Johnson, P. A. Probing slow earthquakes with deep learning. *Geophys. Res. Lett.* **47**, e2019GL085870 (2020).
- Perol, T., Gharbi, M. & Denolle, M. Convolutional neural network for earthquake detection and location. *Sci. Adv.* **4**, e1700578 (2018).
- Mousavi, S. M. & Beroza, G. C. A machine-learning approach for earthquake magnitude estimation. *Geophys. Res. Lett.* **47**, e2019GL085976 (2020).
- van den Ende, M. P. A. & Ampuero, J.-P. Automated seismic source characterisation using deep graph neural networks. *Geophys. Res. Lett.* **47**, e2020GL088690 (2020).
- Lomax, A., Michelini, A. & Jozinović, D. An investigation of rapid earthquake characterization using single-station waveforms and a convolutional neural network. *Seismol. Res. Lett.* **90**, 517–529 (2019).
- Zhang, X., Zhang, M. & Tian, X. Real-time earthquake early warning with deep learning: application to the 2016 Central Apennines, Italy earthquake sequence. *Geophys. Res. Lett.* **48**, e2020GL089394 (2021).
- Hayes, G. P. et al. Slab2, a comprehensive subduction zone geometry model. *Science* **362**, 58–61 (2018).
- LeCun, Y., Bottou, L., Bengio, Y. & Haffner, P. Gradient-based learning applied to document recognition. *Proc. IEEE* **86**, 2278–2324 (1998).
- Bletery, Q. et al. A detailed source model for the  $M_w$  9.0 Tohoku-Oki earthquake reconciling geodesy, seismology, and tsunami records. *J. Geophys. Res. Solid Earth* **119**, 7636–7653 (2014).
- Böse, M. et al. FinDer v.2: improved real-time ground-motion predictions for M2–M9 with seismic finite-source characterization. *Geophys. J. Int.* **212**, 725–742 (2018).

42. Fukushima, K. & Miyake, S. Neocognitron: a new algorithm for pattern recognition tolerant of deformations and shifts in position. *Pattern Recognit.* **15**, 455–469 (1982).
43. Rumelhart, D., Hinton, G. & Williams, R. Learning representations by back-propagating errors. *Nature* **323**, 533–536 (1986).
44. Li, Z., Zhang, Y. & Arora, S. Why are convolutional nets more sample-efficient than fully connected nets? Preprint at <https://arxiv.org/abs/2010.08515> (2021).
45. Krizhevsky, A., Sutskever, I. & Hinton, G. E. ImageNet classification with deep convolutional neural networks. In *Advances in Neural Information Processing Systems 25 (NIPS 2012)* (eds Pereira, F. et al.) (2012).
46. Pham, H., Dai, Z., Xie, Q. & Le, Q. V. Meta pseudo labels. In *Proceedings of the IEEE/CVF Conference on Computer Vision and Pattern Recognition* 11557–11568 (2021).
47. Bergen, K. J., Johnson, P. A., de Hoop, M. V. & Beroza, G. C. Machine learning for data-driven discovery in solid Earth geoscience. *Science* **363**, eaau0323 (2019).
48. Ren, C. X., Hulbert, C., Johnson, P. A. & Rouet-Leduc, B. Machine learning and fault rupture: a review. In *Machine Learning in Geosciences* (eds Moseley, B. & Krischer, L.) 57–107 (Elsevier, 2020).
49. Kingma, D. P. & Ba, J. L. Adam: a method for stochastic optimization. In *Intl Conf. Learning Representations* (eds Bengio, Y. & LeCun, Y.) (ICLR, 2015).
50. Zhu, W., Mousavi, S. M. & Beroza, G. C. Seismic signal denoising and decomposition using deep neural networks. *IEEE Trans. Geosci. Remote Sens.* **57**, 9476–9488 (2019).

**Publisher's note** Springer Nature remains neutral with regard to jurisdictional claims in published maps and institutional affiliations.



**Open Access** This article is licensed under a Creative Commons Attribution 4.0 International License, which permits use, sharing, adaptation, distribution and reproduction in any medium or format, as long as you give appropriate credit to the original author(s) and the source, provide a link to the Creative Commons license, and indicate if changes were made. The images or other third party material in this article are included in the article's Creative Commons license, unless indicated otherwise in a credit line to the material. If material is not included in the article's Creative Commons license and your intended use is not permitted by statutory regulation or exceeds the permitted use, you will need to obtain permission directly from the copyright holder. To view a copy of this license, visit <http://creativecommons.org/licenses/by/4.0/>.

© The Author(s) 2022

## Methods

### Construction of the training database

We train PEGSNet on a database of synthetic data augmented with empirical noise. For each example in the database, three-component waveforms at each station location are obtained as follows.

**Source parameters.** The event source location is randomly picked from 1,400 possible locations extracted from the Slab2.0 model of subduction geometry<sup>38</sup> at two different depths (20 and 30 km). Given latitude, longitude and depth, strike and dip angles are determined by the subduction geometry and rake is randomly extracted from a normal distribution with mean = 90° and standard deviation of 10°. The event final  $M_w$  is drawn from a uniform distribution with min = 5.5 and max = 10.0. We deliberately choose not to use a Gutenberg–Richter distribution for  $M_w$  to avoid a sampling bias during training, by which the model might better estimate certain magnitude values simply because they are more represented in the training database. Finally, from  $M_w$  we compute the scalar moment  $M_0 = 10^{1.5M_w+9.1}$ .

**Source time function.** Given  $M_0$ , a pseudo-empirical STF is computed using the STF model described in a previous work<sup>3</sup>, which includes a multiplicative error term and is valid for earthquakes with  $M_w > 7.0$ . In summary,

$$\text{STF}(t) = M_0 \frac{f(t)}{\int f(t) dt}, \quad (1)$$

with:

$$f(t) = t \exp\{-0.5(\lambda t)^2\} [1 + N(t)], \quad (2a)$$

$$\lambda = 10^{(7.24 - 0.41 \log(M_0) + \varepsilon)}, \quad (2b)$$

$$N(t) = 0.38 \frac{n(t)}{\sigma}, \quad (2c)$$

where  $\varepsilon$  is drawn from a Gaussian distribution with zero mean and standard deviation of 0.15,  $n(t)$  is the time integral of a Gaussian noise time series with zero mean and  $\sigma$  is the standard deviation of  $n(t)$ . The term  $\varepsilon$  accounts for variability in the STF duration for a given  $M_0$ , whereas  $N(t)$  models the characteristics of noise observed in real STF<sup>5</sup>. Examples of final STF<sup>5</sup> for different magnitude values are shown in Extended Data Fig. 1.

**Computing synthetic waveforms.** With the selected source parameters and STF<sup>5</sup>, we use the normal-mode approach described in a previous work<sup>14</sup> to compute three-component synthetic waveforms in a spatial domain of about 20° around the source epicentre. The resulting seismometer responses are convolved with the STF of the corresponding synthetic event and multiplied by the scalar moment to obtain synthetic traces of acceleration sampled at 1 Hz at each station location. Finally, traces are bandpass-filtered between 2.0 mHz (Butterworth, two poles, causal) and 30.0 mHz (Butterworth, six poles, causal). The final seismograms are 700 s long centred at the event origin time.

**Noise database.** The noise database consists of 259 days of three-component waveforms for two non-continuous time intervals: between January 2011 and October 2011 (excluding March 2011) and between January 2014 and April 2014. These intervals have been chosen to sample variable (seasonal) noise conditions. We note that the temporal range spanned by the noise database does not overlap with any of the earthquakes used for real data cases (Extended Data Fig. 10a). We first divide the daily recordings into 1-h-long traces and then apply limited preprocessing, removing the instrument response, the mean and the

linear trend, converting to acceleration and decimating the original traces from 20 to 1 Hz. Finally, each trace is filtered using the same bandpass filter applied to the synthetic seismograms (see previous step) and stored. Note that no a priori assumptions on levels and characteristics of the selected noise are made. On the contrary, we include all real noise conditions found in continuous seismic recordings in the specified period range. This is because, in principle, we want the model to be able to generalize well under a broad range of noise conditions.

**Adding empirical noise to synthetics.** From the noise database described in the previous step, a realization of noise (700 s long) is extracted by randomly selecting a starting time point. In this process, we make sure to use different noise data in training, validation and test sets. To preserve spatial coherence of noise across the seismic network, the same time interval is used for all stations for a given event. The selected noise traces are then added to the corresponding acceleration seismograms to produce the final input data for PEGSNet. If noise data are not available for one or more stations in the selected time window for a given event, we discard those stations by setting the corresponding final trace amplitudes (noise and PEGS) to zero in the input data.

**Preprocessing of input data.** Before being fed to PEGSNet, we first sort the input waveform for each example based on station longitude. We found this approach to be effective, but we note that the problem of concatenating station waveforms in a meaningful way in deep learning is an active area of research<sup>35</sup>. Then, on the basis of the theoretical P-wave arrival time ( $T_p$ ) at each station for a given event, we set the amplitude of the seismograms to zero for  $t \geq T_p$ . Note that PEGSNet does not perform P-wave triggering itself. Instead, it relies on theoretical P-wave arrivals. In a real-time scenario, any existing P-wave triggering algorithm (whether based on machine learning or not) can be used to set the switch on the corresponding stations whose data can then be passed to PEGSNet.

To limit the influence of very noisy traces and to suppress high amplitudes (possibly related to the background regional seismicity), we further clipped the resulting trace using a threshold of  $\pm 10 \text{ nm s}^{-2}$ . This threshold is chosen according to the maximum PEGS amplitude for an  $M_w = 10$  earthquake at 315 s as found in the calculated database of noise-free synthetics. Amplitudes are finally scaled by  $10 \text{ nm s}^{-2}$  to facilitate convergence of the optimizer, and at the same time, to preserve information about the relative amplitudes of the PEGS radiation pattern across the seismic network. Finally, to simulate missing data and/or problematic sensors, we randomly mute 5% of the stations for each event by setting to zero the amplitudes of the corresponding traces.

### Deep learning and PEGSNet

**Previous work.** Convolutional neural networks (CNNs) originated in neocognitron<sup>42</sup> and became practical once it was found that the backpropagation procedure<sup>43</sup> can be used to compute the gradient of an objective function with respect to the weights of the network. CNNs are a regularized form of neural networks, that is, the function space they represent is simpler and they are more sample-efficient than fully connected neural networks<sup>44</sup>. Deep CNNs have brought about a revolution in computer vision, and have had a role in almost every state-of-the-art approach for tasks related to recognition and detection in images<sup>45,46</sup>. In geoscience, machine learning has shown strong potential for data-driven discovery of previously unknown signals and physical processes hidden in large volumes of noisy data<sup>47,48</sup>.

We note, however, that our choice of a deep learning model over classical machine learning models offers an appealing framework to directly deal with raw seismograms. As a consequence, this choice enables us to explore a larger function space that is not limited by building an a priori set of features, which is a requirement for applying classical machine learning models on seismogram data.

# Article

Successful applications of deep learning in seismology have provided new tools for pushing the detection limit of small seismic signals<sup>31,32</sup> and for the characterization of earthquake source parameters (magnitude and location)<sup>33–35</sup> with EEWs applications<sup>29,36,37</sup>. We present a deep learning model, PEGSNet, trained to estimate earthquake location and track the time-dependent magnitude,  $M_w(t)$ , from PEGS data, before P-wave arrivals.

**Description of PEGSNet architecture.** PEGSNet is a deep CNN that combines convolutional layers and fully connected layers in sequence (Extended Data Fig. 2a). The input of the network is a multi-channel image of size  $(M, N, c)$  where  $M$  is 315 (corresponding to 315-s-long traces sampled at 1 Hz),  $N$  is the number of stations (74) and  $c$  is the number of seismogram components used (three: east, north and vertical). The outputs of the network are three values corresponding to moment magnitude ( $M_w$ ), latitude ( $\varphi$ ) and longitude ( $\lambda$ ), where  $M_w$  is time dependent. The training strategy used to learn  $M_w(t)$  from the data is described below.

The first part of the model (the CNN) consists of eight convolutional blocks. Each block is made of one convolutional layer with a rectified linear unit (ReLU) activation function followed by a dropout layer. The number of filters in each convolutional layer increases from 32 (blocks 1–5) to 64 (blocks 6–7) to 128 (block 8) to progressively extract more detailed features of the input data. A fixed kernel size of  $3 \times 3$  is used in each convolutional layer. We use spatial dropout with a fixed rate of 4% to reduce overfitting of the training set. Maximum pooling layers are added starting from block 4 to reduce the overall dimension of the input features by a factor of 4. The output of the CNN is then flattened and fed to a sequence of two dense layers of size 512, and 256 with a ReLU activation function and standard dropout with a 4% rate. Fully connected layers perform the high-level reasoning and map the learned features to the desired outputs. The output layer consists of three neurons that perform regression through a hyperbolic tangent activation function (tanh). The labelling strategy for  $M_w(t)$ ,  $\varphi$  and  $\lambda$  is discussed in detail below. The total number of parameters in the network is 1,479,427.

**Learning strategy.** The purpose of the model is to track the moment released by a given earthquake as it evolves from the origin time. A specific learning strategy has been developed to address this task (Extended Data Fig. 2).

**Labelling.** Labels are  $\varphi$ ,  $\lambda$  and a time-dependent  $M_w$ .  $\varphi$ ,  $\lambda$  simply correspond to the true values for each event.  $M_w(t)$  is the time integration of the STF for each event. As detailed in the next section, the model is trained by randomly perturbing the ending time of the input seismograms, so that for a given ending time the input data are associated with the value of  $M_w(t)$  at that time. To enforce the role of the tanh activation function in the output layer, we further scale all the labels to fall in the  $[-1, 1]$  interval through min/max normalization.

**Learning the time-dependent moment release.** In order for PEGSNet to learn  $M_w(t)$ , we randomly perturb the starting time of the input data during training (Extended Data Fig. 2c). Every time that an example is extracted from the dataset, a value ( $T_1$ ) is drawn at random from a uniform distribution between  $-315$  and  $0$  (s).  $T_1$  is the time relative to the earthquake origin time ( $T_0$ ) corresponding to the starting time of the selected seismograms for that example. In practice, from the 700-s-long seismograms (centred on  $T_0$ ) in the database, we extract traces from  $T_1$  to  $T_2 = T_1 + 315$  s: for  $T_1 = -315$  s the extracted traces end at  $T_0$ ; for  $T_1 = 0$  s the traces start at  $T_0$  and end 315 s after. Once a value for  $T_1$  is selected, the value of  $M_w(T_2)$  is assigned as the corresponding label for this example (Extended Data Fig. 2d). This enables the model to learn patterns in the data as the STF evolves with time.

**Training.** The full database (500,000 examples of synthetic earthquakes) is split into training (350,000) validation (100,000) and test (50,000) sets, following a 70/20/10 strategy. The network is trained for

200 epochs (using batches of size 512) on the training set by minimizing the Huber loss between the true values and the predicted earthquake source parameters using the Adam algorithm<sup>49</sup>, with its default parameters ( $\beta_1 = 0.9$  and  $\beta_2 = 0.999$ ) and a learning rate of 0.001. At the end of each epoch, the model is tested on the validation set to assess the learning performance and avoid overfitting (Extended Data Fig. 2b). After learning, the model that achieved the best performance (lowest loss value) on the validation set is selected as the final model. The final model is then tested against the test set (therefore with data that has never been seen by PEGSNet during training) to assess its final performance.

**Testing strategy.** Once PEGSNet is trained, it can be used to estimate  $M_w(t)$  in a real-time scenario. We assess the latency performance of PEGSNet on the test set with the following procedure (Extended Data Fig. 4). For each example in the test set, we slide a 315-s-long window [ $T_1, T_2 = T_1 + 315$  s] through the data with a time step of 1 s. The starting window ends at the earthquake origin time  $T_0$  ( $T_2 = T_0$  and  $T_1 = T_0 - 315$  s) and the final window starts at the earthquake origin time ( $T_2 = T_0 + 315$  s and  $T_1 = T_0$ ). We let PEGSNet predict  $M_w(T_2)$  at each time step, thus progressively reconstructing the STF. Each  $M_w(t)$  estimate made by PEGSNet only makes use of information in the past 315 s. The same procedure is also applied to real data (Fig. 3 and Extended Data Fig. 10), to simulate a playback of the data as if they were fed to PEGSNet in real-time.

**Test on noise-free synthetics.** We investigate the performance of PEGSNet by using the same database described above but without including noise in the input data. Training and testing on noise-free synthetic data provides an upper limit of PEGSNet performance. Although this experiment represents a virtually impossible scenario for real-world applications, the results can reveal inherent limitations of our model or in the input data. Extended Data Fig. 6a shows the accuracy map for the test set. As expected, the model is able to determine the final  $M_w$  of the events with high accuracy and similar performance regardless of the actual  $M_w$  of the event, except at early times. To look at the latency performance more in detail, Extended Data Fig. 6b shows the density plot of the residuals as a function of time for the whole noise-free test set. Errors are mostly confined within  $\pm 0.1$  but are relatively higher in the first 10–15 s after origin. We relate this observation to a combination of two factors: first, in the first 15 s after origin, very small PEGS amplitudes are expected at very few stations in the seismic network, partially owing to the cancelling effect between the direct and induced terms. This can lead to a situation in which little information is present in the input images and the model ends up predicting the mean value of the labels at these early times. Second, the seismic network geometry may not be optimal for recording PEGS amplitudes in this time window. Finally, we note that similar behaviour is observed for the results obtained on the noisy database (Fig. 2a, b) but with a higher latency (30–40 s). This highlights the role of noise in degrading the optimal performance of PEGSNet.

## Preprocessing of real data

The preprocessing steps for real data closely follow the procedure detailed in previous work<sup>7</sup>. For each station and each component:

1. Select 1-h-long raw seismograms ending at the theoretical  $T_p$  calculated using the source location from the United States Geological Survey (USGS) catalogue (Extended Data Fig. 10a);
2. Remove the mean;
3. Remove the instrument response and obtain acceleration signals;
4. Lowpass 30.0 mHz (Butterworth, six poles, causal);
5. Decimate to 1 Hz;
6. Highpass 2.0 mHz (Butterworth, two poles, causal);
7. Clip to  $\pm 10$  nm s<sup>-2</sup> and scale by the same value;
8. Pad with zeros for  $t \geq T_p$  and select 700-s-long trace centred on  $T_0$ .



This procedure is the same as that used to generate the synthetic database, except that here, traces need to be cut at the P-wave arrival first to avoid contamination of PEGS by the P-wave during instrument response removal.

To speed up our testing procedure (see Methods subsection ‘Testing strategy’), the data are preprocessed once and then sliced into input for PEGSNet at each time step. In an online version of our model, this is unfeasible as all the preprocessing steps need to be applied each time that new packets of data are streamed in. We simulate the conditions of a real-time workflow on the Tohoku-Oki data to assess potential discrepancies with the simplified workflow in the results: at each time step, we apply the preprocessing steps described above, using 1-h-long trace ending at the current time step. We find that the resulting PEGSNet predictions obtained using the two workflows are essentially indistinguishable from each other (Extended Data Fig. 11).

### Predictions on additional real data

We tested PEGSNet on all the subduction earthquakes (dip-slip mechanism within 40 km from the megathrust) with  $M_w \geq 7$  that have occurred since January 2003, without considering aftershocks (Extended Data Fig. 10). Among them, the 2003  $M_w = 8.2$  Hokkaido earthquake is at the edge of PEGSNet’s lower sensitivity limit of 8.3. For this event, PEGSNet estimates the final  $M_w$  after about two minutes (Extended Data Fig. 10b), in agreement with what was previously observed on the test set for events with similar magnitude (Fig. 2a). However, given the expected lower accuracy and higher errors for this event, we consider these predictions less reliable. For lower-magnitude events, PEGSNet predictions converge toward the noise baseline of 6.5 or never exceed its lower sensitivity limit, confirming that PEGS from  $M_w < 8.0$  earthquakes are essentially indistinguishable from noise (Extended Data Fig. 10c–f). Deep learning denoising techniques for coherent noise removal<sup>50</sup> might prove successful in enhancing PEGSNet performance and will be the subject of future work.

### Data availability

Waveforms and metadata used in this study were provided by the Global Seismograph Network<sup>51</sup>, the New China Digital Seismograph Network<sup>52</sup>, GEOSCOPE<sup>53</sup> (IPGP/EOST, 1982), the Japan Meteorological Agency Seismic Network (<https://www.jma.go.jp/en/quake>) and the National Research Institute for Earth Science and Disaster Resilience/F-net<sup>54</sup>, all publicly available from the IRIS Data Management Center (<https://ds.iris.edu/ds/nodes/dmc>) and the F-net data centre (<https://www.fnet.bosai.go.jp/top.php>). Source data are provided with this paper.

### Code availability

The codes used to generate and analyse the data shown within this paper are available from the corresponding author upon request. PEGSNet is built and trained using PyTorch<sup>55</sup>. Waveforms were retrieved from IRIS with Obspy<sup>56</sup> and obspyDMT<sup>57</sup>. Figures were produced with the Generic Mapping Tool (GMT)<sup>58</sup> and matplotlib<sup>59</sup>.

51. Albuquerque Seismological Laboratory (ASL)/USGS. *Global Seismographic Network (GSN-IRIS/USGS)* (International Federation of Digital Seismograph Networks, 1988); <https://doi.org/10.7914/SN/IU>.
52. ASL/USGS. *New China Digital Seismograph Network (NCDSN)* (International Federation of Digital Seismograph Networks, 1992); <https://doi.org/10.7914/SN/IC>.
53. Institut de physique du globe de Paris (IPGP) and École et Observatoire des Sciences de la Terre de Strasbourg (EOST). *GEOSCOPE. French Global Network of Broad Band Seismic Stations* (IPGP, 1982); <https://doi.org/10.18715/GEOSCOPE.G>.
54. Okada, Y. et al. Recent progress of seismic observation networks in Japan — Hi-net, F-net, K-NET and KIK-net. *Earth Planets Space* **56**, xv–xxviii (2004).
55. Paszke et al. PyTorch: an imperative style, high-performance deep learning library. In *Advances in Neural Information Processing Systems 32 (NeurIPS 2019)* (eds Wallach, H. et al.) 8024–8035 (Curran Associates, 2019).
56. Beyreuther, M. et al. Obspy: a Python toolbox for seismology. *Seismol. Res. Lett.* **81**, 530–533 (2010).
57. Hosseini, K. & Sigloch, K. ObspyDMT: a Python toolbox for retrieving and processing large seismological data sets. *Solid Earth* **8**, 1047–1070 (2017).
58. Wessel, P. et al. The Generic Mapping Tools version 6. *Geochem. Geophys. Geosyst.* **20**, 5556–5564 (2019).
59. Hunter, J. D. Matplotlib: a 2D graphics environment. *Comput. Sci. Eng.* **9**, 90–95 (2007).

**Acknowledgements** This project has received funding from the European Research Council (ERC) under the European Union’s Horizon 2020 research and innovation programme (grant agreement 949221). This work has been supported by the French government, through the UCAJEDI Investments in the Future project managed by the National Research Agency (ANR), ANR-15-IDEX-01. This work was granted access to the HPC resources of IDRIS under the allocations 2020-AD011012142, 2021-AP011012536 and 2021-A0101012314 made by GENCI. B.R.-L.’s work was supported by Institutional Support (LDRD) at Los Alamos (20200278ER). Numerical computations for the synthetic database of PEGS were performed on the S-CAPAD platform, IPGP, France. We thank M. Böse for providing the results of FinDer2 on Tohoku-Oki data.

**Author contributions** A.L. developed PEGSNet and produced all the results and figures presented here. Q.B. had the original idea and supervised the study. B.R.-L. designed the preliminary algorithm and provided the raw noise data. J.-P.A. provided expertise in modelling PEGS and realistic source time functions. K.J. provided the synthetic database of PEGS necessary to produce the training database. All the authors contributed to writing the manuscript.

**Competing interests** The authors declare no competing interests.

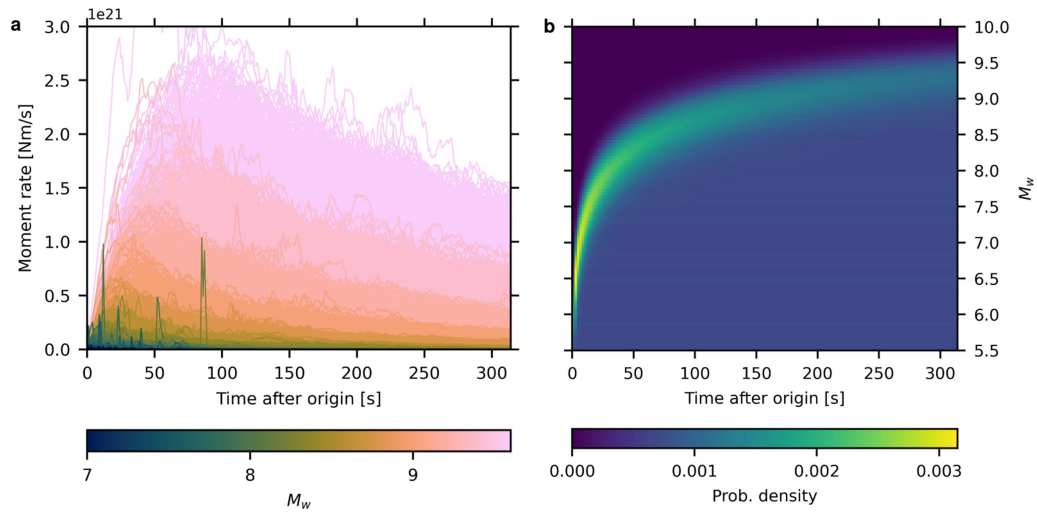
### Additional information

**Supplementary information** The online version contains supplementary material available at <https://doi.org/10.1038/s41586-022-04672-7>.

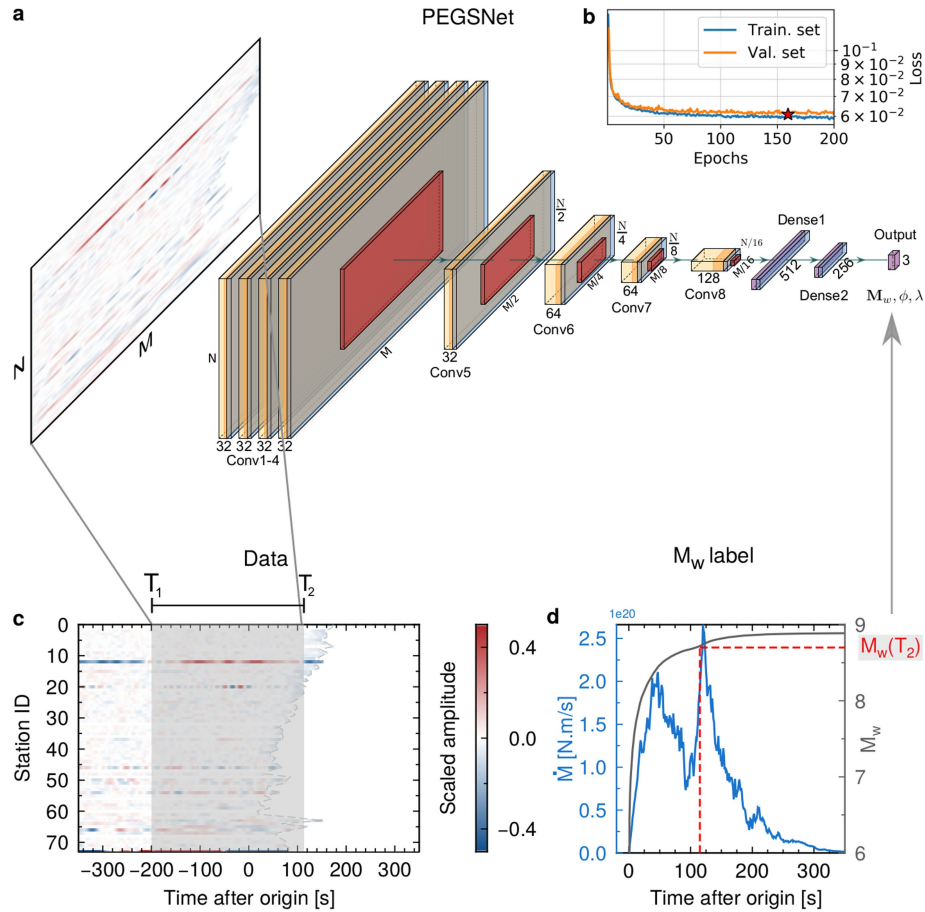
**Correspondence and requests for materials** should be addressed to Andrea Licciardi.

**Peer review information** *Nature* thanks Benjamin Fong Chao and the other, anonymous, reviewer(s) for their contribution to the peer review of this work. Peer reviewer reports are available.

**Reprints and permissions information** is available at <http://www.nature.com/reprints>.



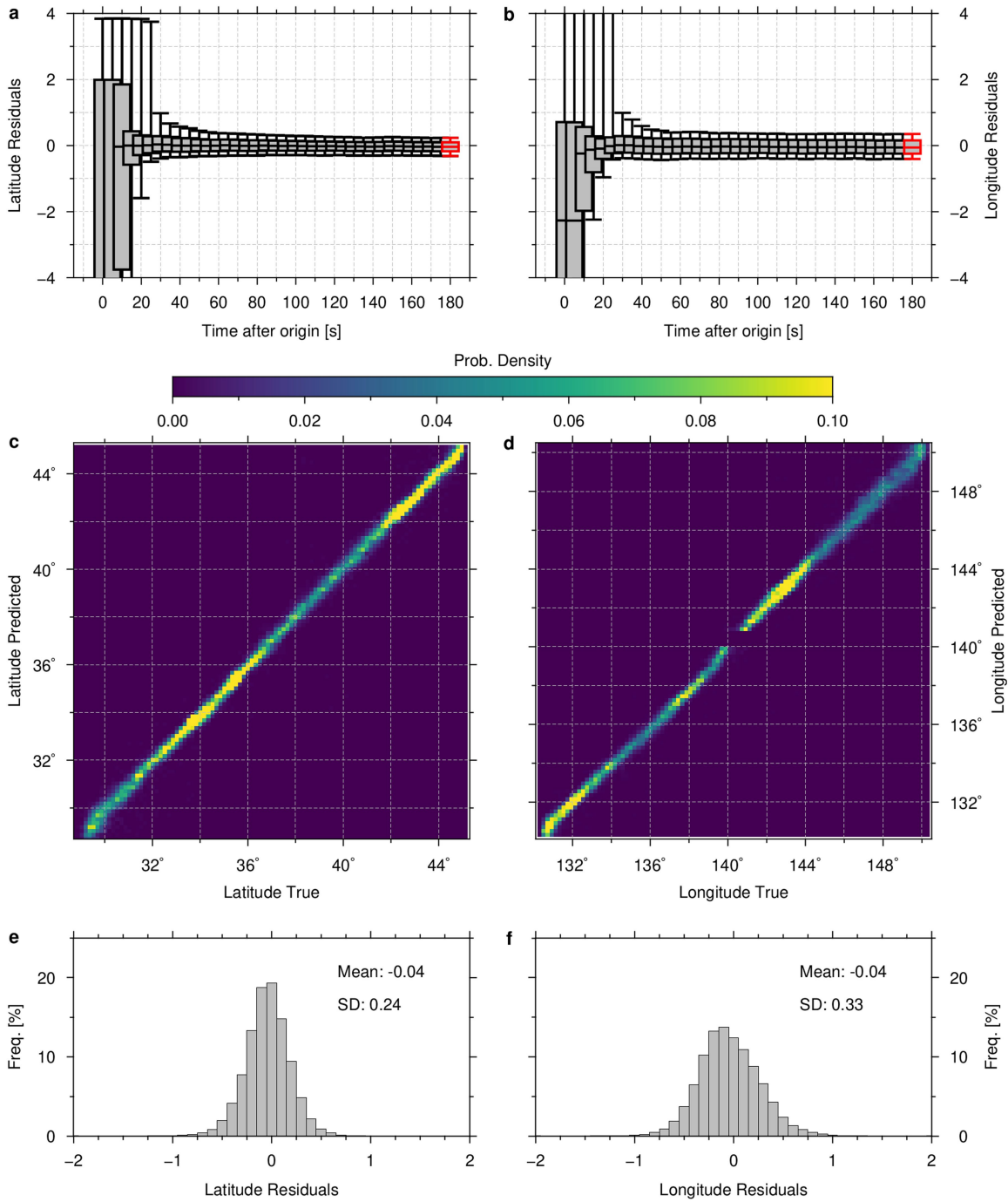
**Extended Data Fig. 1 | STF database. a**, STFs (moment rate) coloured by their final magnitude in the training database from a previous model<sup>5</sup> (see description in Methods). Only STFs for events with final  $M_w$  between 7.0 and 9.5 are shown. **b**, The complete  $M_w(t)$  distribution is used for labelling the database.



**Extended Data Fig. 2 | PEGSNet architecture and training strategy.**

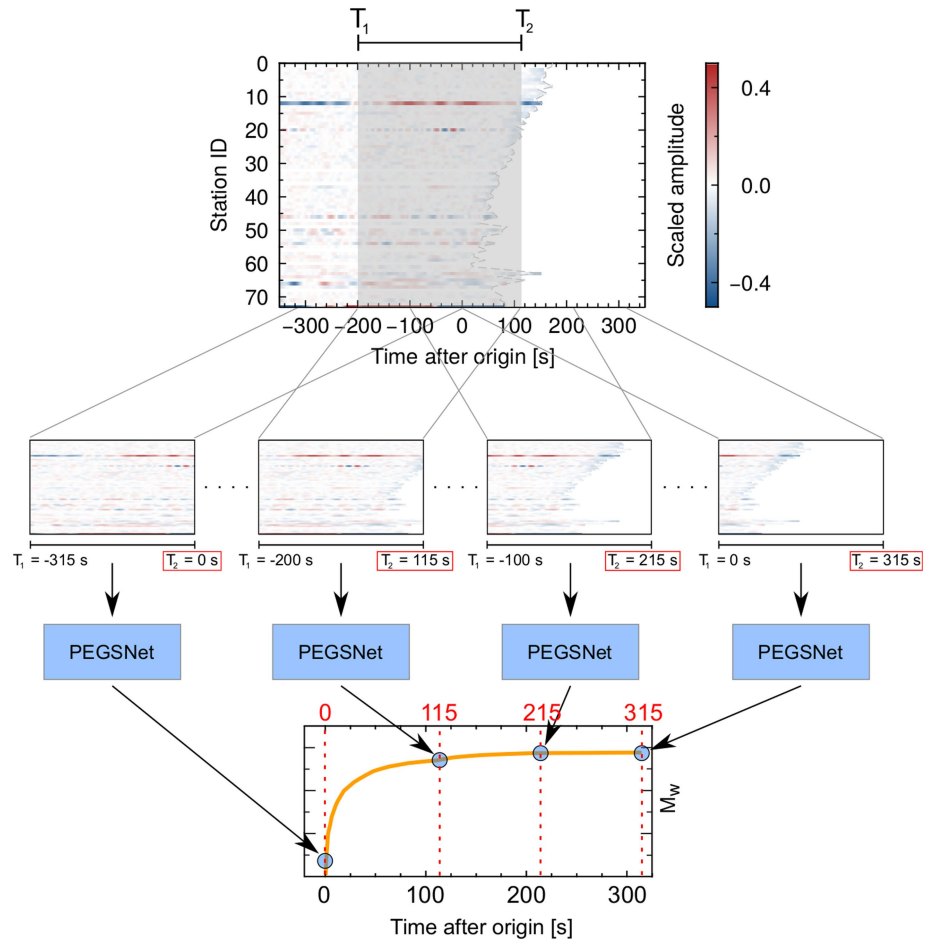
**a**, The input data for one example consists of a three-channel image of shape  $M \times N$ , where  $M$  is the number of time samples and  $N$  is the number of seismic stations. Only the vertical component of the input data is displayed for simplicity. Each convolutional block is composed of a convolutional layer (yellow) with a ReLu activation (orange), a spatial dropout layer (light blue). Max pooling layers (red) reduce each dimension of the input data by a factor of two. The number of filters used in each convolutional layer is indicated for clarity. The last convolutional block is connected to dense layers (purple) (using a ReLu activation function), with dropout (light blue). The output layer uses a tanh activation function to predict values of  $M_w$ , latitude ( $\phi$ ) and longitude ( $\lambda$ ). **b**, The value of the Huber loss is plotted as a function of epochs

for the training (Train.) and validation (Val.) sets. Each epoch corresponds to a full pass over the training set in batches of size 512. The red star indicates the epoch with the minimum value of the loss on the validation set. The corresponding model is used for predictions on the test set and real data. **c**, Data from one example from the training database (vertical component). The grey shaded area corresponds to the input data for PEGSNet shown in **a**.  $T_1$  and  $T_2$  are the beginning and end of the selected input window. During training,  $T_1$  is selected at random and  $T_2 = T_1 + 315$  s. **d**, Moment rate (blue) and  $M_w(t)$  (dark grey) for the selected event. Given the randomly selected value for  $T_1$  for this example, the corresponding label is  $M_w(T_2)$ , that is, at the end of the selected window. This is compared with the predicted  $M_w$  estimated by PEGSNet in **a** and used for training.



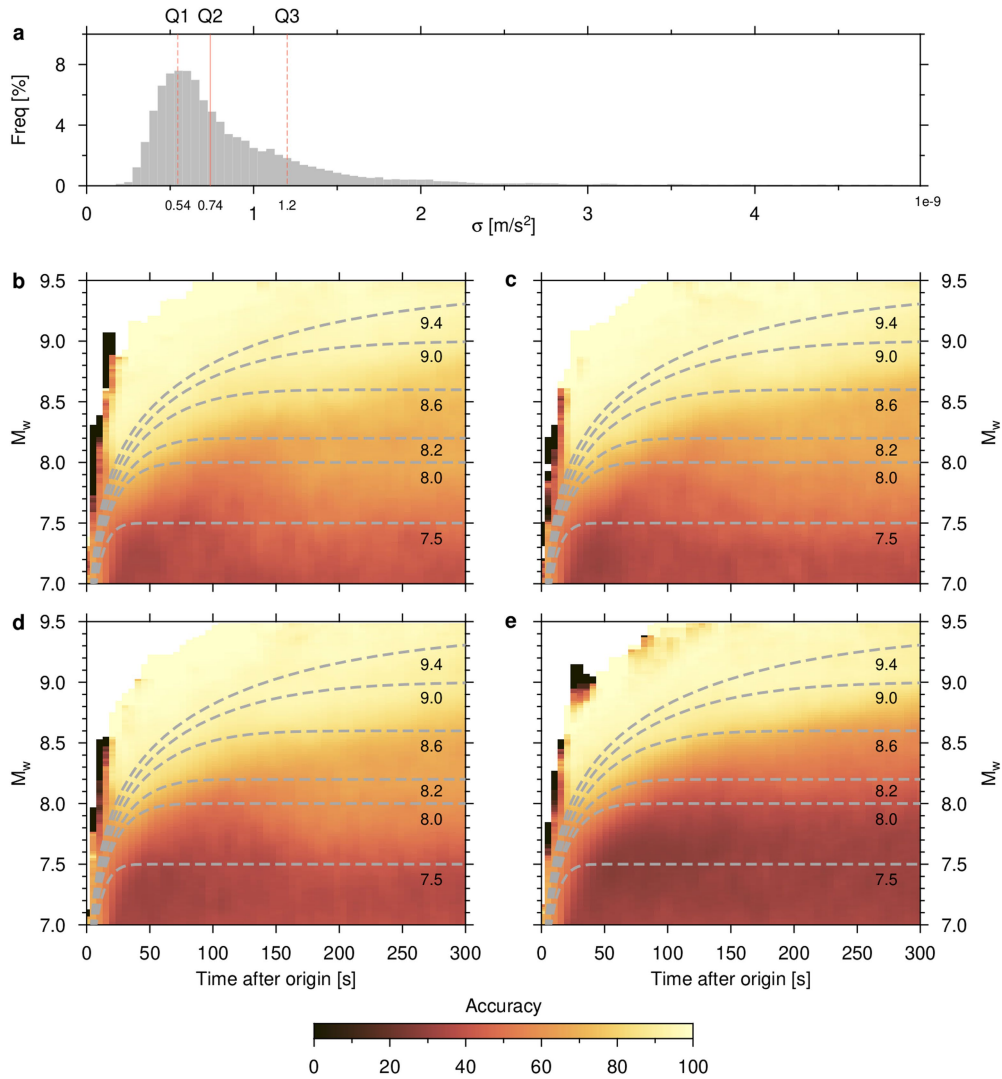
**Extended Data Fig. 3 | Results of predictions on the test set for location.** **a, b**, Analysis of the residuals as a function of time (only the first 180 s from origin time are shown) for latitude (**a**) and longitude (**b**). Boxes correspond to the third to first (Q3–Q1) interquartile range, the black line within the boxes is the median and whiskers indicate the 5th and 95th percentiles. **c, d**, Density

plot of true versus predicted latitude (**c**) and longitude (**d**) values at 180 s after origin (red boxes in **a, b**). **e, f**, Corresponding histogram of the residuals with reported mean and standard deviations for latitude (**e**) and longitude (**f**) at 180 s after origin.



**Extended Data Fig. 4 | Testing procedure.** Each input example (top row) is parsed with a time window of length 315 s sliding with 1-s time step. At each time step, the data between  $T_1$  and  $T_2$  are passed to PEGSNet (middle row). For display purposes, only four specific time steps are shown here with their  $T_1$  and  $T_2$  indicated for clarity. The window with  $T_1 = -200$  s and  $T_2 = 115$  s corresponds to

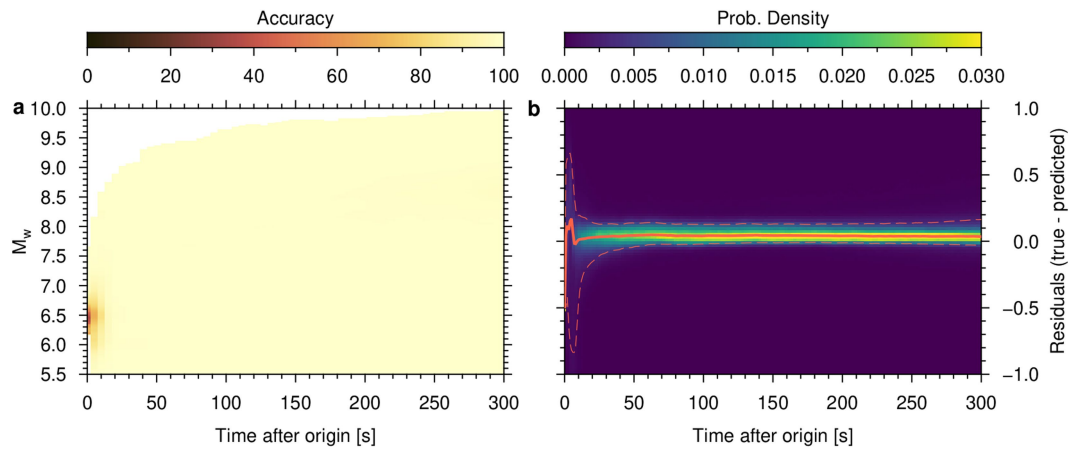
the grey shaded area in the top row. At each time step, PEGSNet makes a prediction of  $M_w$  at the end of the input window, that is,  $M_w(T_2)$  (blue circles in the bottom figure), to reconstruct the STF (yellow line) in a real-time scenario. Red dashed lines indicate the value of  $T_2$  of each input window.



**Extended Data Fig. 5 | Effect of noise on PEGSNet predictions.** **a**, Frequency distribution of the mean standard deviation of the noise ( $\sigma$ ) for the whole seismic network, in a pre-event time window of five minutes, for test set only. The solid red line is the median of the distribution (second quartile, Q2), dashed lines are the first (Q1) and third (Q3) quartiles. **b–e**, As in Fig. 2a, but computed

on subsets of the test set for which  $\sigma < Q1$  (**b**),  $Q1 < \sigma < Q2$  (**c**),  $Q2 < \sigma < Q3$  (**d**), and  $\sigma > Q3$  (**e**). Note the high accuracy below 8.3 after 150 s from origin time for low-noise conditions (**b**). These maps give empirical limits on the noise levels that could potentially be useful to interpret the performance of our model in real time.

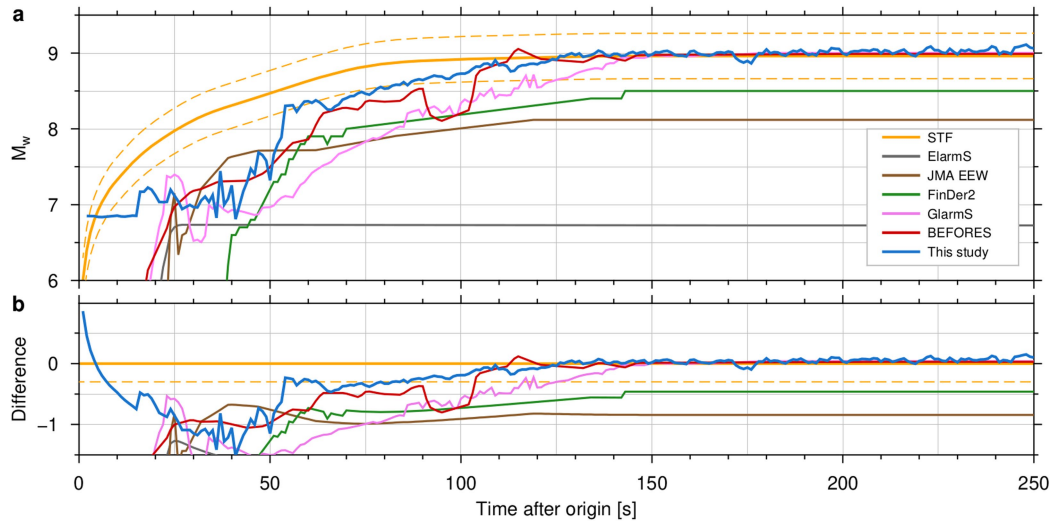




**Extended Data Fig. 6 | Results on noise-free test set.** **a**, As in Fig. 2a, but for a test set including only noise-free PEGS waveforms. **b**, Density plot of the residuals as a function of time for the same test set. The solid red line is the

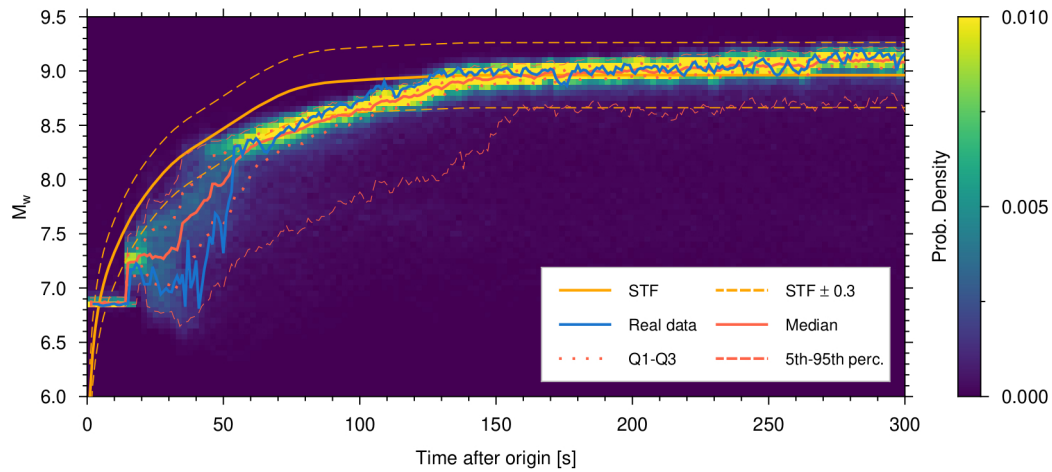
median, the dashed lines are the 5th and 95th percentiles of the distribution. Note that both in **a** and **b**, the predictions are obtained for a model that has been trained on a database of noise-free synthetics.

2011/03/11 05:46:24 -- Tohoku-Oki



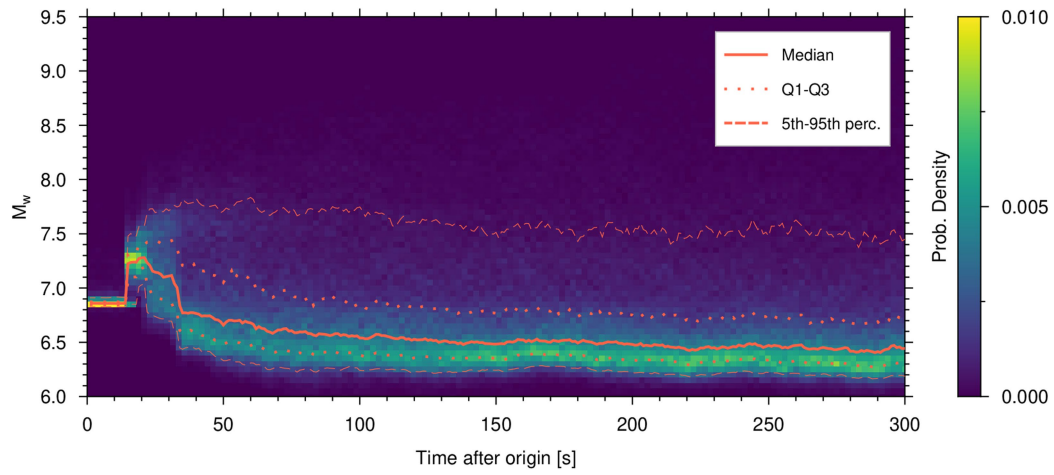
**Extended Data Fig. 7 | Comparison of PEGSNet with existing EWS.** **a, b,** As in Fig. 3, but with two additional EWS algorithms included. The results for Tohoku of finite-fault GNSS-based G-larmS<sup>28</sup> and seismic point-source ElarmS

are taken from an earlier work<sup>28</sup>. In the main text, only the best-performing algorithm for each type (JMA, point-source; FinDer2, seismic finite-fault; and BEFORES, GNSS-based finite-fault) are shown.



**Extended Data Fig. 8 | Synthetic test with Tohoku STF.** Density plot of the predictions on 1,000 examples obtained by combining different noise recordings (randomly extracted from the test set) with PEGS waveforms, from a synthetic source that mimics that of the Tohoku-Oki earthquake. The median, Q1-Q3 interquartile range and the 5th-95th percentiles of the distribution are reported with solid, dotted and dashed red lines, respectively. The synthetic Tohoku-like source is obtained from the 'true' STF (orange line, same as in Fig. 3 with  $\pm 0.3 M_w$  indicated by dashed lines), the hypocentre location (Extended Data Fig. 10a), and the following values for the strike, dip and rake:  $193.0^\circ$ ,  $8.9^\circ$  and  $78.4^\circ$  (USGS catalogue). The workflow described in Methods is used to

combine synthetics and noise. PEGSNet prediction for real Tohoku data is reported for comparison (blue line, same as in Fig. 3). Even if it has been trained on synthetic data plus noise, PEGSNet is able to generalize well to real data (the blue line is within the expected variability of the predictions obtained on synthetics). In the first 50 s after origin, the variability of the predictions is high and strongly affected by noise (similar to Fig. 2c), whereas after 50 s, predictions have similar  $M_w(t)$  values and therefore are more robust. Note that for the lowest noise conditions, faster PEGSNet response is virtually possible, as early as about 30 s after origin (as indicated by the 95th percentile of the distribution).

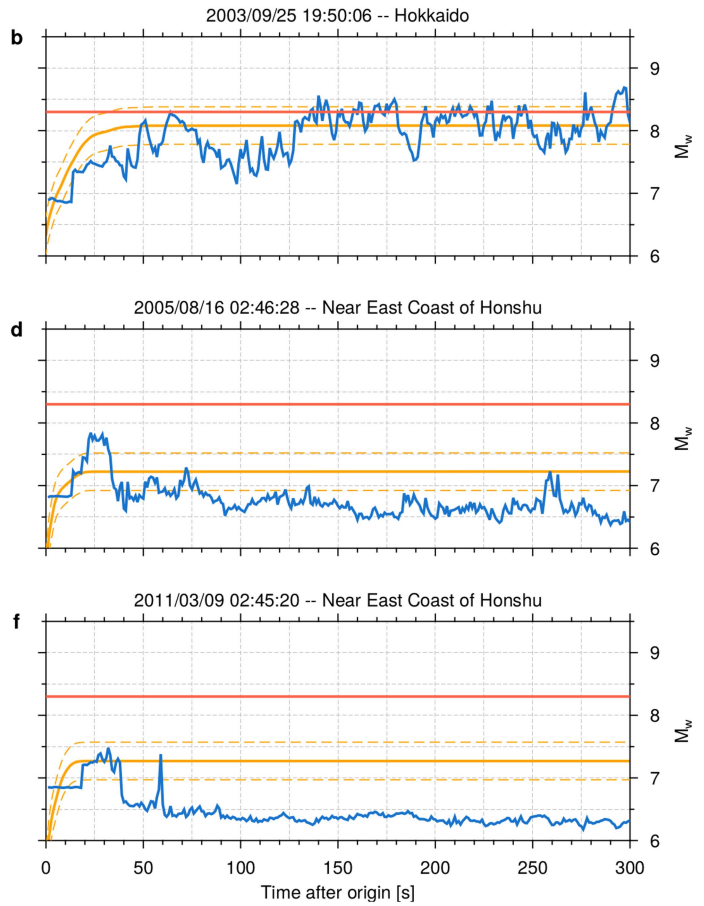
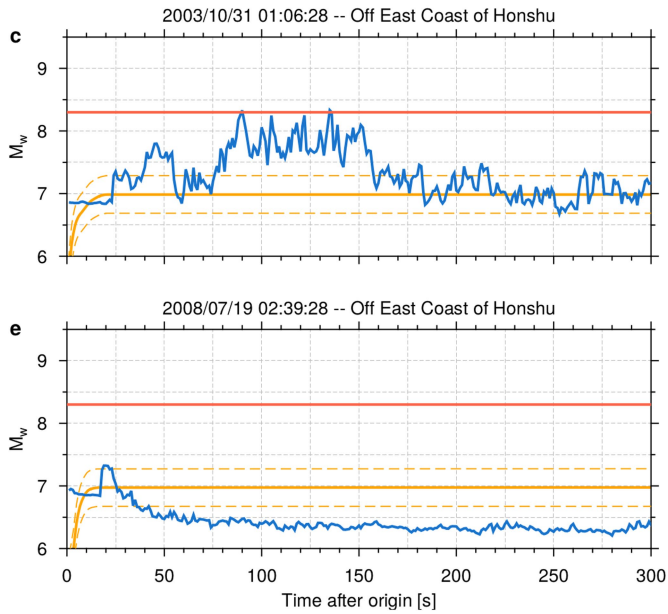


**Extended Data Fig. 9 | PEGSNet noise test.** Density plot of the predictions obtained for 1,000 real noise recordings (the same used in Extended Data Fig. 8) assuming P-wave arrivals (but no PEGS) as in the real data for the Tohoku-Oki earthquake. The median, Q1-Q3 interquartile range and the 5th-95th percentiles of the distribution are reported with solid, dotted and dashed

red lines respectively. This test confirms that the results of Fig. 3 are indeed constrained by the data in the pre-P-wave time window (PEGS). The predicted  $M_w(t)$  tends towards a constant value of 6.5, which is considered as the baseline value when no information can be extracted from PEGS.

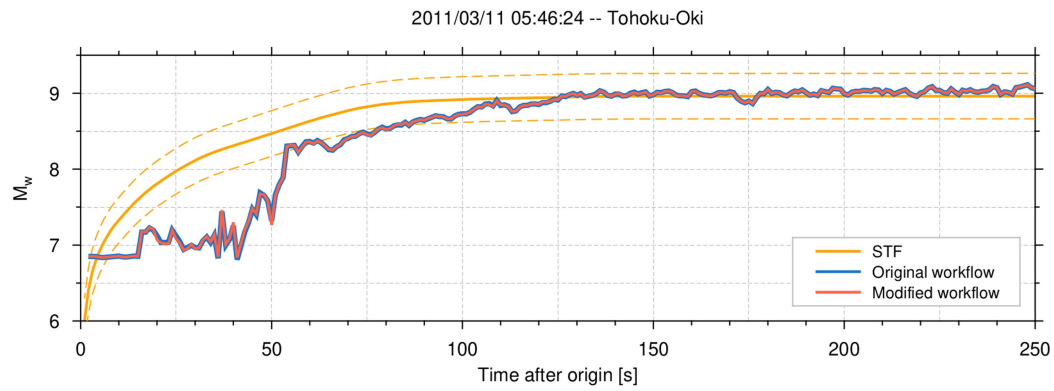
**a**

Name	$M_w$	Longitude	Latitude	Depth [km]
2003-09-25T19:50:06	8.2	143.910	41.815	27.0
2003-10-31T01:06:28	7.0	142.619	37.812	10.0
2005-08-16T02:46:28	7.2	142.039	38.276	36.0
2008-07-19T02:39:28	7.0	142.214	37.552	22.0
2011-03-09T02:45:20	7.3	142.842	38.435	32.0
2011-03-11T05:46:24	9.1	142.373	38.297	29.0



**Extended Data Fig. 10 | PEGSNet predictions on real data. a**, List of earthquakes used for the real data cases. All parameters are taken from the USGS catalogue. Earthquakes were selected according to the following criteria:  $M_w \geq 7.0$ , dip-slip focal mechanism and located within 40 km from the source locations used for training (green lines in Fig. 1). **b–f**, PEGSNet  $M_w(t)$  predictions are indicated by the blue line. The integrated STFs (orange lines) are taken from the SCARDEC database with dashed lines representing  $\pm 0.3$  magnitude units.

The red horizontal line marks the empirical lower limit of PEGSNet sensitivity (8.3). Note that for the 2003  $M_w$  8.2 Hokkaido earthquake (**b**), this limit is crossed several times after 120 s from origin time. Out of four events with final  $M_w$  below 8 (**c–f**), three (**d–f**) show a predicted  $M_w(t)$  that is constant around the noise baseline (see Extended Data Fig. 9) indicating that no information can be extracted from the pre-P-wave time window.

**Extended Data Fig. 11 | PEGSNet predictions for two data workflows.**

The predictions for the Tohoku-Oki data obtained through the original workflow described in Methods (blue line, same as in Fig. 3) are compared with those obtained with a modified workflow (red line). Instead of preprocessing the data once and then slice them into input windows for PEGSNet (original

workflow), the data are preprocessed and fed to PEGSNet at each time step (modified workflow, see details in Methods) to simulate an online scenario. The results of two workflows show negligible differences. Note that the blue line is twice as thick as the red line. For reference, the orange lines indicate the true STF (solid) and  $\pm 0.3$  magnitude units (dashed).



### 3 Perspectives

Le développement de PEGSnet est un projet d'envergure, financé par l'ERC Starting EARLI. Ce financement me permet d'encadrer une équipe de 2 doctorants et 2 postdoctorants, Gabriela Arias, Pablo Lara, Andrea Licciardi et Kévin Juhel. À court terme, nous travaillons sur des applications régionales ainsi que sur une technique de débruitage des PEGS par IA. À moyen terme, nous envisageons une application globale : un algorithme pouvant estimer quasi-instantanément la magnitude et la localisation des grands séismes partout sur Terre à partir de données sismologiques disponibles en temps réel partout sur Terre. Enfin, nous travaillons sur un algorithme d'IA complémentaire pour l'alerte des séismes de magnitude inférieure à 8.

#### 3.1 Applications régionales

##### Rétrospective du séisme de Maule ( $M_w$ 8.8, Chili 2010)

Dans le cadre de sa thèse débutée en Janvier 2021, Gabriela Arias exporte au Chili (Figure IV.2) l'approche développée par Andrea Licciardi au Japon.

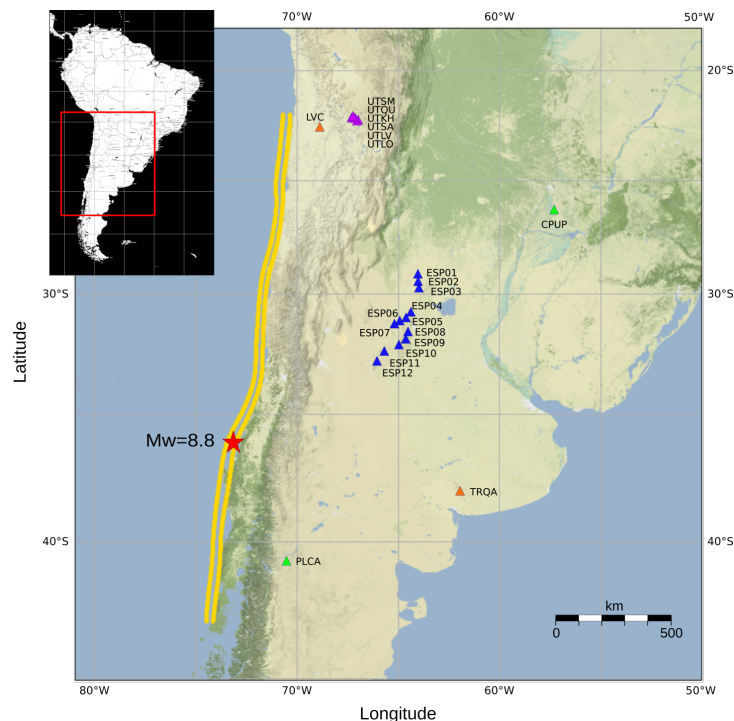


**Figure IV.2** – Stations ayant enregistré le séisme de Maule et sources synthétiques considérées pour construire la base de données d'entraînement (équivalent de la Figure 1 de la partie IV.2 pour application au Chili) [Arias et al., in prep.].

Bien que les données soient beaucoup plus bruitées et moins nombreuses qu’au Japon, les résultats indiquent que PEGSnet aurait pu estimer la magnitude du séisme de Maule après une centaine de secondes (Figure IV.3). La magnitude minimale pour que PEGSnet fonctionne dans la configuration du séisme de Maule est toutefois  $M_w = 8.6$  – en dessous de cette valeur PEGSnet échoue à discerner les PEGS du bruit – [Arias et al., in prep.], très au dessus du seuil dans la configuration du séisme de Tohoku-Oki.

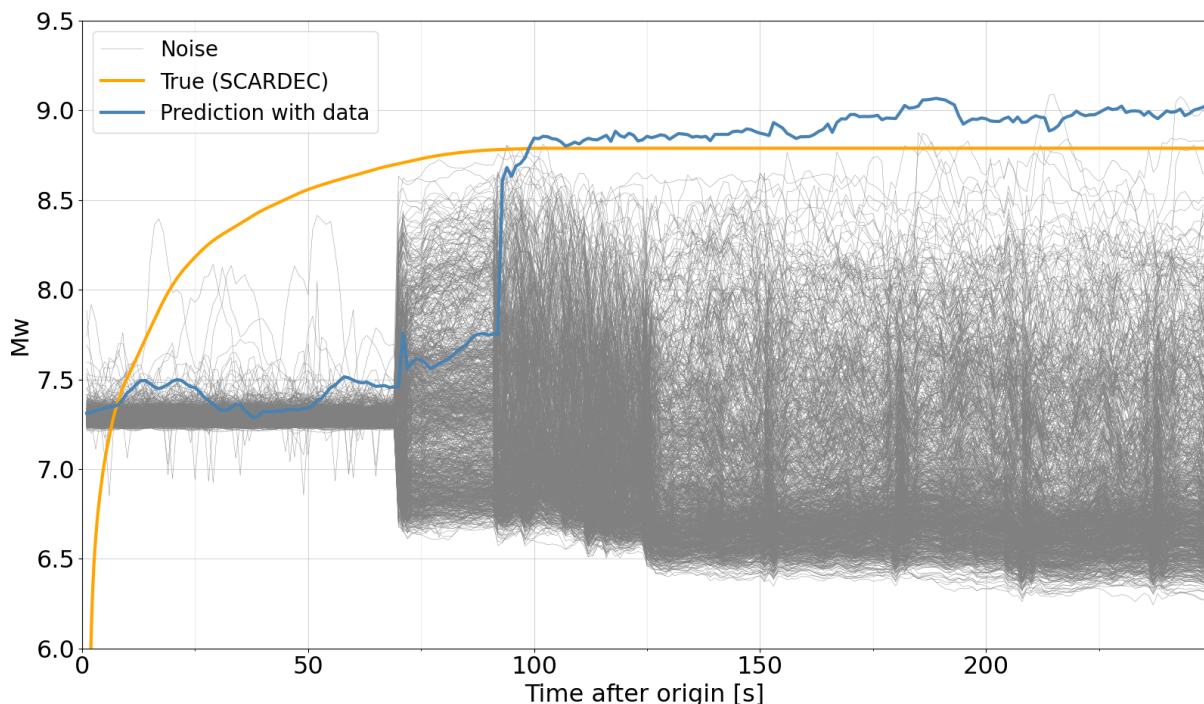


**Figure IV.3** – Estimation de la magnitude du séisme de Maule (courbe bleue) en fonction du temps comparée à l’évolution réelle de la magnitude (solution SCARDEC [Vallée et al., 2011]) et à la même estimation pour 1,000 échantillons de bruit empirique sans PEGS (courbes grises) [Arias et al., in prep.].

### Implémentation dans le système d’alerte Péruvien

Les études évoquées ci-avant démontrent le potentiel de PEGSnet pour l’alerte rapide, en particulier tsunami. L’étape suivante est l’implémentation concrète dans un système d’alerte opérationnel. En collaboration avec Adolfo Inza à l’Instituto Geofísico del Peru (IGP), nous travaillons à l’implémentation de PEGSnet en temps réel sur le réseau de stations large-bande, riche d’une soixantaine de stations dans lequel le gouvernement péruvien a récemment investi (Figure IV.4). Cette application concrète au Pérou est une priorité à moyen terme, avec des visites longues durées dans les 2 sens. J’ai ainsi passé 2 mois à l’IGP en 2021, accompagné

d'Andrea Licciardi et Gabriela Arias. Adolfo Inza fera le chemin inverse pour 2 mois en 2022.

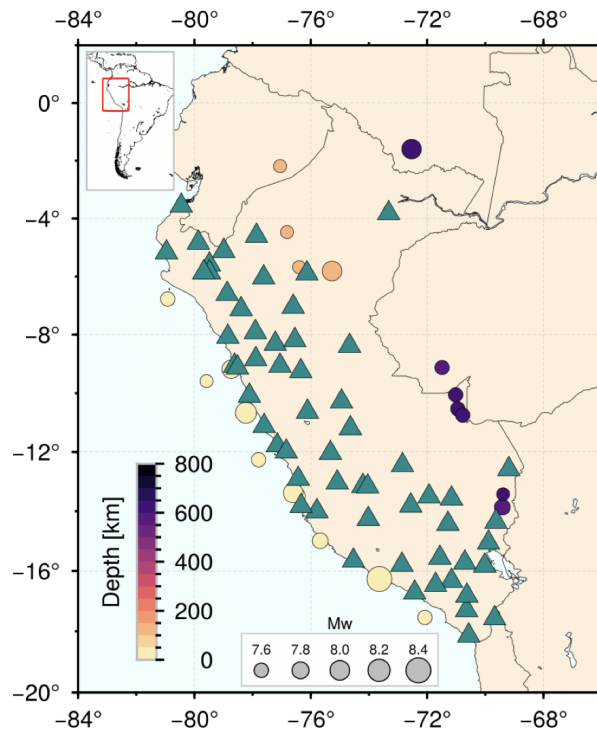


**Figure IV.4** – Stations large-bande transmettant en temps-réel au Pérou (triangles verts) et séismes importants ( $M_w > 7.5$ ) depuis 1950.

### 3.2 Débruitage des PEGS par IA

Nous avons vu dans la section IV.2 (Extended Data Figure 6) que si les données étaient dépourvues de bruit, PEGSnet permettrait une estimation instantanée de la magnitude de n'importe quel séisme, quelque soit sa magnitude. PEGSnet n'est donc limité que par le bruit sur les stations. Si l'on parvenait à éliminer ce bruit, on pourrait donc améliorer très significativement les performances de PEGSnet, en particulier pour les séismes de magnitude modérée ( $7 < M_w < 8.5$ ). Nous développons ainsi un algorithme de débruitage des PEGS par Deep Learning. L'architecture de l'algorithme est très semblable à PEGSnet. Les données d'entrée sont les mêmes, mais au lieu d'estimer, en sortie, la latitude, la longitude et la magnitude de l'évènement, cet algorithme de débruitage estime les PEGS débruités (Figure IV.5).

L'algorithme prend avantage de la cohérence spatio-temporelle entre les PEGS attendus d'un bout à l'autre du réseau pour reconstruire les signaux et éliminer le bruit. Le résultat station par station est ainsi très supérieur à ce que l'on pourrait attendre d'un simple filtre

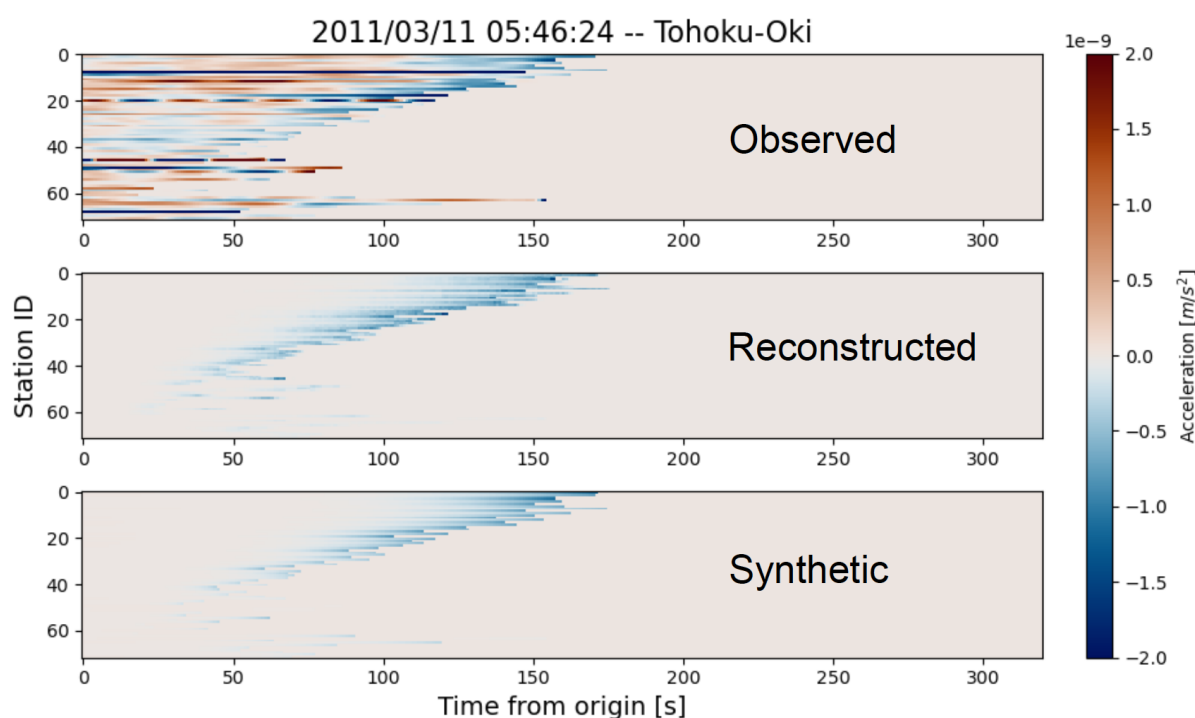


**Figure IV.5** – Exemple de débruitage des PEGS sur le réseau de stations de l’étude de la section IV.2. En haut les données observées, composées des PEGS et du bruit. En bas le signal attendu dépourvu du bruit. Au milieu, les signaux débruités par l’algorithme [Licciardi et al., in prep.].

dans la gamme de fréquence des PEGS (Figure IV.6).

L’étape suivante est de configurer l’algorithme pour permettre un débruitage seconde par seconde, puis d’utiliser les PEGS débruités comme donnée d’entrée dans PEGSnet.

### 3.3 Vers un algorithme d’alerte global

Les caractéristiques exceptionnelles des PEGS permettent d’imaginer quelque chose d’in-  
 envisageable avec les signaux sismiques « classiques » : un algorithme d’alerte utilisant toutes  
 les stations de la planète transmettant en temps réel. En effet, les PEGS se propageant à la  
 vitesse de la lumière, il est, en théorie, possible d’enregistrer des signaux utiles aux antipodes  
 de l’épicentre avant l’arrivée du tsunami – et peut-être même avant les premières secousses  
 – dans les régions proches de la source. Un algorithme global de ce type présente plusieurs  
 intérêts. Le premier est la quantité d’information que l’on peut potentiellement extraire d’un  
 réseau global pour contraindre l’estimation. Le second est qu’un tel système pourrait fonction-  
 ner pour n’importe quel séisme partout sur Terre, offrant ainsi une « couverture » d’alerte dans  
 des régions ne bénéficiant pas de système opérationnel. Pour mettre au point un tel algorithme

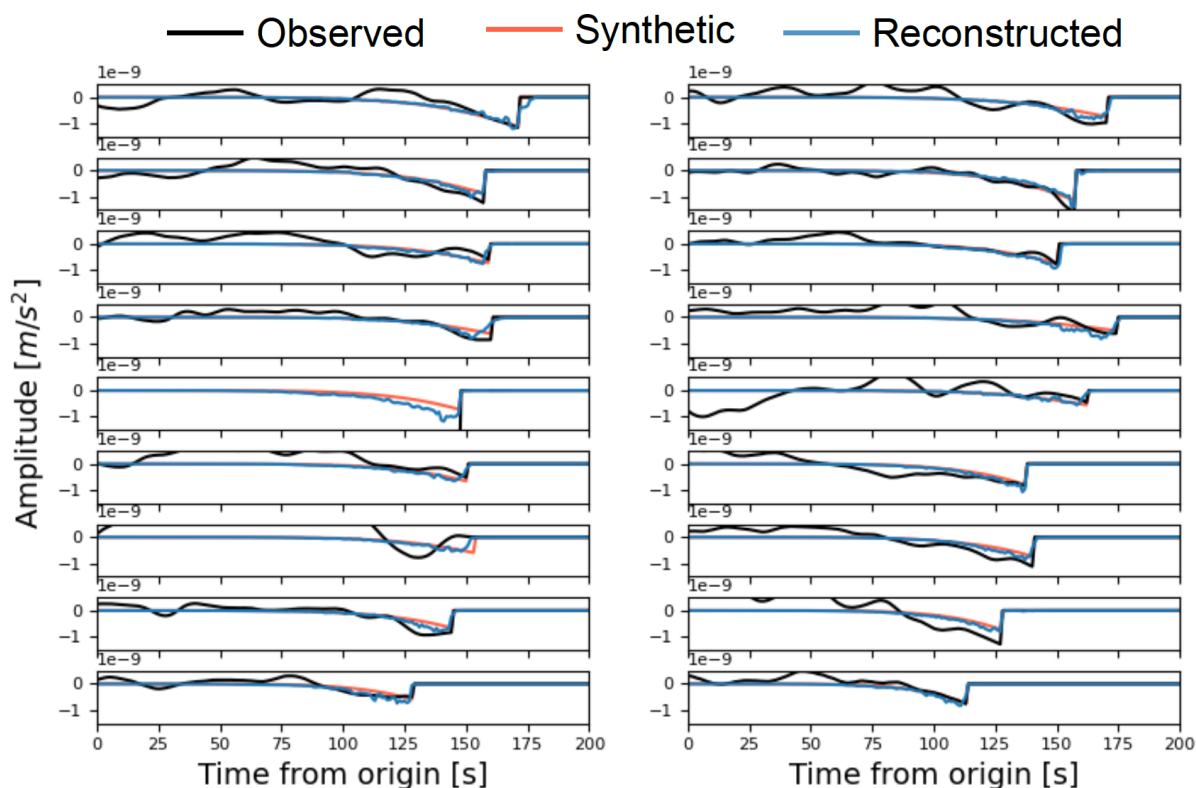


Figure IV.6 – Résultat station par station du débruitage sur le réseau entier [Licciardi et al., in prep.].

global, l’obstacle majeur est de calculer les PEGS synthétiques sur la planète entière pour un ensemble exhaustif de paramètres de source. Construire la base de données synthétiques nécessaire à l’entraînement d’une version globale de PEGSnet constitue un challenge important sur le plan numérique. Dans le cadre de son postdoctorat, Kévin Juhel a réussi à construire cette base de données en adaptant une astuce numérique proposée par [Zhang et al. \[2020\]](#) afin de réduire drastiquement les temps de calcul [Juhel et al., in prep.]. L’étape suivante sera de collecter les données de toutes les stations transmettant en temps réel dans le monde afin de pouvoir réaliser l’entraînement.

### 3.4 Un algorithme alternatif efficace dans les toutes premières secondes

Nous avons montré que PEGSnet, notre algorithme d’IA basé sur les PEGS, est capable d’estimer de manière fiable et quasi-instantanée la magnitude des très grands séismes. Cela fait d’ores-et-déjà de PEGSnet un algorithme très utile pour l’alerte tsunami. La question demeure,

en revanche sur le potentiel de PEGSnet pour l’alerte sismique en temps que telle – i.e., la prédiction des mouvements forts. En l’état actuel – et même si nous travaillons sur des pistes pour baisser ce seuil (section IV.3.2) – PEGSnet ne permet pas d’estimer la magnitude d’évènements de magnitude inférieure à 8.3 (au Japon). La plupart des séismes n’atteignent une telle magnitude qu’après quelques dizaines de secondes, ce qui rendrait un système d’alerte n’utilisant que PEGSnet inopérant durant ce temps. Pour combler ce manque, nous développons, dans le cadre de la thèse de Pablo Espinoza Lara, un algorithme d’IA complémentaire qui estime la magnitude et la localisation d’un séisme dans des temps records après son origine.

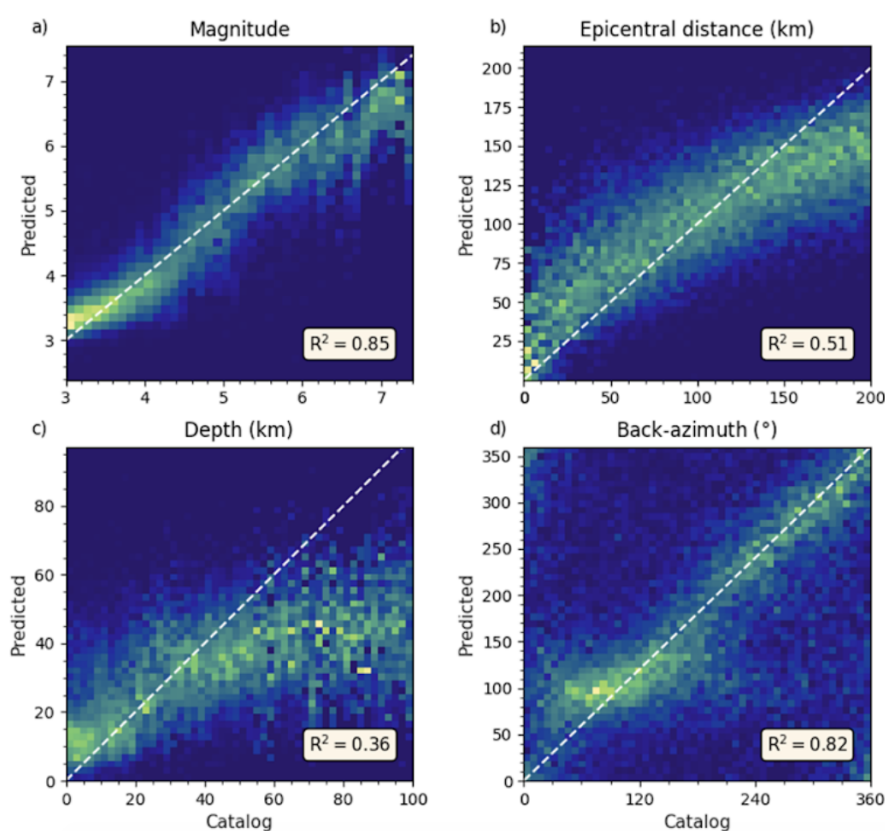


**Figure IV.7** – Performance de l’algorithme 3 secondes après l’arrivée de l’onde P [Lara et al., in prep.]. a) Densité de probabilité des estimations de la magnitude sur le jeu de données test (en abscisse la magnitude « réelle », en ordonnée l’estimation après 3 s). b) Idem pour la distance épacentrale. c) Idem pour la profondeur. d) Idem pour le back-azimut.

La première phase de l’algorithme est la détection. Un premier algorithme d’IA opère continuellement, en temps réel, sur toutes les stations indépendamment. Lorsque un séisme est détecté sur une station, un deuxième algorithme est déclenché pour l’estimation. Cet algorithme est entraîné sur une centaine de milliers de formes d’ondes compilée à partir du catalogue glo-



## Chapitre IV. Comment anticiper les grands séismes ?

---

bal STEAD [Mousavi *et al.*, 2019] et des catalogues régionaux du Chili, du Japon et du Pérou. L'objectif est d'estimer la magnitude, la distance épicentrale, le back-azimut et la profondeur du séisme à partir d'une seule station. L'entraînement n'est pas réalisé directement à partir des données brutes comme dans le cas de PEGSnet. 162 attributs sont calculés à partir des formes d'ondes dans les domaines temporel, spectral et cepstral et nourrissent la base de données d'entraînement. De manière intéressante, le domaine cepstral fournit les informations les plus importantes dans la décision de l'algorithme.

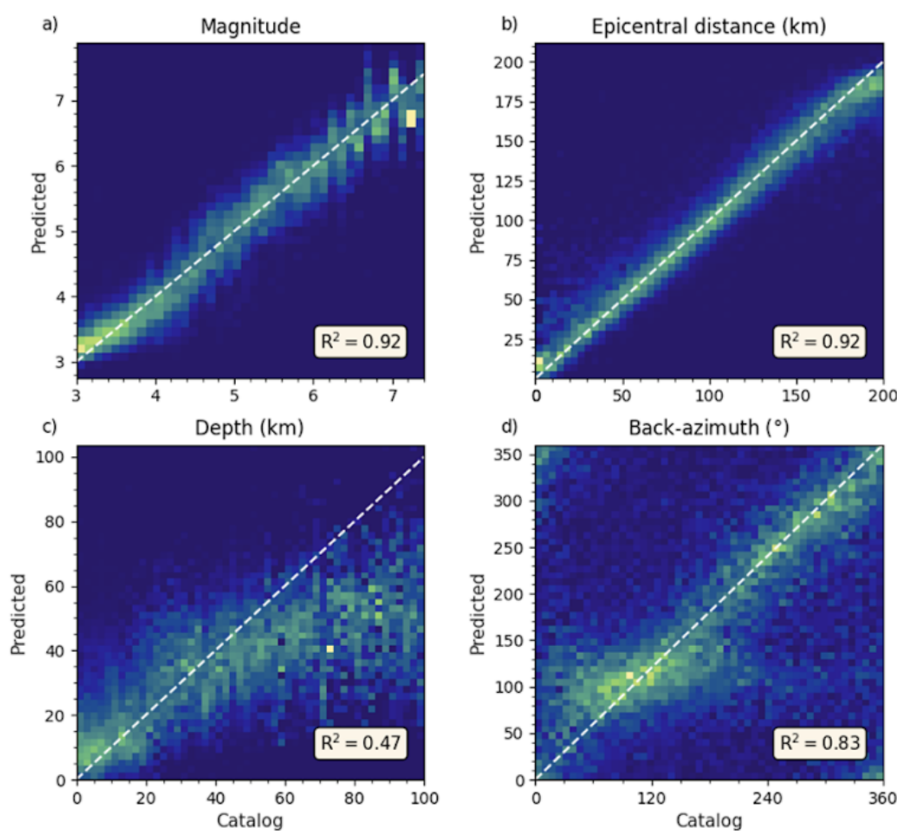


**Figure IV.8** – Performance de l'algorithme 30 secondes après l'arrivée de l'onde P [Lara *et al.*, in prep.]. Idem à la figure IV.7 avec 30 s d'enregistrement après l'arrivée de l'onde P.

La première estimation est réalisée à partir de 3 secondes d'enregistrement, i.e. 3 secondes après l'arrivée de l'onde P sur la première station. Les performances après 3 secondes indiquent qu'une estimation grossière de la magnitude est possible très tôt après le début de l'évènement (Figure IV.7.a), d'autant que l'estimation est réalisée sur une seule station, entraînant un gain de temps significatif par rapport aux approches multi-stations pour lesquels il est nécessaire d'attendre que le signal atteignent 4 ou 5 stations. Le back-azimut est également relativement

bien estimé après 3 s (Figure IV.7.d), autorisant une estimation grossière de la localisation, même si la distance épacentrale est moins bien estimée (Figure IV.7.b), à l’instar de la profondeur (Figure IV.7.c).

Avec 30 secondes d’enregistrement, les estimations sont toutefois nettement améliorées (Figure IV.8). Le progrès le plus spectaculaire est celui de la distance épacentrale (Figure IV.8.b), très fiablement estimée à partir de 30 s d’enregistrement sur une seule station. La magnitude est également mieux estimée (Figure IV.8.a), de même que la profondeur – même si celle-ci reste assez mal contrainte – (Figure IV.8.c). Aucun progrès significatif n’est observé pour le back-azimut. Globalement, la fiabilité des estimations augmente avec le nombre de secondes d’enregistrement fournies à l’algorithme (Figure IV.9), mais celui-ci montre un potentiel intéressant pour l’alerte très rapide.

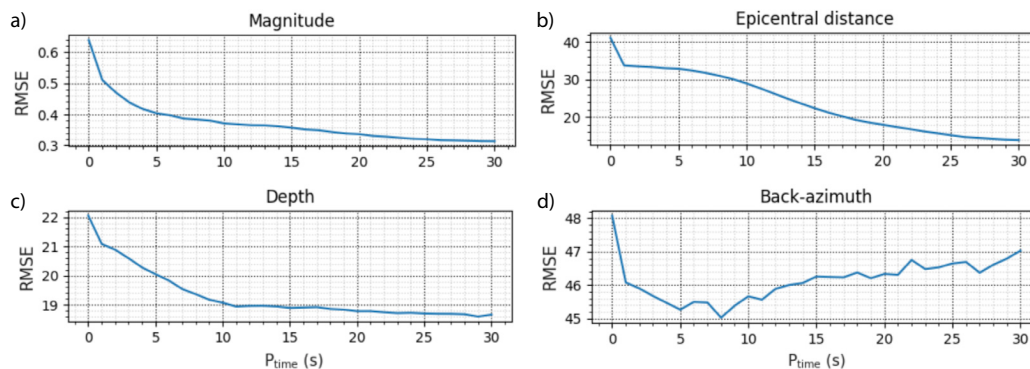


**Figure IV.9** – Erreur sur les estimations de la magnitude (a), de la distance épacentrale (b), de la profondeur (c) et du back-azimut (d) en fonction du temps d’enregistrement après l’arrivée de l’onde P [Lara et al., in prep.].

L’algorithme est implémenté en version bêta dans le système d’alerte péruvien et a montré des performances très encourageantes sur les séismes enregistrés ces derniers mois. Un grand nombre de stations accélérométriques transmettant en temps réel est actuellement déployé sur la côte péruvienne (tous les 30 km) dans le cadre du programme Sistema de Alerta Sísmica Peruano (SASPe). L’algorithme développé par Pablo y est systématiquement intégré.

Cet algorithme peut par ailleurs être utilisé pour d’autres applications que l’alerte sismique. Il est en effet capable de quantifier la sismicité à partir d’une seule station, ce qui peut s’avérer très utiles dans des régions mal instrumentées. Nous avons ainsi utilisé cet algorithme pour caractériser l’activité des répliques suivant le séisme de Nippes en Haïti (2021,  $M_w$  7.2) à partir d’une seule station à bas coût (très bruitée) installée chez l’habitant, avec des résultats équivalents, voire supérieurs, à ceux obtenus par les approches classiques sur le réseau régional

## Chapitre IV. Comment anticiper les grands séismes ?

---

entier [[Calais et al., 2022](#)]. Des applications similaires sont planifiées, notamment sur l'île de La Plata, en Équateur.

---

## Conclusion

Nous n'avons pas répondu aux questions « Où ? » et « Quand ? » se dérouleront les prochains grands séismes. Ces questions resteront probablement sans réponses pour de longues années encore. Nous avons toutefois proposer des pistes pour avancer dans cette direction et apporté des éléments pour mieux anticiper les séismes. Pourra-t-on un jour aller plus loin ?

La découverte récente des PEGS illustre qu'un signal sismologique majeur – le plus précoce identifié à ce jour – est resté inconnu, caché dans le bruit sismique, pendant des années. L'idée que d'autres signaux, plus précoces encore – i.e. précédant l'origine du séisme – restent encore à détecter dans le bruit sismique n'est donc pas déraisonnable. L'IA offre des perspectives nouvelles pour extraire ce type de signaux. Pourra-t-elle, un jour, permettre la prédiction des séismes ? La réponse dépend de la nature déterministe des ces phénomènes. Si les séismes sont des processus purement chaotiques, se produisant sans phase précurserice, alors ils resteront ontologiquement imprévisibles pour toujours. Si, en revanche, notre incapacité à prédire ces événements résulte de notre connaissance limitée des conditions physiques contrôlant la genèse des ruptures en profondeur, alors la prédiction des séismes devient théoriquement possible. Même si les conditions physiques en profondeur restent insuffisamment contraintes pour construire des modèles capables de prédire de manière fiable les séismes à venir, l'IA est un outil pour la détection « donnée orientée » qui ne requiert aucune modélisation ni aucune connaissance des conditions physiques en profondeur. Si un signal précurseur existe dans les données, l'IA représente ainsi un réel espoir de le découvrir.



---

## Références bibliographiques

- Ader, T. J., N. Lapusta, J.-P. Avouac, and J.-P. Ampuero (2014), Response of rate-and-state seismogenic faults to harmonic shear-stress perturbations, *Geophysical Journal International*, *198*(1), 385–413. [15](#)
- Aki, K., and P. G. Richards (2002), *Quantitative seismology*. [6](#)
- Allen, R. M. (2006), Probabilistic warning times for earthquake ground shaking in the san francisco bay area, *Seismological Research Letters*, *77*(3), 371–376. [84](#)
- Allen, R. M., and D. Melgar (2019), Earthquake early warning : Advances, scientific challenges, and societal needs, *Annual Review of Earth and Planetary Sciences*, *47*, 361–388. [21](#)
- Allgeyer, S., and P. Cummins (2014), Numerical tsunami simulation including elastic loading and seawater density stratification, *Geophysical Research Letters*, *41*(7), 2368–2375. [7](#)
- Altamimi, Z., P. Sillard, and C. Boucher (2002), Itrf2000 : A new release of the international terrestrial reference frame for earth science applications, *Journal of Geophysical Research : Solid Earth*, *107*(B10), ETG–2. [4](#)
- Altamimi, Z., X. Collilieux, J. Legrand, B. Garayt, and C. Boucher (2007), Itrf2005 : A new release of the international terrestrial reference frame based on time series of station positions and earth orientation parameters, *Journal of Geophysical Research : Solid Earth*, *112*(B9). [4](#)
- Altamimi, Z., X. Collilieux, and L. Métivier (2011), Itrf2008 : an improved solution of the international terrestrial reference frame, *Journal of Geodesy*, *85*(8), 457–473. [4](#)



- Altamimi, Z., P. Rebischung, L. Métivier, and X. Collilieux (2016), Itrf2014 : A new release of the international terrestrial reference frame modeling nonlinear station motions, *Journal of Geophysical Research : Solid Earth*, 121(8), 6109–6131. [4](#)
- Amitrano, D. (2003), Brittle-ductile transition and associated seismicity : Experimental and numerical studies and relationship with the b value, *Journal of Geophysical Research : Solid Earth*, 108(B1). [17](#)
- Ampuero, J.-P., and A. M. Rubin (2008), Earthquake nucleation on rate and state faults—aging and slip laws, *Journal of Geophysical Research : Solid Earth*, 113(B1). [15](#), [18](#)
- Avouac, J.-P. (2015), From geodetic imaging of seismic and aseismic fault slip to dynamic modeling of the seismic cycle, *Annual Review of Earth and Planetary Sciences*, 43, 233–271. [10](#), [12](#), [15](#), [16](#)
- Bachmann, C. E., S. Wiemer, B. Goertz-Allmann, and J. Woessner (2012), Influence of pore-pressure on the event-size distribution of induced earthquakes, *Geophysical Research Letters*, 39(9). [17](#)
- Bagiya, M. S., D. Thomas, E. Astafyeva, Q. Bletery, P. Lognonné, and D. S. Ramesh (2020), The ionospheric view of the 2011 tohoku-oki earthquake seismic source : the first 60 seconds of the rupture, *Scientific reports*, 10(1), 1–15. [5](#)
- Barbot, S., N. Lapusta, and J.-P. Avouac (2012), Under the hood of the earthquake machine : Toward predictive modeling of the seismic cycle, *Science*, 336(6082), 707–710. [15](#)
- Bartlow, N. M., S. Miyazaki, A. M. Bradley, and P. Segall (2011), Space-time correlation of slip and tremor during the 2009 cascadia slow slip event, *Geophysical Research Letters*, 38(18). [12](#)
- Bergen, K. J., and G. C. Beroza (2018), Detecting earthquakes over a seismic network using single-station similarity measures, *Geophysical Journal International*, 213(3), 1984–1998. [26](#)
- Bergen, K. J., P. A. Johnson, V. Maarten, and G. C. Beroza (2019), Machine learning for data-driven discovery in solid earth geoscience, *Science*, 363(6433). [24](#), [26](#)
- Bletery, Q. (2015), Analyse probabiliste et multi-données de la source de grands séismes, Ph.D. thesis, Nice. [5](#), [9](#)

- Bletery, Q., and J.-M. Nocquet (2020), Slip bursts during coalescence of slow slip events in cascadia, *Nature communications*, *11*(1), 1–6. [60](#), [73](#)
- Bletery, Q., A. Sladen, B. Delouis, M. Vallée, J.-M. Nocquet, L. Rolland, and J. Jiang (2014), A detailed source model for the mw9.0 tohoku-oki earthquake reconciling geodesy, seismology, and tsunami records, *Journal of Geophysical Research : Solid Earth*, *119*(10), 7636–7653. [8](#), [9](#)
- Bletery, Q., A. Sladen, B. Delouis, and L. Mattéo (2015), Quantification of tsunami bathymetry effect on finite fault slip inversion, *Pure and Applied Geophysics*, *172*(12), 3655–3670. [7](#)
- Bletery, Q., A. Sladen, J. Jiang, and M. Simons (2016a), A bayesian source model for the 2004 great sumatra-andaman earthquake, *Journal of Geophysical Research : Solid Earth*, *121*(7), 5116–5135. [9](#)
- Bletery, Q., A. M. Thomas, A. W. Rempel, L. Karlstrom, A. Sladen, and L. De Barros (2016b), Mega-earthquakes rupture flat megathrusts, *Science*, *354*(6315), 1027–1031. [28](#)
- Bletery, Q., A. M. Thomas, A. W. Rempel, and J. L. Hardebeck (2017a), Imaging shear strength along subduction faults, *Geophysical Research Letters*, *44*(22), 11–329. [35](#)
- Bletery, Q., A. M. Thomas, J. C. Hawthorne, R. M. Skarbek, A. W. Rempel, and R. D. Krogstad (2017b), Characteristics of secondary slip fronts associated with slow earthquakes in cascadia, *Earth and Planetary Science Letters*, *463*, 212–220. [62](#)
- Bletery, Q., O. Cavalié, J.-M. Nocquet, and T. Ragon (2020), Distribution of interseismic coupling along the north and east anatolian faults inferred from insar and gps data, *Geophysical Research Letters*, *47*(16), e2020GL087,775. [47](#)
- Böse, M., E. Hauksson, K. Solanki, H. Kanamori, and T. Heaton (2009), Real-time testing of the on-site warning algorithm in southern california and its performance during the july 29 2008 mw5.4 chino hills earthquake, *Geophysical Research Letters*, *36*(5). [20](#)
- Böse, M., T. H. Heaton, and E. Hauksson (2012), Real-time finite fault rupture detector (finder) for large earthquakes, *Geophysical Journal International*, *191*(2), 803–812. [20](#)
- Böse, M., C. Felizardo, and T. H. Heaton (2015), Finite-fault rupture detector (finder) : Going real-time in californian shakealert warning system, *Seismological Research Letters*, *86*(6), 1692–1704. [20](#)

- Böse, M., D. E. Smith, C. Felizardo, M.-A. Meier, T. H. Heaton, and J. F. Clinton (2018), Finder v. 2 : Improved real-time ground-motion predictions for m2–m9 with seismic finite-source characterization, *Geophysical Journal International*, 212(1), 725–742. [20](#)
- Bouchon, M. (1981), A simple method to calculate green’s functions for elastic layered media, *Bulletin of the Seismological Society of America*, 71(4), 959–971. [6](#)
- Bouchon, M., H. Karabulut, M. Aktar, S. Özalaybey, J. Schmittbuhl, and M.-P. Bouin (2011), Extended nucleation of the 1999 mw 7.6 izmit earthquake, *science*, 331(6019), 877–880. [18](#)
- Bouchon, M., V. Durand, D. Marsan, H. Karabulut, and J. Schmittbuhl (2013), The long precursory phase of most large interplate earthquakes, *Nature geoscience*, 6(4), 299–302. [18](#)
- Brodsky, E. E., and T. Lay (2014), Recognizing foreshocks from the 1 april 2014 chile earthquake, *Science*, 344(6185), 700–702. [18](#)
- Calais, E., and J. B. Minster (1995), Gps detection of ionospheric perturbations following the january 17, 1994, northridge earthquake, *Geophysical Research Letters*, 22(9), 1045–1048. [5](#)
- Calais, E., J. Han, C. DeMets, and J. Nocquet (2006), Deformation of the north american plate interior from a decade of continuous gps measurements, *Journal of geophysical research : solid earth*, 111(B6). [4](#)
- Calais, E., S. Symithe, T. Monfret, B. Delouis, A. Lomax, F. Courboulex, J.-P. Ampuero, P. Lara, Q. Bletery, J. Chèze, F. Peix, A. Deschamps, B. de Lépinay, B. Raimbault, R. Jolivet, S. Paul, S. St-Fleur, D. Boisson, Y. Fukushima, Z. Duputel, L. Xu, and L. Meng (2022), Citizen seismology helps decipher the 2021 haiti earthquake, *Science*, 376(6590), 283–287. [114](#)
- Cao, T., and K. Aki (1986), Seismicity simulation with a rate-and state-dependent friction law, in *Friction and Faulting*, pp. 487–513, Springer. [27](#)
- Cavalié, O., C. Lasserre, M.-P. Doin, G. Peltzer, J. Sun, X. Xu, and Z.-K. Shen (2008), Measurement of interseismic strain across the haiyuan fault (gansu, china), by insar, *Earth and Planetary Science Letters*, 275(3-4), 246–257. [5](#)
- Choy, G. L., and S. H. Kirby (2004), Apparent stress, fault maturity and seismic hazard for normal-fault earthquakes at subduction zones, *Geophysical Journal International*, 159(3), 991–1012. [27](#)

- Chung, A. I., I. Henson, and R. M. Allen (2019), Optimizing earthquake early warning performance : Elarms-3, *Seismological Research Letters*, 90(2A), 727–743. [20](#)
- Crowell, B. W., D. A. Schmidt, P. Bodin, J. E. Vidale, J. Gomberg, J. Renate Hartog, V. C. Kress, T. I. Melbourne, M. Santillan, S. E. Minson, et al. (2016), Demonstration of the cascadia g-fast geodetic earthquake early warning system for the nisqually, washington, earthquake, *Seismological Research Letters*, 87(4), 930–943. [21](#)
- Crowell, B. W., D. A. Schmidt, P. Bodin, J. E. Vidale, B. Baker, S. Barrientos, and J. Geng (2018), G-fast earthquake early warning potential for great earthquakes in chile, *Seismological Research Letters*, 89(2A), 542–556. [21](#)
- Dai, H., and C. MacBeth (1995), Automatic picking of seismic arrivals in local earthquake data using an artificial neural network, *Geophysical journal international*, 120(3), 758–774. [24](#)
- DeMets, C., P. E. Jansma, G. S. Mattioli, T. H. Dixon, F. Farina, R. Bilham, E. Calais, and P. Mann (2000), Gps geodetic constraints on caribbean-north america plate motion, *Geophysical Research Letters*, 27(3), 437–440. [4](#)
- Derras, B., P. Y. Bard, and F. Cotton (2014), Towards fully data driven ground-motion prediction models for europe, *Bulletin of Earthquake Engineering*, 12(1), 495–516. [26](#)
- DeVries, P. M., T. B. Thompson, and B. J. Meade (2017), Enabling large-scale viscoelastic calculations via neural network acceleration, *Geophysical Research Letters*, 44(6), 2662–2669. [26](#)
- Dieterich, J. (1994), A constitutive law for rate of earthquake production and its application to earthquake clustering, *Journal of Geophysical Research : Solid Earth*, 99(B2), 2601–2618. [15](#)
- Dieterich, J. H. (1979), Modeling of rock friction : 1. experimental results and constitutive equations, *Journal of Geophysical Research : Solid Earth*, 84(B5), 2161–2168. [14](#)
- Dieterich, J. H. (1987), Nucleation and triggering of earthquake slip : effect of periodic stresses, *Tectonophysics*, 144(1-3), 127–139. [15](#), [18](#)
- Doin, M.-P., C. Lasserre, G. Peltzer, O. Cavalié, and C. Doubre (2009), Corrections of stratified tropospheric delays in sar interferometry : Validation with global atmospheric models, *Journal of Applied Geophysics*, 69(1), 35–50. [5](#)

- Dowla, F. U., S. R. Taylor, and R. W. Anderson (1990), Seismic discrimination with artificial neural networks : preliminary results with regional spectral data, *Bulletin of the Seismological Society of America*, 80(5), 1346–1373. [24](#)
- Dragert, H., K. Wang, and T. S. James (2001), A silent slip event on the deeper cascadia subduction interface, *Science*, 292(5521), 1525–1528. [12](#)
- Duputel, Z., L. Rivera, H. Kanamori, G. P. Hayes, B. Hirshorn, and S. Weinstein (2011), Real-time w phase inversion during the 2011 off the pacific coast of tohoku earthquake, *Earth, planets and space*, 63(7), 535–539. [21](#)
- Duputel, Z., L. Rivera, H. Kanamori, and G. Hayes (2012), W phase source inversion for moderate to large earthquakes (1990–2010), *Geophysical Journal International*, 189(2), 1125–1147. [21](#)
- Duputel, Z., P. S. Agram, M. Simons, S. E. Minson, and J. L. Beck (2014), Accounting for prediction uncertainty when inferring subsurface fault slip, *Geophysical Journal International*, 197(1), 464–482. [9](#)
- Dysart, P. S., and J. J. Pulli (1990), Regional seismic event classification at the noress array : seismological measurements and the use of trained neural networks, *Bulletin of the Seismological Society of America*, 80(6B), 1910–1933. [24](#)
- Ellsworth, W. L., and G. C. Beroza (1998), Observation of the seismic nucleation phase in the ridgecrest, california, earthquake sequence, *Geophysical research letters*, 25(3), 401–404. [84](#)
- Ellsworth, W. L., and F. Bulut (2018), Nucleation of the 1999 izmit earthquake by a triggered cascade of foreshocks, *Nature Geoscience*, 11(7), 531–535. [18](#)
- Espinosa-Aranda, J. M., A. Cuellar, A. Garcia, G. Ibarrola, R. Islas, S. Maldonado, and F. Rodriguez (2009), Evolution of the mexican seismic alert system (sasmex), *Seismological Research Letters*, 80(5), 694–706. [83](#)
- Frank, W. B., B. Rousset, C. Lasserre, and M. Campillo (2018), Revealing the cluster of slow transients behind a large slow slip event, *Science advances*, 4(5), eaat0661. [14](#)
- Fujinawa, Y., and Y. Noda (2013), Japan’s earthquake early warning system on 11 march 2011 : performance, shortcomings, and changes, *Earthquake Spectra*, 29(1\_suppl), 341–368. [83](#)

- Geller, R. J. (1997), Earthquake prediction : a critical review, *Geophysical Journal International*, 131(3), 425–450. [18](#), [19](#)
- Gerstenberger, M. C., S. Wiemer, L. M. Jones, and P. A. Reasenber (2005), Real-time forecasts of tomorrow’s earthquakes in california, *Nature*, 435(7040), 328–331. [17](#)
- Goebel, T., D. Schorlemmer, T. Becker, G. Dresen, and C. Sammis (2013), Acoustic emissions document stress changes over many seismic cycles in stick-slip experiments, *Geophysical Research Letters*, 40(10), 2049–2054. [17](#)
- Gomberg, J., C. 2007, and B. W. Group (2010), Slow-slip phenomena in cascadia from 2007 and beyond : A review, *Bulletin*, 122(7-8), 963–978. [18](#)
- Gomberg, J., A. Wech, K. Creager, K. Obara, and D. Agnew (2016), Reconsidering earthquake scaling, *Geophysical Research Letters*, 43(12), 6243–6251. [14](#)
- Grapenthin, R., I. Johanson, and R. M. Allen (2014a), The 2014 mw 6.0 napa earthquake, california : Observations from real-time gps-enhanced earthquake early warning, *Geophysical Research Letters*, 41(23), 8269–8276. [21](#)
- Grapenthin, R., I. A. Johanson, and R. M. Allen (2014b), Operational real-time gps-enhanced earthquake early warning, *Journal of Geophysical Research : Solid Earth*, 119(10), 7944–7965. [21](#)
- Gulia, L., and S. Wiemer (2010), The influence of tectonic regimes on the earthquake size distribution : A case study for italy, *Geophysical Research Letters*, 37(10). [17](#)
- Gulia, L., and S. Wiemer (2019), Real-time discrimination of earthquake foreshocks and aftershocks, *Nature*, 574(7777), 193–199. [17](#), [18](#)
- Gulia, L., A. P. Rinaldi, T. Tormann, G. Vannucci, B. Enescu, and S. Wiemer (2018), The effect of a mainshock on the size distribution of the aftershocks, *Geophysical Research Letters*, 45(24), 13–277. [17](#)
- Gutenberg, B., and C. F. Richter (1944), Frequency of earthquakes in california, *Bulletin of the Seismological society of America*, 34(4), 185–188. [17](#)
- Hanks, T. C., and H. Kanamori (1979), A moment magnitude scale, *Journal of Geophysical Research : Solid Earth*, 84(B5), 2348–2350. [4](#)



- Hardebeck, J. L. (2015), Stress orientations in subduction zones and the strength of subduction megathrust faults, *Science*, *349*(6253), 1213–1216. [59](#)
- Harms, J. (2016), Transient gravity perturbations from a double-couple in a homogeneous half-space, *Geophysical Journal International*, *205*(2), 1153–1164. [22](#)
- Harms, J., J.-P. Ampuero, M. Barsuglia, E. Chassande-Mottin, J.-P. Montagner, S. Somala, and B. Whiting (2015), Transient gravity perturbations induced by earthquake rupture, *Geophysical Journal International*, *201*(3), 1416–1425. [22](#)
- Hayes, G. P., D. J. Wald, and R. L. Johnson (2012), Slab1. 0 : A three-dimensional model of global subduction zone geometries, *Journal of Geophysical Research : Solid Earth*, *117*(B1). [7](#)
- Hayes, G. P., G. L. Moore, D. E. Portner, M. Hearne, H. Flamme, M. Furtney, and G. M. Smoczyk (2018), Slab2, a comprehensive subduction zone geometry model, *Science*, *362*(6410), 58–61. [7](#)
- Heaton, T. H. (1985), A model for a seismic computerized alert network, *Science*, *228*(4702), 987–990. [84](#)
- Hecker, S., T. Dawson, and D. Schwartz (2010), Normal-faulting slip maxima and stress-drop variability : A geological perspective, *Bulletin of the Seismological Society of America*, *100*(6), 3130–3147. [28](#)
- Heki, K., Y. Otsuka, N. Choosakul, N. Hemmakorn, T. Komolmis, and T. Maruyama (2006), Detection of ruptures of andaman fault segments in the 2004 great sumatra earthquake with coseismic ionospheric disturbances, *Journal of Geophysical Research : Solid Earth*, *111*(B9). [5](#)
- Hicks, S. (2015), Seismic properties and processes along the subduction plate interface : the february 2010 mw 8.8 maule, chile earthquake, Ph.D. thesis, University of Liverpool. [27](#)
- Hino, R., Y. Tanioka, T. Kanazawa, S. Sakai, M. Nishino, and K. Suyehiro (2001), Micro-tsunami from a local interplate earthquake detected by cabled offshore tsunami observation in northeastern japan, *Geophysical research letters*, *28*(18), 3533–3536. [5](#)
- Holtzman, B. K., A. Paté, J. Paisley, F. Waldhauser, and D. Repetto (2018), Machine learning reveals cyclic changes in seismic source spectra in geysers geothermal field, *Science advances*, *4*(5), eaao2929. [26](#)

- Hoshiaba, M., and S. Aoki (2015), Numerical shake prediction for earthquake early warning : Data assimilation, real-time shake mapping, and simulation of wave propagation, *Bulletin of the Seismological Society of America*, *105*(3), 1324–1338. [20](#)
- Hoshiaba, M., K. Iwakiri, N. Hayashimoto, T. Shimoyama, K. Hirano, Y. Yamada, Y. Ishigaki, and H. Kikuta (2011), Outline of the 2011 off the pacific coast of tohoku earthquake (mw 9.0)—earthquake early warning and observed seismic intensity—, *Earth, planets and space*, *63*(7), 547–551. [83](#)
- Hulbert, C., B. Rouet-Leduc, P. A. Johnson, C. X. Ren, J. Rivière, D. C. Bolton, and C. Marone (2019), Similarity of fast and slow earthquakes illuminated by machine learning, *Nature Geoscience*, *12*(1), 69–74. [26](#)
- Ide, S., G. C. Beroza, D. R. Shelly, and T. Uchide (2007), A scaling law for slow earthquakes, *Nature*, *447*(7140), 76–79. [13](#), [14](#), [62](#)
- Ito, Y., K. Obara, K. Shiomi, S. Sekine, and H. Hirose (2007), Slow earthquakes coincident with episodic tremors and slow slip events, *Science*, *315*(5811), 503–506. [13](#)
- Jiang, J., and N. Lapusta (2016), Deeper penetration of large earthquakes on seismically quiescent faults, *Science*, *352*(6291), 1293–1297. [15](#)
- Jolivet, R., and W. Frank (2020), The transient and intermittent nature of slow slip, *AGU Advances*, *1*(1), e2019AV000,126. [13](#), [14](#)
- Jolivet, R., R. Grandin, C. Lasserre, M.-P. Doin, and G. Peltzer (2011), Systematic insar tropospheric phase delay corrections from global meteorological reanalysis data, *Geophysical Research Letters*, *38*(17). [5](#)
- Jolivet, R., M. Simons, P. Agram, Z. Duputel, and Z.-K. Shen (2015), Aseismic slip and seismogenic coupling along the central san andreas fault, *Geophysical Research Letters*, *42*(2), 297–306. [12](#)
- Jolivet, R., M. Simons, Z. Duputel, J.-A. Olive, H. Bhat, and Q. Bletery (2020), Interseismic loading of subduction megathrust drives long-term uplift in northern chile, *Geophysical Research Letters*, *47*(8), e2019GL085,377. [12](#), [60](#)
- Jordan, M. I., and T. M. Mitchell (2015), Machine learning : Trends, perspectives, and prospects, *Science*, *349*(6245), 255–260. [24](#)

- Jordan, T. H., Y.-T. Chen, P. Gasparini, R. Madariaga, I. Main, W. Marzocchi, G. Papadopoulos, G. Sobolev, K. Yamaoka, and J. Zschau (2011), Operational earthquake forecasting. state of knowledge and guidelines for utilization, *Annals of Geophysics*, *54*(4). [19](#)
- Juhel, K., J.-P. Ampuero, M. Barsuglia, P. Bernard, E. Chassande-Mottin, D. Fiorucci, J. Harms, J.-P. Montagner, M. Vallée, and B. Whiting (2018), Earthquake early warning using future generation gravity strainmeters, *Journal of Geophysical Research : Solid Earth*, *123*(12), 10–889. [24](#)
- Kagan, Y. Y. (1997), Are earthquakes predictable?, *Geophysical Journal International*, *131*(3), 505–525. [18](#), [19](#)
- Kanamori, H. (2005), Real-time seismology and earthquake damage mitigation, *Annu. Rev. Earth Planet. Sci.*, *33*, 195–214. [84](#)
- Kanamori, H., and J. W. Given (1981), Use of long-period surface waves for rapid determination of earthquake-source parameters, *Physics of the Earth and Planetary interiors*, *27*(1), 8–31. [21](#)
- Kanamori, H., and L. Rivera (2008), Source inversion ofwphase : speeding up seismic tsunami warning, *Geophysical Journal International*, *175*(1), 222–238. [21](#), [22](#)
- Kaneko, Y., J.-P. Avouac, and N. Lapusta (2010), Towards inferring earthquake patterns from geodetic observations of interseismic coupling, *Nature Geoscience*, *3*(5), 363–369. [15](#)
- Kato, A., K. Obara, T. Igarashi, H. Tsuruoka, S. Nakagawa, and N. Hirata (2012), Propagation of slow slip leading up to the 2011 mw 9.0 tohoku-oki earthquake, *Science*, *335*(6069), 705–708. [18](#)
- Käuffl, P., A. P. Valentine, and J. Trampert (2016), Probabilistic point source inversion of strong-motion data in 3-d media using pattern recognition : A case study for the 2008 mw 5.4 chino hills earthquake, *Geophysical Research Letters*, *43*(16), 8492–8498. [26](#)
- Kawamoto, S., Y. Hiyama, Y. Ohta, and T. Nishimura (2016), First result from the geonet real-time analysis system (regard) : the case of the 2016 kumamoto earthquakes, *Earth, Planets and Space*, *68*(1), 1–12. [21](#)
- Kawamoto, S., Y. Ohta, Y. Hiyama, M. Todoriki, T. Nishimura, T. Furuya, Y. Sato, T. Yahagi, and K. Miyagawa (2017), Regard : A new guss-based real-time finite fault modeling system for geonet, *Journal of Geophysical Research : Solid Earth*, *122*(2), 1324–1349. [21](#)

- Kennett, B., and E. Engdahl (1991), Traveltimes for global earthquake location and phase identification, *Geophysical Journal International*, 105(2), 429–465. [7](#)
- Kilb, D., and J. Gomberg (1999), The initial subevent of the 1994 northridge, california, earthquake : Is earthquake size predictable ?, *Journal of Seismology*, 3(4), 409–420. [84](#)
- King, R. (1995), Documentation for the gamit gps analysis software, *Mass. Inst. of Technol.* [4](#)
- Kohler, M. D., E. S. Cochran, D. Given, S. Guiwits, D. Neuhauser, I. Henson, R. Hartog, P. Bodin, V. Kress, S. Thompson, et al. (2018), Earthquake early warning shakealert system : West coast wide production prototype, *Seismological Research Letters*, 89(1), 99–107. [83](#)
- Kong, Q., R. M. Allen, and L. Schreier (2016a), Myshake : Initial observations from a global smartphone seismic network, *Geophysical Research Letters*, 43(18), 9588–9594. [20](#)
- Kong, Q., R. M. Allen, L. Schreier, and Y.-W. Kwon (2016b), Myshake : A smartphone seismic network for earthquake early warning and beyond, *Science advances*, 2(2), e1501,055. [20](#), [26](#)
- Lasserre, C., G. Peltzer, F. Crampé, Y. Klinger, J. Van der Woerd, and P. Tapponnier (2005), Coseismic deformation of the 2001 mw= 7.8 kokoxili earthquake in tibet, measured by synthetic aperture radar interferometry, *Journal of Geophysical Research : Solid Earth*, 110(B12). [5](#)
- Lay, T. (2018), A review of the rupture characteristics of the 2011 tohoku-oki mw 9.1 earthquake, *Tectonophysics*, 733, 4–36. [9](#)
- Licciardi, A., Q. Bletery, B. Rouet-Leduc, J.-P. Ampuero, and K. Juhel (2022), Instantaneous tracking of earthquake growth with elastogravity signals, *Nature*, 606, 319–324. [85](#)
- Lin, J.-T., D. Melgar, A. Thomas, and J. Searcy (2021), Early warning for great earthquakes from characterization of crustal deformation patterns with deep learning, *Journal of Geophysical Research : Solid Earth*, 126(10), e2021JB022,703. [26](#)
- Loveless, J. P., and B. J. Meade (2011), Spatial correlation of interseismic coupling and coseismic rupture extent of the 2011 mw= 9.0 tohoku-oki earthquake, *Geophysical Research Letters*, 38(17). [12](#)
- Maeda, T., T. Furumura, S. Sakai, and M. Shinohara (2011), Significant tsunami observed at ocean-bottom pressure gauges during the 2011 off the pacific coast of tohoku earthquake, *Earth, Planets and Space*, 63(7), 803–808. [5](#)

- Manighetti, I., M. Campillo, S. Bouley, and F. Cotton (2007), Earthquake scaling, fault segmentation, and structural maturity, *Earth and Planetary Science Letters*, 253(3-4), 429–438. [27](#), [28](#)
- Manighetti, I., D. Zigone, M. Campillo, and F. Cotton (2009), Self-similarity of the largest-scale segmentation of the faults : Implications for earthquake behavior, *Earth and Planetary Science Letters*, 288(3-4), 370–381. [28](#)
- Mansinha, L., and D. Smylie (1971), The displacement fields of inclined faults, *Bulletin of the Seismological Society of America*, 61(5), 1433–1440. [6](#)
- Marone, C. (1998), Laboratory-derived friction laws and their application to seismic faulting, *Annual Review of Earth and Planetary Sciences*, 26(1), 643–696. [14](#)
- Marone, C. J., C. Scholtz, and R. Bilham (1991), On the mechanics of earthquake afterslip, *Journal of Geophysical Research : Solid Earth*, 96(B5), 8441–8452. [15](#)
- Marzocchi, W., M. Taroni, and G. Falcone (2017), Earthquake forecasting during the complex amatrice-norcia seismic sequence, *Science advances*, 3(9), e1701,239. [17](#)
- Massonnet, D., M. Rossi, C. Carmona, F. Adragna, G. Peltzer, K. Feigl, and T. Rabaute (1993), The displacement field of the landers earthquake mapped by radar interferometry, *nature*, 364(6433), 138–142. [5](#)
- McCann, M. T., K. H. Jin, and M. Unser (2017), Convolutional neural networks for inverse problems in imaging : A review, *IEEE Signal Processing Magazine*, 34(6), 85–95. [26](#)
- Meier, M.-A. (2017), How “good” are real-time ground motion predictions from earthquake early warning systems ?, *Journal of Geophysical Research : Solid Earth*, 122(7), 5561–5577. [21](#), [84](#)
- Meier, M.-A., T. Heaton, and J. Clinton (2015), The gutenber algorithm : Evolutionary bayesian magnitude estimates for earthquake early warning with a filter bank, *Bulletin of the Seismological Society of America*, 105(5), 2774–2786. [20](#)
- Meier, M.-A., J. Ampuero, and T. H. Heaton (2017), The hidden simplicity of subduction megathrust earthquakes, *Science*, 357(6357), 1277–1281. [23](#), [84](#)
- Melgar, D., T. I. Melbourne, B. W. Crowell, J. Geng, W. Szeliga, C. Scrivner, M. Santillan, and D. E. Goldberg (2020), Real-time high-rate gnss displacements : Performance demonstration

- during the 2019 ridgecrest, california, earthquakes, *Seismological Research Letters*, 91(4), 1943–1951. [4](#)
- Metois, M., C. Vigny, and A. Socquet (2016), Interseismic coupling, megathrust earthquakes and seismic swarms along the chilean subduction zone (38–18 s), *Pure and Applied Geophysics*, 173(5), 1431–1449. [12](#)
- Michel, S., A. Gualandi, and J.-P. Avouac (2019), Similar scaling laws for earthquakes and cascadia slow-slip events, *Nature*, 574(7779), 522–526. [14](#)
- Mignan, A. (2015), Modeling aftershocks as a stretched exponential relaxation, *Geophysical Research Letters*, 42(22), 9726–9732. [16](#)
- Mignan, A. (2016), Reply to “comment on ‘revisiting the 1894 omori aftershock dataset with the stretched exponential function’ by a. mignan” by s. hainzl and a. christophersen, *Seismological Research Letters*, 87(5), 1134–1137. [16](#)
- Miller, M. M., T. Melbourne, D. J. Johnson, and W. Q. Sumner (2002), Periodic slow earthquakes from the cascadia subduction zone, *Science*, 295(5564), 2423–2423. [12](#)
- Minson, S., M. Simons, and J. Beck (2013), Bayesian inversion for finite fault earthquake source models i—theory and algorithm, *Geophysical Journal International*, 194(3), 1701–1726. [9](#)
- Minson, S. E., J. R. Murray, J. O. Langbein, and J. S. Gombert (2014), Real-time inversions for finite fault slip models and rupture geometry based on high-rate gps data, *Journal of Geophysical Research : Solid Earth*, 119(4), 3201–3231. [21](#)
- Minson, S. E., M.-A. Meier, A. S. Baltay, T. C. Hanks, and E. S. Cochran (2018), The limits of earthquake early warning : Timeliness of ground motion estimates, *Science advances*, 4(3), eaaq0504. [84](#)
- Montagner, J.-P., K. Juhel, M. Barsuglia, J. P. Ampuero, E. Chassande-Mottin, J. Harms, B. Whiting, P. Bernard, E. Clévéde, and P. Lognonné (2016), Prompt gravity signal induced by the 2011 tohoku-oki earthquake, *Nature communications*, 7(1), 1–7. [22](#)
- Mori, J., and H. Kanamori (1996), Initial rupture of earthquakes in the 1995 ridgecrest, california sequence, *Geophysical Research Letters*, 23(18), 2437–2440. [84](#)
- Mousavi, S. M., Y. Sheng, W. Zhu, and G. C. Beroza (2019), Stanford earthquake dataset (stead) : A global data set of seismic signals for ai, *IEEE Access*, 7, 179,464–179,476. [112](#)



- Nabelek, J. L. (1984), Determination of earthquake source parameters from inversion of body waves, Ph.D. thesis, M. I. T., Dept. of Earth, Atmospheric and Planetary Sciences. [6](#)
- Nissen-Meyer, T., M. van Driel, S. C. Stähler, K. Hosseini, S. Hempel, L. Auer, A. Colombi, and A. Fournier (2014), Axisem : broadband 3-d seismic wavefields in axisymmetric media, *Solid Earth*, *5*(1), 425–445. [6](#)
- Nocquet, J.-M., and E. Calais (2004), Geodetic measurements of crustal deformation in the western mediterranean and europe, *Pure and applied geophysics*, *161*(3), 661–681. [4](#)
- Obara, K. (2002), Nonvolcanic deep tremor associated with subduction in southwest japan, *Science*, *296*(5573), 1679–1681. [12](#)
- Obara, K., and A. Kato (2016), Connecting slow earthquakes to huge earthquakes, *Science*, *353*(6296), 253–257. [13](#), [14](#), [18](#), [61](#)
- Ochoa, L. H., L. F. Niño, and C. A. Vargas (2018), Fast magnitude determination using a single seismological station record implementing machine learning techniques, *Geodesy and Geodynamics*, *9*(1), 34–41. [26](#)
- Ogata, Y. (1988), Statistical models for earthquake occurrences and residual analysis for point processes, *Journal of the American Statistical association*, *83*(401), 9–27. [16](#)
- Ogata, Y. (1998), Space-time point-process models for earthquake occurrences, *Annals of the Institute of Statistical Mathematics*, *50*(2), 379–402. [16](#)
- Ogata, Y., and K. Katsura (2014), Comparing foreshock characteristics and foreshock forecasting in observed and simulated earthquake catalogs, *Journal of Geophysical Research : Solid Earth*, *119*(11), 8457–8477. [17](#)
- Okada, Y. (1985), Surface deformation due to shear and tensile faults in a half-space, *Bulletin of the seismological society of America*, *75*(4), 1135–1154. [6](#)
- Omori, F. (1894), On the after-shocks of earthquakes, *J. Coll. Sci., Imp. Univ., Japan*, *7*, 111–200. [16](#)
- Ozawa, S., T. Nishimura, H. Suito, T. Kobayashi, M. Tobita, and T. Imakiire (2011), Coseismic and postseismic slip of the 2011 magnitude-9 tohoku-oki earthquake, *Nature*, *475*(7356), 373–376. [4](#)

- Perol, T., M. Gharbi, and M. Denolle (2018), Convolutional neural network for earthquake detection and location, *Science Advances*, 4(2), e1700,578. [26](#)
- Perrin, C., I. Manighetti, J.-P. Ampuero, F. Cappa, and Y. Gaudemer (2016), Location of largest earthquake slip and fast rupture controlled by along-strike change in fault structural maturity due to fault growth, *Journal of Geophysical Research : Solid Earth*, 121(5), 3666–3685. [28](#)
- Pollitz, F. F. (1996), Coseismic deformation from earthquake faulting on a layered spherical earth, *Geophysical Journal International*, 125(1), 1–14. [6](#)
- Radiguet, M., F. Cotton, I. Manighetti, M. Campillo, and J. Douglas (2009), Dependency of near-field ground motions on the structural maturity of the ruptured faults, *Bulletin of the Seismological Society of America*, 99(4), 2572–2581. [28](#)
- Ragon, T., A. Sladen, and M. Simons (2018), Accounting for uncertain fault geometry in earthquake source inversions–i : theory and simplified application, *Geophysical Journal International*, 214(2), 1174–1190. [9](#)
- Ragon, T., A. Sladen, and M. Simons (2019a), Accounting for uncertain fault geometry in earthquake source inversions–ii : application to the m w 6.2 amatrice earthquake, central italy, *Geophysical Journal International*, 218(1), 689–707. [9](#)
- Ragon, T., A. Sladen, Q. Bletery, M. Vergnolle, O. Cavalié, A. Avallone, J. Balestra, and B. Delouis (2019b), Joint inversion of coseismic and early postseismic slip to optimize the information content in geodetic data : Application to the 2009 m w 6.3 l’aquila earthquake, central italy, *Journal of Geophysical Research : Solid Earth*, 124(10), 10,522–10,543. [11](#), [60](#)
- Ragon, T., M. Simons, Q. Bletery, O. Cavalié, and E. Fielding (2021), A stochastic view of the 2020 elaziğ mw 6.8 earthquake (turkey), *Geophysical Research Letters*, 48(3), e2020GL090,704. [9](#), [60](#)
- Reddy, R., and R. R. Nair (2013), The efficacy of support vector machines (svm) in robust determination of earthquake early warning magnitudes in central japan, *Journal of Earth System Science*, 122(5), 1423–1434. [26](#)
- Rogers, G., and H. Dragert (2003), Episodic tremor and slip on the cascadia subduction zone : The chatter of silent slip, *Science*, 300(5627), 1942–1943. [12](#)

- Rolland, L. M., P. Lognonné, E. Astafyeva, E. A. Kherani, N. Kobayashi, M. Mann, and H. Munekane (2011), The resonant response of the ionosphere imaged after the 2011 off the pacific coast of tohoku earthquake, *Earth, planets and space*, *63*(7), 853–857. [5](#)
- Romano, F., E. Trasatti, S. Lorito, C. Piromallo, A. Piatanesi, Y. Ito, D. Zhao, K. Hirata, P. Lanucara, and M. Cocco (2014), Structural control on the tohoku earthquake rupture process investigated by 3d fem, tsunami and geodetic data, *Scientific reports*, *4*(1), 1–11. [6](#)
- Rong, K., C. E. Yoon, K. J. Bergen, H. Elezabi, P. Bailis, P. Levis, and G. C. Beroza (2018), Locality-sensitive hashing for earthquake detection : A case study of scaling data-driven science, *arXiv preprint arXiv :1803.09835*. [26](#)
- Ross, Z. E., M.-A. Meier, E. Hauksson, and T. H. Heaton (2018a), Generalized seismic phase detection with deep learning, *Bulletin of the Seismological Society of America*, *108*(5A), 2894–2901. [26](#)
- Ross, Z. E., M.-A. Meier, and E. Hauksson (2018b), P wave arrival picking and first-motion polarity determination with deep learning, *Journal of Geophysical Research : Solid Earth*, *123*(6), 5120–5129. [26](#)
- Ross, Z. E., Y. Yue, M.-A. Meier, E. Hauksson, and T. H. Heaton (2019a), Phaselink : A deep learning approach to seismic phase association, *Journal of Geophysical Research : Solid Earth*, *124*(1), 856–869. [26](#)
- Ross, Z. E., D. T. Trugman, E. Hauksson, and P. M. Shearer (2019b), Searching for hidden earthquakes in southern california, *Science*, *364*(6442), 767–771. [26](#)
- Rouet-Leduc, B., C. Hulbert, N. Lubbers, K. Barros, C. J. Humphreys, and P. A. Johnson (2017), Machine learning predicts laboratory earthquakes, *Geophysical Research Letters*, *44*(18), 9276–9282. [26](#)
- Rouet-Leduc, B., C. Hulbert, D. C. Bolton, C. X. Ren, J. Riviere, C. Marone, R. A. Guyer, and P. A. Johnson (2018), Estimating fault friction from seismic signals in the laboratory, *Geophysical Research Letters*, *45*(3), 1321–1329. [26](#)
- Rouet-Leduc, B., C. Hulbert, and P. A. Johnson (2019), Continuous chatter of the cascadia subduction zone revealed by machine learning, *Nature Geoscience*, *12*(1), 75–79. [26](#)
- Rousset, B., C. Lasserre, N. Cubas, S. Graham, M. Radiguet, C. DeMets, A. Socquet, M. Campillo, V. Kostoglodov, E. Cabral-Cano, et al. (2016), Lateral variations of interplate coupling

- along the mexican subduction interface : Relationships with long-term morphology and fault zone mechanical properties, *Pure and Applied Geophysics*, 173(10), 3467–3486. [11](#), [12](#)
- Rousset, B., M. Campillo, C. Lasserre, W. B. Frank, N. Cotte, A. Walpersdorf, A. Socquet, and V. Kostoglodov (2017), A geodetic matched filter search for slow slip with application to the mexico subduction zone, *Journal of Geophysical Research : Solid Earth*, 122(12), 10–498. [14](#)
- Rousset, B., R. Bürgmann, and M. Campillo (2019), Slow slip events in the roots of the san andreas fault, *Science advances*, 5(2), eaav3274. [14](#)
- Rubin, A. M., and J.-P. Ampuero (2005), Earthquake nucleation on (aging) rate and state faults, *Journal of Geophysical Research : Solid Earth*, 110(B11). [15](#), [18](#)
- Ruhl, C., D. Melgar, A. Chung, R. Grapenthin, and R. Allen (2019), Quantifying the value of real-time geodetic constraints for earthquake early warning using a global seismic and geodetic data set, *Journal of Geophysical Research : Solid Earth*, 124(4), 3819–3837. [21](#)
- Ruina, A. (1983), Slip instability and state variable friction laws, *Journal of Geophysical Research : Solid Earth*, 88(B12), 10,359–10,370. [14](#)
- Ruiz, S., M. Metois, A. Fuenzalida, J. Ruiz, F. Leyton, R. Grandin, C. Vigny, R. Madariaga, and J. Campos (2014), Intense foreshocks and a slow slip event preceded the 2014 iquique mw 8.1 earthquake, *Science*, 345(6201), 1165–1169. [18](#)
- Rydelek, P., and S. Horiuchi (2006), Is earthquake rupture deterministic?, *Nature*, 442(7100), E5–E6. [84](#)
- Rydelek, P., C. Wu, and S. Horiuchi (2007), Comment on “earthquake magnitude estimation from peak amplitudes of very early seismic signals on strong motion records” by aldo zollo, maria lancieri, and stefan nielsen, *Geophysical Research Letters*, 34(20). [84](#)
- Sato, T., and H. Kanamori (1999), Beginning of earthquakes modeled with the griffith’s fracture criterion, *Bulletin of the Seismological Society of America*, 89(1), 80–93. [84](#)
- Satriano, C., L. Elia, C. Martino, M. Lancieri, A. Zollo, and G. Iannaccone (2011), Presto, the earthquake early warning system for southern italy : Concepts, capabilities and future perspectives, *Soil Dynamics and Earthquake Engineering*, 31(2), 137–153. [20](#)
- Schellart, W. P., and N. Rawlinson (2013), Global correlations between maximum magnitudes of subduction zone interface thrust earthquakes and physical parameters of subduction zones, *Physics of the Earth and Planetary Interiors*, 225, 41–67. [28](#)

- Scholz, C. (1968), The frequency-magnitude relation of microfracturing in rock and its relation to earthquakes, *Bulletin of the seismological society of America*, 58(1), 399–415. [17](#)
- Scholz, C. H. (2019), *The mechanics of earthquakes and faulting*, Cambridge university press. [15](#)
- Scholz, C. H., L. R. Sykes, and Y. P. Aggarwal (1973), Earthquake prediction : A physical basis, *Science*, 181(4102), 803–810. [19](#)
- Schorlemmer, D., S. Wiemer, and M. Wyss (2005), Variations in earthquake-size distribution across different stress regimes, *Nature*, 437(7058), 539–542. [17](#)
- Schwartz, S. Y., and J. M. Rokosky (2007), Slow slip events and seismic tremor at circum-pacific subduction zones, *Reviews of Geophysics*, 45(3). [12](#), [18](#)
- Serdar Kuyuk, H., R. M. Allen, H. Brown, M. Hellweg, I. Henson, and D. Neuhauser (2014), Designing a network-based earthquake early warning algorithm for california : Elarms-2, *Bulletin of the Seismological Society of America*, 104(1), 162–173. [20](#)
- Sheen, D.-H., J.-H. Park, H.-C. Chi, E.-H. Hwang, I.-S. Lim, Y. J. Seong, and J. Pak (2017), The first stage of an earthquake early warning system in south korea, *Seismological Research Letters*, 88(6), 1491–1498. [20](#)
- Shelly, D. R., G. C. Beroza, S. Ide, and S. Nakamura (2006), Low-frequency earthquakes in shikoku, japan, and their relationship to episodic tremor and slip, *Nature*, 442(7099), 188–191. [13](#)
- Shelly, D. R., G. C. Beroza, and S. Ide (2007), Non-volcanic tremor and low-frequency earthquake swarms, *Nature*, 446(7133), 305–307. [12](#), [62](#)
- Sladen, A., D. Rivet, J.-P. Ampuero, L. De Barros, Y. Hello, G. Calbris, and P. Lamare (2019), Distributed sensing of earthquakes and ocean-solid earth interactions on seafloor telecom cables, *Nature communications*, 10(1), 1–8. [5](#)
- Spada, M., T. Tormann, S. Wiemer, and B. Enescu (2013), Generic dependence of the frequency-size distribution of earthquakes on depth and its relation to the strength profile of the crust, *Geophysical research letters*, 40(4), 709–714. [17](#)
- Steketee, J. (1958), On volterra’s dislocations in a semi-infinite elastic medium, *Canadian Journal of Physics*, 36(2), 192–205. [6](#)

- Stevens, V., and J. Avouac (2015), Interseismic coupling on the main himalayan thrust, *Geophysical Research Letters*, *42*(14), 5828–5837. [12](#)
- Stirling, M. W., S. G. Wesnousky, and K. Shimazaki (1996), Fault trace complexity, cumulative slip, and the shape of the magnitude-frequency distribution for strike-slip faults : A global survey, *Geophysical Journal International*, *124*(3), 833–868. [28](#)
- Sun, T., and K. Wang (2015), Viscoelastic relaxation following subduction earthquakes and its effects on afterslip determination, *Journal of Geophysical Research : Solid Earth*, *120*(2), 1329–1344. [11](#)
- Sunil, A., M. S. Bagiya, Q. Bletery, and D. Ramesh (2021), Association of ionospheric signatures to various tectonic parameters during moderate to large magnitude earthquakes : case study, *Journal of Geophysical Research : Space Physics*, *126*(3), e2020JA028,709. [5](#)
- Tamaribuchi, K., Y. Yagi, B. Enescu, and S. Hirano (2018), Characteristics of foreshock activity inferred from the jma earthquake catalog, *Earth, Planets and Space*, *70*(1), 1–13. [17](#)
- Tanioka, Y., and K. Satake (1996), Tsunami generation by horizontal displacement of ocean bottom, *Geophysical research letters*, *23*(8), 861–864. [7](#)
- Thomas, A., N. M. Beeler, Q. Bletery, R. Burgmann, and D. R. Shelly (2018), Using low-frequency earthquake families on the san andreas fault as deep creepmeters, *Journal of Geophysical Research : Solid Earth*, *123*(1), 457–475. [13](#), [61](#)
- Thomas, A. M., R. M. Nadeau, and R. Bürgmann (2009), Tremor-tide correlations and near-lithostatic pore pressure on the deep san andreas fault, *Nature*, *462*(7276), 1048–1051. [13](#)
- Tibi, R., C. Young, A. Gonzales, S. Ballard, and A. Encarnacao (2017), Rapid and robust cross-correlation-based seismic signal identification using an approximate nearest neighbor method, *Bulletin of the Seismological Society of America*, *107*(4), 1954–1968. [26](#)
- Toda, S., R. S. Stein, K. Richards-Dinger, and S. B. Bozkurt (2005), Forecasting the evolution of seismicity in southern california : Animations built on earthquake stress transfer, *Journal of Geophysical Research : Solid Earth*, *110*(B5). [17](#)
- Tormann, T., S. Wiemer, and J. L. Hardebeck (2012), Earthquake recurrence models fail when earthquakes fail to reset the stress field, *Geophysical Research Letters*, *39*(18). [17](#)



- Tormann, T., S. Wiemer, and A. Mignan (2014), Systematic survey of high-resolution b value imaging along californian faults : Inference on asperities, *Journal of Geophysical Research : Solid Earth*, *119*(3), 2029–2054. [17](#)
- Tormann, T., B. Enescu, J. Woessner, and S. Wiemer (2015), Randomness of megathrust earthquakes implied by rapid stress recovery after the japan earthquake, *Nature Geoscience*, *8*(2), 152–158. [17](#)
- Trugman, D. T., and P. M. Shearer (2018), Strong correlation between stress drop and peak ground acceleration for recent m 1–4 earthquakes in the san francisco bay area, *Bulletin of the Seismological Society of America*, *108*(2), 929–945. [26](#)
- Tsai, V. C., J.-P. Ampuero, H. Kanamori, and D. J. Stevenson (2013), Estimating the effect of earth elasticity and variable water density on tsunami speeds, *Geophysical Research Letters*, *40*(3), 492–496. [7](#)
- Tse, S. T., and J. R. Rice (1986), Crustal earthquake instability in relation to the depth variation of frictional slip properties, *Journal of Geophysical Research : Solid Earth*, *91*(B9), 9452–9472. [15](#)
- Twardzik, C., M. Vergnolle, A. Sladen, and A. Avallone (2019), Unravelling the contribution of early postseismic deformation using sub-daily gnss positioning, *Scientific reports*, *9*(1), 1–12. [11](#)
- Uchide, T., and S. Ide (2010), Scaling of earthquake rupture growth in the parkfield area : Self-similar growth and suppression by the finite seismogenic layer, *Journal of Geophysical Research : Solid Earth*, *115*(B11). [84](#)
- Utsu, T. (1961), A statistical study on the occurrence of aftershocks, *Geophys. Mag.*, *30*, 521–605. [16](#)
- Utsu, T., Y. Ogata, et al. (1995), The centenary of the omori formula for a decay law of aftershock activity, *Journal of Physics of the Earth*, *43*(1), 1–33. [16](#)
- Valera, M., Z. Guo, P. Kelly, S. Matz, V. A. Cantu, A. G. Percus, J. D. Hyman, G. Srinivasan, and H. S. Viswanathan (2018), Machine learning for graph-based representations of three-dimensional discrete fracture networks, *Computational Geosciences*, *22*(3), 695–710. [26](#)

- Vallée, M., and K. Juhel (2019), Multiple observations of the prompt elastogravity signals heralding direct seismic waves, *Journal of Geophysical Research : Solid Earth*, *124*(3), 2970–2989. [23](#)
- Vallée, M., J. Charléty, A. M. Ferreira, B. Delouis, and J. Vergoz (2011), Scardec : a new technique for the rapid determination of seismic moment magnitude, focal mechanism and source time functions for large earthquakes using body-wave deconvolution, *Geophysical Journal International*, *184*(1), 338–358. [107](#)
- Vallée, M., J. P. Ampuero, K. Juhel, P. Bernard, J.-P. Montagner, and M. Barsuglia (2017), Observations and modeling of the elastogravity signals preceding direct seismic waves, *Science*, *358*(6367), 1164–1168. [22](#), [23](#)
- Villegas-Lanza, J. C., M. Chlieh, O. Cavalié, H. Tavera, P. Baby, J. Chire-Chira, and J.-M. Nocquet (2016), Active tectonics of peru : Heterogeneous interseismic coupling along the nazca megathrust, rigid motion of the peruvian sliver, and subandean shortening accommodation, *Journal of Geophysical Research : Solid Earth*, *121*(10), 7371–7394. [12](#)
- Wallace, L. M. (2020), Slow slip events in new zealand, *Annual Review of Earth and Planetary Sciences*, *48*, 175–203. [18](#)
- Watada, S. (2013), Tsunami speed variations in density-stratified compressible global oceans, *Geophysical Research Letters*, *40*(15), 4001–4006. [7](#)
- Wech, A. G. (2010), Interactive tremor monitoring, *Seismological Research Letters*, *81*(4), 664–669. [72](#)
- Wech, A. G., and K. C. Creager (2008), Automated detection and location of cascadia tremor, *Geophysical Research Letters*, *35*(20). [72](#)
- Wesnousky, S. G. (1988), Seismological and structural evolution of strike-slip faults, *Nature*, *335*(6188), 340–343. [28](#)
- Wiemer, S., and K. Katsumata (1999), Spatial variability of seismicity parameters in aftershock zones, *Journal of Geophysical Research : Solid Earth*, *104*(B6), 13,135–13,151. [17](#)
- Wiemer, S., M. Gerstenberger, and E. Hauksson (2002), Properties of the aftershock sequence of the 1999 m w 7.1 hector mine earthquake : implications for aftershock hazard, *Bulletin of the Seismological Society of America*, *92*(4), 1227–1240. [17](#)

- Wu, S., J. L. Beck, and T. H. Heaton (2013), epad : Earthquake probability-based automated decision-making framework for earthquake early warning, *Computer-Aided Civil and Infrastructure Engineering*, *28*(10), 737–752. [83](#)
- Wu, Y.-M., and H. Kanamori (2008), Development of an earthquake early warning system using real-time strong motion signals, *Sensors*, *8*(1), 1–9. [4](#)
- Wyss, M., and S. Wiemer (2000), Change in the probability for earthquakes in southern california due to the landers magnitude 7.3 earthquake, *Science*, *290*(5495), 1334–1338. [17](#)
- Yamamoto, S., P. Rydelek, S. Horiuchi, C. Wu, and H. Nakamura (2008), On the estimation of seismic intensity in earthquake early warning systems, *Geophysical research letters*, *35*(7). [84](#)
- Yamazaki, Y., Z. Kowalik, and K. F. Cheung (2009), Depth-integrated, non-hydrostatic model for wave breaking and run-up, *International journal for numerical methods in fluids*, *61*(5), 473–497. [7](#)
- Yamazaki, Y., K. F. Cheung, and Z. Kowalik (2011), Depth-integrated, non-hydrostatic model with grid nesting for tsunami generation, propagation, and run-up, *International Journal for Numerical Methods in Fluids*, *67*(12), 2081–2107. [7](#)
- Yin, L., J. Andrews, and T. Heaton (2018), Reducing process delays for real-time earthquake parameter estimation—an application of kd tree to large databases for earthquake early warning, *Computers & geosciences*, *114*, 22–29. [26](#)
- Yoon, C. E., O. O’Reilly, K. J. Bergen, and G. C. Beroza (2015), Earthquake detection through computationally efficient similarity search, *Science advances*, *1*(11), e1501,057. [26](#)
- Zechar, J. D., W. Marzocchi, and S. Wiemer (2016), Operational earthquake forecasting in europe : progress, despite challenges, *Bulletin of Earthquake Engineering*, *14*(9), 2459–2469. [19](#)
- Zhang, J., H. Zhang, E. Chen, Y. Zheng, W. Kuang, and X. Zhang (2014), Real-time earthquake monitoring using a search engine method, *Nature communications*, *5*(1), 1–9. [26](#)
- Zhang, S., R. Wang, T. Dahm, S. Zhou, and S. Heimann (2020), Prompt elasto-gravity signals (pegs) and their potential use in modern seismology, *Earth and Planetary Science Letters*, *536*, 116,150. [110](#)

- Zhu, L., and L. A. Rivera (2002), A note on the dynamic and static displacements from a point source in multilayered media, *Geophysical Journal International*, 148(3), 619–627. [6](#)
- Zhu, W., and G. C. Beroza (2019), Phasenet : a deep-neural-network-based seismic arrival-time picking method, *Geophysical Journal International*, 216(1), 261–273. [26](#)
- Zollo, A., M. Lancieri, and S. Nielsen (2006), Earthquake magnitude estimation from peak amplitudes of very early seismic signals on strong motion records, *Geophysical Research Letters*, 33(23). [84](#)

## Références bibliographiques

---

---

# Annexe

## 1 Curriculum Vitae

### Parcours académique

Chargé de recherche, IRD, Géoazur	depuis 2018
Postdoctoral Fellow, University of Oregon (USA)	2016 - 2018
Doctorant chargé d'enseignement, Université Nice Sophia Antipolis	2012 - 2015
Visiting student researcher, California Institute of Technology (USA)	2011 - 2012

### Diplômes

Doctorat, Université Nice Sophia Antipolis	2015
Diplôme d'Ingénieur, École et Observatoire des Sciences de la Terre	2011
Master, École et Observatoire des Sciences de la Terre	2011

### Projets financés en tant que PI

ERC Starting Grant EARLI (1.5 M€)	2021 - 2025
Allocations de ressources de calcul A10-A12 GENCI (233 k€)	2021 - 2023
Postdoc thématique UCA en IA (75 k€)	2019 - 2021
Allocation de Recherche pour une Thèse au Sud	2020 - 2023
Missions Longue Durée (IRD) (×3)	2021 - 2022
Soutien au Sud (10 k€)	2019
Tremplin Complex Académie d'Excellence UCA (5 k€)	2019



## Projets financés (non PI)

ANR S5 (427 k€), PI : J.-M. Nocquet Rôle : Task manager + Encadrement postdoc	2019 - 2023
ANR OSMOSE (483 k€), PI : E. Calais Rôle : Encadrement postdoc	2022 - 2025
ANR ITEC (284 k€), PI : L. Rolland Rôle : Participant	2020 - 2024
ANR E-POST (200 k€), PI : M. Vergnolle Rôle : Participant	2015 - 2019

## Encadrement

### Postdocs

<b>Andrea Licciardi.</b> Encadrement : 100% (ERC EARLI) Encadrement : 80% (postdoc UCA) Développement de PEGSnet, un algorithme d'IA pour l'alerte sismique à partir des PEGS	07/2021 - 12/2022 01/2020 - 06/2021
<b>Kévin Juhel.</b> Encadrement : 100% (ERC EARLI) Construction d'une base de données de PEGS globale exhaustive	03/2021 - 03/2024
<b>Kumar Sunil</b> (Indian Inst. of Geomag.). Encadrement : 30% Analyse de la sensibilité des signaux ionosphériques à la source sismique	03/2020 - 02/2021

### Doctorants

<b>Gabriela Arias.</b> Encadrement : 80% (ERC EARLI) Application de PEGSnet en Amérique du Sud	01/2021 - 12/2023
<b>Pablo Lara.</b> Encadrement : 80% (ARTS) Développement d'un algorithme d'IA pour l'alerte sismique au Pérou	10/2020 - 09/2023
<b>Théa Ragon.</b> Encadrement : 30% Quantification des incertitudes dans les modèles de source par inversion Bayésienne	05/2016 - 05/2019

### Masters

<b>Tyler Newton</b> (U. of Oregon). Encadrement : 30 % Détermination de l'orientation des contraintes le long de la faille de Nankai	09/2016 - 08/2018
<b>Alexander Babb</b> (U. of Oregon). Encadrement : 30 % Analyse de la sensibilité des LFEs aux marées	09/2016 - 08/2018

## Stagiaires

- Théodore Michel** (M1, Mines de Paris). Encadrement : 100% 05/2021 - 07/2021  
Optimisation d’algorithmes de Deep Learning pour le débruitage de PEGS
- Lionel Mattéo** (L3, U. Nice Sophia Antipolis). Encadrement : 80% 05/2014 - 06/2014  
Quantification de l’excitation tsunami par la déformation horizontale du fond de l’océan

## Enseignements

<b>Monitorat (Université Nice Sophia Antipolis).</b> Total : 187 h EqTD		2012 - 2015
Rhéologie et Sismologie, L3	12 h/an	2013 - 2015
Méthodes numériques et gestion des données, L3	26 h/an	2013 - 2015
Physique de la Terre, L2	13.5 h/an	2013 - 2015
Outils Mathématiques, L2	9 h/an	2013 - 2015
Rhéologie et Sismologie, L3	36 h/an	2012 - 2013
Physique de la Terre, L2	20 h/an	2012 - 2013
Outils Mathématiques, L2	10 h/an	2012 - 2013

## Cours magistraux ponctuels

Introduction à l’IA pour les Géosciences, M2 (U. Quisqueya, Haïti)	4 h	2022
Volcanoes and Earthquakes, Geology 306 (U. of Oregon, USA)	4 h	2016
Fault Mechanics, Geology 467 (U. of Oregon, USA)	4 h	2016

## Animation de la recherche

PI du projet ERC EARLI		2021 - 2025
Organisateur des séminaires à Géoazur		2018 - 2021
Membre du comité scientifique du workshop “Artificial Intelligence for waves” (AI4W)		2022
Membre du panel pour l’obtention du label européen HRS4R à l’IRD		2019
Examineur d’une thèse :		
Emmanuel Caballero (Université de Strasbourg, 2022)		
Membre de 3 comités de thèse :		
Audrey Chouli (Université Grenoble Alpes, 2021 - 2024)		
Philippe Danré (Université Côte d’Azur, 2020 - 2023)		
Daniel Mata (Université Côte d’Azur, 2019 - 2022)		

Reviewer pour les journaux : Science, PNAS, Nature Com., EPSL, GRL, EPS, JGR : Solid

## Annexe

---

Earth, GJI, Pure Appl. Geophys., Front. Earth Sci.

Reviewer pour les agences de financement : CNES, NERC (UK)

### Prix

Prix d'Excellence de l'Université Côte d'Azur 2020

### Diffusion scientifique

#### Conférences grand public

De l'IA pour anticiper les tremblements de terre. *Science pour tous 06*. 2022

L'IA dans la Science d'aujourd'hui. *Festival Nice fictions*. 2021

#### Interviews TV

IA, big data et numérique : l'algorithme dans la peau. *L'Esprit Sorcier*. 2021

De l'IA pour prévenir les séismes. *Le Journal d'Arte*. 2021

#### Interviews radio

Pourra-t-on bientôt mieux prédire les séismes? *RFI*. 2022

U of O researchers publish new theory on mega-quakes. *KLCC (USA)*. 2016

#### Interviews presse écrite

Des nouvelles méthodes pour avertir des séismes, *La Croix*. 2022

Une intelligence artificielle pour parer aux tsunamis, *l'Humanité*. 2022

Un signal éclair pour détecter les séismes, *Le Monde*. 2022

Un algorithme pour mieux anticiper les tsunamis. *AFP*. 2022

Une IA capable de détecter en temps réel un signal précoce de séisme. *Le Figaro*. 2022

Catastrophes naturelles : des chercheurs ont découvert comment mieux anticiper la taille des tsunamis. *Le Parisien*. 2022

La prévision des tsunamis devrait faire un grand pas. *Le Temps*. 2022

Keeping one step ahead of earthquakes. *Horizon (UE)*. 2021

Horizon 2040 : 4 grands défis pour demain. *Ça m'intéresse*. 2020

Séismes : l'IA redonne l'espoir de les prédire! *Science et Vie*. 2019

Les mégaséismes, une affaire de géométrie. *La Recherche*. 2017

La géométrie des zones de subduction, un indicateur des méga-séismes. *Pour la Science*. 2016

#### Échanges chercheur-journaliste (programme AJSPI)

1 semaine passée dans la rédaction du journal *Libération* 2022

Accueil (1 semaine) d'une journaliste du journal *La croix* 2022

## Présentations invitées

European Geophysical Union (EGU) General Assembly, Vienne (Autriche)	2021
Seismological Society of America (SSA) Annual Meeting, Denver (USA)	2017
American Geophysical Union (AGU) Fall Meeting, San Francisco (USA)	2016
US-Japan Cooperative Program in Natural Resources (UJNR) Meeting, Napa (USA)	2016

## Séminaires invités

Instituto Geofísico del Perú (Pérou)	2021
Portland State University (USA)	2018
University of California Berkeley (USA)	2017
USGS Earthquake Science Center (USA)	2017
Institut de Physique du Globe de Strasbourg	2017
Ecole Normale Supérieure de Paris	2017
USGS Cascades Volcano Observatory (USA)	2016
Institut des Sciences de la Terre de Grenoble	2015

## 2 Liste des publications

\* : articles dont le premier auteur est un doctorant ou post-doctorant encadré ou co-encadré

- \* **16.** Licciardi A., **Q. Bletery**, B. Rouet-Leduc, J.-P. Ampuero and K. Juhel (2022). Instantaneous tracking of earthquake growth using Elasto-Gravity Signals. *Nature*, 606, 319–324.
- 15.** Calais E., S. Symithe, T. Monfret, B. Delouis, A. Lomax, F. Courboulex, J.P. Ampuero, P. Lara, **Q. Bletery**, J. Chèze, F. Peix, A. Deschamps, B. de Lépinay, B. Raimbault, R. Jolivet, S. Paul, S. St-Fleur, D. Boisson, Y. Fukushima, Z. Duputel, L. Xu and L. Meng (2022). Citizen seismology helps decipher the 2021 Haiti earthquake. *Science*, 376, 6590, 283–287.
- \* **14.** Sunil A. S., M. Bagiya, **Q. Bletery** and D. Ramesh (2021). Association of ionospheric signatures to various tectonic parameters during moderate to large magnitude earthquakes : case study. *Journal of Geophysical Research : Space Physics*, 126(3), e2020JA028709.
- \* **13.** Ragon T., M. Simons, **Q. Bletery**, O. Cavalié and E. Fielding (2021). A stochastic view of the 2020 Elazığ Mw 6.8 earthquake. *Geophysical Research Letters*, 48(3), e2020GL090704.

12. **Bletery Q.**, O. Cavalié, J.-M. Nocquet and T. Ragon (2020). Distribution of interseismic coupling along the North and East Anatolian Faults inferred from InSAR and GPS data. *Geophysical Research Letters*, 47(16), e2020GL087775.
11. **Bletery, Q.** and J.-M. Nocquet (2020). Slip bursts during coalescence of slow slip events in Cascadia. *Nature Communications*, 11(1), 1-6.
10. Jolivet, R., M. Simons, Z. Duputel, J.-A. Olive, H. Bhat and **Q. Bletery** (2020). Interseismic loading of subduction megathrust drives long term uplift in northern Chile. *Geophysical Research Letters*, 47(8), e2019GL085377.
9. Bagiya M. S., D. Thomas, E. Astafayeva, **Q. Bletery**, P. Lognonné, D. S. Ramesh (2020). The Ionospheric view of the 2011 Tohoku-Oki earthquake seismic source : the first 60 seconds of the rupture. *Scientific Reports*, 10(1), 1-15.
- \* 8. Ragon, T., A. Sladen, **Q. Bletery**, M. Vergnolle, O. Cavalié, A. Avallone, J. Balestra and B. Delouis (2019). Joint inversion of co-seismic and early post-seismic slip to optimize the information content in geodetic data : Application to the 2009 Mw 6.3 L'Aquila earthquake, Central Italy. *Journal of Geophysical Research : Solid Earth*, 124(10), 10522-10543.
7. Thomas, A. M., N. M. Beeler, **Q. Bletery**, R. Bürgmann and D. R. Shelly (2018). Using low frequency earthquake families on the San Andreas as deep creep meters, *Journal of Geophysical Research : Solid Earth*, 23(1), 457-475.
6. **Bletery, Q.**, A. M. Thomas, A. W. Rempel and J. L. Hardebeck (2017). Imaging shear strength along subduction faults, *Geophysical Research Letters*, 44(22), 11-329.
5. **Bletery, Q.**, A. M. Thomas, J. C. Hawthorne, R. M. Skarbek, A. W. Rempel and R. D. Krogstad (2017). Characteristics of secondary slip fronts associated with slow earthquakes in Cascadia, *Earth and Planetary Science Letters*, 463, 212-220.
4. **Bletery, Q.**, A. M. Thomas, A. W. Rempel, L. Karlstrom, A. Sladen and L. De Barros (2016). Mega-earthquakes rupture flat megathrusts, *Science*, 354, 6315, 1027-1031.
3. **Bletery, Q.**, A. Sladen, J. Jiang and M. Simons (2016). A Bayesian source model for the great 2004 Sumatra-Andaman earthquake, *Journal of Geophysical Research : Solid Earth*,

121(7), 5116–5135.

**2. Bletery, Q.**, A. Sladen, B. Delouis and L. Mattéo (2015). Quantification of tsunami bathymetry effect on finite fault slip inversion, *Pure and Applied Geophysics*, 172(12), 3655–3670.

**1. Bletery, Q.**, A. Sladen, B. Delouis, M. Vallée, J.-M. Nocquet, L. Rolland and J. Jiang (2014). A detailed source model for the  $M_w$ 9.0 Tohoku-Oki earthquake reconciling geodesy, seismology and tsunami records. *Journal of Geophysical Research : Solid Earth*, 119(10), 7636–7653.